Turbulent Flow Visualization over Surface-mounted Finite-height Cylinders and Square Prisms

A Thesis Submitted to the
College of Graduate and Postdoctoral Studies
in Partial Fulfillment of the Requirements
for the degree of Doctor of Philosophy
in the Department of Mechanical Engineering
University of Saskatchewan
Saskatoon

By
Rajat Chakravarty

Permission to Use

In presenting this thesis in partial fulfilment of the requirements for a Postgraduate degree from the University of Saskatchewan, I agree that the Libraries of this University may make it freely available for inspection. I further agree that permission for copying of this thesis in any manner, in whole or in part, for scholarly purposes may be granted by the professors who supervised my thesis work or, in their absence, by the Head of the Department or the Dean of the College in which my thesis work was done. It is understood that any copying or publication or use of this thesis or parts thereof for financial gain shall not be allowed without my written permission. It is also understood that due recognition shall be given to me and to the University of Saskatchewan in any scholarly use which may be made of any material in my thesis.

Requests for permission to copy or to make other use of material in this thesis in whole or part should be addressed to:

Head of the Department of Mechanical Engineering
University of Saskatchewan
57 Campus Drive
Saskatoon, Saskatchewan S7N 5A9
Canada

OR

Dean
College of Graduate and Postdoctoral Studies
University of Saskatchewan
116 Thorvaldson Building, 110 Science Place
Saskatoon, Saskatchewan S7N 5C9
Canada

Abstract

The study of turbulent flows over surface-mounted, finite-height bluff bodies like cylinders and square prisms have various engineering and industrial applications. The flow field around and in the wake of these bodies is sufficiently complex due to the interactions of the ground plane boundary layer with the separating shear layers from the free end and the sides of these bodies. As such straightforward geometries produce large, complex wakes, there has been increased interest in the literature in the past few decades on examining this flow field experimentally. Recent advancements in computational power have also facilitated the numerical calculation of these flows at higher spatial and temporal resolutions, which were otherwise inestimable by experiments alone. However, the instantaneous flow field in the wake, and specifically above the free end, which is a major contributor to the three-dimensionality of this flow field, has not been well understood.

Beyond numerical simulations or experiments, a modern challenge in turbulence research has been to identify and classify the instantaneous energetic structures ensconced in a turbulent flow field. Velocity gradient methods like the swirling strength criterion and the Q-criterion have successfully tendered a mathematical definition to isolate vortex structures embedded in turbulent flow. Another promising approach called proper orthogonal decomposition (POD) has also become popular in the past couple of decades, as it provides for a low-dimensional approximation of a high-dimensional turbulent flow field. Thus, the aim of this thesis is to pursue fundamental studies of the flow topologies above the free end of a surface-mounted cylinder and square prism, as well as in the wake of a surface-mounted square prism, to obtain insightful representations of these flow fields using enhanced post-processing methodologies like the swirling strength criterion, Q-criterion, and POD.

The first manuscript (presented as Chapter 2) investigated the flow field obtained from Particle Image Velocimetry (PIV) above the free end of a surface-mounted finite square prism in the vertical symmetry plane at a Reynolds number of Re_D = 4.2 x 10^4 for four different aspect ratios AR = 9, 7, 5 and 3. The POD methodology was able to capture the energetic flow features within a small number of energy modes. A qualitative analysis of the energy modes revealed a pair of shear sub-layers from the free end, as well as several vortex structures within these layers, likely evidence of Kelvin-Helmholtz (KH) instabilities. The swirling strength criterion was also used to find other structural features in the near-wake above and behind the free end, and the changes in the flow topologies with aspect ratio were demonstrated.

The second manuscript (presented in Chapter 3) investigated the flow field obtained from PIV above a surface-mounted finite cylinder in several horizontal planes close to the free end and parallel to it, at a Reynolds number of Re_D = 4.2 x 10^4 for four different aspect ratios AR = 9, 7, 5 and 3. The POD methodology was able to capture the energetic flow features within a small number of energy modes. A qualitative analysis of the energy modes revealed pairs of symmetric, side-tip counter-rotating vortices, a pair of counter-rotating vortices on each side of the midline, as well as evidence of alternate undulation of flow on either side of the midline. Flow topologies were shown to vary with aspect ratio, with a general trend

of a vertical compression of the wake at higher aspect ratios due to a stronger entrainment of flow from the outer freestream velocity and a weakening influence of the ground plane.

The third manuscript (presented in Chapter 4) investigated the time-averaged three-dimensional flow field obtained from Large Eddy Simulation (LES) around and in the wake of a surface-mounted finite square prism at a Reynolds number of $\mathrm{Re}_D = 500$ for aspect ratio AR = 3. The dominant flow features include the horseshoe vortex enclosing the base junction, and a pair of counter-rotating tip vortices emerging from the sides of the prism close to the free end. The tip vortices were shown to descend towards the ground plane in the wake owing to downwash effects. Other flow features using streamlines and vorticity were also demonstrated, including the mean recirculation zone (Bt vortex) and the base junction vortex (Nw vortex) in the vertical symmetry plane, a pair of symmetric vortices in the horizontal planes, as well as several separating shear layers and foci around the square prism surfaces.

The fourth manuscript (presented in Chapter 5) performed a 3D POD analysis on the instantaneous flow field obtained from Large Eddy Simulation (LES) in the wake of a surface-mounted finite-height square prism at a Reynolds number of $\mathrm{Re}_D = 500$ for aspect ratio AR = 3. The energetic POD energy modes revealed several dominant streamwise vortex tubes. A bifurcation of a streamwise vortex strand across the vertical symmetry plane was also observed, manifesting evidence of an alternating, upward-inclined streamwise connector strand traversing downstream and culminating in a vortex core. The POD temporal coefficients revealed strong periodicity and were used to obtain the phase information for this flow field. Accordingly, two lower order reconstructions opposite in phase were corroborated with the instantaneous flow field, further substantiating the alternating half-loop structure traversing downstream.

Acknowledgements

Firstly, I would like to truly thank my research supervisors Prof. D. J. Bergstrom and Prof. D. Sumner. Under their supervision, I was provided excellent guidance, motivation and patience for all my academic and career goals. I thank my advisory committee Prof. F. X. Wu, Prof. J. Bugg, and Prof. R. Spiteri for their kind and thoughtful feedback that have improved the quality of this thesis.

This work is supported by the technical expertise of departmental assistants S. Reinink and D. Deutscher. Honours, awards and research fellowships from the Department of Mechanical Engineering, Toyota, and invaluable financial support from the National Sciences and Engineering Research Council are appreciated. Special thanks also goes out to my labmates for their collaboration and stimulating conversations.

This work would also be incomplete without personal support from my parents and wife, Torsa Ghosal. Her companionship and encouragement throughout the completion of my research programme was priceless. Every roommate in Saskatoon has tolerated my tantrums, and I thank them for their infinite tenacity. Scholarship in teaching has been important to me, and I thank K. West and Prof. D. Sumner for being instrumental in my development as an instructor. For their leadership opportunities, I thank the Graduate Students Association, and CFCR 90.5FM for the much needed productive distractions from research.

Contents

List of Figures

List of Abbreviations and Symbols

Abbreviations

2D	Two-Dimensional
3D	Three-Dimensional
CCW	Counter ClockWise
CFD	Computational Fluid Dynamics
CFL	Courant Friedrichs Lewy
CW	ClockWise
DNS	Direct Numerical Simulation
DSM	Dynamic Smagorinsky Model
FFT	Fast Fourier Transform
FVM	Finite Volume Method
ICA	Independent Component Analysis
KH	Kelvin-Helmholtz
LES	Large Eddy Simulation
MG	Multi Grid
PIV	Particle Image Velocimetry
POD	Proper Orthogonal Decomposition
RANS	Reynolds Averaged Navier-Stokes
SGS	Sub Grid Scale

English Symbols

a_i	POD temporal coefficient
A_i	POD eigenvectors for autocorrelation matrix
AR	Aspect ratio, H/D
$\mathrm{AR}_{\mathrm{critical}}$	Critical Aspect ratio
C	POD autocovariance matrix
C_D	Mean drag coefficient
C_s	LES model parameter
D	Prism width or cylinder diameter [m]
f	Frequency [s^{-1}]
H	Prism or cylinder height [m]
M	Number of snapshots for POD reconstruction
N	Number of snapshots
Q	Q-criterion [1/s]
Re_D	Reynolds number based on prism width or cylinder diameter D
S_{ij}	Rate of strain tensor [s^-1]
t	Time [s]
u, v, w	Streamwise, cross-stream and wall-normal velocity respectively [m/s]
u^*	Streamwise fluctuating velocity [m/s]
u_i	POD Fluctuating velocity column matrix [m/s]
U	Combined POD fluctuating velocity matrix
U_∞	Freestream velocity [m/s]
v_0	Velocity matrix for the mean flow field
x, y, z	Streamwise, cross-stream and wall-normal distance from the prism/cylinder center respectively [m]

Greek Symbols

α	Angle of incidence of square prism [degrees]
δ	Boundary layer thickness [m]
Δ	LES characteristic length scale [m]
λ_i	i-th eigenvalue
λ_{cr}, λ_{ci}	Real and imaginary component of the velocity gradient eigenvalue
ν	Kinematic viscosity [m^2/s]
ρ	Density [kg/m^3]
ω_x, ω_y, ω_z	Streamwise, cross-stream and wall-normal vorticity respectively [s^{-1}]
ω_x^*, ω_y^*, ω_z^*	Streamwise, cross-stream and wall-normal normalized vorticity respectively
φ_m	Velocity matrix for POD spatial modes
τ_{ij}	Subgrid-scale stress tensor [$\mathrm{m}^2/\mathrm{s}^2$]

Chapter 1

Introduction

When I meet God, I am going to ask him two questions: Why relativity, and why turbulence? I really believe he will have an answer for the first.

Werner Heisenberg [53]

Big whorls have little whorls,
which feed on their velocity,
and little whorls have lesser whorls,
and so on to viscosity.

Lewis Richardson [67]

1.1 Motivation

The study of turbulence in fluid sciences over the last century has intrigued one and all by its sheer complexity and no comprehensive established theory yet exists. Hypotheses and technological approaches have evolved and led to significant progress in engineering applications, but there is still a way to go before arriving at a comprehensive theory.

Engineering design of structures often goes hand in hand with the analysis of the physical mechanisms of flows around them. A popular flow field that has been often investigated but yet not fully understood is the flow over surface-mounted bluff bodies like cylinders [1, 41, 45, 65, 74, 84] and square prisms [8, 73, 77, 95, 96, 101]. Such flow situations are often realized over chimneys, heat exchangers, electronic components on circuit boards, buildings and aerospace applications to name a few. Due to its significant resistance to flow, a surface-mounted bluff body experiences large pressure drag forces. The wake produced is large and

characterized by interactions with the boundary layer on the ground plane and the separating shear layers of flow from the body. These interactions offer sufficient complexity in itself and ample scope to explore turbulent flow phenomena.

A popular approach in the fluid science community to unravel these phenomena for engineering purposes has been to study a turbulent flow either experimentally or using computational simulations and analyze the dynamics of its coherent structures. While experiments on surface-mounted bluff bodies placed in wind tunnels can be performed to determine many time-averaged turbulence and aerodynamic parameters, experiments are often limited by the latitude of spatio-temporal information as well as the availability and accuracy of the required instrumentation. With rapid innovations in computational power, computational fluid dynamics (CFD) has proven to be an important complementing approach to study turbulence. By enabling the calculation of flow parameters across locations, times and resolutions that were previously unavailable and still largely immeasurable through experimental methods, CFD has become an insightful research technique for the present and future.

Modeling techniques in CFD need to account for the wide range of time and length scales that are inherent to turbulence and three such broad procedures stand classified accordingly: the Reynolds Averaged Navier-Stokes (RANS) method, Direct Numerical Simulation (DNS) and Large Eddy Simulation (LES). The RANS method involves solving the temporally averaged Navier-Stokes equations with semi-empirical turbulence modeling. While computationally efficient, the RANS method is ineffective in revealing small-scale unsteady motions and thus is unsuitable for advanced turbulence analysis. Conversely, DNS resolves all scales of motion across time and space without any turbulence modelling. While DNS is the most accurate method available owing to the absence of any model approximations, its demanding computational requirements typically exceed those readily available today. LES however seeks to optimize both approaches by resolving the large scales directly and using theoretical and semi-empirical sub-grid scale models for the small scales. Recent advancements in both RANS and LES have sought to employ more sophisticated methods to calculate the Reynolds stress tensor (e.g. the second moment closure (SMC)) or devise specialized approaches for near-wall treatments (e.g. Detached Eddy Simulation (DES)).

Post simulations or experiments, it still remains a challenge to identify and classify turbulence structures from velocity fields alone. To understand the features of a multi-scale

process (such as turbulence) as well as the nature of its coherent structures is an important part of turbulence research. The main difficulty lies in giving a mathematical definition of energetic structures. One method is to use Proper Orthogonal Decomposition (POD) to select the most energetic structures. POD is a powerful method of data analysis that helps to obtain a low-dimensional approximation of a high-dimensional process [5]. POD did not receive attention until the mid-80s due to its computational requirements as a lot of flow data were required, with large computer memory and fast processors needed to process the data. But this has changed in the last couple of decades and the use of POD in fluid flow analysis is becoming more common [43, 52, 92, 94].

In addition to statistical methods, several localized methods to identify coherent turbulent structures, like vortices, using the velocity-gradient tensor have also been used extensively in the last two decades. Two of the more popular methods are the swirling strength criterion, and the Q-criterion, which are based on the interrelationships between the rate of strain tensor and the vorticity tensor. These methods are particularly useful in distinguishing swirling motions in shear-dominated flows [13, 30, 42].

Thus, the motivation of this thesis is to use enhanced post-processing techniques on data obtained from experimental data and LES to visualize flows over surface-mounted finite-height bluff bodies like the square prism and the circular cylinder. It is intended that using these sophisticated tools would give a more insightful representation of the flow structures, advance the understanding of these flow fields, and make a meaningful contribution to the existing literature.

1.2 Objectives and Scope

The principal objective of this research is to explore the time-averaged and instantaneous flow structures above the free end and in the wake of surface-mounted finite-height bluff bodies. Two geometries, namely a finite-height cylinder and a finite-height square prism, are chosen for this analysis. Flow velocity data obtained from Large Eddy Simulation (LES) and experiments conducted in a wind tunnel will be post-processed using advanced flow visualization techniques to spatially track the motion and topologies of coherent structures and their composition above the free end and in the wake. In order to achieve the above, four separate studies will be conducted.

The first study will investigate the flow field above the free-end of a surface-mounted finite-height square prism at zero incidence (i.e. where a prism face is normal to the flow). It has been shown that the free end flow field varies with the cross-sectional shape of the surface-mounted bluff body, and therefore, characteristic flow structures are expected. This study will also be done using experimental data obtained from wind tunnel experiments at a Reynolds number of $\mathrm{Re}_D = 4.2 \times 10^4$ (based on freestream velocity U_∞, prism width D, and kinematic viscosity ν). Of interest would also be to identify turbulent flow structures above the free-end surface in the vertical symmetry plane, and the effect of the aspect ratio ($\mathrm{AR} = H/D$ i.e. the ratio of height to width) of the prism on these structures.

In the second study, the flows above the free end of a surface-mounted finite-height circular cylinder will be explored. This will be done using experimental data obtained from wind tunnel experiments at a Reynolds number of $\mathrm{Re}_D = 4.2 \times 10^4$ (based on cylinder width D). Velocity measurements were made with a two-component particle image velocimetry (PIV) system in different measurement planes. Of interest would be to identify turbulent flow structures above the free-end surface, as well as to investigate the effect of the cylinder aspect ratio of these structures.

In the third study, the mean flow structures over a surface-mounted finite-height square prism at zero incidence will be studied using LES. While several studies exist on the mean flow field in the wake of a surface-mounted square prism [17, 38, 50, 80], most of these have observed structures on 2D (two-dimensional) planes and have heuristically extrapolated these structures in three dimensions. A detailed understanding of the three-dimensional flow field in this wake would enrich the existing literature by providing clearer insight on the mechanisms of formation of the mean flow structures as they extend downstream from the square prism. The flow fields will be generated using Large Eddy Simulation (LES) at a Reynolds number of $\mathrm{Re}_D = 500$.

The fourth study will investigate the instantaneous three-dimensional flow structures in the wake of a surface-mounted finite-height square prism at zero incidence. Instantaneous flow data obtained from the LES simulation in the third study will be post-processed using three-dimensional POD and the Q-criterion. As mentioned earlier, these methods are becoming increasingly popular in the literature to investigate the dominant, energy-containing features of the flow as well as visualizing small-scale flow features and their contributions

to the overall flow field. However, most POD studies in the literature have been in two-dimensional (2D) planes, and therefore a POD investigation in three-dimensions (3D) will provide an innovative numerical methodology to investigate more complete flow structures. Furthermore, the temporal coefficients obtained from POD analysis can also be used to analyse the periodic features of this flow and can help find temporally dominant flow structures using a reduced order POD reconstruction.

1.3 Research Contributions

Throughout this thesis, it is expected that the application of advanced post-processing techniques will provide for a more insightful representation of the flow fields being considered. This would then be used to obtain an improved understanding of turbulent structures in these types of flows. While there has been considerable research on the flow fields over circular cylinders and square prisms, the flow fields above the free end have not been well understood. Thus, a detailed investigation in the first two studies of the flows above the free end will provide for a novel contribution to the literature on three-dimensional bluff-body flows. Several studies have also explored the time-averaged flow field in various 2D planes at higher Reynolds number [37, 46, 99]. Studies of the 3D time-averaged and instantaneous flow features in the wake of finite-height square prisms at lower Reynolds number have only recenly been pursued [73, 101], but the complex nature of the flow field provides for adequate room for more comprehensive representations of the flow structures. Thus, the results of the third and fourth study will also provide an original contribution to the current understanding of these flow fields. The fourth study specifically will use three-dimensional proper orthogonal decomposition (3D POD). While POD has grown in popularity over the past several decades in the analysis of flow fields, it has mostly been used to explore flow fields in 2D. Thus, the 3D POD will provide a novel perspective on the dominant flow features in this flow field. In summary, the research contributions thus sought are as follows:

1. To use POD to study the spatial distribution of dominant structures like vortices, shear layers, and instabilities above the free end of a wall-mounted finite-height square prism in the vertical symmetry plane above the free end, and the influence on the flow configuration due to the change in aspect ratio.

2. To use POD to study the spatial distribution of dominant structures like vortices and shear layers, above the free end of a wall-mounted finite-height cylinder in horizontal planes parallel to the free end surface, and the influence on the flow configuration and its structures of a change in aspect ratio.

3. To document flow structures in the time-averaged three-dimensional flow field in the wake of a surface-mounted finite-height square prism and study their interaction with the square prism, the ground plane, and each other.

4. To examine the spatial and temporal distribution of dominant structures in the three-dimensional wake of a wall-mounted finite-height square prism using improved flow visualization tools like three-dimensional proper orthogonal decomposition and localized vortex identification methods like the Q-criterion.

1.4 Literature Review

Compared to the flow around a 2D cylinder or square prism, flow around a wall mounted finite cylinder or finite square prism (also called square cylinder in some studies) offers additional complexity due to the free end and the ground plane boundary layer, which dramatically alter the wake and vortex formation [59]. This is also true of surface-mounted bluff bodies of other cross-sectional geometries, like triangular prisms [39]. The flow topology is strongly affected by the bluff body's aspect ratio AR $= H/D$, i.e. the ratio of its height (H) to its width (D), the Reynolds number (Re_D) based on the width of the prism (D), the angle of incidence of the body, and the boundary layer thickness δ on the ground plane. The coordinate axes are assigned as x, y and z along the freestream, transverse and wall-normal directions, respectively. Permissions for figures taken from journal papers have been duly added in Appendix A.

Park and Lee [62] suggested that the occurrence of streamwise (longitudinal) vortices in the upper part of the wake are responsible for the three-dimensional (3D) nature of the finite-cylinder flow even at lower Reynolds numbers. For relatively large aspect ratios (AR > 13), the free-end and wall effects are mutually exclusive [22] and the flow patterns in the middle regions resemble those of the 2D cylinder. Wang and Zhou [95] suggested that the main flow features of finite cylinder and square prism wakes are almost similar. Due to the complex

nature of this flow, structures seen in the mean, phase-averaged and instantaneous flow fields are considerably different. A sketch of the flow around a wall-mounted finite circular cylinder for a Cartesian coordinate system with a boundary layer profile $U(z)$ on the ground plane is shown in Figure 1.1.

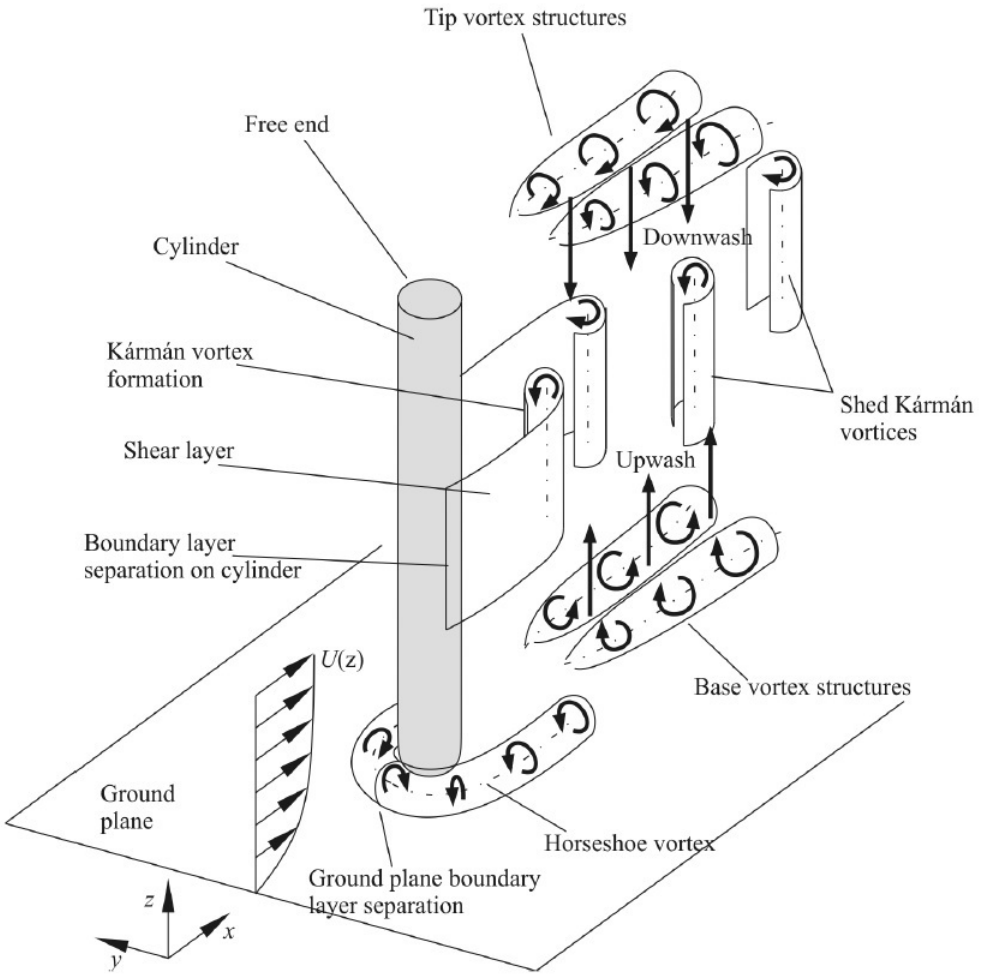

Figure 1.1: Flow around a surface-mounted finite-height cylinder for AR > $AR_{critical}$.

The free end is a major contributor to the three-dimensionality of the flow and a time-averaged representation reveals a pair of counter-rotating tip vortices that generates a downward-directed flow called downwash [19,74]. Near the cylinder-wall junction, flow separation occurs, due to an adverse pressure gradient. The boundary layer then wraps around the cylinder-wall junction downstream forming a necklace-like horseshoe vortex [8]. Depending on the nature of the approaching boundary layer and the cylinder aspect ratio (discussed in the next sec-

tion), an additional distinct pair of weak, counter-rotating base vortices that produce an upwash flow from the ground plane is also observed in time-averaged representations close to the wall. The base vortices are shown to be opposite in rotational direction to the horseshoe and tip vortices [41].

1.4.1 Effect of Aspect Ratio (AR) on the Wake

For wall-mounted cylinders and square prisms, a critical value of aspect ratio is observed across which the wake structure shows significant changes in structure. For AR greater than this critical value $\mathrm{AR}_{\mathrm{critical}}$ (the values of which have varied across studies), the middle region of the cylinder sandwiched by the tip and base vortex pairs is characterized by antisymmetric Kármán vortex shedding from the cylinder sides [6,41]. The formation of the Kármán vortex core varies with distance from the ground plane along the height of the body in the wake, with the vortex cores bending back towards the bluff body near the free end and the ground plane. For values of $\mathrm{AR} < \mathrm{AR}_{\mathrm{critical}}$, the Kármán vortices disappear completely and the wake is characterized by an arch-type vortex shedding [74]. This leaves only the tip vortices at $\mathrm{AR} = 3$ as shown in Figure 1.2 [84], for a $\mathrm{Re}_D = 6 \times 10^4$ and a dimensionless boundary layer thickness of $\delta/D = 2.6$. This is because at low aspect ratios, there is a strong influence of downwash from the tip towards the ground plane that prevents the development of base vortices. Any further decrease of AR causes the downwash from the tip vortices to reach the ground plane replacing the longitudinal tip and base vortices with streamwise-downward arch-type vortex shedding [74]. The vortex shedding frequency [84] has been observed to decrease with decreasing aspect ratio. Wang and Zhou [95] observed an almost constant Strouhal number of $\mathrm{St} = fD/U_\infty \approx 0.12$, where f is the frequency of vortex shedding, D is the width of the prism, and U_∞ is the freestream velocity, for sufficiently small AR prisms. Saha [73] in his DNS studies of a wall-mounted square prism showed that the Strouhal number is a function of the AR and that both the Strouhal number and drag coefficient C_D (based on the mean drag force and the reference frontal area $H \times D$) decrease with decreasing aspect ratio.

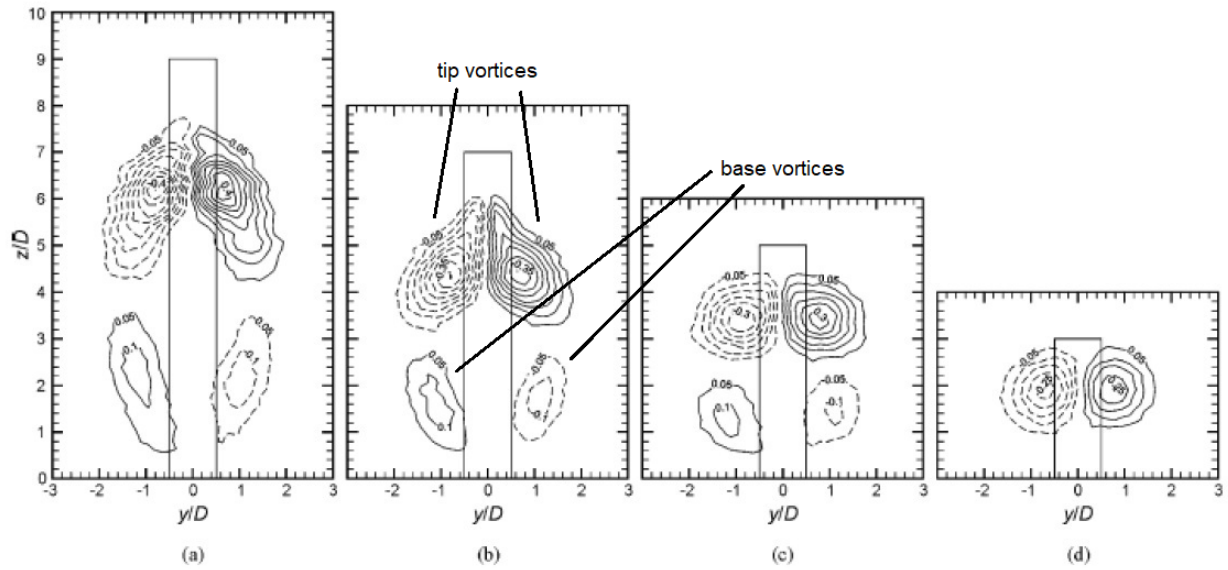

Figure 1.2: The time-averaged streamwise vorticity in the wake of a surface-mounted finite cylinder at $\mathrm{Re}_D = 6 \times 10^4$ and boundary layer thickness $\delta/D = 2.6$ as seen from downstream at $x/D = 6$ for (a) AR = 9, (b) AR = 7, (c) AR = 5 and (d) AR = 3. The normalized streamwise vorticity contour increment is 0.05 and minimum vorticity contour is 0.05, solid lines represent positive (CCW) vorticity and dashed lines represent negative (CW) vorticity [84]. Permission for this figure is attached in Appendix A.

1.4.2 Effect of the Boundary Layer on the Ground Plane

In surface-mounted finite cylinder and square prism studies, a boundary layer is present on the ground plane and studies have shown that thick boundary layers further strengthen the base vortices and enhance upwash flow downstream of the body. This opposes the movement of the downwash flow towards the ground plane and thus serves to weaken the tip vortex effects [96]. This then causes the spanwise Kármán vortices to strengthen closer to the free end and distort the ratio of asymmetrically and symmetrically arranged vortices. Wang *et al.* [96] observed the presence of both symmetric and antisymmetric vortex shedding modes with the latter increasing with boundary layer thickness. Additionally, the vortex-formation distance, vortex shedding frequency [96] and Strouhal number [74] all decrease with increasing boundary layer thickness. El Hassan *et al.* [18] studied the influence of a tripped boundary layer over a wall-mounted prism and showed that it enhances the upwash and tendency of formation of the base vortices, thereby yielding a quadrupole wake configuration.

On the other hand, when boundary layers are thin and the AR sufficiently small ($AR = 3 < AR_{critical}$), the base vortices are absent [84]. As a result of the dominance of downwash flow, symmetrically arranged wall-normal vortex structures parallel to the cylinder tend to dominate over the antisymmetric shedding case [96].

1.4.3 Flow above the Free End

There have been fewer studies in the literature on the flow above the free end compared to the wake of surface-mounted finite-height bluff bodies [83]. For the finite cylinder, the flow above the free end is complex due to flow separation from the round (semi-circular) leading edge of the free-end surface, a mean recirculation zone above the free-end surface, a mean cross-stream arch (mushroom) vortex inside this recirculation zone, and reattachment of the separated flow onto the free-end surface. A schematic, shown in Figure 1.3, shows the main flow features across varying aspect ratios, Reynolds numbers, and boundary layers.

Unlike the cylinder case, flows above the free end of the square prism do not reattach for $AR > 1$. Flow separation occurs from the leading edge of the free end and the separated flow extends into the near-wake region [69]. A prominent clockwise vortex is found in the vertical symmetry plane within the mean recirculation zone above the free end. A second clockwise vortex is found downstream in the upper part of the near wake. Elevated levels of

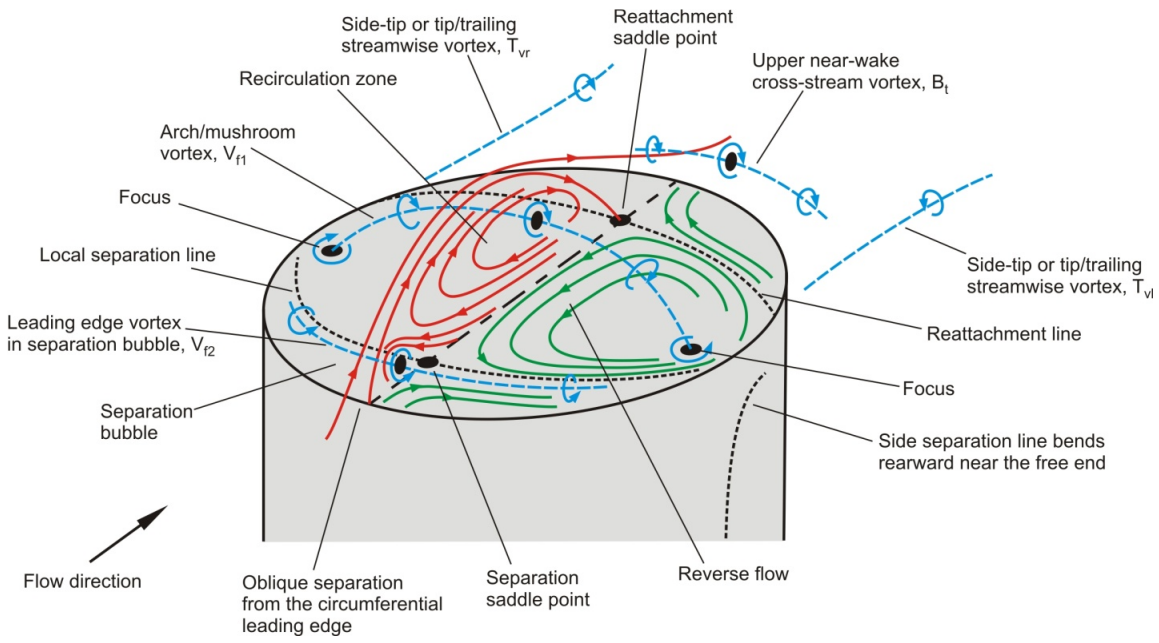

Figure 1.3: Schematic of the free-end flow field for higher-aspect-ratio surface-mounted finite-height cylinders, showing the main flow features [83]. Permission for this figure is attached in Appendix A.

turbulence intensity and Reynolds shear stress occur above the free end. Characteristics of the reverse flow and its local separation from the trailing edge of the free end surface vary with the aspect ratio of the prism as shown in Figure 1.4.

1.4.4 Computational Studies

Numerical studies of finite-cylinder and finite square prism flows with LES have only been underway for less than a decade. At the very least, they have tried to corroborate available experimental results and provide greater temporal and spatial resolution difficult to achieve through experiments. The gradual advent and adoption of more advanced computational tools and algorithms to process and visualize flows has enabled CFD to reveal additional small-scale structures that have not been identified in previous studies [45]. Fröhlich and Rodi [26] have successfully substantiated the use of Smagorinsky and Dynamic Smagorinsky LES modeling with their corresponding experimental results. Frederich *et al.* [24] applied the 2D POD technique and matched their results with near-wake experimental findings. Krajnović [45] simulated an AR = 6 finite cylinder problem using parallelized, high-resolution LES and also observed both legs of the mushroom vortex attached to the top surface in the

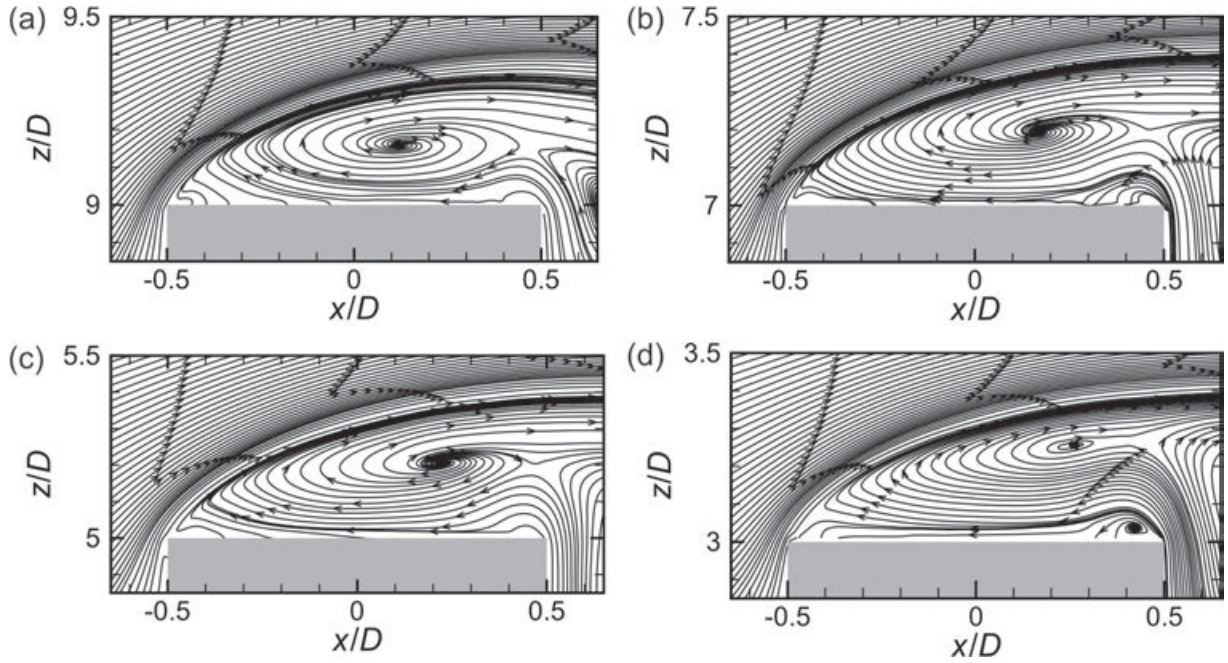

Figure 1.4: Mean streamlines above the free end on the mid plane of a surface-mounted square prism for $\mathrm{Re}_D = 4.2 \times 10^4$ and boundary layer thickness $\delta/D = 1.6$ with varying aspect ratios: (a) AR = 9; (b) AR = 7; (c) AR = 5; (d) AR = 3 [69]. Permission for this figure is attached in Appendix A.

recirculation zone. What makes his study a benchmark inspiration for this research is the profound and insightful details his LES has managed to capture. The study additionally revealed two pairs of unsteady horseshoe vortices that change shape with time showing three complete horseshoe vortices in the time-averaged flow. The study also revealed two pairs of counter-rotating tip vortices consistent with the model proposed by Roh and Park [68]. Palau-Salvador *et al.* [61] employed the immersed boundary method with LES of the flow over two surface-mounted finite cylinders in tandem to show a fruitful match between their computational and experimental findings.

1.4.5 Recent Developments

While heuristic approaches have resolved the different wake regions of the cylinder and prism, recent studies have attempted to propose unifying flow theories of the interaction dynamics between the vortices in the wake. Wang and Zhou [95] suggested that the instantaneous flow for a prism is predisposed towards forming arch-type vortices regardless of aspect ratio and is characterised by two spanwise vertical legs towards the ground plane and a connecting

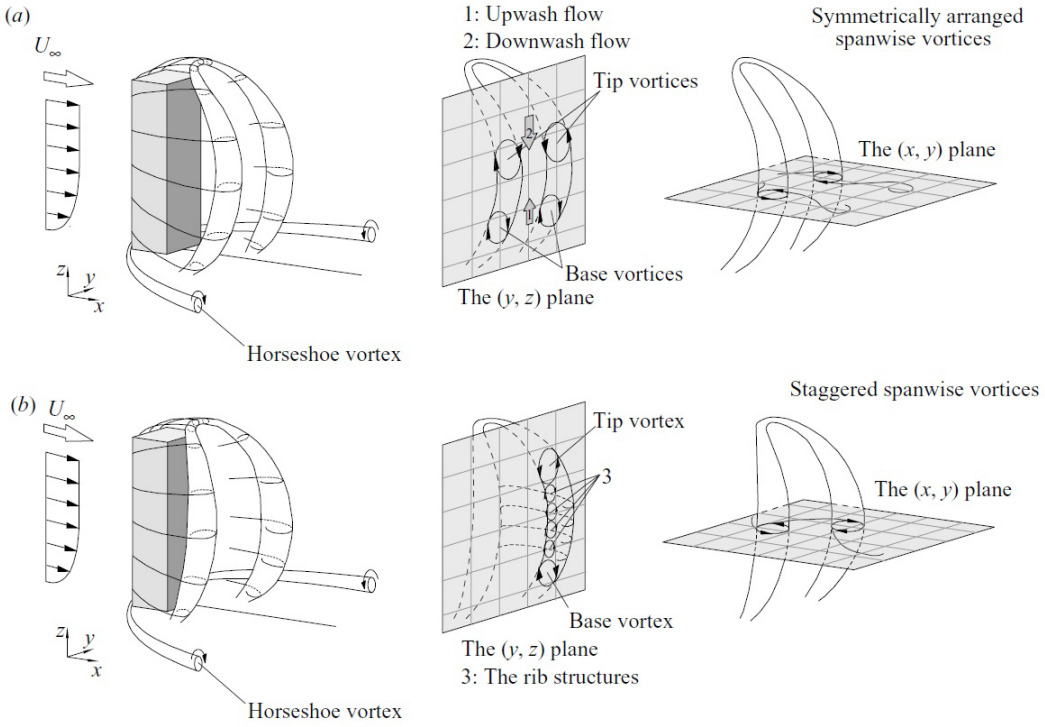

Figure 1.5: Model of the flow structure around a wall-mounted finite-height square prism at a $\mathrm{Re}_D = 9.3 \times 10^3$: (a) symmetrically arranged spanwise vortex roll, (b) staggered arranged spanwise vortex roll [95]. Permission for this figure is attached in Appendix A.

bridge at the free end. Through probabilistic studies and 2D interpolated Particle Image Velocimetry (PIV) measurements at $\mathrm{Re}_D = 9300$ and $\delta/D = 1.35$ for square prisms ranging in aspect ratios AR = 3 to 11, they concluded that the three vortex structures essentially arise out of the same structure and tend to flow outwards from the centerline plane. Their model of an outward-bulging arch vortex, as shown in Figure 1.5 [95], was intended to fit most findings of the flow characteristics across and downstream of the finite prism.

More recently, Bourgeois *et al.* [8] proposed a different interpretation, namely the alternating half-loop vortex shedding in the finite prism wake arising from the free end as shown in Figure 1.6 for an AR = 4 square prism at a slightly higher Reynolds number of $\mathrm{Re}_D = 12000$ with a boundary layer thickness $\delta/D = 0.72$. While they measured a Strouhal number St = 0.149 for this flow, which was slightly higher than other studies, their final large scale vortex structures showed good agreement with the corresponding experimental literature. Cesur *et al.* [12] used POD on the flow over a wall-mounted finite square prism to demonstrate that the first two energy modes were successfully able to detect the low-frequency vortex shedding.

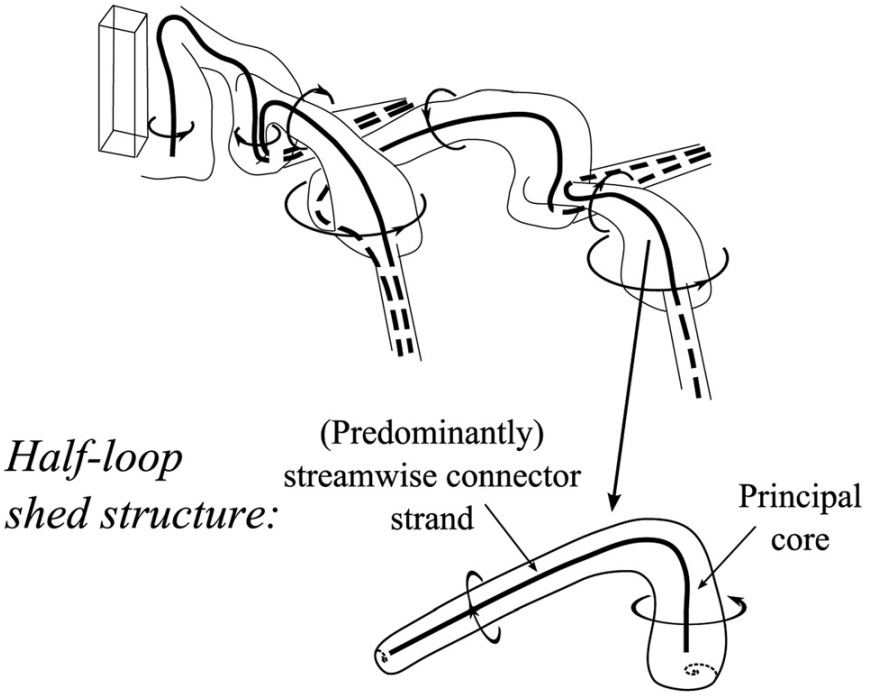

Figure 1.6: Schematic of the educed phase-averaged vortex structure identified by Bourgeois *et al.* [8]. Permission for this figure is attached in Appendix A.

Wang *et al.* [94] investigated the periodic features of the flow over a finite square prism using POD and concluded that the first two POD temporal coefficients exhibit periodicity that correspond to antisymmetric vortex shedding, while the higher modes possibly correspond to symmetric vortex shedding characteristics.

Sattari *et al.* [77] studied the wake of a surface-mounted finite square prism using phase averaging and found two regimes of co-existing and out-of-phase vortex structures in the wake depending on the amplitude of the pressure fluctuations on the side-walls of the prism as well as its proximity to the prism free end. Hosseini *et al.* [34] suggested that a thin boundary layer favours the formation of one streamwise vortex pair (dipole wake) while a thicker boundary layer favours a quadrupole wake. Zhang *et al.* [101] reported a new transitional six-vortices type time-averaged streamwise vortices around $\mathrm{Re}_D = 150$-250 between the dipole and quadrupole wake configurations at lower and higher Reynolds number, respectively, for a wall-mounted finite square prism of $\mathrm{AR} = 4$.

In conclusion, while most studies have independently observed various regions with distinct vortex structures, there lies no real consensus on the overall dynamics of these vortex

interactions. There is a need to further observe the instantaneous flow characteristics to explain these structures. Only a few studies have delved into studying the local flow fields around surface-mounted finite square prisms and cylinders, particularly above the free end. The free end has a profound influence on the nature of the wake in these flows, including causing the formation of the mean streamwise trailing vortex structures and the subsequent downwash. It is thus important to further investigate the flow above the free end and its contributions to the overall flow field. The flow field in the wake has mostly been explored using approximations of 2D flow fields, and thus, a 3D representation of the time-averaged and instantaneous flow fields around and in the wake of a square prism provides a novel contribution to the understanding of this flow field.

1.5 Numerical Methodologies

While the first two studies employ data obtained experimentally using PIV, the third and fourth study use data obtained from an in-house LES code. The mathematical model consists of the filtered Navier-Stokes equations which are discretised using the finite-volume method (FVM) for incompressible, turbulent fluid flow with constant properties (density and viscosity). The discrete form of the momentum equations is solved using a fractional step method, where the convective and diffusive terms are numerically modeled using the Crank-Nicolson method and numerically advanced in time using the Adams-Bashforth method. For incompressible flow, the velocity field is corrected to ensure mass conservation using a pressure-correction method. A multi-grid (MG) method was used to efficiently solve the linear algebraic equations obtained from the pressure-correction method. The dynamic subgrid-scale model (DSM) was be used to represent the subgrid-scale (SGS) stresses.

Using advanced tools to visualize this complex flow field will prove beneficial to better understanding the topologies of this flow field. Using instantaneous and phase-averaged calculations of velocity fields will give a better insight into the dominant structures. However, to study turbulent flows, detailed analysis of instantaneous flow fields is also required. The techniques mentioned below are especially useful to extract both large-scale and small-scale coherent structures in flows that are not discernible from instantaneous velocity snapshots of the flow field. It is thus vital to resolve vortical structures at different scales to study their importance to the overall flow dynamics.

There is an important distinction between visualizing and identifying vortex structures. While vorticity can readily visualize vortices, it is unable to make a distinction between shearing and swirling motions. Furthermore, different thresholds for vorticity isosurfaces reveal different structures. Thus, in complex flow fields where multiple flow structures interact with each other, using vorticity is insufficient.

Velocity gradient methods present a sophisticated, localized approach for identifying vortices. Based on calculations derived from the velocity gradient tensor, these methods seek to decompose the fluid motion into its shearing and swirling components. Contours of the structures identified by these methods are used to demonstrate rotational structures. Two methods used are mentioned below:

- The swirling strength criterion (λ_{ci}) – For incompressible flow, the swirling strength criterion of Zhou *et al.* [102] postulates that vortices are present locally in regions where the velocity gradient tensor Δu yields complex conjugate eigenvalues (i.e. $\lambda_{ct} \mp \lambda_{ci}$). The swirling strength, λ_{ci} measures the angular velocity of the local swirl inside the vortex.

- The Q-criterion (Q) – First proposed by Cantwell and Coles [11], this method identifies rotational structures where $Q > 0$, i.e. regions where the vorticity tensor dominate the strain rate tensor.

  As mentioned earlier, extracting deterministic features from a complex turbulent flow is challenging. A powerful method that is used to obtain an approximate, low-dimensional description of a high-dimensional turbulent flow field is called proper orthogonal decomposition (POD). It is also known as principal component analysis, singular value decomposition, or the Karhunen-Loeve decomposition, and has been used in a variety of dynamic systems like structural vibrations, signal processing etc. The objective of POD is to use an orthogonal transformation to obtain a set of basis functions or modes, that represent the dynamic system. Lumley [49] suggested that the velocity field is a projection based on energetic modes as its 'building blocks'. Each mode consists of coherent energetic structures. The POD technique then determines the modes, which capture most of the kinetic energy of the system. Once arranged in descending order, the higher modes would represent the organized energetic features in a random field.

The POD methodology (further elaborated in Berkooz *et al.* [5]) is thus used to extract motions of different scales within the evolving dynamics of a flow. This method can be used for both numerical and experimental data. In this thesis, the snapshot POD method by Sirovich is applied [78]. The procedure can be summarized as follows:

1. To obtain the velocity fluctuation, the average of all the instantaneous velocity snapshots is subtracted from each snapshot. The fluctuating velocity components in each direction (streamwise, transverse and wall-normal) are then stacked into a single column matrix for each snapshot.
2. These fluctuating velocity column vectors are then combined in a matrix U with N columns (where N represents the total number of instantaneous snapshots), in which each column represents a single fluctuating velocity column vector (as shown in Equation 1.1).

$$U = \left[u^1, u^2 \dots u^N\right] = \begin{bmatrix} u_1^1 & u_1^2 & \dots & u_1^N \\ v_1^1 & v_1^2 & \dots & v_1^N \\ \vdots & \vdots & \vdots & \vdots \\ u_M^1 & u_M^2 & \dots & u_M^N \\ v_M^1 & v_M^1 & \dots & v_M^1 \end{bmatrix} \tag{1.1}$$

3. The autocovariance matrix is then calculated as $C = U^T U$. This gives a square $N \times N$ matrix.
4. The autocovariance matrix C is then decomposed into an orthonormal system of spatial velocity modes ($\varphi_i(x)$) and associated temporal coefficients $a_i(t)$ (shown in Equation 1.2-1.4). The spatial velocity modes are then normalized by dividing it by its inner product.

$$CA^i = \lambda^i A^i \tag{1.2}$$

$$\varphi^i = \frac{\sum_1^N A_n^i u^n}{\left\| \sum_1^N A_n^i u^n \right\|}, \quad i = 1, 2, \dots N \tag{1.3}$$

$$a^n = [\varphi^1, \varphi^2 \dots \varphi^N] \times u^N \tag{1.4}$$

5. The relative magnitude of the eigenvalues (λ_i) determines the respective energy contributions in each mode. These are thus arranged in descending order to capture the more energetic structures in the higher energy modes.

6. The lower order POD reconstruction at a particular instant of time n, is then computed using a subset of the linear combination of the temporal coefficients and the normalized POD modes (shown in Equation 1.5).

$$u^n = \sum_{i=1}^{N} a_i^n \varphi^i \tag{1.5}$$

It is important to recognize some limitations of POD. Firstly, POD represents a linear transformation to represent flow structures in a turbulent flow field, which is inherently a nonlinear phenomenon. Another limitation is that while the orthogonality of POD modes ensure they are uncorrelated, that does not mean they are independent. As an example, in many periodic flows, POD modes having similar energy content represent features similar to vortex shedding but are opposite in phase. It is thus an expected outcome to find similar structures in consecutive POD modes that are just opposite in vorticity. The focus of this thesis, however, is to investigate the large-scale coherent flow features seen in the first few energy modes. Despite these limitations, POD is largely successful in capturing the dominant flow features in the higher energy modes, which ultimately is the focus of this thesis. Should statistically independent components be desired, the newer method called independent component analysis (ICA) can be used [91].

The in-house LES code used in this thesis was implemented using FORTRAN code on Microsoft Visual Studio. All flow visualization implementations were done on MATLAB, taking data outputs from either PIV or LES data from the FORTRAN code. The code used for the POD implementation can be found in Appendix B.

1.6 Outline

This manuscript-based thesis has six chapters, with one comprehensive reference list at the end of the thesis. Chapters 2 to 5 consist of manuscripts covering each of the aforementioned studies. All of the manuscripts have been co-authored by Rajat Chakravarty with research supervisors Prof. D. J. Bergstrom and Prof. D. Sumner of the Department of Mechanical

Engineering at the University of Saskatchewan. The manuscripts in Chapters 2 and 3 employ experimental data obtained from PIV experiments conducted by Noorallah Rostamy, while Chapter 4 and 5 employ numerical data obtained from LES using a finite-volume code obtained from Nader Moazamigoodarzi. For their contributions, they have been added as co-authors to the work in the respective manuscripts.

Chapter 2 will cover the flow above the free end of a surface-mounted finite-height square prism using POD and the swirling strength criterion, thereby fulfilling the first objective of this thesis. It will begin with an introduction to the literature on the flow above the free end of surface-mounted square prisms. The experimental methodology and numerical techniques used for visualizing the flow fields will be briefly discussed. This will be followed by a discussion of the results and major conclusions of the work.

Chapter 3 will investigate the flow above the free end of a surface-mounted finite-height cylinder, once again using the POD and the swirling strength criterion, fulfilling the second objective of this thesis. The literature on the flow field above the free end of a circular cylinder will be introduced with a brief summary of the experimental methodology and numerical techniques used. This will be followed by a discussion of the results and major conclusions of the work.

Chapter 4 will investigate the 3D mean flow field in the wake of a surface-mounted finite-height square prism. This study will complete the third objective of the thesis. This study will begin with an overview of the studies that have investigated this flow field, specifically identifying a few works that this study would like to corroborate. This will be followed by a brief outline of the LES methodology and the flow visualization techniques used. Both 3D results and 2D results in some strategic locations around the prism will be analyzed for further insight.

Chapter 5 will investigate the flow field in the wake of a surface-mounted finite-height square prism using the novel technique of 3D POD, accomplishing the final objective of this thesis. After a brief summary of the studies that have used POD as tool for studying complex flow fields, the various 3D POD results will be discussed.

Chapter 6 will summarize the major conclusions and research contributions of this thesis, and demonstrate key findings that achieve the objectives of this thesis. Additional considerations and future research opportunities that result from this study will be discussed.

Chapter 2

The fluctuating velocity field above the free end of a surface-mounted finite-height square prism

Preamble

This study aims to fulfill the first objective of the thesis mentioned in Section 1.2 and pursue the first research contribution outlined in Section 1.3. The contribution of this chapter to the overall study is to provide new insight into the spatial distribution of dominant structures above the free end of a wall-mounted, finite-height square prism in the vertical symmetry plane above the free end and the influence on the flow configuration and its structures due to the change in aspect ratio.

This study will investigate the fluctuating flow field above the free end of surface-mounted finite-height square prisms of AR = 9, 7, 5 and 3, at a Reynolds number of $\mathrm{Re}_D = 4.2\times10^4$ using POD and the swirling strength criterion. The analysis will be performed on the symmetry mid-plane above the surface-mounted finite height square prism free end. This study will first attempt to validate the POD algorithm by analyzing the energy distribution with varying number of snapshots. The dominant spatial features and vortex instabilities in the higher POD energy modes will be demonstrated. The variation of these flow topologies with aspect ratio will be also be observed with an emphasis on the rotational structures with the swirling strength criterion.

The data was obtained from PIV measurements made in a low-speed wind tunnel by Noorallah Rostamy. The development of the POD and swirling strength codes, the subsequent analysis and discussion of the results were done by Rajat Chakravarty. This was subsequently edited by Prof. Bergstrom and Prof. Sumner.

A similar version of this chapter is in preparation for submission as:

1. R. Chakravarty, D. J. Bergstrom and D. Sumner, 'The fluctuating velocity field above the free end of a surface-mounted finite-height square prism', *Journal of Turbulence*

Parts of this chapter were presented at the following conferences:

1. R. Chakravarty, N. Rostamy, D. J. Bergstrom and D. Sumner, 'Vortex Identification above the free-end of finite-height prisms and cylinders', 66th Annual Meeting of the APS Division of Fluid Dynamics, November 24-26, 2013, Pittsburgh, USA. Bulletin of the American Physical Society, Vol. 58, No. 18, Abstract M35:00006.

2. R. Chakravarty, N. Rostamy, D. J. Bergstrom and D. Sumner, 'The fluctuating velocity field above the free end of a surface-mounted finite-height square prism', 10th International Symposium on Turbulence and Shear Flow Phenomena (TSFP-10), July 6-9, 2017, Chicago, USA.

Abstract

This study investigates the features of the fluctuating velocity field above the free end of a surface-mounted finite-height square prism, at a Reynolds number of $\mathrm{Re}_D = 4.2 \times 10^4$, using two state-of-the-art post-processing methodologies, namely Proper Orthogonal Decomposition (POD) and the swirling strength criterion. Instantaneous velocity measurements obtained from particle image velocimetry, for the flow past finite square prisms of aspect ratios AR = 9, 7, 5 and 3, were analyzed. The prisms were partially immersed in a turbulent boundary layer with a dimensionless thickness of $\delta/D = 1.6$. POD modes were used to extract the dominant flow features, which revealed a pair of shear sub-layers above the free end, flow entrainment from the freestream above, as well as several vortex structures located in the shear-sub layers. Combined with the swirling strength results, evidence of Kelvin-Helmholtz (KH) instability vortices were found within the shear layer region. Some structural features in the near wake, above and behind the prism trailing edge, were identified.

Key Words: bluff body, finite square prism, separation, free end, vortex structures, proper orthogonal decomposition, swirling strength criterion.

2.1 Introduction

Flows over surface-mounted finite-height square prisms (of height H and width D) have been studied for related industrial applications, such as buildings and electronic components on circuit boards, as well as to advance the fundamental understanding of complex turbulent wake flows. Compared to the flow around two-dimensional (2D) or infinite square prisms, which has been more extensively studied [4,35,98], the flow around the finite prism is strongly three-dimensional due to the effects of the free end and the boundary layer on the ground plane, which dramatically alter the wake and its vortex structures [8, 9, 95], as well as the fluid forces and vortex shedding frequencies [54].

Flow characteristics around and in the wake of a surface-mounted finite-height square prism have been shown to be primarily influenced by the aspect ratio of the prism, AR = H/D [70, 73, 74, 75, 86], the boundary layer thickness on the ground plane, expressed as the ratio δ/D [18, 34, 96], and the angle of incidence of the prism with respect to the incoming flow, α, [57, 60, 90]. Several studies have identified a critical aspect ratio below which the

wake structure is distinct [86], and shows significant changes in vortex shedding from an anti-symmetrical to a symmetrical tendency [95]. The Reynolds number, $\mathrm{Re}_D = DU_\infty\nu$ (for freestream velocity U_∞ and kinematic viscosity ν) has somewhat less influence on the flow due to the fixed separation points on the sharp upstream edges of the prism. However, the recent direct numerical simulations of Zhang *et al.* [101] have shown that the value of Re_D may have a pronounced effect at low Reynolds numbers. The mean flow field (demonstrated in Section 4) introduces additional three-dimensional vortex structures like tip vortices and base vortices in the wake depending on the aspect ratio, boundary layer thickness, and Reynolds number of the flow field.

While heuristic approaches have identified the different regions of the prism near-wake, some studies have attempted to propose a unifying flow theory based on the dynamics of the vortical structures shed from the prism. Wang and Zhou [95] suggested a three-dimensional model based on both the instantaneous and mean flow characteristics of this flow. Based on probabilistic analysis and 2D particle image velocimetry (PIV) measurements, they developed this model of an outward-bulging arch vortex. Their study suggested an arch-type vortex regardless of aspect ratio and is characterized by two spanwise vertical legs perpendicular to the ground plane and a connecting horizontal bridge at the free end.

Bourgeois *et al.* [8] proposed a different flow paradigm, namely the alternating half-loop vortex structure shed by the finite square prism into the wake. They indicated that the mean flow structure of the wake could be explained by averaging the quasi-periodic half-loop structure over the shedding period. A single half-loop structure is made up of a principal core which is aligned approximately perpendicular to the ground plane and a streamwise connector strand. The strand connects the top of the principal core to the base of the principal core of the next half-loop located upstream. Since the principal cores occur on alternate sides of the wake, each connector strand stretches diagonally across the wake, with an orientation which also alternates.

Both of the studies above considered finite square prisms of larger aspect ratio for relatively higher Reynolds numbers. Saha [73] studied the flow past a finite-height surface-mounted square prism using direct numerical simulation (DNS) at a lower Reynolds number of $\mathrm{Re}_D = 250$ for four different aspect ratios: AR = 2, 3, 4 and 5. Without trying to propose a unifying theory, Saha [73] observed tip vortices, base vortices and horseshoe vortices in the prism

wake regardless of aspect ratio. For AR $>$ 2, the near wake shows a symmetric shear layer separation while the far wake shows greater anti-symmetric vortex shedding characteristics.

It is clear that the free end and the ground plane are responsible for the formation of additional vortices (tip, arch and base) and their configuration varies with aspect ratio, Reynolds number and boundary layer thickness. It would thus be of interest to closely explore the flow specifically above the free end to look for structures that contribute to the formation of these vortices in the wake. Proper Orthogonal Decomposition (POD) has been increasingly used in the literature to investigate the dominant energy-containing features of a bluff body flow field and its interaction with the turbulence in the surrounding flow. The POD technique has been used to study the near wake of surface-mounted finite-height cylinders [23] and square prisms [12,94]. Additionally, in flow fields dominated by shear, such as the flow above the free end of a surface-mounted finite-height square prism, identifying and characterizing rotational structures in separated shear layers by vorticity contours alone can be misleading. The present study, therefore, also uses the swirling strength criterion to gain greater insight into the flow field. This criterion has been used previously in channel flows [102] and to investigate shear layer vortices in the near wake of a cylinder [66].

In the present study, POD and the swirling strength criterion are used to study the flow field above the free end of a surface-mounted finite-height square prism, which is a region of the flow that has not been extensively or systematically investigated, nor have the aforementioned techniques been used to analyze the flow patterns. Of specific interest is the effect of aspect ratio on the free-end instantaneous flow field.

2.2 Experimental Approach and Post-processing Methodologies

The present study uses the experimental data reported in Rostamy *et al.* [70] and Sumner *et al.* [86] for the flow above the free end of surface-mounted finite-height square prisms of AR = 9, 7, 5 and 3. A schematic of the flow field is shown in Figure 2.1. The prisms were oriented at an incidence angle of $\alpha = 0°$. The data were obtained from 2D PIV measurements in a low-speed wind tunnel, at a Reynolds number of $\mathrm{Re}_D = 4.2 \times 10^4$ and with a relative boundary layer thickness of $\delta/D = 1.6$. Complete details of the experimental set-up and PIV analysis can be found in Sumner *et al.* [86].

Of specific interest in the present study are the PIV velocity field measurements in the

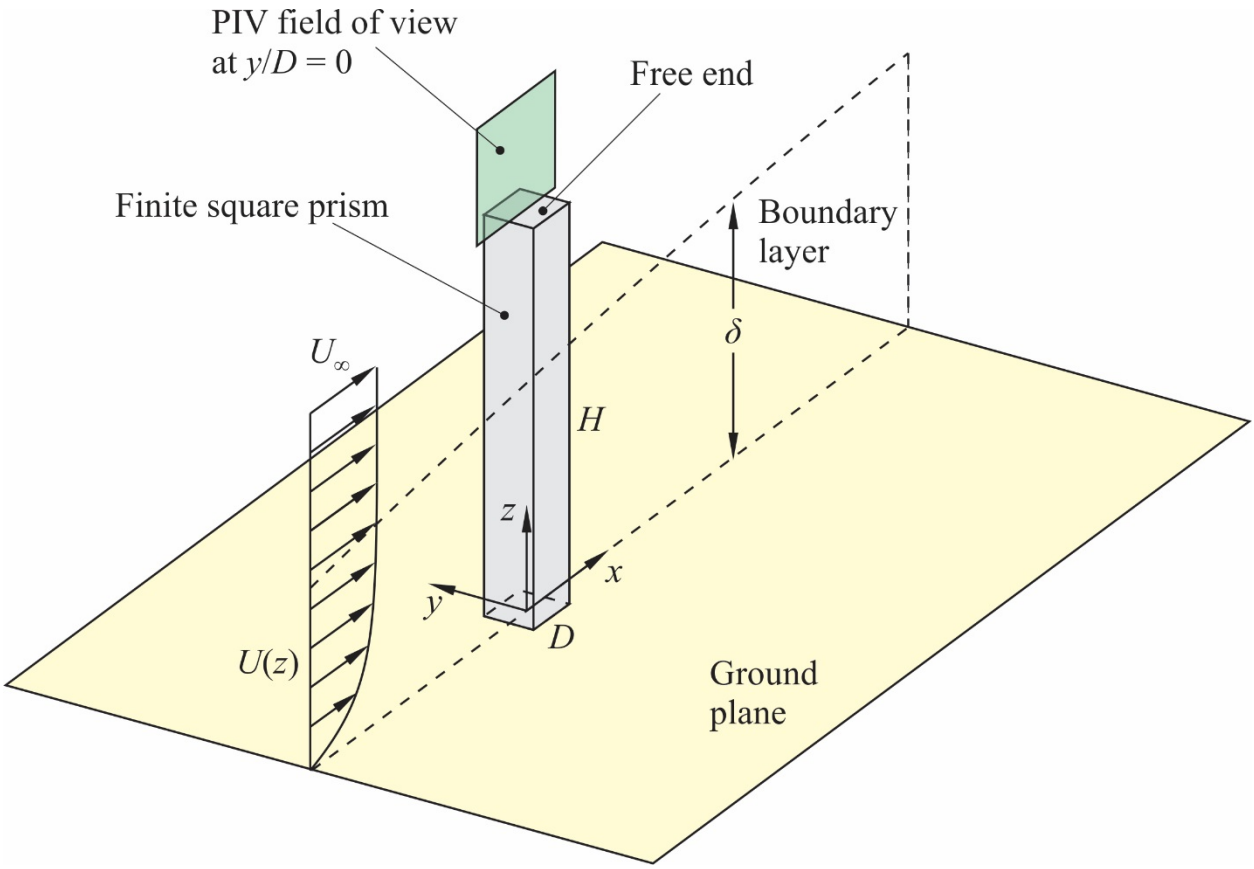

Figure 2.1: Schematic of the flow around a surface-mounted finite-height square prism, showing the field of view for the particle image velocimetry (PIV) measurements reported in Rostamy *et al.* [70] and Sumner *et al.* [86]. $U(z)$ = mean streamwise velocity profile of the boundary layer on the ground plane.

vertical (x-z) symmetry plane shown in Figure 2.1 (where x is the streamwise coordinate measured from the centre of the prism, and z is the vertical coordinate measured from the ground plane), which are located at $y/D = 0$ (corresponding to the vertical symmetry plane, where y is the cross-stream coordinate). In each plane, and for each AR, an ensemble of 1000 image pairs was acquired using 20 sets of 50 instantaneous snapshots. Each velocity vector field was a uniform grid of 127×127 vectors in the x and z directions with a spacing of approximately $\Delta x = \Delta z = 0.015D$. The uncertainty in the mean velocity measurements was estimated to be about 2%.

In its 2D form, POD has been used extensively as a flow visualization tool to extract the dominant flow features through a modal decomposition of the fluctuating energy of the flow field. Additionally, local vortex identification schemes have also been recently documented in the literature using point-wise analysis of the velocity gradient tensor (such as the swirling strength criterion, delta criterion, second invariant, among others). The interrelationships between various schemes used are discussed in Chakraborty *et al.* [13]. While there are considerable differences between these schemes when implemented in three-dimensional (3D) flows, local approaches to identify vortices in 2D flows remain in general invariant to the scheme used as they all share the same principle of identifying regions where the eigenvalues of the velocity gradient tensor are complex. It is thus without loss of generality, the swirling strength criterion has been used to identify vortices.

2.2.1 Proper Orthogonal Decomposition (POD)

The POD methodology (further elaborated in Berkooz *et al.* [5]) can be used to extract motions of different scales within the evolving dynamics of a flow. The snapshot POD method of Sirovich [78] is applied in the present study to decompose the time-dependent fluctuating part of the flow field into an orthonormal system of spatial velocity modes ($\varphi_m(x)$) and associated temporal coefficients $a_n(t)$.

The autocovariance matrix C of the fluctuating velocity field is decomposed into an orthonormal system by implementing an eigenvalue problem with eigenvalues and eigenvectors λ^i and A^i, respectively as $CA^i = \lambda^i A^i$. The eigenvectors are then normalized, as shown in Equation 2.1.

$$\varphi^i = \frac{\sum_1^N A_n^i u^n}{\left\| \sum_1^N A_n^i u^n \right\|}, \quad i = 1, 2, \ldots N \tag{2.1}$$

The relative magnitude of the eigenvalues (λ_m) determines the respective energy contribution in each mode. The temporal coefficients are computed using a matrix multiplication $a^n = [\varphi^1, \varphi^2 \ldots \varphi^N] \times u^N$. Finally, the POD modes taking a subset of M snapshots are computed as

$$u^n = \sum_{i=1}^{N} a_i^n \varphi^i \tag{2.2}$$

2.2.2 Swirling Strength Criterion

Hunt *et al.* [36], among others, defined vortices as regions where the velocity gradient tensor, Δu, has complex-conjugate eigenvalues. In this study, 2D velocity field data were used to obtain the local velocity gradients. Regions where complex-conjugate eigenvalues were found were presumed to have localized vortices. Though inherently a 3D concept, complex-conjugate eigenvalues should indicate the presence of a finite component of a vortex tube normal to a 2D plane. Thus, the swirling strength criterion should be able to reveal vortex structures in 2D flow fields. In Equation 2.3 given below, $eig()$ represents the eigenvalue function. A central differencing scheme was used to evaluate the velocity gradient tensor, Δu, at every control volume in the domain. The regions where $\lambda_{ci} \neq 0$ (where λ_{cr} and λ_{ci} represent the real and imaginary values of the complex number, respectively) have been presumed as regions where vortices are present.

$$eig(\Delta u) = eig\left(\begin{bmatrix} \frac{\partial u}{\partial x} & \frac{\partial u}{\partial z} \\ \frac{\partial w}{\partial x} & \frac{\partial w}{\partial z} \end{bmatrix}\right) = eig\left(\begin{bmatrix} \frac{u_{i+1}-u_{i-1}}{x_{i+1}-x_{i-1}} & \frac{u_{i+1}-u_{i-1}}{z_{i+1}-z_{i-1}} \\ \frac{v_{i+1}-v_{i-1}}{x_{i+1}-x_{i-1}} & \frac{v_{i+1}-v_{i-1}}{z_{i+1}-z_{i-1}} \end{bmatrix}\right) = \lambda_{cr} \pm i\lambda_{ci} \tag{2.3}$$

2.3 Results and Discussion

Detailed descriptions of the flow fields above the free end of the prism, for the four aspect ratios, can be found in Rostamy *et al.* [70] for the instantaneous flow fields and Sumner *et al.* [86] for the mean flow fields; however, a summary is presented in Section 2.3.1. The results of the POD analysis of the flow are presented in Section 2.3.2. The swirling strength analysis

is presented in Section 2.3.3.

2.3.1 Mean Flow Field

Figure 2.2 shows the mean streamlines in the vertical symmetry plane (at $y/D = 0$) for the prisms of AR = 9, 7, 5 and 3. The in-plane mean vorticity contours are shown in Figure 2.3. The flow is characterized by separation from the leading edge of the prism, which leads to the formation of a shear layer above the free end. The shear layer is clearly shown by the mean vorticity contours (Figure 2.3). The location of the shear layer coincides with the dividing streamline between the external flow outside the shear layer and the mean recirculation zone beneath the shear layer. For all four aspect ratios, this shear layer does not reattach back on to the free end of the prism, in contrast to flows above the free end of surface-mounted finite cylinders and cubes.

Below this shear layer, a weak clockwise recirculation flow structure is seen within the region of separated flow above the free-end surface. A focus (Figure 2.2) denotes the centre of this recirculating flow. Downstream of the prism, in the upper near wake, a saddle point occurs between the free-end and near-wake vortex structures [86]. Upward moving flow from the near wake is seen to locally separate from the trailing edge before it enters the recirculating flow beneath the dividing streamline. For the prism of AR = 3, a small vortex forms above the free-end surface near the trailing edge (Figure 2.2(d)); this vortex is not as clearly seen for the other aspect ratios [86].

The mean flow field for the prism of AR = 3 (Figures 2.2(d) and 2.3(d)) shows some small differences compared to the other prisms. This suggests that this prism is below the critical aspect ratio for these flow conditions [86]. A more detailed analysis of the mean flow field is given by Rostamy *et al.* [70] and Sumner *et al.* [86].

2.3.2 POD Results

Energy Distribution

When applied to a set of instantaneous fluctuating velocity fields, the POD technique is able to capture regions of high energy in a flow using a finite number of eigenmodes. The validation of POD in the literature, especially for aperiodic flows, have often revolved around the appropriateness of the number of snapshots, the time interval between successive snapshots,

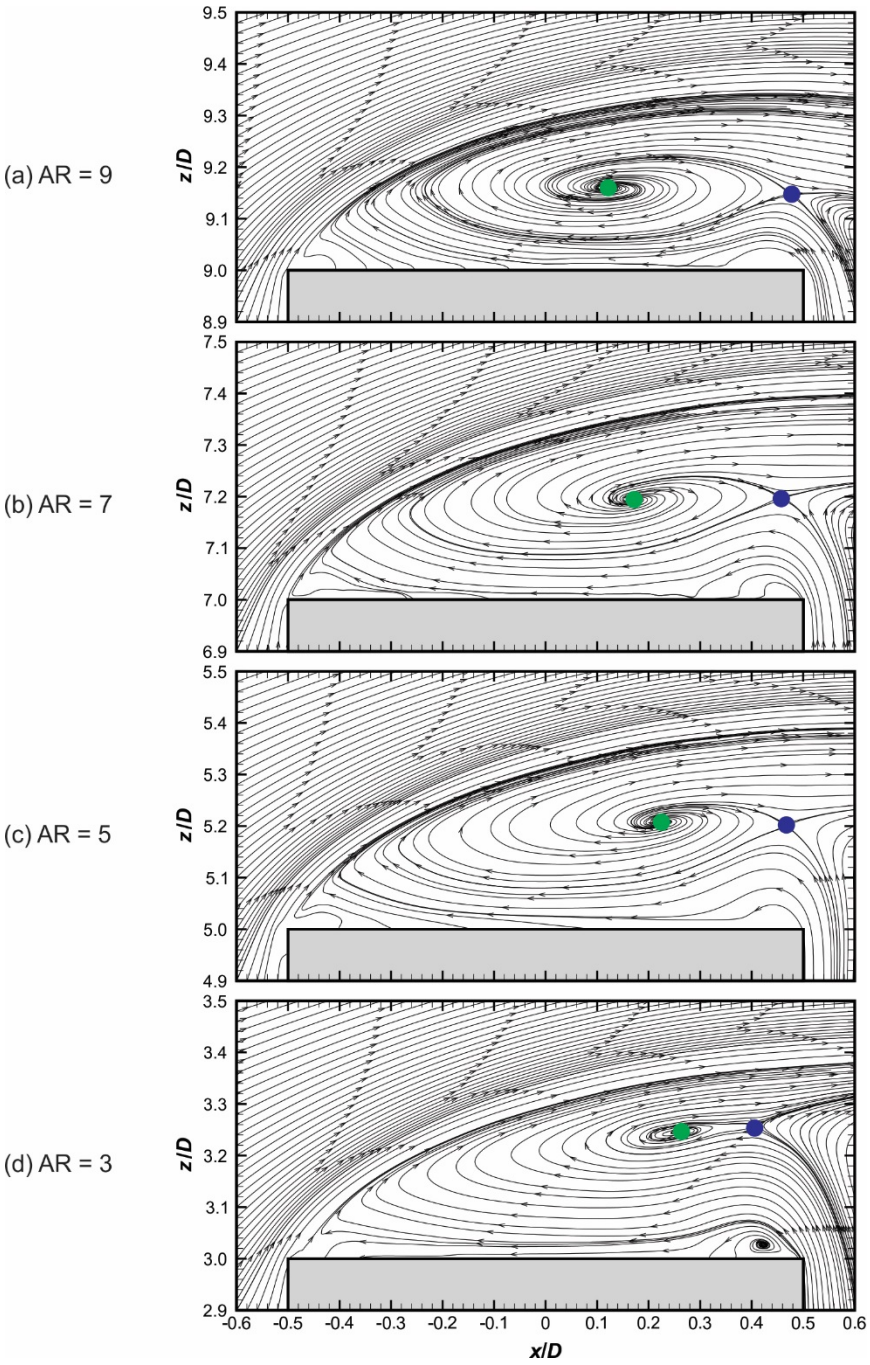

Figure 2.2: Mean streamlines above the free end of the surface-mounted finite-height square prism, in the vertical symmetry plane (at $y/D = 0$), from data reported in Rostamy *et al.* [70] and Sumner *et al.* [86]: (a) AR = 9; (b) AR = 7; (c) AR = 5; (d) AR = 3. Green circles represent foci, blue circles represent saddle points.

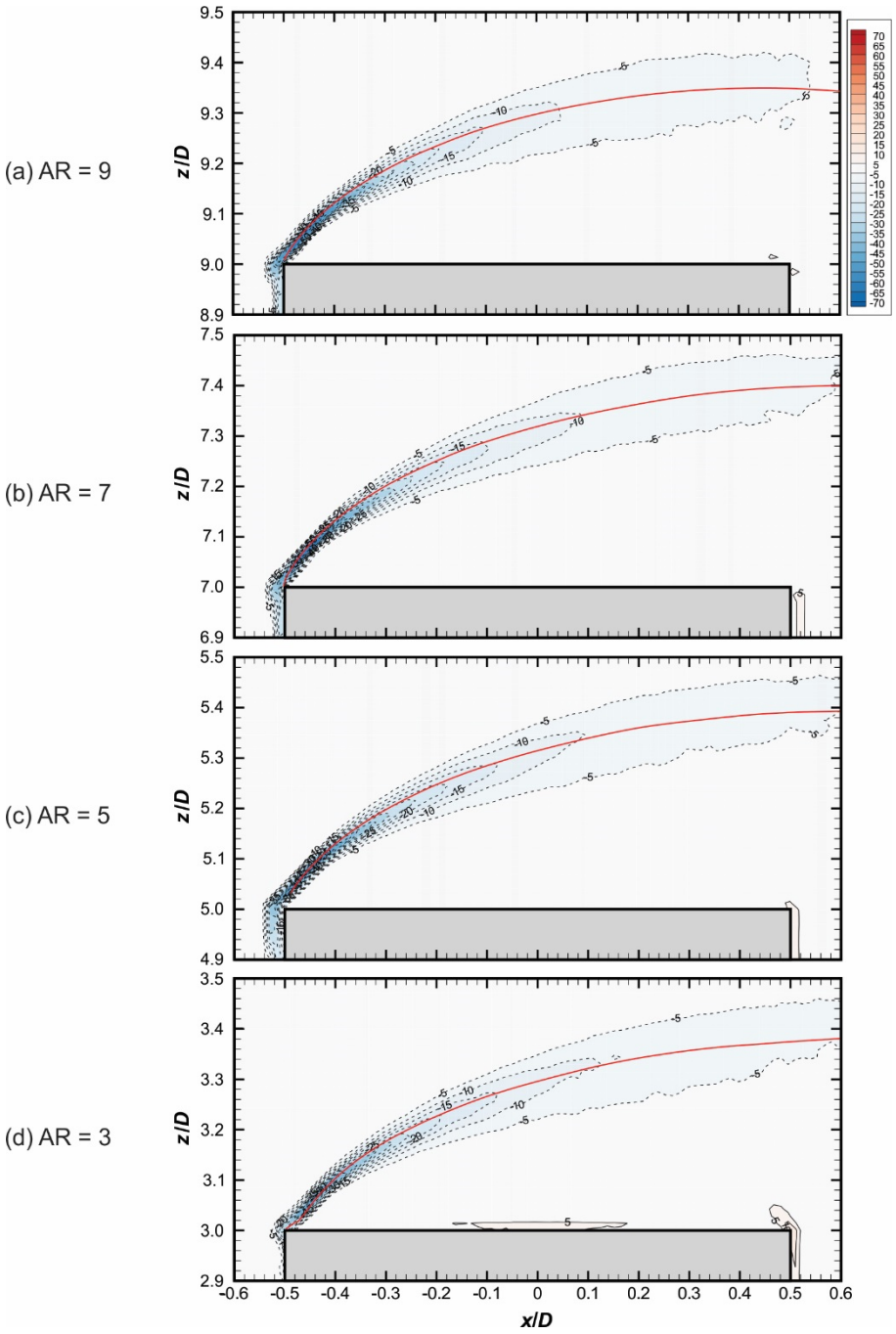

Figure 2.3: Mean in-plane vorticity field (contour lines of constant dimensionless cross-stream vorticity, $\omega_y^* = \omega_y D/u_\infty$), in the vertical symmetry plane (at $y/D = 0$), from data reported in Rostamy *et al.* [70] and Sumner *et al.* [86]: (a) AR = 9; (b) AR = 7; (c) AR = 5; (d) AR = 3. Solid lines represent positive (counter-clockwise (CCW)) vorticity. Dashed lines represent negative (clockwise (CW)) vorticity. Minimum vorticity contour magnitude is 0.05, contour increment of 0.05. Solid red curves are the dividing streamlines from Figure 2.2.

and the time resolution. To address these concerns, two separate cases of varying the number of snapshots and the time interval between successive snapshots have been considered to ascertain whether these parameters affect the overall POD energy distribution. In the first case, five sets of 50, 100, 200, 500 and 1000 snapshots, respectively, for the AR = 3 vertical symmetry plane (at $y/D = 0$) were used to compare the energy distribution. In the second case, the time interval between successive snapshots was varied. Two sets of 500 snapshots at successive time intervals of 0.25 s and 0.5 s were used for the POD analysis.

As shown in Figure 2.4(a), there are marginal differences in the distribution of energy in each snapshot when increasing the number of snapshots, with minimal change in energy distribution beyond 500 snapshots. In the present study, the POD analysis is conducted using the complete data set of 1000 snapshots; however, this figure shows that using a smaller basis of 500 snapshots should not affect the results significantly. Furthermore, two separate bases of 500 snapshots with differing time intervals between successive snapshots of 0.25 s and 0.5 s were also chosen for POD analysis (not shown). No significant differences were observed when the time interval between snapshots was changed. It was thus concluded that for a set of uncorrelated snapshots, the energy distribution and the flow features seen in the higher energy modes demonstrate little change with the number of snapshots as well as the time interval between successive snapshots.

Figure 2.4(b) shows the POD energy mode distribution as a percentage of the total across the various eigenmodes for the flow in the vertical symmetry plane (at $y/D = 0$) for prisms of AR = 3, 5, 7 and 9. The higher energy distribution is seen consistently in the first two energy modes for all four aspect ratios. The energy capture reaches a total of 50% of the total energy for just two energy modes for AR = 9, which increases to 21 energy modes for AR = 3. All four prisms require in the range of 280-300 modes to reach a cumulative 90% of the total energy. As this study was performed on the fluctuating velocity field of a flow dominated primarily by only a shear layer with a recirculation zone below (as shown in Figures 2.2 and 2.3), it was inferred that energy distribution across the eigenmodes would be more gradual owing to the presence of small-scale structures along the shear layer that make a small contribution to the overall energy. The temporal coefficients of the first few POD modes were analyzed, and no flow periodicity was determined. This is consistent with the absence of a strong periodic signal in the upper wake [54]. The energy percentage captured

in the first energy mode is lower as the aspect ratio is decreased, suggesting that there are fewer but stronger coherent structures above the free end at higher aspect ratios. This may suggest that the flow field at lower aspect ratios is more strongly influenced by the ground plane and potentially the contributions of the turbulent fluctuations at smaller scales due to the ground-plane boundary layer.

Energy modes for the prism of AR = 3

The AR = 3 prism is chosen first for POD analysis as it is expected to be more strongly influenced by the ground plane. Figure 2.5 shows the 2D velocity vector field and ω_y^* contours for the first, second, third and fourth energy mode in the vertical symmetry plane (at $y/D = 0$) above the free end. All vectors in the figures have been made with an index skip of 2 to increase visibility of the contours.

The POD modes exhibit the building blocks of the flow structure, which combined with their weighted temporal coefficients can be used to reconstruct the instantaneous flow field. It is thus of interest to explore the underlying energetic flow structures that constitute the free-end flow field. The first mode (Figure 2.5(a)) shows that the flow is mainly characterized by a strong shear layer originating from the leading edge and gradually expanding downstream without reattachment, as well as a small rotational structure in the upper wake above the free end of the prism at approximately $x/D = 0.35$ in the region of the mean recirculation zone (marked as a blue dot). This is an interesting result given that after the mean flow has been removed for the POD analysis, the first mode reveals structures that are similar to those seen in the mean flow field (see Figures 2.2(d) and 2.3(d)). The shear layer in the first mode is characterized by two adjacent regions (or sub-layers) of vorticity of opposite sign. These shear sub-layers align themselves along the dividing streamline seen in the mean flow field (Figure 3(d)), with the counter-clockwise (CCW) vorticity sub-layer sitting above the clockwise (CW) sub-layer. These two sub-layers are most characteristic in the vertical symmetry plane; in planes away from the symmetry plane (not shown), the CW shear sub-layer dominates the flow field compared to the CCW sub-layer. The two sub-layers suggest a complex interaction between the separating shear layer and the recirculation zone below; this undulating effect (i.e. the changing distance of the separating shear layer from the prism surface) has been previously observed in the separating shear layer from the forward corner

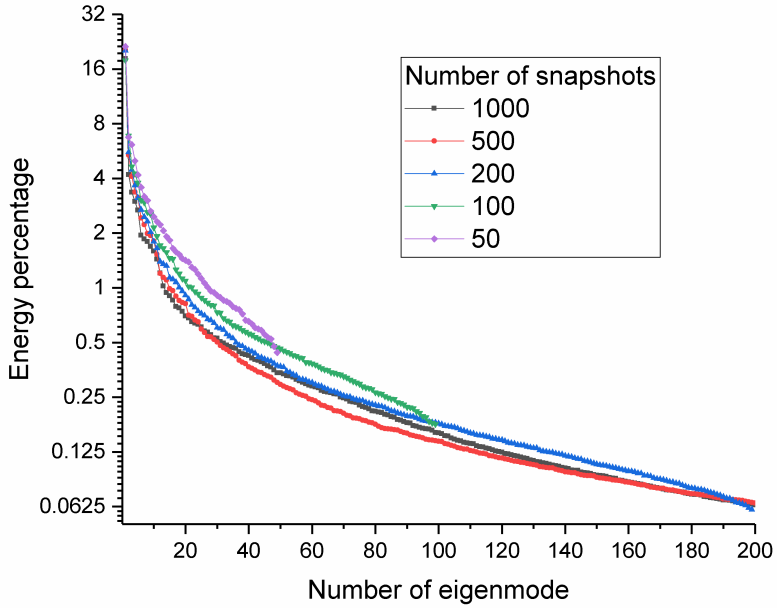

(a)

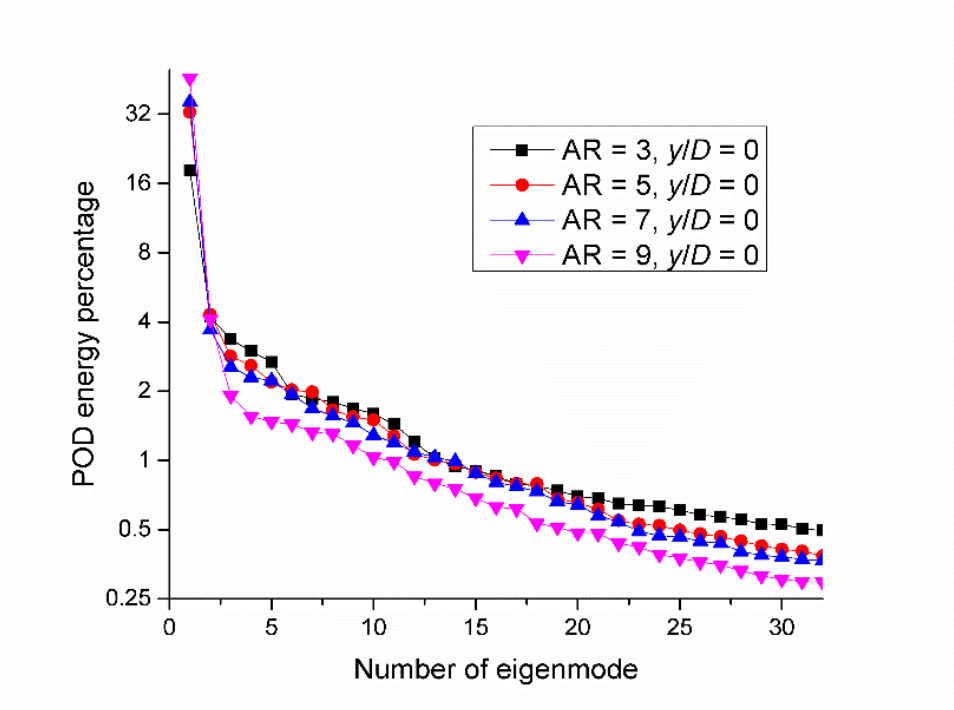

(b)

Figure 2.4: POD energy mode distributions in vertical (x-z) planes above the free end of the surface-mounted finite-height square prisms: (a) for the prism of AR = 3 in the vertical symmetry plane (at $y/D = 0$), varying the number of snapshots; and (b) for the prisms of AR = 9, 7, 5 and 3 in the vertical symmetry plane (at $y/D = 0$).

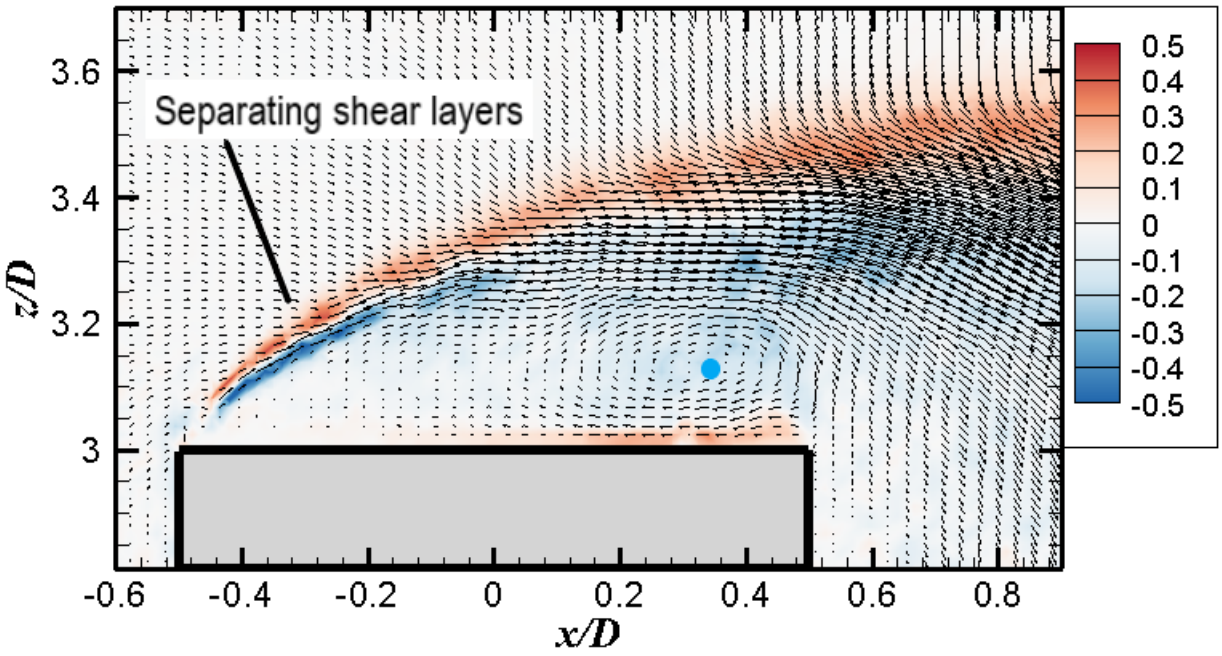
Separating shear layers
3.6
3.4
3.2
3
z/D
-0.6
-0.4
-0.2
0
0.2
0.4
0.6
0.8
x/D
0.5
0.4
0.3
0.2
0.1
0
-0.1
-0.2
-0.3
-0.4
-0.5

(a)

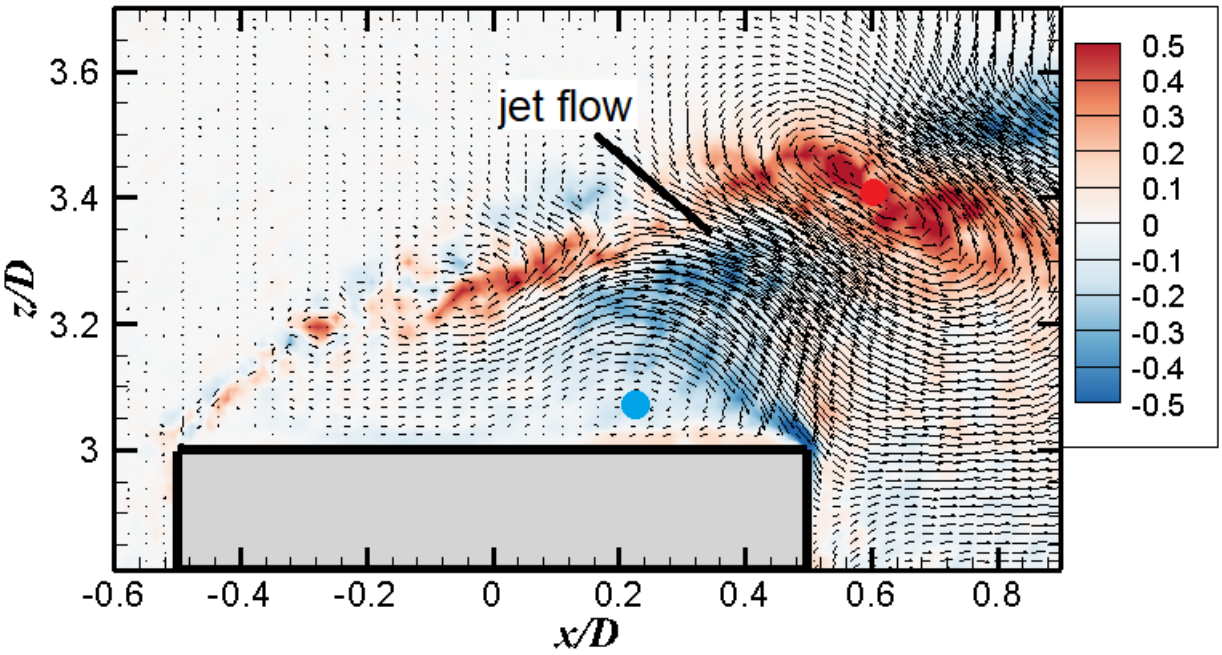
jet flow
3.6
3.4
3.2
3
z/D
-0.6
-0.4
-0.2
0
0.2
0.4
0.6
0.8
x/D
0.5
0.4
0.3
0.2
0.1
0
-0.1
-0.2
-0.3
-0.4
-0.5

(b)

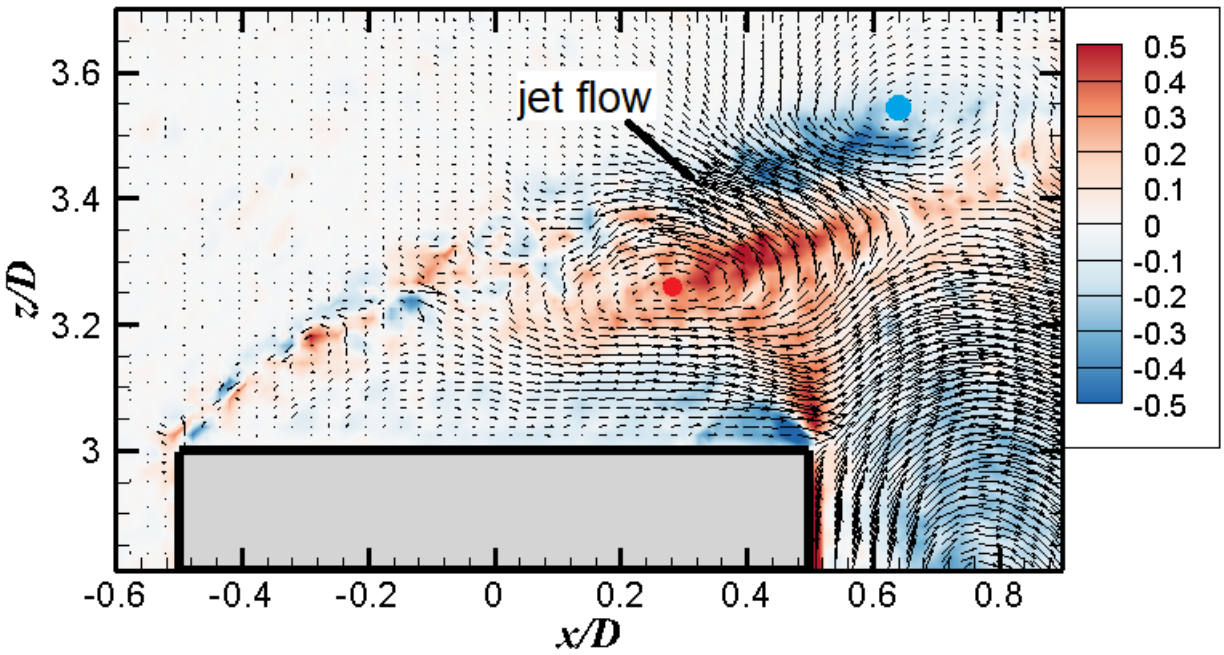

(c)

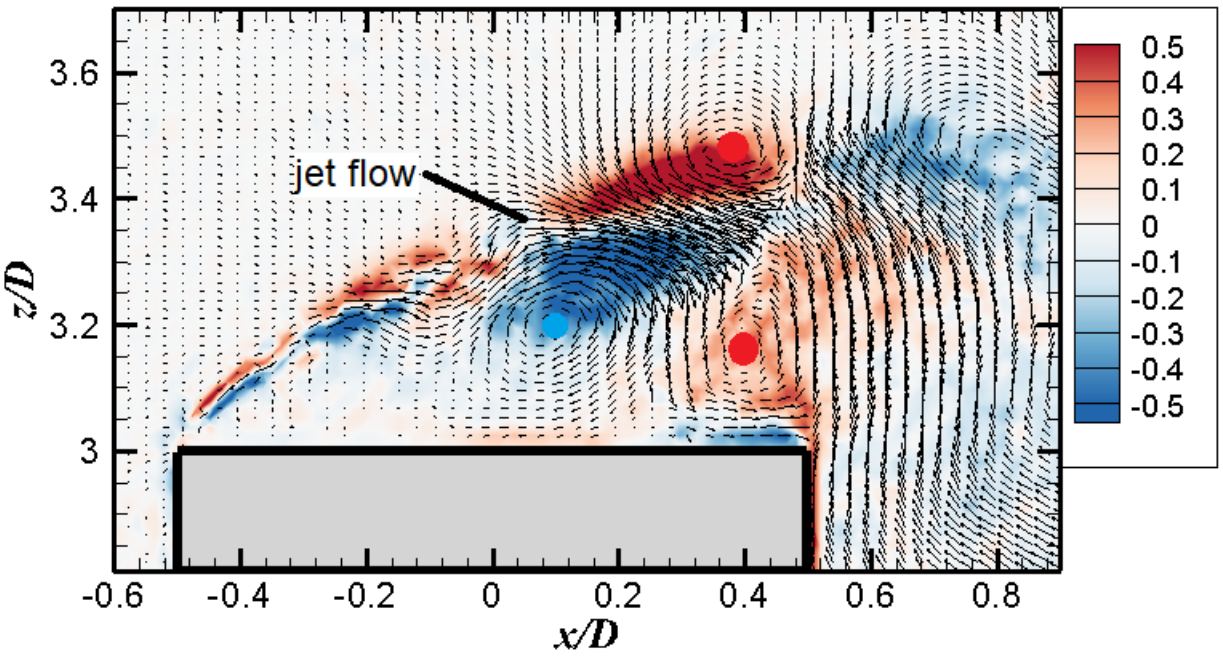

(d)

Figure 2.5: In-plane velocity vector field in the vertical symmetry plane (at $y/D = 0$) above the free end of the prism of AR = 3, along with in-plane vorticity (ω_y^*) contours, for the (a) first, (b) second, (c) third, and (d) fourth energy modes.

of a 2D square prism [51]. These sub-layers progressively become weaker farther from the leading edge.

In contrast to the first mode, the second mode (Figure 2.5(b)) and third mode (Figure 2.5(c)) do not show the distinct shear sub-layers seen in the first energy mode. These modes are dominated by additional rotational structures along the region of the separating shear layer. The second energy mode shows some localized entrainment of flow from the freestream towards the diffusing shear layer vertically above the trailing edge of the prism, which exhibits some characteristics of a jet. This jet-like flow is due to the presence of oppositely oriented vortex structures above (counterclockwise at (x/D, z/D) = (0.6, 3.4) marked in red) and below it (clockwise at (x/D, z/D) = (0.2, 3.1) marked in blue) in the region above the trailing edge. The lower vortex structure directly above the free end surface is in approximately the same general location as the structure seen in the first energy mode. The second energy mode shows these rotational structures along the region of the separating shear layer increasing in size in the streamwise direction, with the largest vortex structure being above the trailing edge of the prism in the region of the separating shear layer (counterclockwise at (x/D, z/D) = (0.6, 3.4) marked in red). Recall that the velocity vectors in the first energy mode (Figure 2.5(a)) show that the flow speed is slower below and faster above the separating shear sub-layers, respectively. This suggests that these separating shear sub-layers can be idealized as a vortex sheet based on to this velocity difference. Any perturbations in the outer flow would cause a deformation of this vortex sheet, giving rise to Kelvin-Helmholtz (KH) instabilities. The initial small-scale structures in the separating shear layer in the second energy mode represent these KH instabilities such as those seen by Hain *et al.* [31] and Palau-Salvador *et al.* [61] for a finite cylinder, Wang *et al.* [95] for a finite prism, and Bourgeois *et al.* [7] for finite cylinders and prisms.

The third energy mode (Figure 2.5(c)) further characterizes the separating shear layer into smaller scale vortex structures, however distinct, and often opposite, to those contained by the second energy mode. Moving downstream along the separating shear layer, these vortex structures grow larger in size, similar to those seen in the second energy mode. However, the rotation of the larger vortex structures (i.e. the counterclockwise structure at (x/D, z/D) = (0.3, 3.3) marked in red) and the clockwise structure at (x/D, z/D) = (0.6, 3.5) marked in blue) is opposite to that seen in the second energy mode, and the jet flow created by these

vortices is now in the opposite direction (i.e. towards the outer freestream flow). The third mode also shows the presence of a clockwise vortex just downstream of the trailing edge (at $x/D = 0.8$), which, in some ways, resembles vortex B_t, identified in other studies of the mean flow [86]. This specific vortex structure is not seen in any of the first three energy modes for higher aspect ratios (not shown). This may be because the AR = 3 prism has the strongest upward-directed flow from the ground plane (compared to the other prisms of AR = 9, 7 and 5) which contributes to the formation of this structure in the instantaneous flow field. Sumner *et al.* [86] have shown that vortex B_t, in the mean field, exists for all aspect ratios, but is largest in size for the prism of AR = 3.

Figure 2.5(d) shows the in-plane velocity field and the ω_y^* contours for the fourth energy mode for a vertical plane at $y/D = 0$. In this figure, the vorticity contours in the separating shear layer just beyond the leading edge corner appear more stretched in the streamwise direction. Larger counter-rotating vortex structures are observed further downstream. Once again, a jet-like flow is seen between two larger-sized vortices in the separated flow region above the trailing edge. The orientation of these structures is similar to the second energy mode and opposite to the third energy mode (i.e. the clockwise structure at (x/D, z/D) = (0.1, 3.2) marked in blue and the clockwise structure at (x/D, z/D) = (0.4, 3.5) marked in red, indicating that these structures may alternate in succession with increasing energy modes. Furthermore, an additional clockwise vortex structure is seen above the trailing edge of the prism at (x/D, z/D) = (0.4, 3.2) marked in red formed due to the entrainment of flow from the separating shear layer above, and the reverse flow below it due to the flow separation at the trailing edge.

Energy modes for the higher aspect ratios

For prisms of higher AR, the first POD energy mode in the symmetry plane above the free end shows similar characteristics to the AR = 3 case (Figure 2.5(a)). Two examples for AR = 5 and AR = 9 are shown in Figures 2.6(a) and 2.6(b), respectively. Once again, a distinct pair of shear sub-layers in the vicinity of the dividing streamline of the mean flow is observed. Vorticity in the shear sub-layers is strongest just beyond the prism leading edge and once again becomes progressively weaker downstream. The thickness of the recirculation zone is seen to reduce with increasing aspect ratio. The small vortical structure near the

trailing edge (clockwise at (x/D, z/D) = (0.35, 5.1) marked in blue) evident in the AR = 3 mean flow (Figure 2.5(a)) is also present in the AR = 5 flow (Figure 2.6(a)), but is weaker. This structure is not evident for prisms of AR = 7 (not shown) and AR = 9 (Figure 2.6(b)) indicating that the structure is perhaps an artefact of the strength of the recirculation zone above the free end of the prism, which simultaneously gets weaker with increasing aspect ratio. Above the trailing edge within the separating shear layers, the strength of the vector field increases with aspect ratio, suggesting the influence of the downward flow from the freestream flow above is stronger at higher aspect ratios. This region moves from $x/D = 0.6$, to $x/D = 0.5$ and subsequently $x/D = 0.4$ in the first energy mode for aspect ratio AR = 3, 5 and 9, respectively.

Downstream of the prism, just after the trailing edge of the free end, the flow penetrates deeper into the wake with increasing aspect ratio based on the velocity vectors. This may be attributed to the reduction in size of mean vortex B_t in the upper part of the near wake [86] with increasing aspect ratio.

The second POD energy mode for the higher aspect ratios AR = 5, 7 and 9 (not shown) also reveals the strong shear sub-layers seen in the first POD energy mode This is in contrast to the second mode in the AR = 3 case, where no shear sub-layers are seen. Figure 2.7 shows the third energy mode in the vertical symmetry plane for AR = 5, 7 and 9. Once again, similar vortex structures associated with shear-layer instabilities are observed (from x/D = -0.5 onwards) above the free end front corner of the prism. An interesting observation is that the number of vortex structures reduces with increasing aspect ratio. Figure 2.6(a), for AR = 5, already shows a reduced number of vortex structures compared to the AR = 3 case (Figure 2.5(c)), and this number progressively reduces until the AR = 9 case (Figure 2.6(c)), where only a couple of weakly rotating structures are observed and the induced flow pattern is quite different. This suggests that with increasing aspect ratio, the velocity disparity between the shear layer from the leading edge and the surrounding freestream flow is further reduced with fewer instabilities. The formation of these alternating, small-scale structures across the shear sub-layers is thus a strong function of the aspect ratio, and may be influenced by effects of the ground plane and/or the boundary layer, or the strength of the flow being deflected upwards on the upstream face of the prism.

An unusual feature of the third energy mode for the AR = 9 case is that the sign of

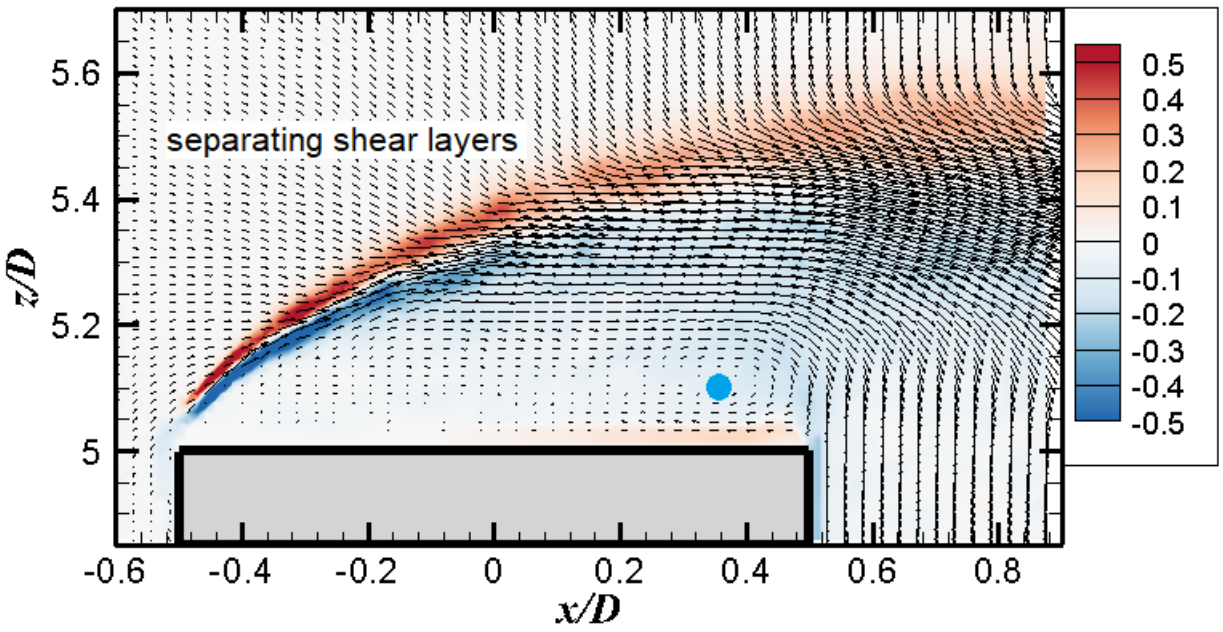

(a)

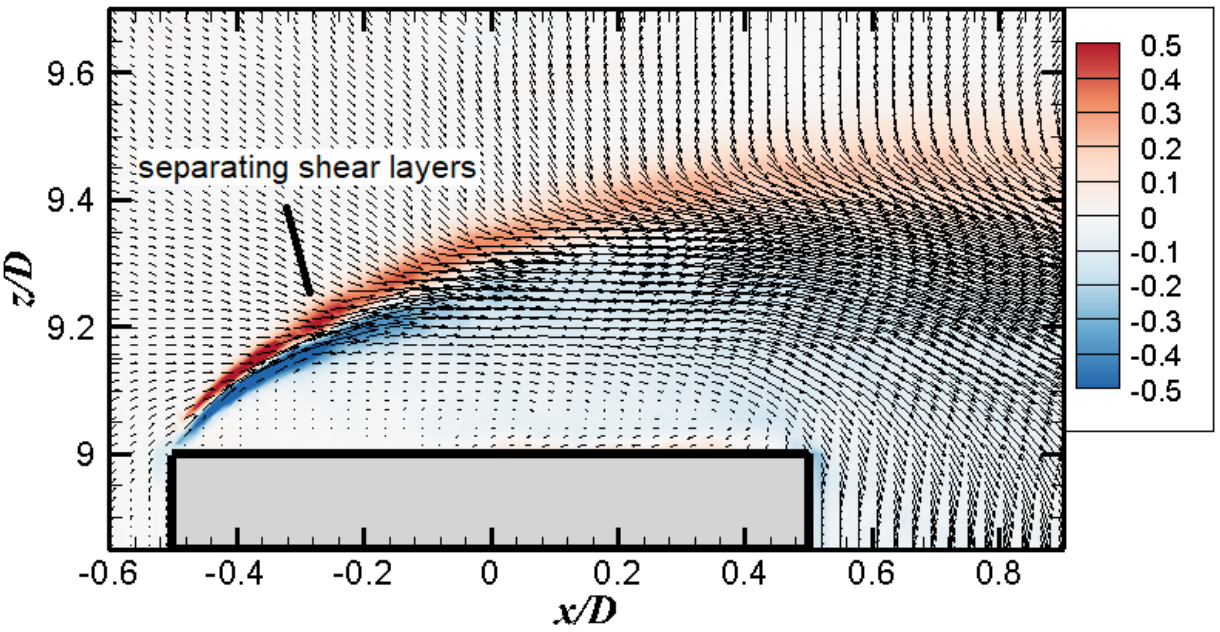

(b)

Figure 2.6: In-plane velocity vector field above the free end of the prism, in the vertical symmetry plane ($y/D = 0$), along with in-plane vorticity (ω_y^*) contours, for the first energy mode for the prisms of (a) AR = 5 and (b) AR = 9.

vorticity of the dominant elongated structure above the free end in the separating shear layer is different from the other aspect ratios. However, the sign of vorticity resembles that of the separating shear layers of the first energy mode. It is thus concluded that this energy mode also has contributions from the separating shear layers in the higher energy modes, and further confirms that the KH instabilities may indeed form the building blocks of these separating shear layers for this flow field.

POD Reconstructions

An application and validation of the POD analysis is to reconstruct the instantaneous flow field into its dominant dynamic components using a linear combination of a limited number of energy modes. As POD modes represent energy structures that contribute most to the overall flow field, lower order POD reconstructions offer insightful representations of the original instantaneous flow field. Figure 2.8 shows the reconstruction of the velocity field at an arbitrary instant in time using 5 modes (Figure 2.8(a)) and 10 modes (Figure 2.8(b)), plus a comparison with the instantaneous fluctuating flow field (Figure 2.8(c)). All figures show the development of altenating vortex structures, similar to the KH instabilities explained earlier. These vortex structures increase in size along the separating shear layer. An interesting observation is that Figure 2.8(a) contains the larger vortex structures farther downstream from the leading edge, with limited resolution of smaller-scale structures closer to the free end leading edge. In Figure 2.8(b), the smaller-scale structures near the leading edge are more clearly visible through both vectors and the vorticity contours. However, the number and strength of the vortex structures is still different from the instantaneous fluctuating velocity field. This illustrates that a reconstruction of the instantaneous flow with increased number of modes gives increasingly better resolution of smaller-scale structures as well as refinement of large-scale structures. These vortex structures become progressively larger as they move downstream, and they disappear beyond the trailing edge in the separating shear layer region.

However, it must be pointed out that there are still structures seen in the instantaneous flow field (Figure 2.8(c)) from the vector field that are missing in the reconstructions (e.g. a rotational structure at $(x/D,\, z/D) = (0.8,\, 4.8)$ and another at $(x/D,\, z/D) = (0.2,\, 5.2)$). These structures however show very weak contours of vorticity indicating that they are weak rotational structures. This is consistent with POD as the higher energy modes reveal only

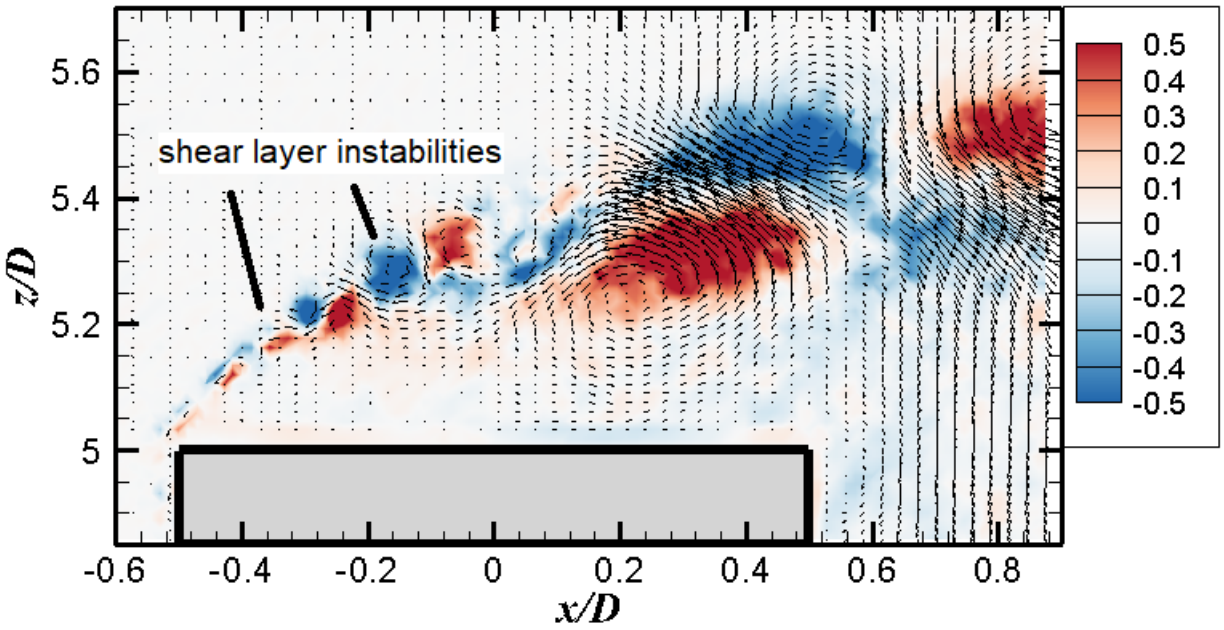
shear layer instabilities
z/D
x/D
5.6
5.4
5.2
5
-0.6
-0.4
-0.2
0
0.2
0.4
0.6
0.8
0.5
0.4
0.3
0.2
0.1
0
-0.1
-0.2
-0.3
-0.4
-0.5

(a)

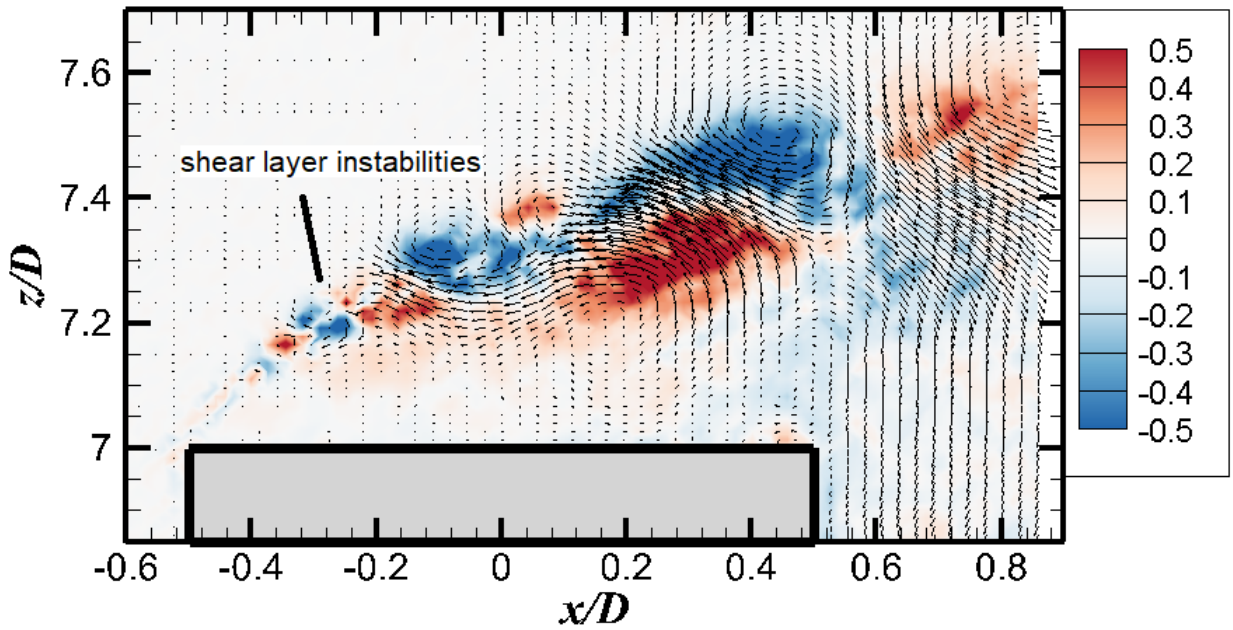
shear layer instabilities
z/D
x/D
7.6
7.4
7.2
7
-0.6
-0.4
-0.2
0
0.2
0.4
0.6
0.8
0.5
0.4
0.3
0.2
0.1
0
-0.1
-0.2
-0.3
-0.4
-0.5

(b)

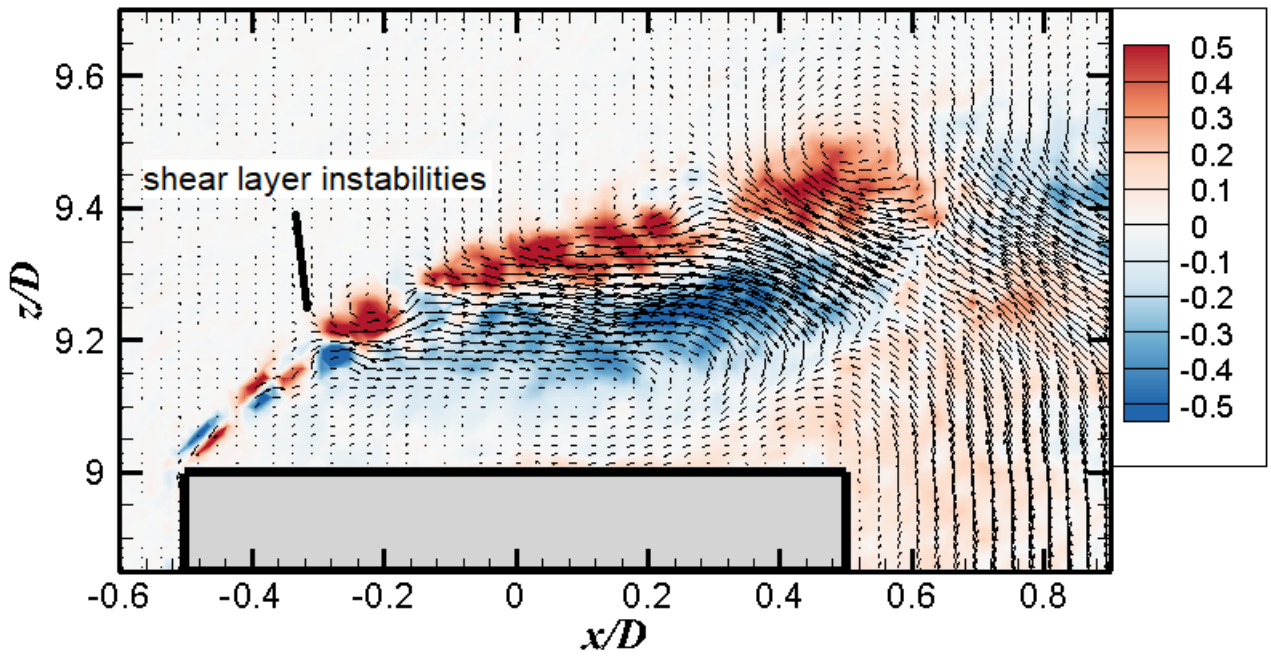

(c)

Figure 2.7: In-plane velocity vector field above the free end of the prism, in the vertical symmetry plane ($y/D = 0$), along with in-plane vorticity (ω_y^*) contours, for the third energy mode for the prisms of a) AR = 5, (b) AR = 7, and (c) AR = 9.

the dominant energetic structures. A reconstruction using a higher number of energy modes would deliver a better resolution to the vector field and show further similarity with the instantaneous flow field.

2.3.3 Swirling Strength Results

The primary advantage of swirling strength is its capability of isolating rotational structures in the ω_y^* contour plots (thereby selectively filtering out the vorticity due to shear). This is particularly useful in decomposing shear flows into their constituent vortex structures. Figure 2.9 shows the application of the swirling strength criterion to the first and third POD energy modes for the vertical symmetry plane above the prism of AR = 3. The vectors have been shown with an index skip of two nodes for lesser obstruction of the swirling strength criterion contours in Figures 2.9 and 2.10.

The first energy mode (Figure 2.9(a)) shows a cluster of small-scale vortex structures along the region of the separated shear layers seen in the first energy mode vorticity contours in Figure 2.5(a). It shows how the beginning of the shear layer is composed of strong vortices, which, on further interaction with the outer flow and the recirculation zone below it, develop into weaker structures downstream. The antisymmetric arrangement of these vortices along this region of the separated shear layers further suggests that these structures are evidence of KH instabilities seen previously in the higher energy modes. Swirling strength can additionally identify some relatively strong small-scale vortex structures even in regions of weaker ω_y^*. As seen in Figure 2.9(a), the clockwise vortex structure seen above the free end near the trailing edge (at $x/D = 0.35$, shown by the black dot) is confirmed by the swirling strength criterion.

The third energy mode (Figure 2.9(b)) shows a counter-clockwise rotation just below the dividing streamline indicating a complex interaction between the separating shear layer and a vortex structure just below the free end trailing edge. The vectors in this energy mode move in the freestream direction relatively close to the free end of the prism. Swirling strength is successful in revealing vortices at a higher resolution that are difficult to visualize from the vector profiles owing to the small size (magnitude) of the vectors in the recirculation zone of the instantaneous field. An example of this are the small-scale vortex structures seen above the trailing edge tip of the square prism in Figure 2.9(b) (at and around (x/D, y/D)

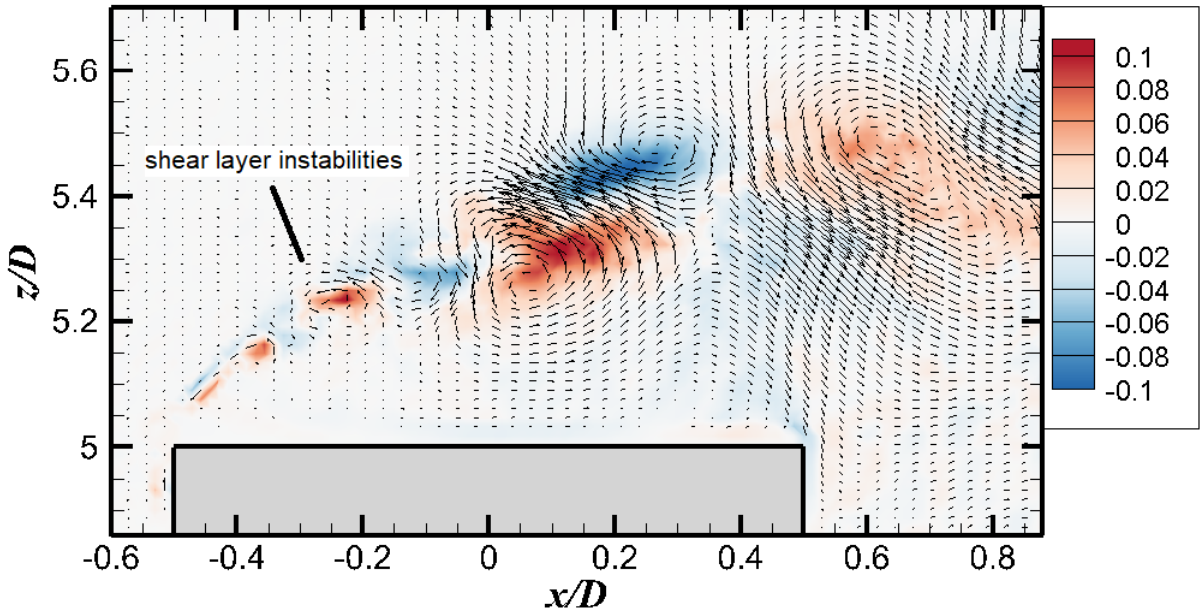
shear layer instabilities
z/D
x/D
5.6
5.4
5.2
5
-0.6
-0.4
-0.2
0
0.2
0.4
0.6
0.8
0.1
0.08
0.06
0.04
0.02
0
-0.02
-0.04
-0.06
-0.08
-0.1

(a)

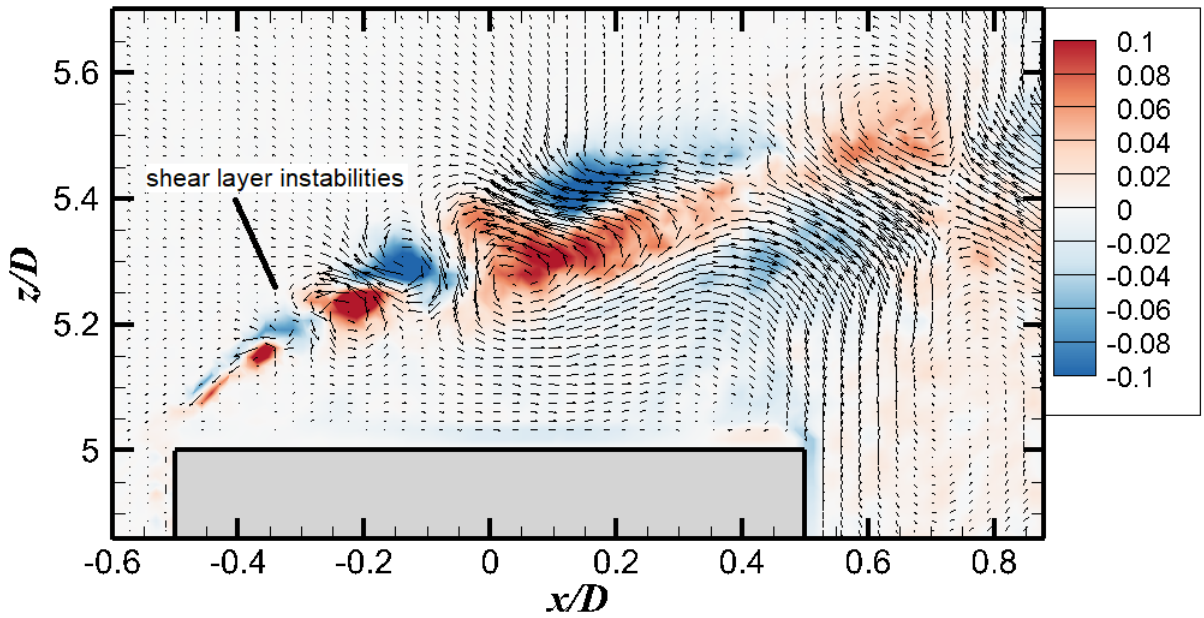
shear layer instabilities
z/D
x/D
5.6
5.4
5.2
5
-0.6
-0.4
-0.2
0
0.2
0.4
0.6
0.8
0.1
0.08
0.06
0.04
0.02
0
-0.02
-0.04
-0.06
-0.08
-0.1

(b)

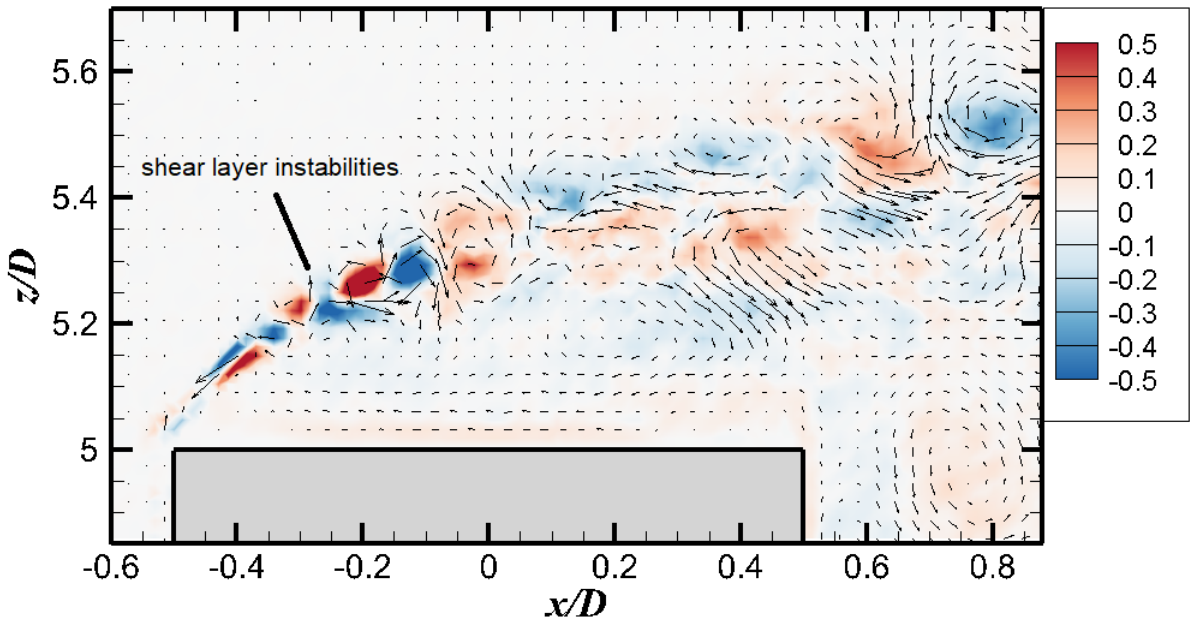

(c)

Figure 2.8: In-plane velocity vector field (u/U_∞ and w/U_∞ components) above the free end of the prism of AR = 5, in the vertical symmetry plane ($y/D = 0$), along with in-plane vorticity (ω_y^*) contours, for a POD reconstruction using (a) the first 5 energy modes, (b) the first 10 energy modes, along with (c) the instantaneous fluctuating velocity field.

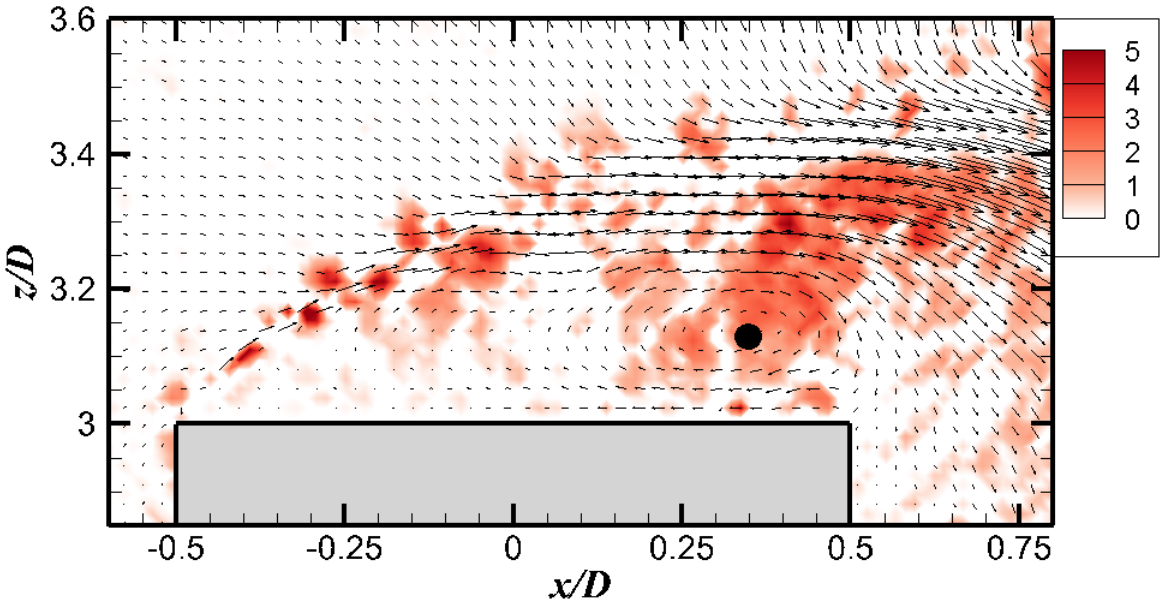

(a)

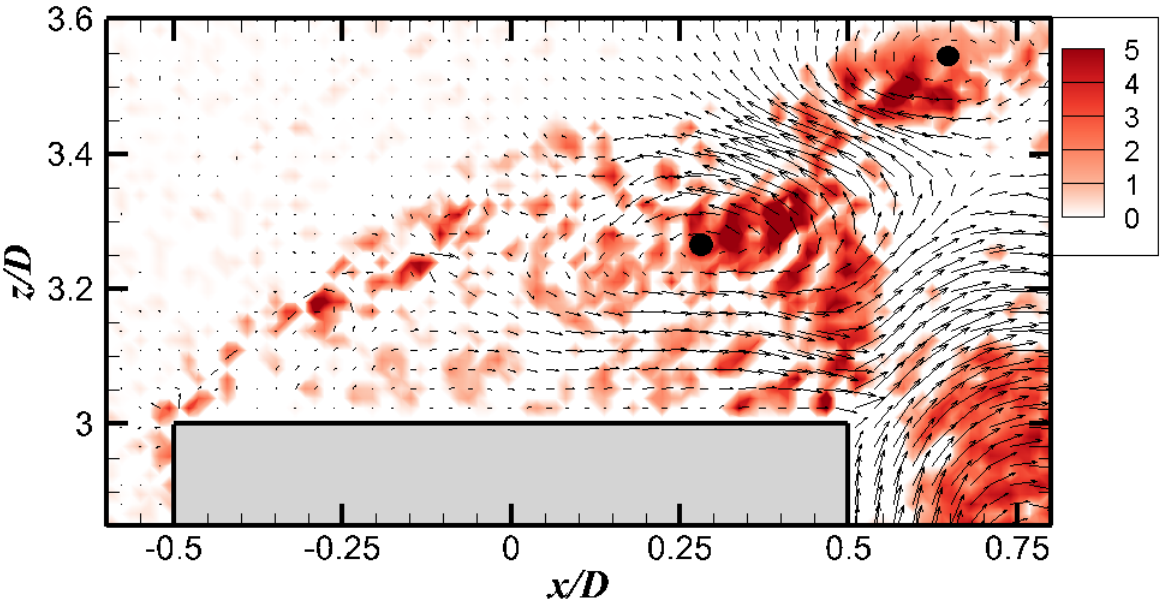

(b)

Figure 2.9: In-plane velocity vector field above the free end of the prism, in the vertical symmetry plane ($y/D = 0$), along with swirling strength contours, for the prism of AR = 3: (a) first energy mode, and (b) third energy mode. The vectors have been shown with an index skip of 2 for better visibility.

= (-0.25, 3.2)), but not clear in the vorticity contours in Figure 2.5(c). Thus, if applied in tandem on 2D flow fields, POD can be used to predict the presence and sign of vorticity in a velocity field, and the swirling strength criterion can be used to further resolve this vorticity as a rotational motion. Swirling strength is able to find additional structures that a vorticity contour alone is unable to capture.

Figure 2.10 shows the swirling strength contours in the vertical symmetry planes above the free end for the AR = 5 and AR = 9 square prisms. In both cases, strong vortices separating from the leading edge are seen extending into the wake, similar to those seen for the AR = 3 prism (Figure 2.10(a)). As the aspect ratio increases, these rotational structures reduce in strength and number, and are only seen closer to the leading edge of the prism. The location above the free end where these structures moves closer to the free-end surface with increasing aspect ratio and the rotational structures appear to be elongated rather than round. An important feature seen in these figures is the stronger downward flow after the prism trailing edge for AR = 9 (Figure 2.10(b)). The swirling strength criterion shows a weaker and broader distribution after the trailing edge at higher aspect ratios compared to the AR = 3 case, where a more scattered distribution of rotational structures was seen throughout the separating shear layer region. (Figure 2.10(a)).

2.4 Conclusions

The objective of this study was to investigate the fluctuating velocity field above the free end of surface-mounted finite-height square prisms of AR = 3, 5, 7 and 9, using POD and the swirling strength criterion. Data for the flow visualization methodologies were obtained from PIV measurements made in a low-speed wind tunnel, which were reported in Rostamy *et al.* [70] and Sumner *et al.* [86]. The mean flow structures remained largely similar for the four aspect ratios, with flow separation from the leading edge, a prominent separated shear layer above the free end, a mean recirculation zone beneath this shear layer, and a saddle point downstream at the end of the recirculation zone where it meets the near-wake region.

For all four prisms, the first POD energy mode characterized the shear layer separating from the leading edge of the prism as consisting of two distinct shear sub-layers of clockwise and counter clockwise vorticity, formed due to opposing effects of the recirculation zone below and the freestream external flow above. With an increase in aspect ratio, the recirculation

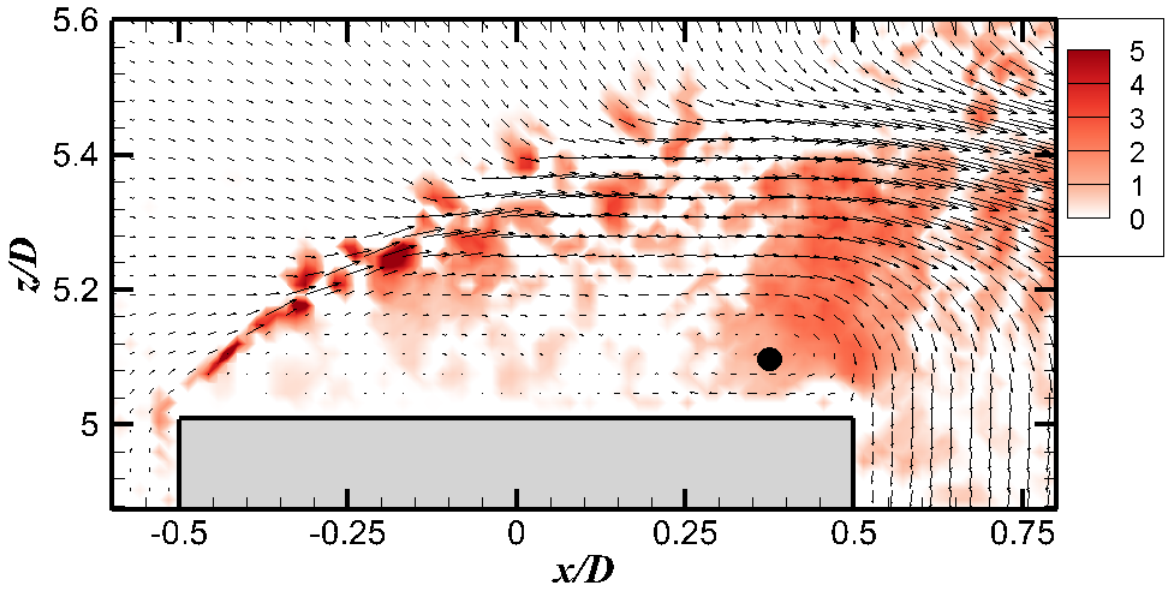

(a)

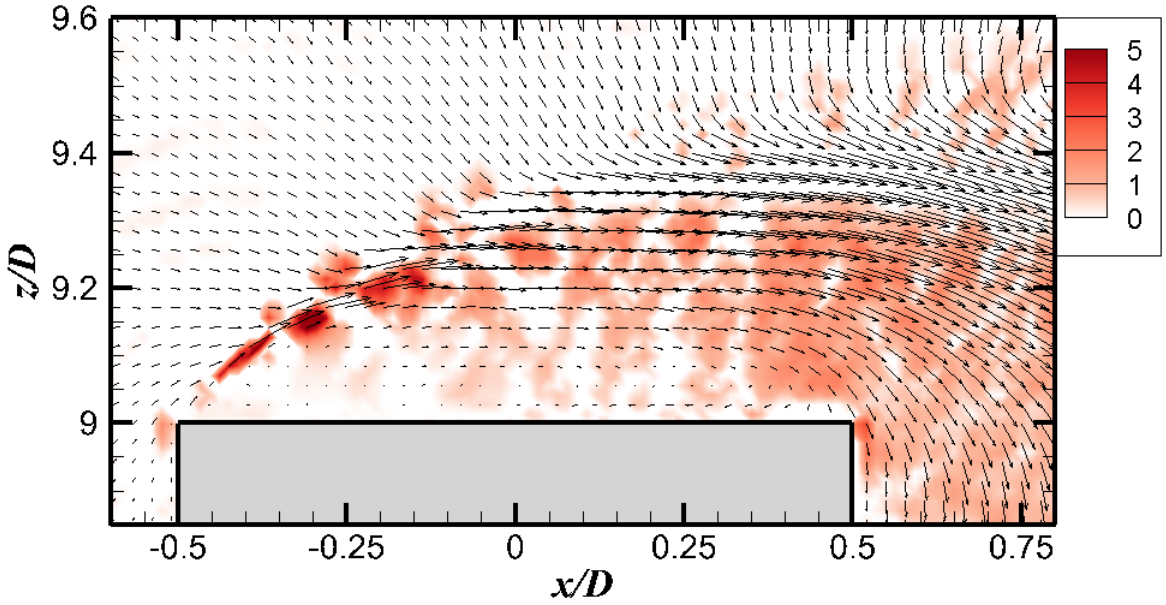

(b)

Figure 2.10: In-plane velocity vector field above the free end of the prism, in the vertical symmetry plane ($y/D = 0$), along with swirling strength contours, for the first energy mode: (a) AR = 5, and (b) AR = 9. The vectors have been shown with an index skip of 2 for lesser obstruction of the swirling strength contours.

zone reduces slightly in thickness as seen by the location of shear layer above the free end. The higher POD modes further characterized these sub-layers as containing distinct small-scale vortices. These vortices were strong near the leading edge, and grew in size moving downstream. They are likely evidence of Kelvin-Helmholtz instabilities seen in similar flows at the boundary of two different fluid layers moving with different velocities. At higher aspect ratios, the tendency for the formation of these instabilities is reduced, possibly due to the weaker influence of the ground plane. Other structures, including some large-scale vortices were seen at various locations, some above the free end of prism, and some in the separating shear layer region. The structures along the separating shear layer showed an alternating pattern of vorticity with some evidence of a jet in between them, due to the passage of flow between two large oppositely-oriented vortex structures. At higher aspect ratios, the number of small-scale structures near the leading edge reduce and become more elongated in the regions above the free end closer to the trailing edge. POD was thus able to identify some novel flow structures and further characterize the evolution of flow structures seen in the mean and instantaneous flow fields. POD provided additional information on the interactions between the outer freestream flow above the prism with the separating shear layers. POD also revealed additional rotational structures near the free end surface and around the trailing edge of the prism unseen in previous studies of this flow field.

To characterize the vorticity into distinct rotational structures, the swirling strength criterion was used. This was important primarily to classify structures embedded within the separating shear layer as vortices and further verify the formation of KH instabilities within the separating shear layers. The swirling strength criterion was able to find rotational structures in regions identified previously by the vorticity contours across all energy modes consistent with KH instabilities. In the AR = 3 case, several rotational structures were also seen above and behind the trailing edge of the prism. With increasing aspect ratio, the rotational structures along the separating shear layer were strong close to the leading edge of the prism but became weaker along the shear layer region towards the wake. The number of small-scale rotational structures at the beginning of the separating shear layer also reduced with increasing aspect ratio indicating that the tendency of formation of KH instabilities decreases with increasing aspect ratio. This is also consistent with the fact that the length of the separating shear layers reduce with increasing aspect ratio thereby providing a reduced region of KH

instability formation.

Acknowledgements

The authors would like to thank the contributions of Dr. Noorallah Rostamy for collecting the experimental data used in this study.

Chapter 3

The fluctuating velocity field above the free end of a surface-mounted finite-height cylinder

Preamble

This study aims to fulfill the second objective of the thesis mentioned in Chapter 1.2 and pursue the second research contribution outlined in Chapter 1.3. The contribution of this chapter to the overall study is to provide new insight into the spatial distribution of dominant structures above the free end of a wall-mounted finite-height cylinder in horizontal planes parallel to the free end surface, and the influence on the flow configuration and its structures due to the change in aspect ratio.

This study will investigate the fluctuating flow field above the free end of surface-mounted finite-height cylinders of AR = 9, 7, 5 and 3, at a Reynolds number of $\mathrm{Re}_D = 4.2\times10^4$ using POD and the swirling strength criterion. The analysis will be performed on several horizontal planes parallel to and close to the free end of the cylinder. The dominant spatial features in the higher energy modes will be analyzed. The changes to these identified flow features in planes moving away from the free end will be used to identify possible three-dimensional structures above the free end. The interactions of these dominant flow features with each other will be explored. The variation of these flow topologies with aspect ratio will be also be observed with an emphasis on the rotational structures with the swirling strength criterion.

The data was obtained from PIV measurements made in a low-speed wind tunnel by Noorallah Rostamy. The development of the POD and swirling strength codes and the subsequent analysis of the results were done by Rajat Chakravarty. This was subsequently edited by Prof. Bergstrom and Prof. Sumner.

A similar version of this chapter is in preparation for submission as:

1. R. Chakravarty, D. J. Bergstrom and D. Sumner, 'The fluctuating velocity field above the free end of a surface-mounted finite-height cylinder', *International Journal of Heat and Fluid Flow*

Parts of this chapter were presented at the following conference:

1. R. Chakravarty, N. Rostamy, D. J. Bergstrom and D. Sumner, 'Visualization of the Flow Above the Free End of a Finite Cylinder', 3rd Symposium on Fluid-Structure-Sound Interactions and Control (FSSIC), pp. 193-198, July 5-9, 2015, Perth, Australia.

Abstract

Particle image velocimetry (PIV) measurements of the flow above the free end of a surface-mounted finite-height cylinder, obtained in wind tunnel experiments, were post-processed using proper orthogonal decomposition (POD). Four different cylinder aspect ratios, AR = 9, 7, 5 and 3, were studied at a Reynolds number of $\mathrm{Re}_D = 4.2\times10^4$. The normalized boundary layer thickness on the ground plane was $\delta/D = 1.7$. Of interest was to identify the dominant flow structures in this flow field and study the changes in the flow configuration with aspect ratio. POD was effective in capturing the prevailing flow structures within a few higher energy modes. The higher energy modes captured a pair of side-tip counter-rotating vortices symmetrically originating from either side of the cylinder across all aspect ratios. The lower modes revealed a pair of counter-rotating vortices on either side of the midline, an incoming flow from the circumferential leading edge as well as evidence of alternate undulations of flow on either side of the cylinder midline. Flow configurations changed with increasing aspect ratio due to a weakening influence of the ground plane and increased downwash. Vorticity sub-layers emerged further downstream with a stronger signature of the outer sub-layer. There was also a vertical compression of the wake flow at higher aspect ratios and evidence of enhanced flow entrainment from the sides of the cylinder at higher aspect ratios.

Key Words: bluff body, cylinder, free end, vortex structures, proper orthogonal decomposition, swirling strength criterion.

3.1 Introduction

The flow of fluid around a circular cylinder is realized in several real-world applications such as airflow around chimneys, buildings, and tanks. The wakes of two-dimensional (2D) cylinders, where the height of the cylinder (H) greatly exceeds its diameter (D), have been extensively studied due to the phenomenon of vortex shedding [15, 82, 97, 100]. The wake characteristics have been shown to largely vary with Reynolds number, $\mathrm{Re}_D = DU_\infty/\nu$ (for freestream velocity U_∞ and kinematic viscosity ν).

Unlike the two-dimensional (2D) cylinder, the flow over a surface-mounted finite-height cylinder is strongly three-dimensional (3D) and far more complex due to the interactions of the flow field with the ground plane and the flow around the free end of the cylinder. The 3D

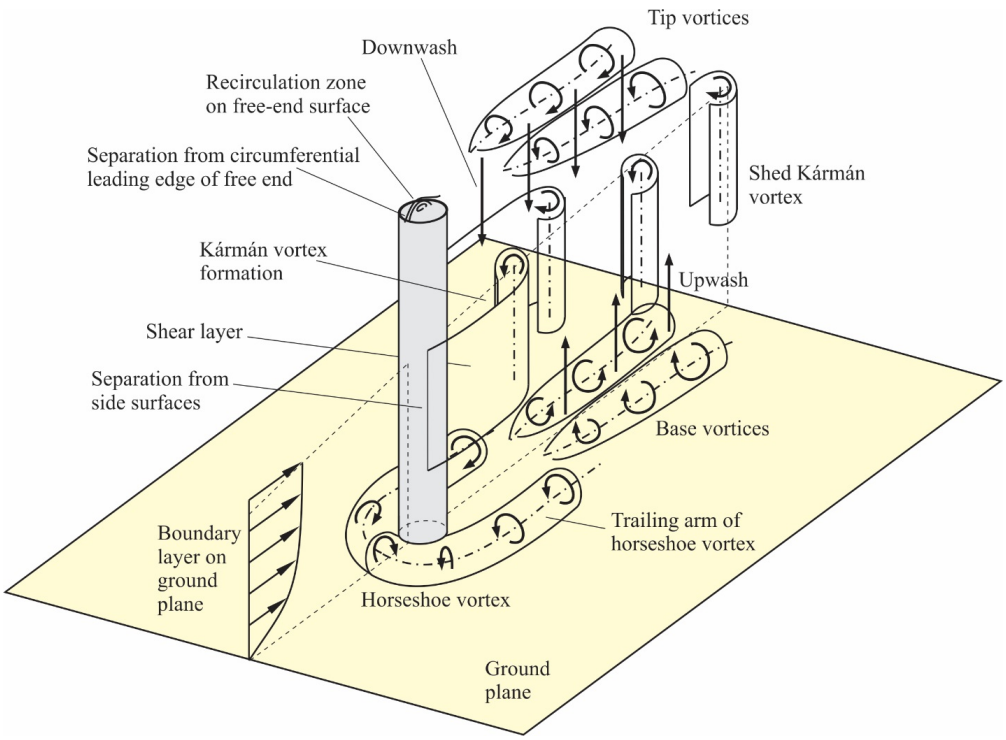

Figure 3.1: Features of the flow past a surface-mounted finite-height cylinder.

configuration of the finite cylinder leads to the formation of four main vortex systems: (i) the horseshoe vortex upstream of the cylinder-wall junction that wraps around the cylinder with two trailing arms that extend downstream; (ii) the antisymmetric Kármán vortex shedding from the sides of the cylinder; (iii) a pair of time-averaged counter-rotating streamwise tip vortices originating from the free end accompanied by an induced downwash flow in the upper part of the wake; and (iv) a pair of time-averaged counter-rotating streamwise base vortices in the lower part of the wake above the ground plane. A schematic of these four main flow features is shown in Figure 3.1. Here, the streamwise, transverse, and vertical directions have been assigned as the x, y, and z axes, respectively. The cylinder is partly immersed in a turbulent boundary layer with a mean streamwise velocity profile $U(z)$ and boundary layer thickness δ.

There are several parameters which affect the flow around a surface-mounted finite-height cylinder, namely the Reynolds number, Re_D [75], the nature of the boundary layer on the ground plane and its relative thickness δ/H or δ/D [63, 74, 96], and the cylinder aspect ratio $\mathrm{AR} = H/D$ [20, 22, 69, 84]. Most studies in the literature have found a critical aspect ratio

below which the wake shows significant changes in structure. For aspect ratios greater than this critical value, $AR_{critical}$ (the values of which itself have widely varied across studies from $AR_{critical} = 1$ to 7 [84]), the middle region of the cylinder sandwiched by the tip and base vortex pairs is characterized by antisymmetric Kármán vortex shedding from the cylinder sides [41].

Some models of the near-wake vortex dynamics have been proposed for surface-mounted finite-height square prisms [8, 95], but these models have not yet been sufficiently extended to finite cylinders where there are differences in the flow patterns. The large eddy simulation (LES) of Krajnović [45] for the flow around a finite cylinder has revealed considerable complexity to the vortex structures close to the cylinder, but only for a single aspect ratio. There has also been interest in studying the instantaneous and phase-averaged representations of the flow in the wake [61, 70, 85]. A few studies have looked at the flow specifically above the free end of cylinders and how this flow field is influenced by aspect ratio [85]. A schematic that describes the flow features through various studies seen above the free end of a finite-height surface-mounted circular cylinder of higher aspect ratios is shown in Figure 3.2 [83]. The present study is aimed at improving the general understanding of the instantaneous free-end flow field for finite cylinders of higher AR, mainly through the use of proper orthogonal decomposition (POD). Some key features of this local flow field are now summarized.

Kawamura *et al.* [41] looked at the flow above the free end for high-aspect-ratio finite cylinders for $Re_D = 1.07\times10^4$ and $Re_D = 3.2\times10^4$ and found an arch (or mushroom) type vortex above the free end. The flow was found to separate from the circular leading edge of the free end and reattach on the top surface, enclosing an averaged recirculation zone within it. A few studies [16, 45, 61, 81, 85] have also seen the presence of a separation bubble just downstream of the leading edge (which is formed due to a reverse flow that is created due to flow separation at the leading edge), examined the variation of the reattachment point on the free end, and studied the characteristics of the separating shear layer.

Several studies have indicated an additional pair of streamwise tip or trailing vortices which originate from either side of the rear surface trailing edge of the finite cylinder across varied aspect ratios [21, 65]. In slight contrast, Holscher and Niemann [32] suggested that these trailing vortices originate from the side circumferential edges of the free end. An alternative model of the flow above the free end that has been topologically distinct from

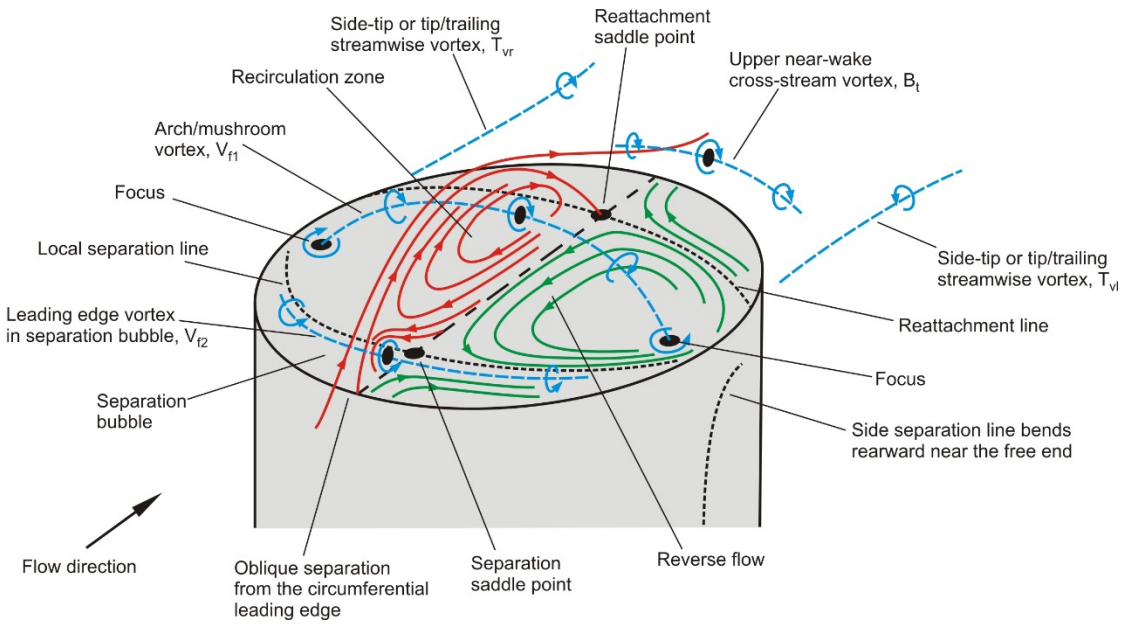

Figure 3.2: Free-end flow field schematic for higher-aspect-ratio surface-mounted finite-height cylinders [83].

most others was suggested by Roh and Park [68]. Their model, based on the flow at $\mathrm{Re}_D = 5.92\times10^3$ and $\mathrm{Re}_D = 1.48\times10^5$, found a saddle point and two foci in the front half of the free-end surface as well as a saddle point, and two nodes with a saddle point in the rear half of the free end surface. They further suggested pairs of streamwise counter-rotating vortices on either side of the cylinder free end, the first pair being the side-tip vortices originating from the circumferential edge of the free end, and the other pair being the 'tornado-like'vortices originating from the foci. No reattachment of the 'tornado-like'vortices on the free end surface was seen in their studies.

Pattenden *et al.* [65], in their particle image velocimetry (PIV) studies at $\mathrm{Re}_D = 2\times10^6$, did not see the localized separation bubble just downstream of the leading edge and further suggested that the unsteady flow features vary considerably from the ensemble-averaged results. Frederich *et al.* [25], through their numerical simulations at $\mathrm{Re}_D = 2\times10^5$, suggested that the side-tip vortices merge into the recirculation region and a separate set of trailing vortices originate downstream of the recirculation zone. Hain *et al.* [31] in their tomographic PIV studies at around $\mathrm{Re}_D = 1.1\times10^5$, found the development of vortex structures and varied dominant frequencies attributed to flapping in the separated shear layer, but did not find any evidence of the leading edge recirculation zone nor the nodes on the rear surface of the

free end. Palau-Salvador *et al.* [61] performed both LES and experimental studies above the free end and, in addition to the leading edge separation bubble mentioned previously, showed three nodes, one just downstream of the leading edge on the centerline and the other two on either side of the centreline on the free end farther downstream. The free-end flow field for cylinders with very low aspect ratios has been studied by several authors [89], where there are marked differences compared to what is seen at higher AR. All these flow features have been described in further detail and reviewed by Sumner [83].

The recent PIV experiments by Sumner *et al.* [85] looked at the mean flow field above the free end of a surface-mounted finite-height cylinders of AR = 9, 7, 5 and 3 at Re = 4.2×10^4. Flow separation from the curved leading edge of the cylinder free end was found to enclose a mean recirculation zone containing the arch vortex. This separated flow then reattached onto to the free-end surface. With a lowering of the aspect ratio, the locations of the arch vortex foci on the free-end surface moved upstream while its location in the vertical symmetry plane moved downstream, causing the arch vortex to become further inclined. This consequently increased the recirculation zone thickness and pushed the reattachment location farther downstream. Finer details of these results can be found in Sumner *et al.* [85].

The present study aims to extend the analysis of Sumner *et al.* [85] to gather new insight on the instantaneous flow characteristics of the free-end flow field. Most studies in the literature have looked at the time-averaged flow topographies with comparatively lesser attention given to the instantaneous flow features. Few studies have analyzed the flow field above the free end using improved flow visualization tools like proper orthogonal decomposition (POD) and vortex identification methods like the swirling strength criterion. These methods are becoming increasingly popular in the literature to investigate the dominant, energy-containing features of a flow as well as visualizing small-scale flow features and their contributions to the overall flow field. It is expected that the application of these advanced methods will provide for a more insightful representation of the flow field above the free end. This would then be used to obtain an improved understanding of turbulent structures in this flow field.

3.2 Experimental Setup and Post-processing Methodologies

The present study uses the experimental data reported in Sumner *et al.* (2015) for the flow above the free end of surface-mounted finite-height cylinders of AR = 9, 7, 5 and 3. The

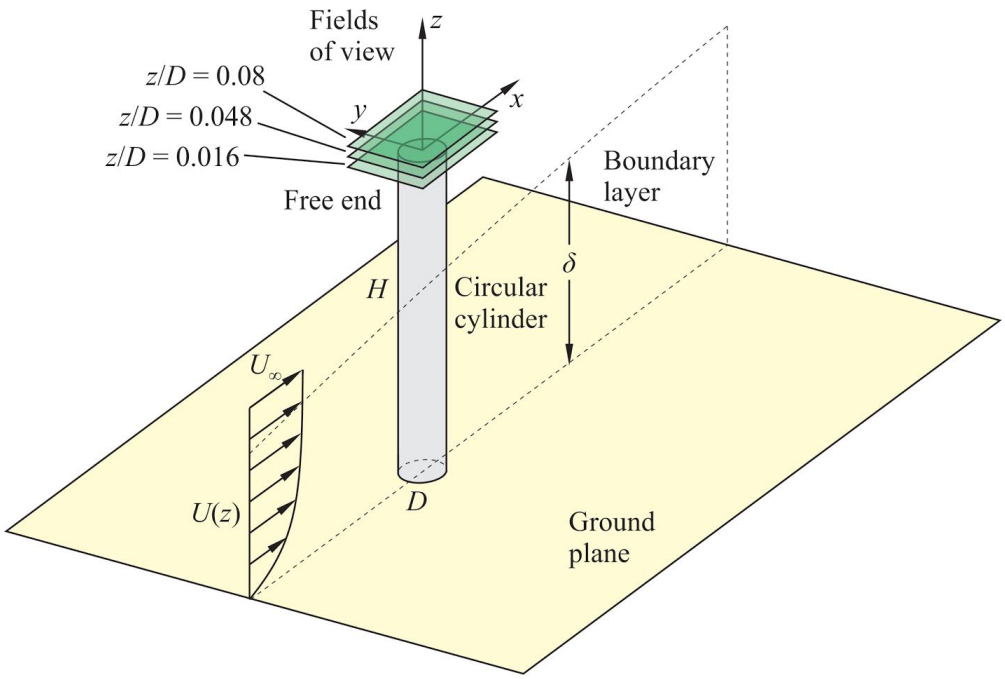

Figure 3.3: Schematic of the experimental setup showing the fields of view.

data were obtained from two-dimensional PIV measurements in a low-speed wind tunnel, at a Reynolds number of $\mathrm{Re}_D = 4.2{\times}10^4$ and with a boundary layer thickness of δ/D=1.7. Complete details of the experimental set-up and PIV analysis can be found in Sumner *et al.* [85].

Of interest here are the PIV measurements made in several horizontal (x-y) planes parallel to and close to the free end surface: for AR = 9, measurements were made at z/D = 0.019, 0.032, 0.048, 0.079, and 0.111; for AR = 7, measurements were made at z/D = 0.016, 0.032, 0.048, and 0.079); for AR = 5, measurements were made at z/D = 0.016, 0.032, 0.048, and 0.079; and for AR = 3, measurements were made at z/D = 0.016, 0.032, 0.048, 0.079, and 0.111 (where $z = 0$ corresponds to the free-end surface). The experimental set-up is shown in Figure 3.3. The field of view of the PIV images was approximately $1.9D{\times}1.9D$ at an image resolution of around 30 μ m/pixel. A 2% mean velocity uncertainty was estimated. In each horizontal plane, 528 instantaneous PIV vector fields (u and v components in the x and y directions, respectively) were obtained and used as the basis for the POD and swirling strength analysis. The images were acquired in batches of 50 images at a rate of 15 Hz.

3.2.1 Proper Orthogonal Decomposition (POD)

The POD methodology (further elaborated in Berkooz *et al.* [5]) can be used to extract motions of different scales within the evolving dynamics of a flow. The snapshot POD method of Sirovich [78] is applied in the present study to decompose the time-dependent fluctuating part of the flow field into an orthonormal system of spatial velocity modes ($\varphi_m(x)$) and associated temporal coefficients $a_n(t)$.

The autocovariance matrix C of the fluctuating velocity field is decomposed into an orthonormal system by implementing an eigenvalue problem with eigenvalues and eigenvectors λ^i and A^i, respectively as $CA^i = \lambda^i A^i$. The eigenvectors are then normalized, as shown in Equation 2.1.

$$\varphi^i = \frac{\sum_1^N A_n^i u^n}{\left\| \sum_1^N A_n^i u^n \right\|}, \quad i = 1, 2, \ldots N \tag{3.1}$$

The relative magnitude of the eigenvalues (λ_m) determines the respective energy contribution in each mode. The temporal coefficients are computed using a matrix multiplication $a^n = [\varphi^1, \varphi^2 \ldots \varphi^N] \times u^N$.

3.2.2 Swirling Strength Criterion

Hunt *et al.* [36], among others, defined vortices as regions where the velocity gradient tensor, ∇u, has complex-conjugate eigenvalues. In this study, 2D velocity field data were used to obtain the local velocity gradients. Regions where complex-conjugate eigenvalues were found were presumed to have localized vortices. Though inherently a 3D concept, complex-conjugate eigenvalues should indicate the presence of a finite component of a vortex tube normal to a 2D plane. Thus, the swirling strength criterion should be able to reveal vortex structures in 2D flow fields. In Equation 3.3, $eig()$ represents the eigenvalue function. A central differencing scheme was used to evaluate the velocity gradient tensor, ∇u, at every control volume in the domain. The regions where $\lambda_{ci} \neq 0$ (where λ_{cr} and λ_{ci} represent the real and imaginary values of the complex number, respectively) have been presumed as regions where vortices are present.

$$eig(\nabla u) = eig\left(\begin{bmatrix} \frac{\partial u}{\partial x} & \frac{\partial u}{\partial z} \\ \frac{\partial w}{\partial x} & \frac{\partial w}{\partial z} \end{bmatrix} \right) = eig\left(\begin{bmatrix} \frac{u_{i+1}-u_{i-1}}{x_{i+1}-x_{i-1}} & \frac{u_{i+1}-u_{i-1}}{z_{i+1}-z_{i-1}} \\ \frac{v_{i+1}-v_{i-1}}{x_{i+1}-x_{i-1}} & \frac{v_{i+1}-v_{i-1}}{z_{i+1}-z_{i-1}} \end{bmatrix} \right) = \lambda_{cr} \pm i\lambda_{ci} \tag{3.2}$$

3.3 Results and Discussion

3.3.1 Mean Flow Field

A brief summary of the mean flow field, as described in Sumner *et al.* [85], is provided to illustrate the main flow features in the horizontal planes above the free end of the cylinder. The mean flow results are a logical starting point for the analysis of the instantaneous flow features that will be seen in the POD and swirling strength results.

Figure 3.4 shows the mean streamlines in the horizontal (x-y) plane closest to the free-end surface of the cylinder. For all four aspect ratios, the flow at the surface is characterized by two regions of rotational flow, one on each side of the streamwise centreline, with the centres of rotation marked by foci near the side edges. A pair of saddle points is also found on the streamwise centreline near the leading edge (a separation saddle point) and on the downstream portion of the free end towards the trailing edge (a reattachment saddle point). Between these two saddle points, a strong reverse flow is seen due to contributions from the recirculation zone (and its arch vortex) above it. Curved dividing streamlines (which intersect at the reattachment saddle point) on the downstream half of the free-end surface correspond to the line of reattachment of the separated flow onto the free end. Another dividing streamline is seen just downstream of the leading edge, which corresponds to local flow separation of the reversing flow as it approaches the main flow separation from the leading edge. As the aspect ratio of the cylinder changes, some variations in the flow pattern are observed. As AR is increased, the foci on either side of the cylinder move farther downstream towards the trailing edge of the free end. The location of the upstream saddle point on the centreline remains relatively constant but the trailing edge saddle point begins moving upstream with increasing AR.

To better understand flow structures evolving from the free end into the wake, Figure 3.5 shows the normalized in-plane vorticity ($\omega_z D/U_\infty$) contours in the plane closest to the cylinder free-end. Vorticity production occurs along the curved leading edge of the free end and along the sides of the cylinder and the near wake. The vorticity appears to become stronger as it approaches the foci, and then weakens in strength farther downstream. This vorticity distribution broadly represents the shear layers forming due to separated flow from the sides and free end of the cylinder, and is shown to be sensitive to the aspect ratio of

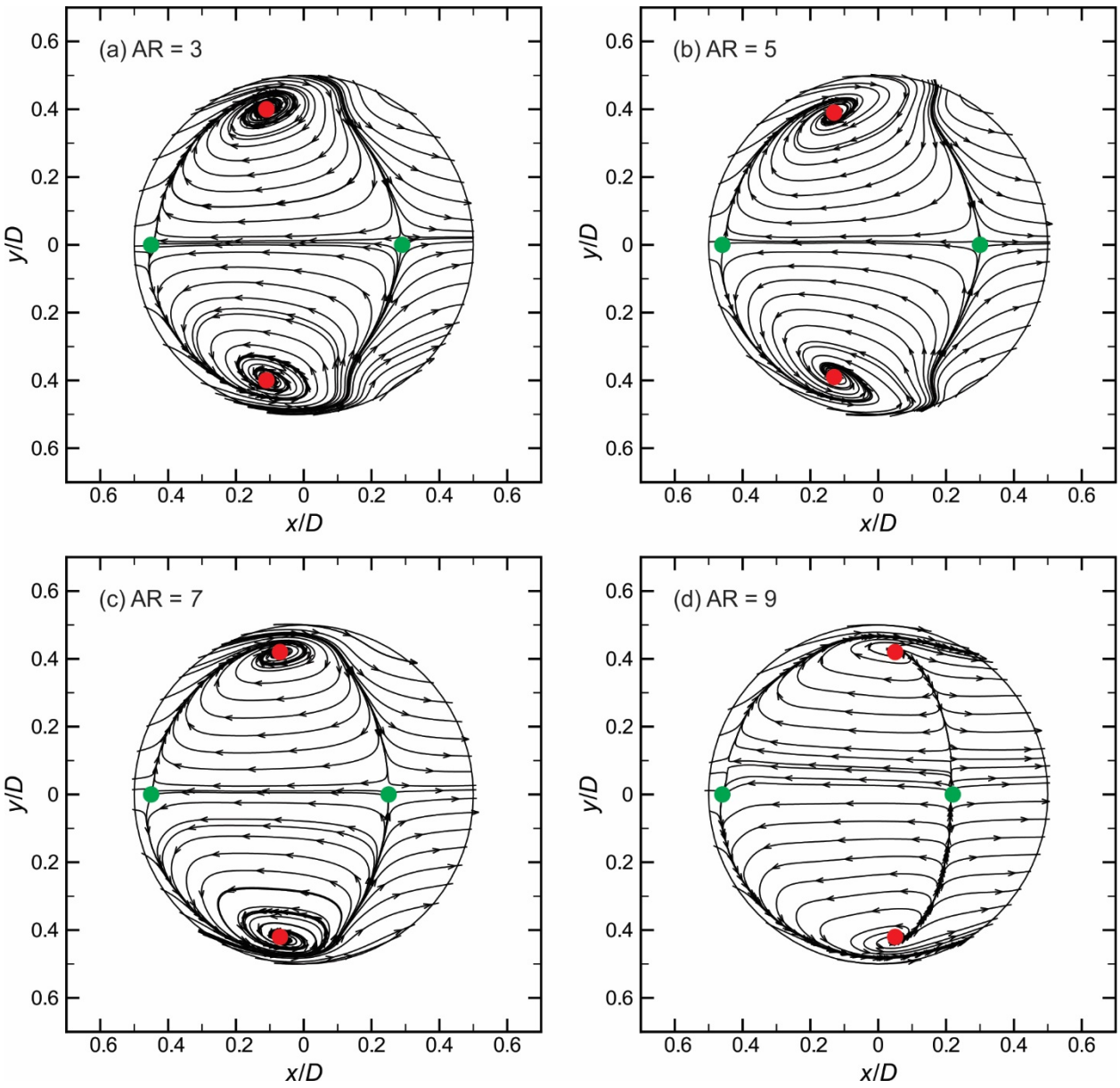

Figure 3.4: Mean streamlines above the free end in the horizontal (x-y) plane closest to the free-end surface, for cylinders of (a) AR = 3 (z/D = 0.019), (b) AR = 5 (z/D = 0.016), (c) AR = 7 (z/D = 0.016), and (d) AR = 9 (z/D = 0.016). The solid green and red circles represent foci and saddle points, respectively.

the cylinder. At higher aspect ratios, the vorticity within this plane appears to abruptly end closer to the sides of the free end, and does not extend beyond the cylinder into the upper near wake.

3.3.2 POD Results

Figure 3.6 shows the POD energy distribution for different measurement planes and cylinder aspect ratios. For all AR and z/D values, the energy cascade is quite consistent with the first mode capturing around 13-21% of the total energy, the first 10 modes capturing around 50% of the total energy, and around 100-120 snapshots cumulatively capturing 90% of the total energy. The temporal coefficients of the first few POD modes were analyzed, and no flow periodicity was determined from this investigation; this is consistent with an absence of a strong periodic signal in the upper wake [83].

The total POD energy (i.e., turbulent kinetic energy) for most of the aspect ratios is found to increase from the measurement plane closest to the free end (at $z/D = 0.016$ to 0.019) up to the $z/D = 0.048$ plane, but thereafter decreases as the freestream is approached. Closer to the free-end surface, therefore, the energetic structures weaken due to the no-slip influence of the surface. Away from the free end, the flow field is dominated by the influence of the freestream flow, which may dampen the turbulent fluxes coming from the free end. A trend of reduction in the total POD energy of the planes with an increase in the aspect ratio was observed (not shown). This result may be caused by a stronger influence of the ground plane and its boundary layer for the cylinders of lower AR, i.e., the ground-plane boundary layer would produce more turbulent fluctuations within the flow field above the free end for the smaller aspect ratio cylinders. Sumner *et al.* [85] noticed that the reattachment flow was more irregular for the cylinder of AR = 3 compared to the other cylinders; this cylinder is also considered to be less than the critical aspect ratio for the present flow and experimental conditions.

As this study was performed on the velocity fluctuation field of a flow dominated primarily by the arch (or mushroom) vortex in the free-end recirculation zone, and the side-tip/trailing vortices originating from the edges of the free end (Figure 3.2), it is expected that the POD modes will capture the small-scale structures that form the building blocks of dominant flow structures seen in the mean flow field. It was thus inferred that energy convergence across

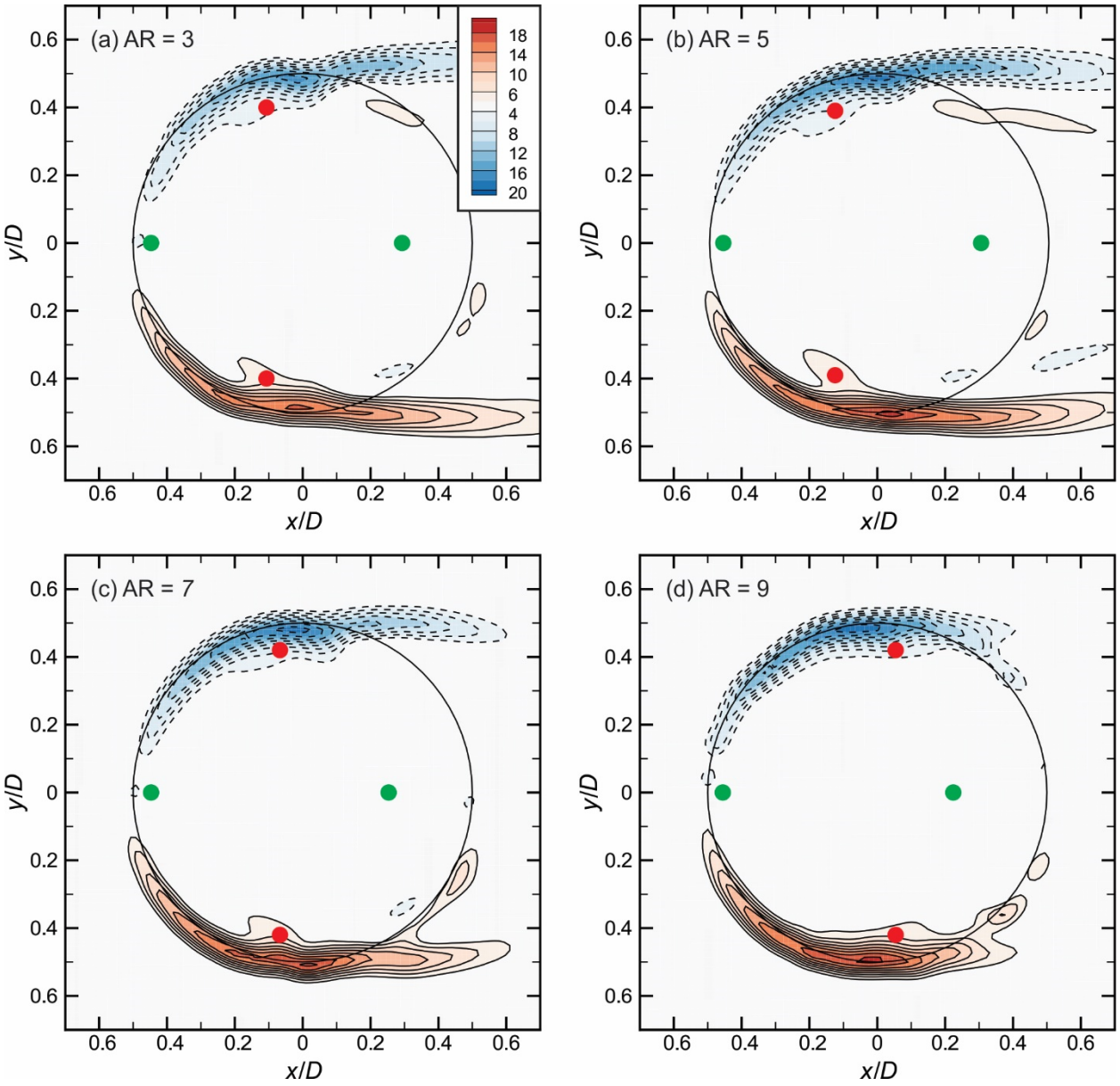

Figure 3.5: Mean in-plane normalized vorticity contours ($\omega_z D/u_\infty$) and contour lines above the free end in the horizontal (x-y) plane closest to the free-end surface, for cylinders of (a) AR = 3 (z/D = 0.019), (b) AR = 5 ($z/D = 0.016$), (c) AR = 7 ($z/D = 0.016$), and (d) AR = 9 ($z/D = 0.016$). The solid green and red circles represent foci and saddle points, respectively.

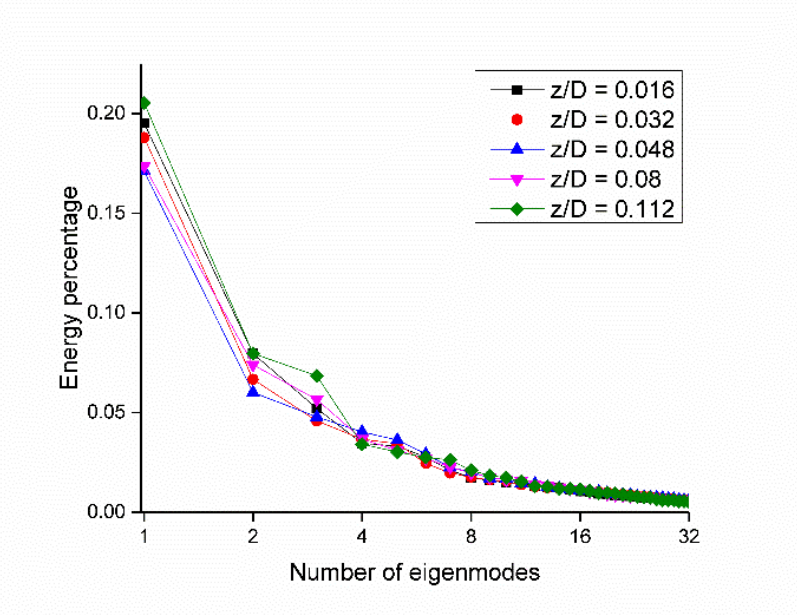
z/D = 0.016
z/D = 0.032
z/D = 0.048
z/D = 0.08
z/D = 0.112
Energy percentage
0.00
0.05
0.10
0.15
0.20
1
2
4
8
16
32
Number of eigenmodes

(a) - AR = 3

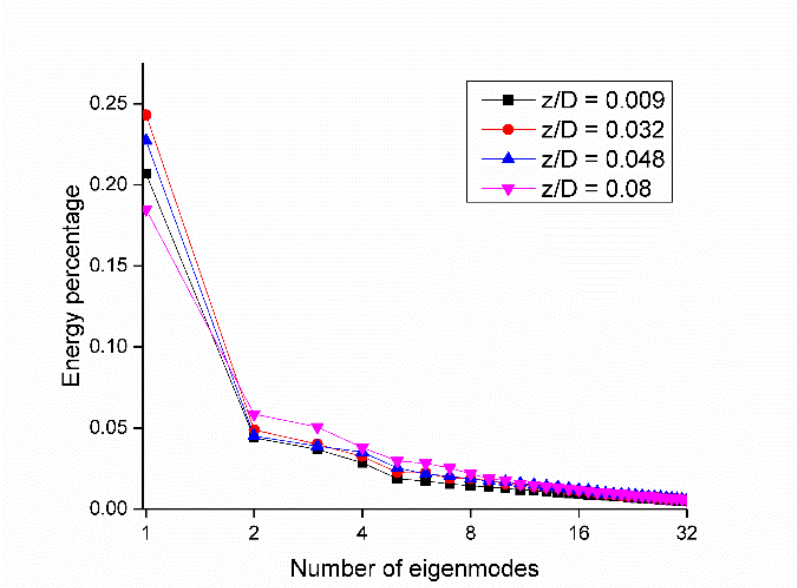
z/D = 0.009
z/D = 0.032
z/D = 0.048
z/D = 0.08
Energy percentage
0.00
0.05
0.10
0.15
0.20
0.25
1
2
4
8
16
32
Number of eigenmodes

(b) - AR = 5

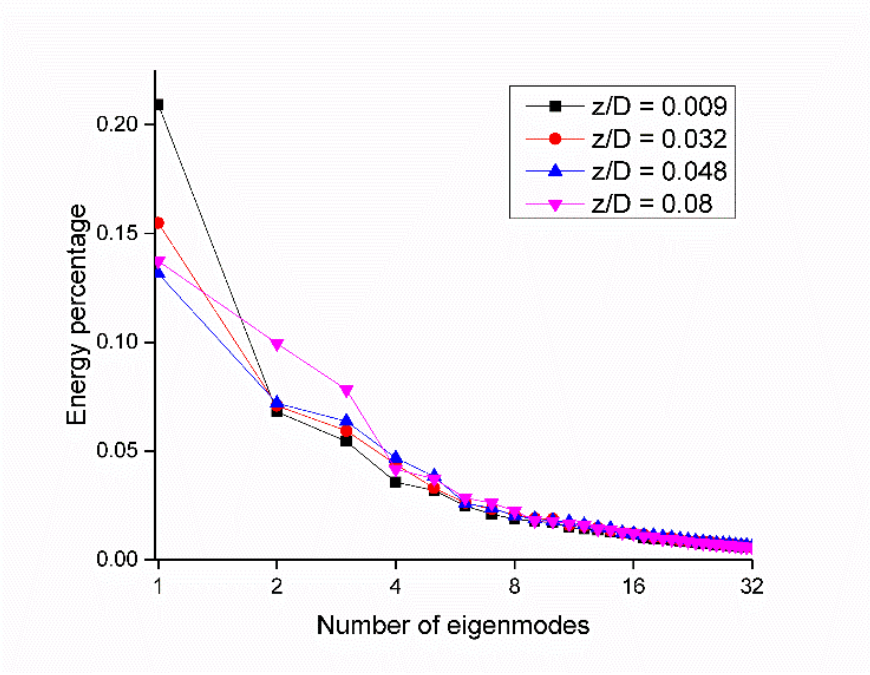

(c) - AR = 7

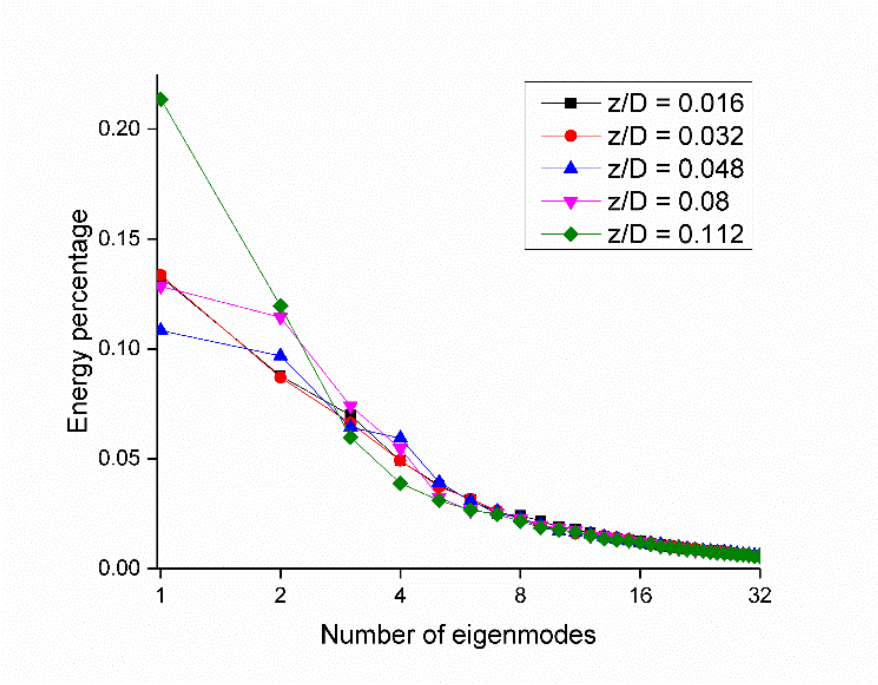

(d) - AR = 9

Figure 3.6: Energy distribution of the POD modes in different horizontal (x-y) planes above the free end of a surface-mounted finite-height cylinder of (a) AR = 3, (b) AR = 5, (c) AR = 7, and (d) AR = 9.

the eigenmodes would be more gradual owing to the more prevalent small-scale structures that individually have a small contribution to the overall energy. The grouping of modes in the POD energy distributions also provides some direction for identifying various flow features. The first energy mode for the AR = 3 and 5 cylinders (Figure 3.6(a-b)) consistently captures around 20% of the overall energy, however this consistency is not seen for AR = 7 and 9 (Figure 3.6(c-d)), with a range of about 10% in the energy capture of the first mode. This suggests that at higher aspect ratios, there are several flow features of equal energy contributions, unlike at lower aspect ratios (and as the critical aspect ratio is approached and reached) where it seems that fewer dominant structures may be characterizing the flow fields.

The energy distributions for most of the AR = 9 planes (Fig. 6(d)) vary considerably from those of the other aspect ratios. For aspect ratios AR = 3, 5 and 7 (Figure 3.6(a-c)), it is expected that the first and second energy mode will show distinct flow features due to the sizeable difference (close to 15%) in their energy contributions. This is not the case for most of the AR = 9 planes, as the energy difference between the first and second mode is relatively small. Thus, to select specific modes for analysis, it would be appropriate to analyze the first two energy modes for the AR = 5 prism to extract the dominant energy structures, as a representative case for flow features for the AR = 3 to 7 cylinders. A separate analysis of other planes to show contrasts in the flow features will follow. These will then to lead to the analysis of the variance in flow structures with AR.

Energy modes for AR = 5

Figure 3.7 shows the velocity vector fields associated with the first POD energy mode, in four horizontal (x-y) planes, for the finite cylinder of AR = 5 with contours of in-plane vorticity ($\omega_z D/U_\infty$) and the swirling strength criterion, separately. In all four horizontal planes, the first energy mode shows two pairs of shear sub-layers originating from each side of the free end (downstream of the foci on the free-end surface) and extending into the upper near wake downstream of the mean recirculation zone above the free end. Each sub-layer of the pair has the opposite sign of vorticity. The outer shear sub-layer of the pair seems to follow the edge of the cylinder wake, while the inner shear sub-layer of the pair is drawn towards the centreline of the flow. The pairs of shear sub-layers are found in the region of the flow where

the side-tip trailing vortices have been identified in other studies. In the two planes closest to the free end, at $z/D = 0.016$ (Figure 3.7(a)) and $z/D = 0.032$ (Figure 3.7(b)), the pair of shear sub-layers is associated with a strong flow directed upstream from the near wake towards the side edges of the free end. In the two planes farthest from the free end, at $z/D = 0.048$ (Figure 3.7(c)) and $z/D = 0.079$ (Figure 3.7(d)), however, the sign of the vorticity of the shear sub-layers changes, along with the direction of the flow associated with the sub-layers, so that this flow is now directed downstream into the near wake. The change in sign of the vorticity and the direction of the flow over a small vertical distance may be associated with the small-diameter streamwise side-tip trailing vortices.

At the plane farthest from the free end, at $z/D = 0.079$ (Figure 3.7(d)), two additional but weaker pairs of shear sub-layers are found above the free end, on either side of the centreline. These pairs seem to lie within the main separated shear layer originating from the curved leading edge, and are associated with velocity that moves away from the centreline, towards the edges and into the near wake. This flow pattern suggests connection between the upstream shear sub-layers, above the free end, and the stronger sub-layers found downstream in the upper part of the near wake that may be associated with the side-tip vortices.

When analyzing contour plots with z-vorticity (ω_z), vorticity contours may conflate shear layers and rotational structures. This makes it challenging to study flows where both are present, specifically in this study at the side-tips of the circular cylinder, where we notice vortices as well as the shear sub-layers can be found. To isolate rotational structures from shearing motion, the swirling strength criterion becomes a useful tool to analyze such flows. Figure 3.7 also demonstrates the swirling strength criterion contours of the first POD energy mode in the same planes. Across all planes, two strong side-tip vortex structures are clearly seen symmetrically at the locations close to $x/D = 0.2$. The vector field indicates that the formation of these vortices may be due to the movement of the reverse flow towards the symmetry plane. In addition to these two dominant vortices, additional weaker structures are seen in the region of separating shear layers downstream of the cylinder trailing edge. These likely represent Kelvin-Helmholtz instabilities, seen in similar flow fields within a separating shear layer from the free ends of bluff bodies, as already seen in Chapter 2 for surface-mounted finite height square prisms. In the plane furthest from the free end, i.e. $z/D = 0.079$ (Fig. 3.7(d)), an additional pair of vortex structures is also seen close to the side-tips at $x/D = 0$.

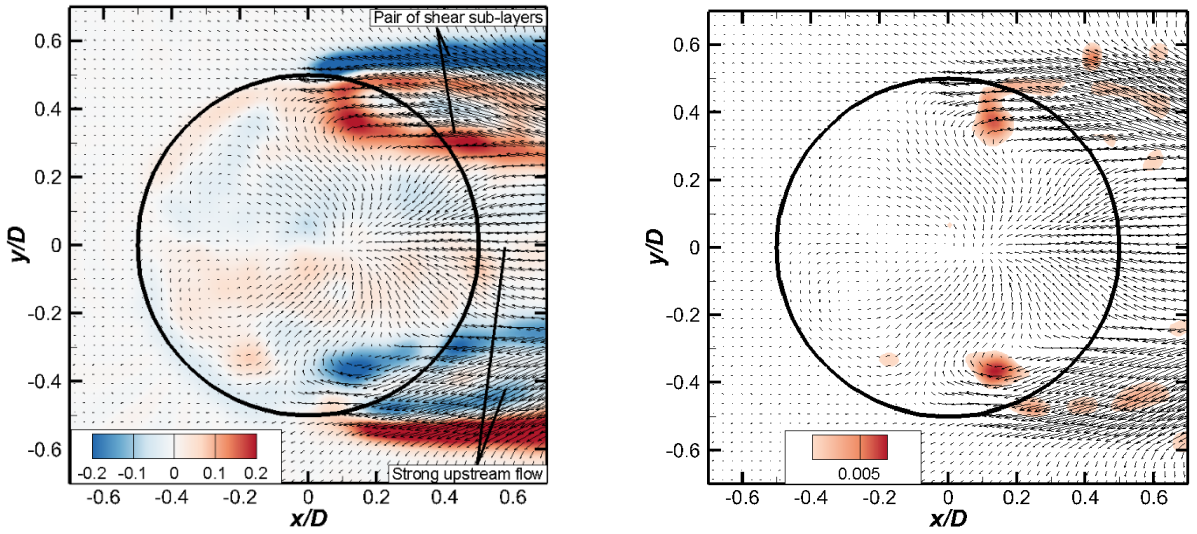

(a) AR = 5, $z/D = 0.016$, First energy mode

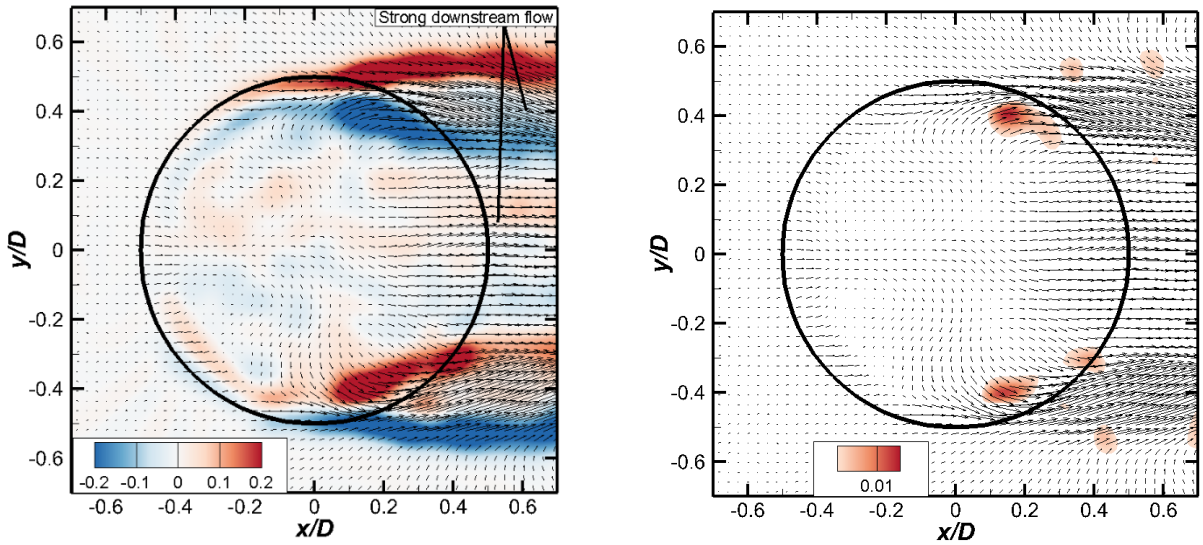

(b) AR = 5, $z/D = 0.032$, First energy mode

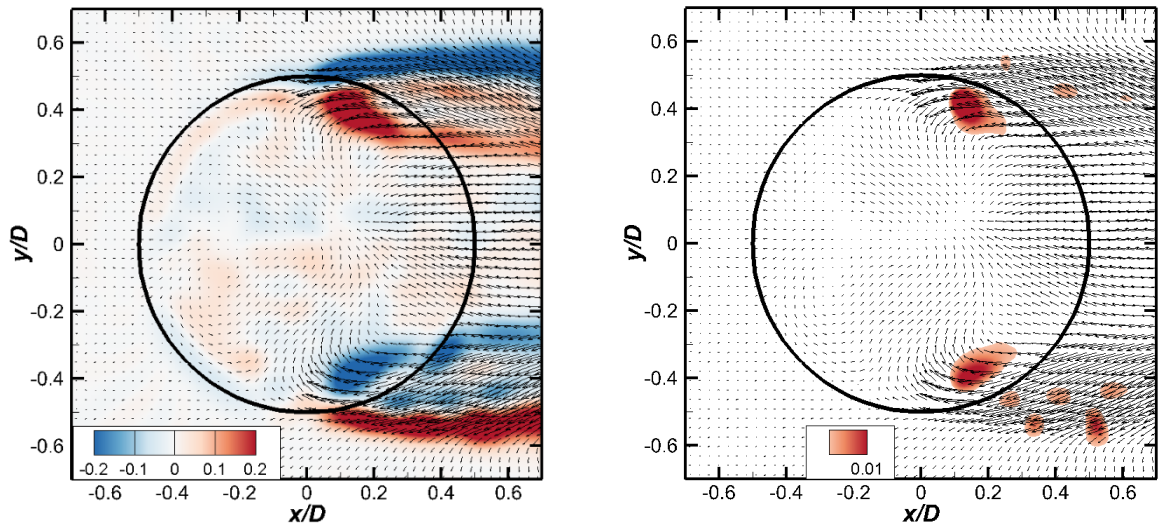

(c) AR = 5, $z/D = 0.048$, First energy mode

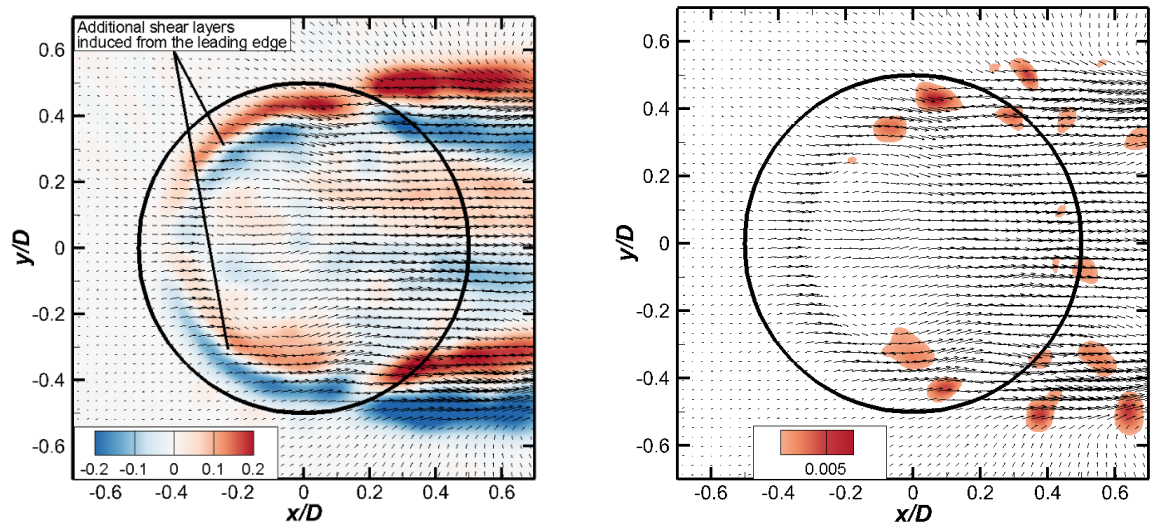

(d) AR = 5, $z/D = 0.079$, First energy mode

Figure 3.7: In-plane normalized vorticity contours ($\omega_z D/u_\infty$) and in-plane velocity vectors (left) and in-plane swirling strength criterion contours (right) for the first POD energy mode in four horizontal (x-y) planes above the free end of a finite cylinder of AR = 5: (a) $z/D = 0.016$, (b) $z/D = 0.032$, (c) $z/D = 0.048$, and (d) $z/D = 0.079$. Red and blue contours represent positive (CCW) vorticity and negative (CW) vorticity, respectively (left).

This may once again be attributed to the Kelvin-Helmholtz instabilities seen in the previous planes due to instabilities that may be triggered during the formation of the separating shear layers at the free-end leading edge. As seen in Fig. 3.7(d), the onset of separating shear layers in this plane is closer to the leading edge, which simultaneously explains the earlier onset of the Kelvin-Helmholtz instabilities along the leading edge as well.

Figure 3.8 shows data for the second POD energy mode. All four horizontal planes have strong anti-symmetry above the free end across the horizontal centreline, although this disappears in the wake. A common feature in all these planes is the large pair of counter-rotating vortices above the free end, one structure on either side of the centreline. Apart from the plane closest to the free end (Figure 3.8(a)), the higher planes (Figure 3.8(b-d)) show a similar rotational orientation on either side of the centreline. These vortices appear to be distorted and symmetrically strained in the streamwise direction on either side of the centreline. The vortex pair moves farther downstream (from $x/D = 0.16$ to $x/D = 0.2$), and more towards the centerline, with increasing distance away from the free end, alluding to a possible three-dimensional structure arching backwards above the free end. The planes closer to the free end show additional flow features than the planes farther away.

Closest to the free end (Figure 3.8(a)), the vortex pair induces a reversing flow (directed upstream, towards the leading edge) on the free end surface, but this disappears in the higher planes with the flow being induced in the downstream direction (Figure 3.8(b-d)). There is a weaker pair of counter-rotating vortices just behind the leading edge on either side of the centreline that is not present in the plane farthest away (Figure 3.8(d), $z/D = 0.08$). This flow winds around the circumferential sides of the leading edge towards the outer edges of the free end. These side regions are characterized by alternating positive and negative vorticities when approaching the centerline, which could either imply a mixing of shear layers or shear layer instabilities. This vorticity then interacts with the downstream flow emerging from the counter-rotating vortex pair at the centre and creates complex flow patterns in the near wake in the lower horizontal planes.

Energy modes for AR = 9

Figure 3.6(d) showed that the first energy mode for the cylinder of AR = 9 captured comparatively less energy than the other cylinders, suggesting that AR = 9 might show distinct

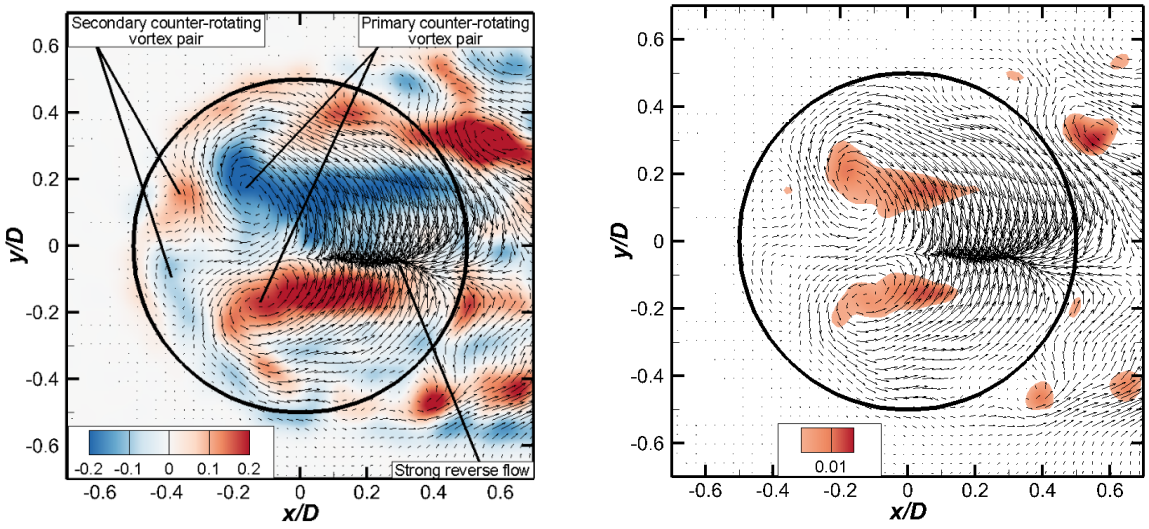

(a) AR = 5, $z/D = 0.016$, Second energy mode

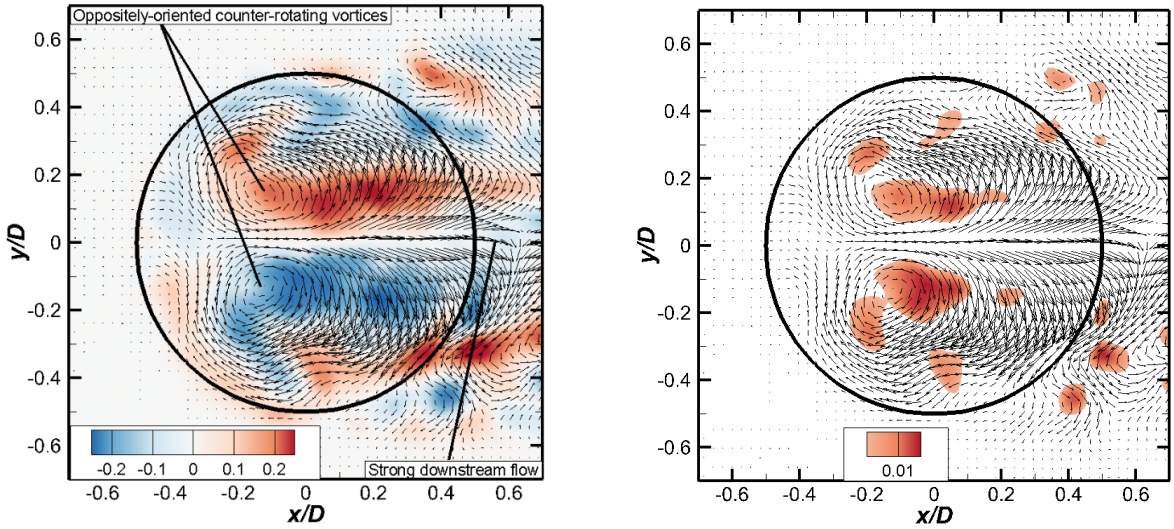

(b) AR = 5, $z/D = 0.032$, Second energy mode

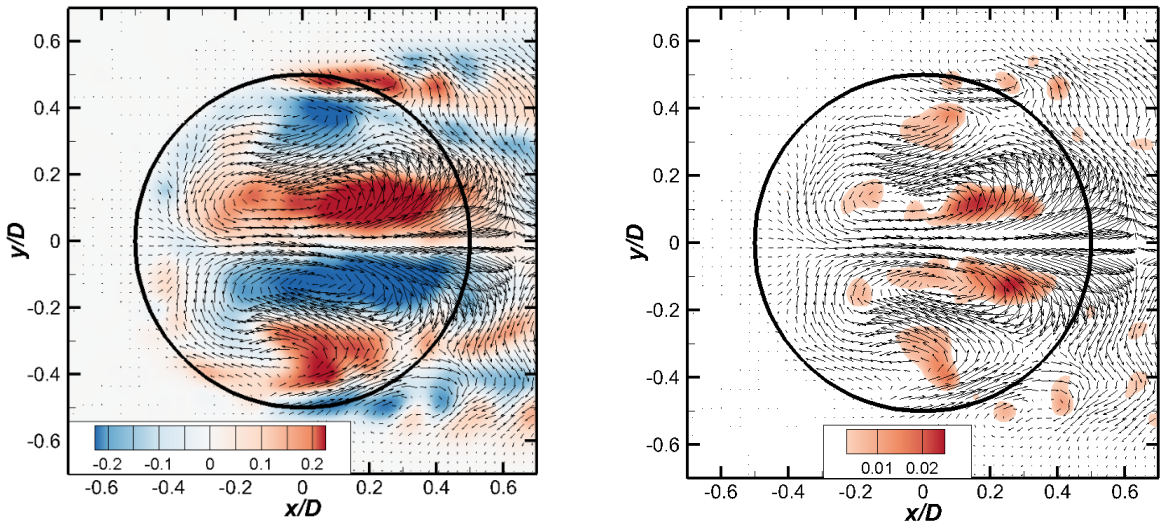

(c) AR = 5, $z/D = 0.048$, Second energy mode

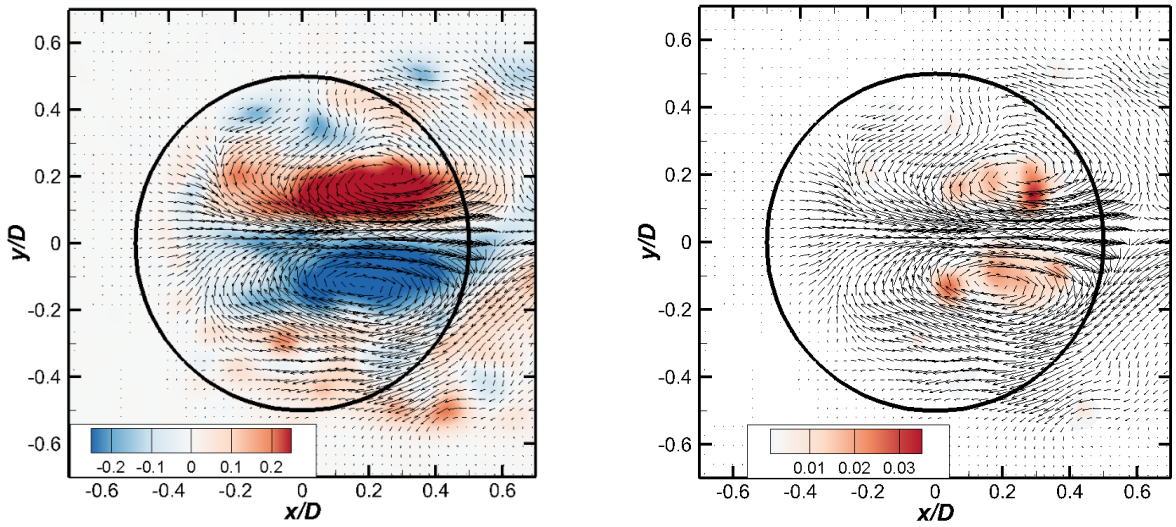

(d) AR = 5, $z/D = 0.079$, Second energy mode

Figure 3.8: In-plane normalized vorticity contours ($\omega_z D/u_\infty$) and in-plane velocity vectors (left) and in-plane swirling strength criterion contours (right) for the second POD energy mode in four horizontal (x-y) planes above the free end of a finite cylinder of AR = 5: (a) $z/D = 0.016$, (b) $z/D = 0.032$, (c) $z/D = 0.048$, and (d) $z/D = 0.079$. Red and blue contours represent positive (CCW) vorticity and negative (CW) vorticity, respectively (left).

flow structures. Figure 3.9 shows the in-plane vorticity ($\omega_z D/U_\infty$) and velocity vector fields associated with the first POD energy mode, in four horizontal (x-y) planes, for the finite cylinder of AR = 9. As expected, the flow fields show some different characteristics.

First, the presence of the side-tip trailing vortices close to the free end surface is now much weaker (Figure 3.9(a)), and the vorticity concentrations where these vortices are found display an antisymmetric organization across the wake at the two elevations closest to the surface (Figure 3.9(a,b); this organization is distinctly different than what was observed for AR = 5 (Figure 3.7), where there was a mirror image symmetry across the wake.

Second, the flow structure above the free end is new, and exhibits a lack of cross-stream symmetry that is consistent with the antisymmetric arrangement of the side-tip trailing vorticity. This lack of symmetry is seen from the surface up to the elevation of $z/D = 0.08$ (Figure 3.9(c)). Symmetry is only seen sufficiently high above the surface, at $z/D = 0.111$ (Figure 3.9(d)). Close to the free end, Figure 3.9(a) shows some strong cross-flow, with flow directed downwards near the leading edge and upwards on the rear half of the free-end surface. This fluid motion results in a CCW vortex above the free end just after the leading edge centred at $x/D = 0.2$. In Figure 3.9(b), this rotational motion is weaker and the sense of rotation becomes CW. Another switch in the rotational direction is seen in Figure 3.9(c).

3.3.3 Influence of Aspect Ratio (AR)

Figure 3.10 shows the in-plane vorticity ($\omega_z D/u_\infty$) contours and velocity vector fields for the first POD energy mode, in the horizontal planes closest to the free-end surface, for four different aspect ratios: AR = 3 (Figure 3.10(a)), AR = 5 (Figure 3.10(b)), AR = 7 (Figure 3.10(c)), and AR = 9 (Figure 3.10(d)). The corresponding vector fields with the swirling strength criterion contours are also shown.

It is noticed for the plane closest to the free end investigated in this study, there is no appreciable change in the flow features with aspect ratio. All figures show a reverse flow just after the trailing edge in the cylinder wake alluding to the possible three-dimensional structure in the near-wake above and slightly after the cylinder trailing edge. Figure 3.10(a), Figure 3.10(b) and Figure 3.10(c) once again show symmetry about the midline with two sub-layers of vorticity emerging from the both side-tips above the free end. In Figure 3.10(a), the vectors seem to indicate that there is an outward movement of flow from the symmetry

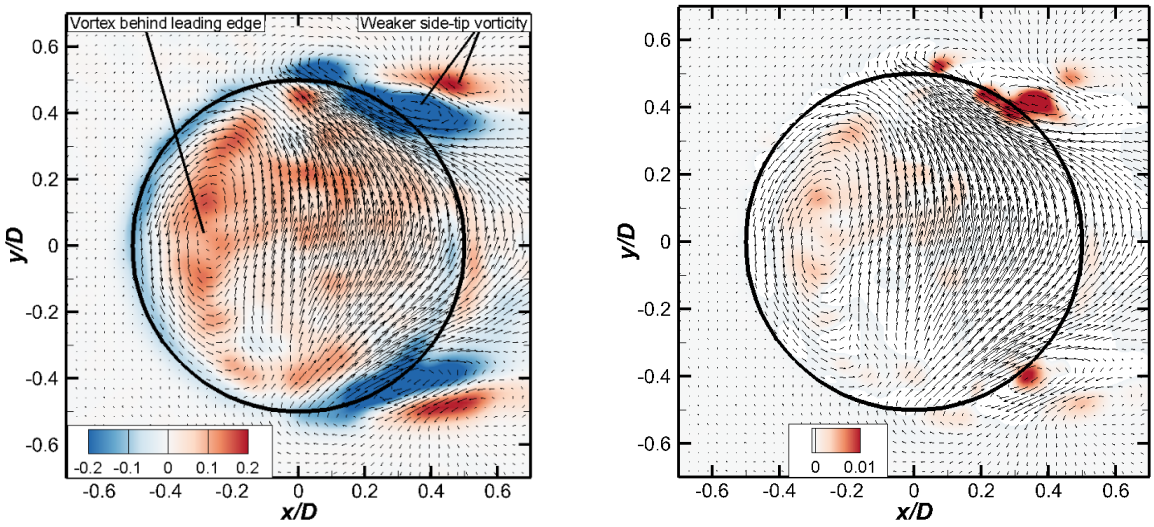

(a) AR = 9, $z/D = 0.019$, First energy mode

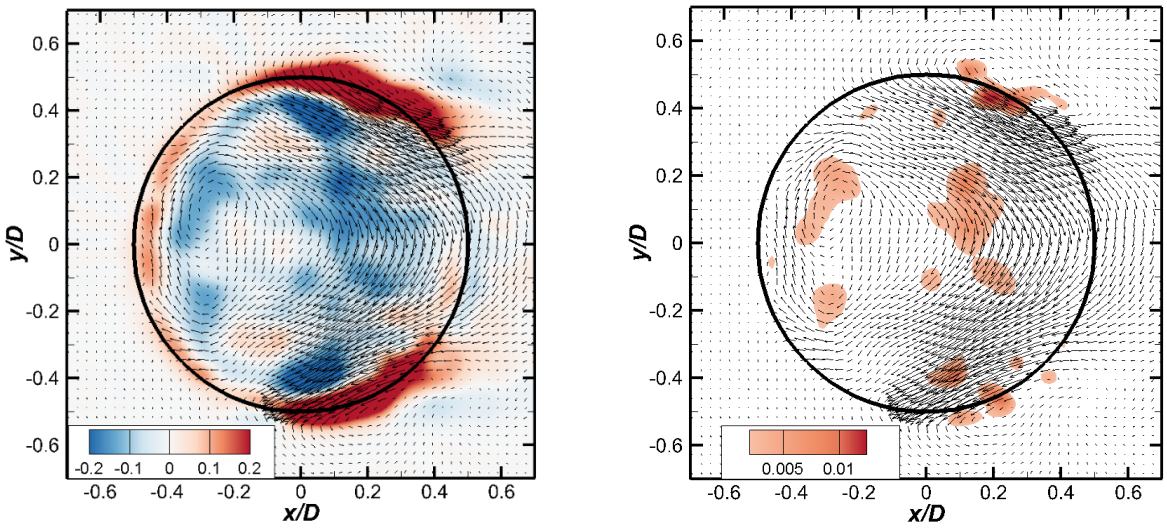

(b) AR = 9, $z/D = 0.048$, First energy mode

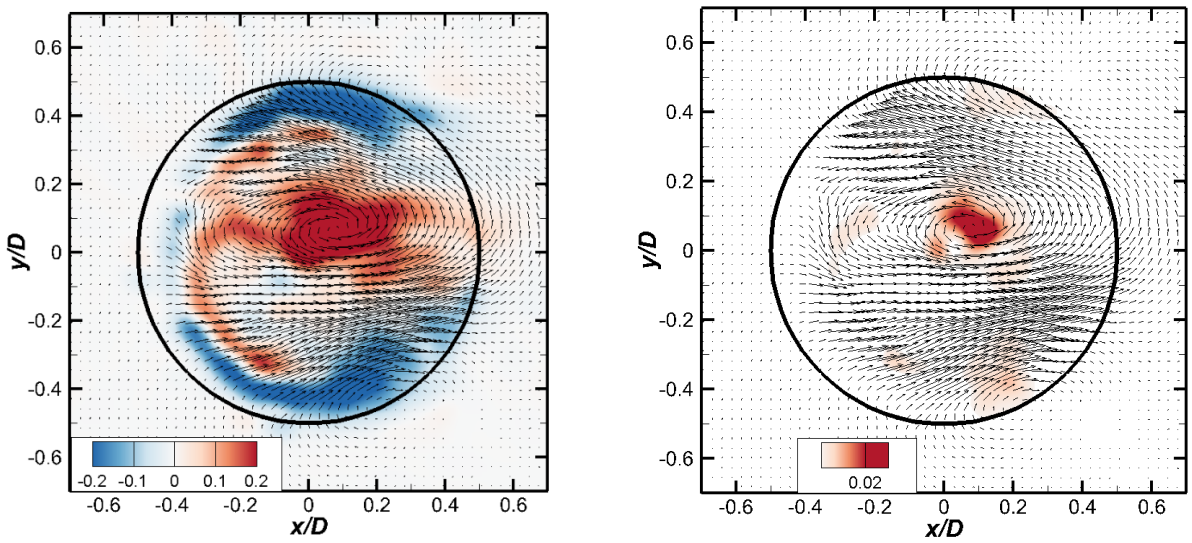

(c) AR = 9, $z/D = 0.08$, First energy mode

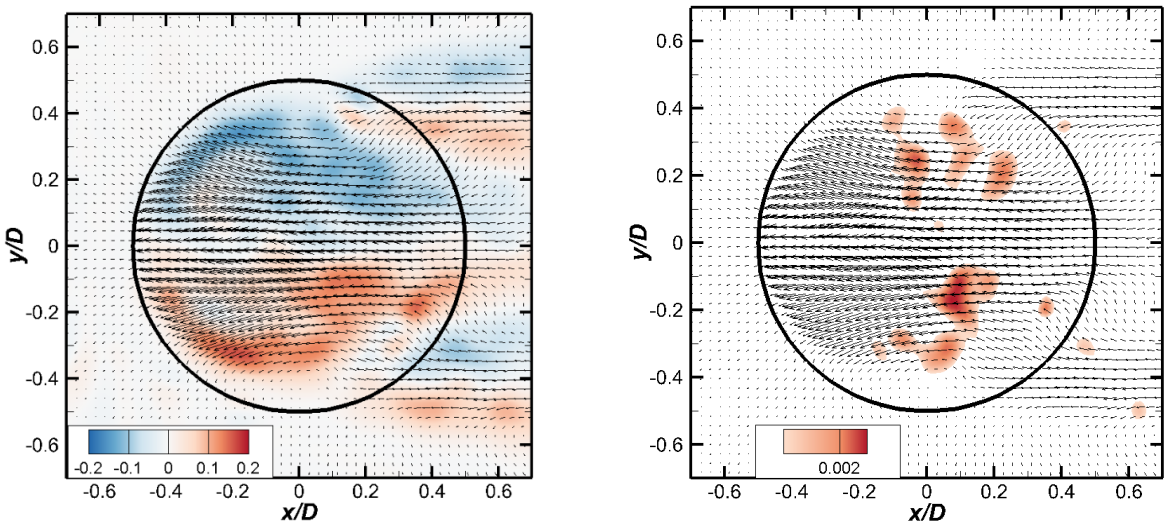

(d) AR = 9, $z/D = 0.111$, First energy mode

Figure 3.9: In-plane normalized vorticity contours ($\omega_z D/u_\infty$) and in-plane velocity vectors (left) and in-plane swirling strength criterion contours (right) for the first POD energy mode in four horizontal (x-y) planes above the free end of a finite cylinder of AR = 9: (a) $z/D = 0.019$, (b) $z/D = 0.048$, (c) $z/D = 0.08$, and (d) $z/D = 0.111$. Red and blue contours represent positive (CCW) vorticity and negative (CW) vorticity, respectively (left).

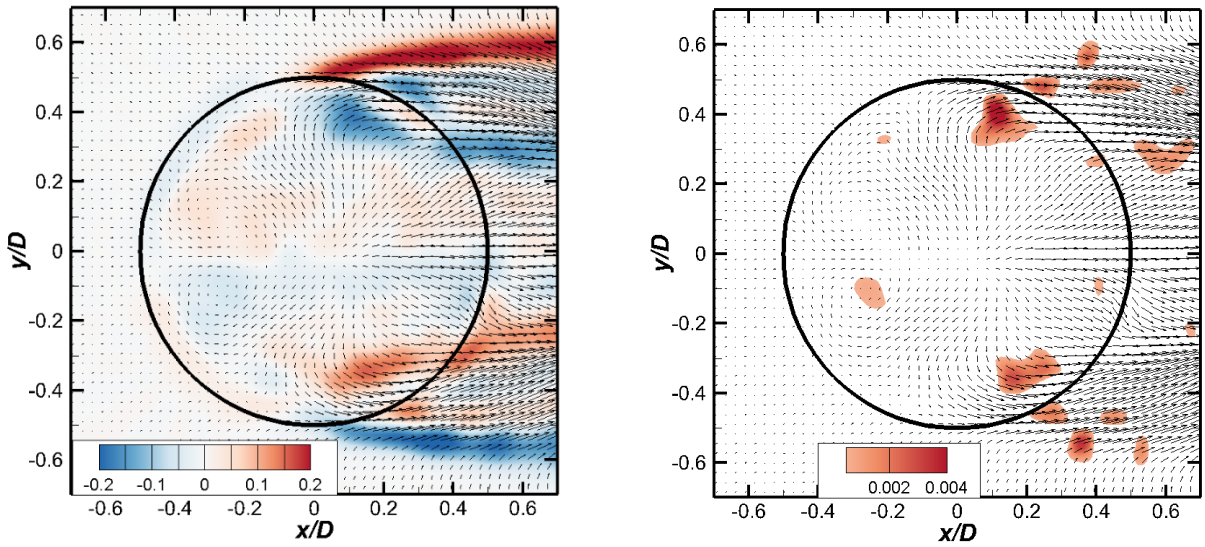

(a) AR = 3, $z/D = 0.016$, First energy mode

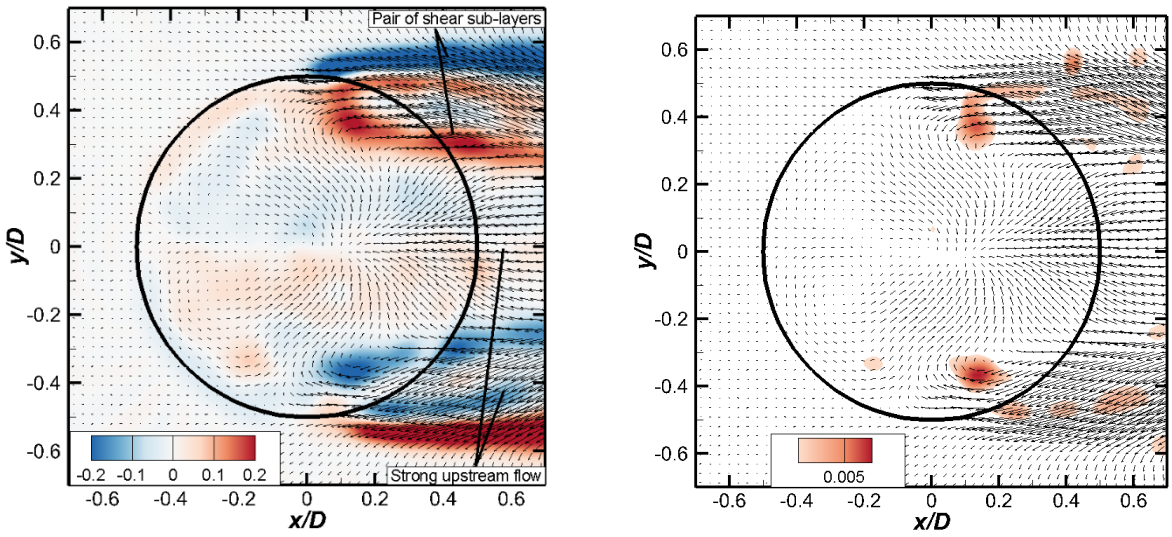

(b) AR = 5, $z/D = 0.016$, First energy mode

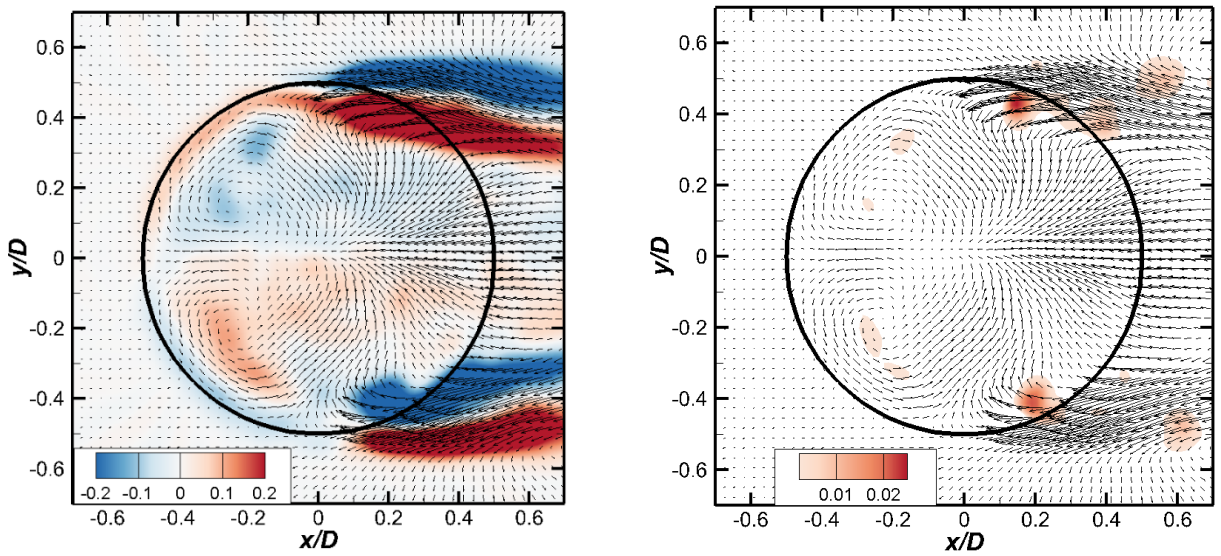

(c) AR = 7, $z/D = 0.016$, First energy mode

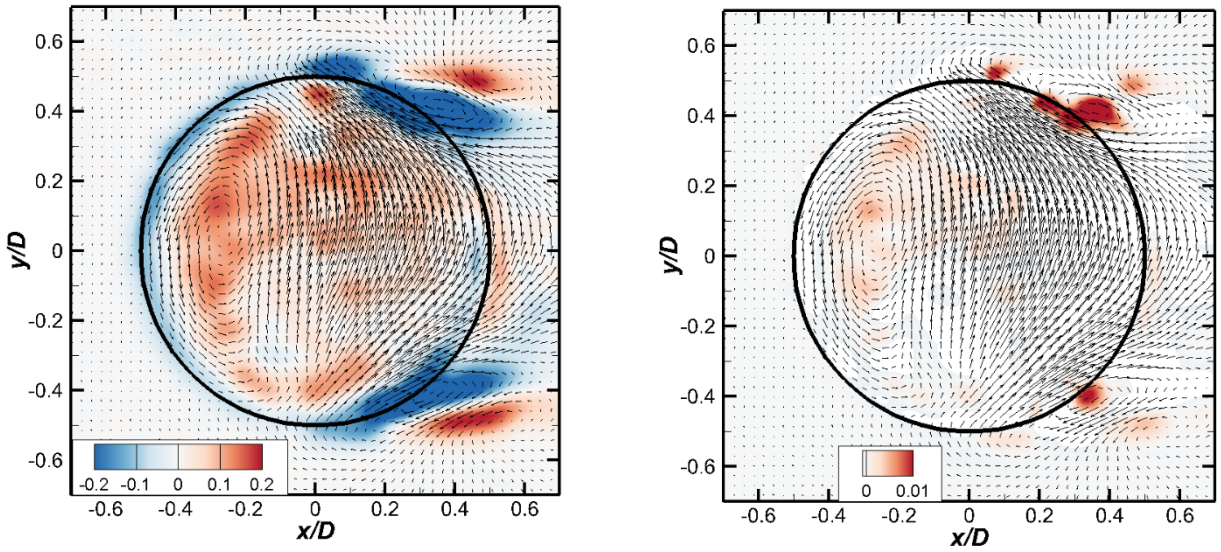

(d) AR = 9, $z/D = 0.019$, First energy mode

Figure 3.10: In-plane normalized vorticity contours ($\omega_z D/u_\infty$) and in-plane velocity vectors (left) and in-plane swirling strength criterion contours (right) for the first POD energy mode in the horizontal (x-y) plane closest to the free end of a finite cylinder for: (a) AR = 3, (b) AR = 5, (c) AR = 7, and (d) AR = 9. Red and blue contours represent positive (CCW) vorticity and negative (CW) vorticity, respectively (left).

mid-plane which interacts with the freestream flow at the side-tips and produces the side-tip vortices. However, with increasing aspect ratio, the outer vorticity sub-layer is observed to get progressively stronger, while the inner layer gets progressively weaker. This is possibly due to a stronger influence of the flow coming from the sides of the cylinder that are progressively less influenced with the effects of the ground plane.

In Figure 3.10(c), the side-tips are strongly dominated by a reverse flow, which pushes flow towards the vertical symmetry plane. These contrasting features indicate a possible antisymmetric fluttering mechanism of flow on either side of the mid-plane, which alternately strengthens each of the side-tip vorticity sub-layers. The inward flow towards the centreline also encourages the formation of a pair of counter-rotating vortices closer to the leading edge symmetrically about the cylinder mid-plane. Figure 3.10(d) shows a strong rotation of flow from both sides of the cylinder towards the centreline indicating some interaction of the side flow with the reverse flow coming in from the trailing edge. This probably indicates that the outer vorticity sub-layer overcomes the weaker inner sub-layer with increasing aspect ratio of the cylinder.

Another feature in Figure 3.10(d) is a strong vortex structure on the free end just after the free end leading edge. This rotation indicates formations of vortices at higher aspect ratio cylinders. As aspect ratio increases, the side-tip vortices show a greater tendency to move closer to the trailing edge indicative of a possible delayed flow separation. This indicates that at higher aspect ratios, the flow around the circular cylinder has greater turbulent kinetic energy due to the predominant freestream flow, which overcomes the skin friction closer to the cylinder trailing edge.

In the swirling strength criterion plots, the contours also show almost symmetrical structures across the vertical symmetry plane. All planes capture a vortex at the side-tips of the circular cylinder. The location of these vortices vary slightly with aspect ratio, with the AR = 3 case (Figure 3.10(e)) showing the structures lying $x/D = 0.15$, the AR = 5 (Figure 10(f)) and AR = 7 (Figure 10(g)) cases lying around $x/D = 0.2$, and the AR = 9 (Figure 3.10(h)) case lying around $x/D = 0.3$. Except for the AR = 3 case, all other figures indicate that these side-tip vortex structures are formed due to the turning of the reverse flow at the side-tips towards the centre of the prism. The location of the vortex structures also follow the general trend of moving further downstream towards the trailing edge of the cylinder

with increasing aspect ratio, similar to the nature of the formation of the side-tip vorticity layers seen earlier.

At lower aspect ratios, smaller vortex structures are also seen downstream of the prism, suggested earlier to be evidence of the Kelvin-Helmholtz instabilities. However, these become less prominent with increasing aspect ratio, with the AR = 9 case (Figure 3.10(h)) showing only a couple of predominant vortex structures at the side-tips. Figure 3.10(h) also shows that the side-tip vortex structures move downstream of the trailing edge of the circular cylinder. It shows additional rotational structures just behind the leading edge of the cylinder unseen in lower aspect ratios. As demonstrated here, swirling strength is a useful tool to extract rotational structures in regions dominated by shear layers, where velocity vectors also do not provide this information. Thus, if used in tandem with POD, swirling strength can provide deeper insight into these flow fields. The swirling strength criterion plots in this study have been restricted to the analysis of the first energy mode, as these flow fields show a predominance of shear from the sides of the circular cylinder.

Figure 3.11 shows a contour plot of the in-plane vorticity superimposed with velocity vectors for the third POD energy mode for the cylinder free end at z/D = 0.016 across all four aspect ratios. Due to the lesser energy content in this mode, the structures shown are going to show some weaker modal decompositions of the flow. The symmetry in most of these modes disappears as compared to the first energy mode and structures look more disorganized. In Fig. 3.11(a), there is still evidence of the two vorticity sub-layers on the side-tips of the cylinder, indicating that these structures dominate in energy content for the low AR cylinder. There still lies some symmetry about the midline with a pair of counter-rorating vortices at x/D = -0.2, followed by flow moving away from it on either side above the free end. The vector field shows that as this flow moves towards the side-tips and beyond, they curl and form the outer vorticity sub-layer due to its interactions with the incoming flow from the circumferential leading edges. Similar to Figure 3.10(a), this explains the formation of the two vorticity sub-layers as a result of the interaction of the flow coming from the centre and from the circumferential edges meeting around the side-tips. The inner vorticity sub-layer gets weaker with increasing aspect ratio possibly due to a weakening of the incoming circumferential flow which results in the dominance of the flow coming from the midline moving towards the sides.

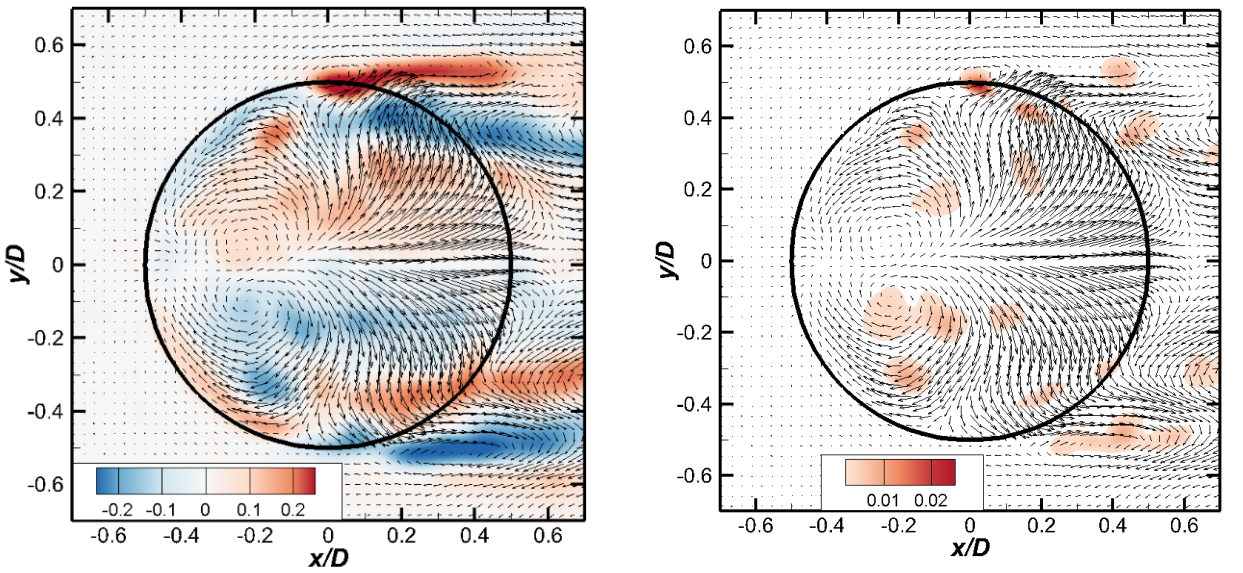

(a) AR = 3, $z/D = 0.016$, Third energy mode

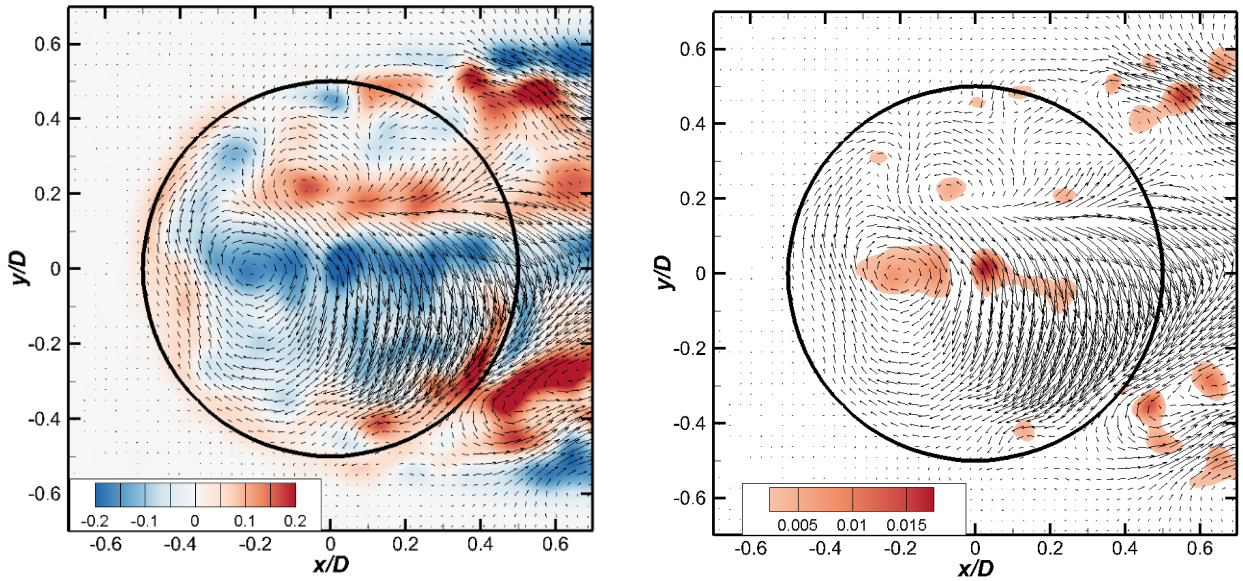

(b) AR = 5, $z/D = 0.016$, Third energy mode

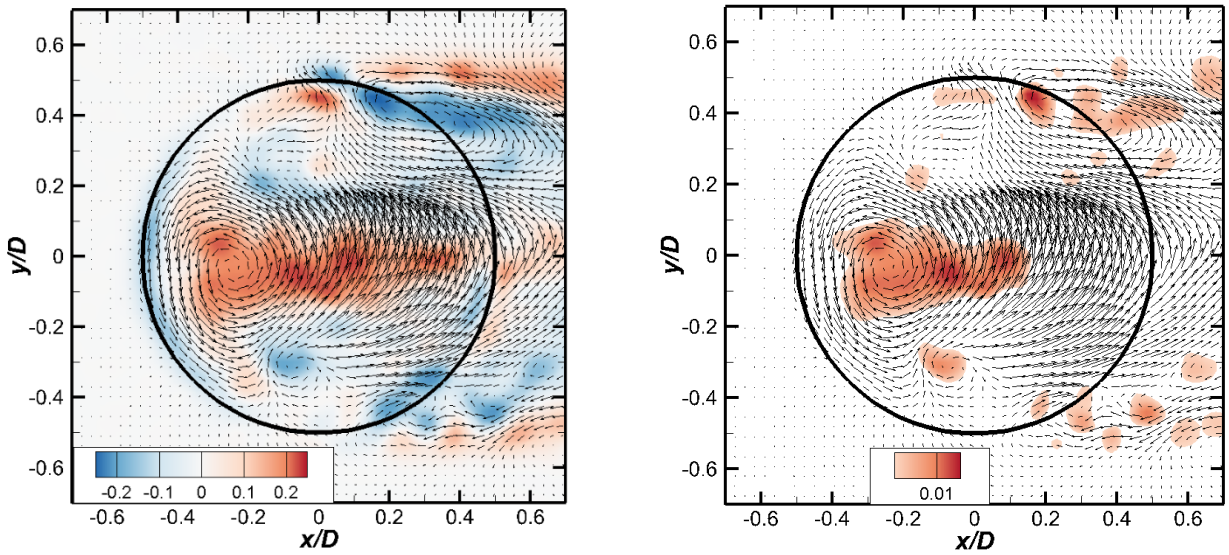

(c) AR = 7, $z/D = 0.016$, Third energy mode

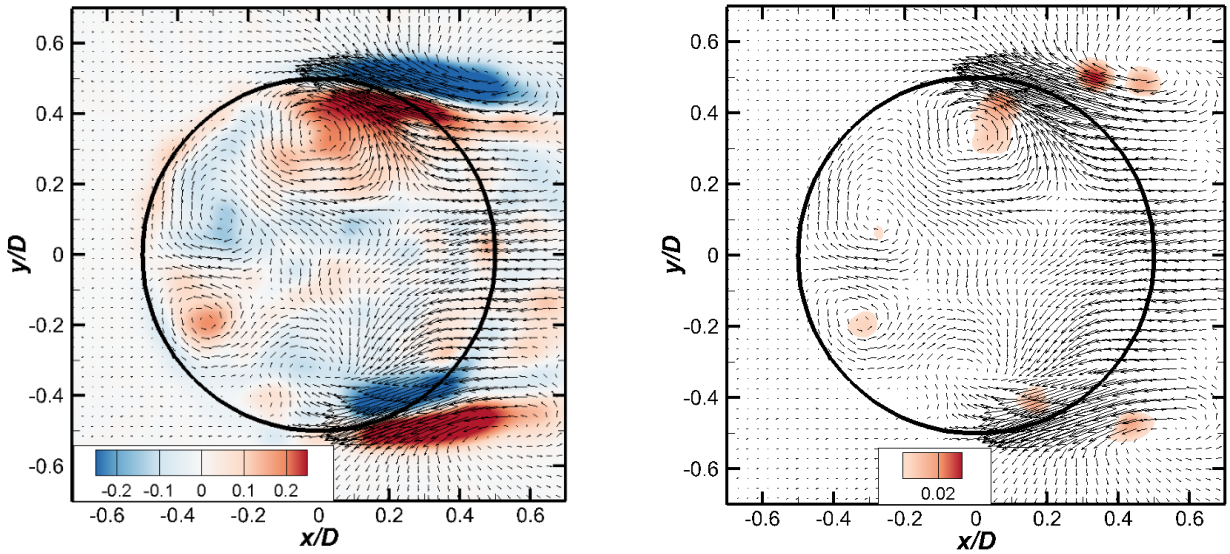

(d) AR = 9, $z/D = 0.019$, Third energy mode

Figure 3.11: In-plane normalized vorticity contours ($\omega_z D/u_\infty$) and in-plane velocity vectors (left) and in-plane swirling strength criterion contours (right) for the third POD energy mode in the horizontal (x-y) plane closest to the free end of a finite cylinder for: (a) AR = 3, (b) AR = 5, (c) AR = 7, and (d) AR = 9. Red and blue contours represent positive (CCW) vorticity and negative (CW) vorticity, respectively (left).

In Figure 3.11(b) and Figure 3.11(c), the side tip vorticity sub layers are weaker, and these planes are marked with a strong single vortex structure on the midline after the leading edge stagnation point (x/D = -0.2). There is a strong cross flow across the midline in both figures on either side indicating a fluttering motion of fluid above the free end moving on either side of the midline. Figure 3.11(d) shows some distinct vortex structures and once again reveals the strong vorticity sub-layers emerging from the side-tips. There is a pair of counter-rotating vortices on either side of the midline just after the leading edge stagnation point. In this mode, the symmetry disappears for the most part except for a couple of antisymmetric vortex structures on the side-tips ($x/D = 0$) and just behind the leading edge free end (x/D = -0.3) respectively. The location of these is similar to those in the lower aspect ratios as well as in the mean flow fields. The side tips show a strong signature of reverse flow with two sub-layers of oppositely oriented vorticity. Two pronounced, trailing rotational structures on either side of the cylinder free end downstream from the side tips (at $x/D = 0.4$) are seen, possibly due to a roll up from the sides of the free end towards the centreline. However, there seems to be no profound influence of the cross stream flow in this plane indicating that the fluttering motion of flow across the midline is more pronounced for smaller aspect ratio cylinders.

3.4 Conclusions

The flow above the free end of a surface-mounted circular cylinder was investigated using POD. POD was applied to experimental data obtained through PIV over several horizontal planes above the free end circular cylinders having aspect ratios AR = 3, 5, 7 and 9. The flow had a Reynolds number of $\mathrm{Re}_D = 4.2\times10^4$ with an approaching turbulent boundary layer thickness of $\delta/D = 1.7$.

The POD energy modes regularly demonstrated that the first mode captured close to 13-21% of the total energy, with close to 90% of the total energy captured within 120 modes. With a similar energy cascade observed for the AR = 3, 5 and 7 cases, it was determined to look at the energy mode planes for the AR = 5 cylinder as an archetypal depiction of the flow for these three aspect ratios and separately analyze the energy modes for the AR = 9 case. Also, to have a look at varying flow structures, selected results in other planes and energy modes were considered.

The first two energy modes across all planes and aspect ratios showed substantial symme-

try in the flow features directly above the free end, with the dominant energetic structures being two vorticity sub-layers emerging from the side-tip, a pair of counter-rotating vortices on either side of the midline, and a strong reverse flow coming from the wake of the free end towards the trailing edge of the cylinder. The location of these flow features varied with the distance from the free end indicating a possible three-dimensional structure arching downwards with the free end and a rotating three-dimensional structure immediately after and above the trailing edge of the cylinder free end. There was also an interaction noted with the side-tip flow structures and the incoming flow from the circumferential leading edge. This has been inferred to be the cause of the formation of the vorticity sub-layers and a local flow rotation just downstream of the side-tips of the cylinder free end. Swirling strength criterion revealed that these vorticity structures at the side-tips indeed emerge from a pair of vortices on either side. Due to the change in direction of the cross flow across snapshots, it is inferred that there exists an alternate sideways flutter of flow above the free end. However, to show this flow feature to be periodic was beyond the scope of the data used.

With increasing aspect ratio, there is a decreased influence of the ground plane on the flow features and a stronger influence of downwash coming from the freestream flow above the free end. This results in altering the locations of the flow features, including pushing the location of the vorticity sub-layers on the side-tips further downstream. Due to the absence of flow features in planes farther away from the free end, higher aspect ratios would have more compressed vertical flow features about the midline. The outer vorticity sub-layer is enhanced compared to the inner sub-layer showing an increased effect of flow entrainment from the sides of the cylinder and the weakening influence of the incoming flow from the circumferential leading edge. It would be interesting to study these flow features in the vertical streamwise planes (i.e. x-z planes) in the future to better understand the three-dimensional nature of these flow features.

Acknowledgements

The authors would like to thank the contributions of Dr. Noorallah Rostamy for collecting the experimental data used in this study.

Chapter 4

The three-dimensional mean flow field around a surface-mounted finite-height square prism

Preamble

This study aims to fulfill the third objective of the thesis mentioned in Section 1.2 and pursue the third research contribution outlined in Section 1.3. The contribution of this chapter to the overall study is to provide an increased understanding of the time-averaged three-dimensional flow field in the wake of a surface-mounted finite-height square prism and study the interaction of the various mean flow structures with the square prism, the ground plane, and with each other.

This study will investigate the time-averaged velocity field of a surface-mounted finite-height square prism of AR = 3 at a Reynolds number of $\mathrm{Re}_D = 500$ around the square prism and in the wake. Data will be obtained from a large eddy simulation using a time-averaged representation from ten vortex shedding periods. The analysis will examine the flow structure in various 2D streamwise, spanwise and transverse planes. The 3D structures in the wake and above the free end will be analyzed using iso-surfaces of the Q-criterion. Of interest would be to document the flow topologies of the tip and horseshoe vortices in the streamwise direction, the symmetric structures in the spanwise direction, and the mean recirculation zone in the transverse direction. An attempt to explain the origin and interaction of these structures using 3D iso-surfaces and surface streamlines will be made.

The set-up of the large eddy simulation code was performed by Nader Moazamigoodarzi. The time-averaged data extraction, the subsequent analysis and discussion of the results were done by Rajat Chakravarty. This was subsequently edited by Prof. Bergstrom and Prof. Sumner.

A similar version of this chapter is in preparation for submission as:

1. R. Chakravarty, N. Moazamigoodarzi, D. J. Bergstrom and D. Sumner, 'The three-dimensional mean flow field around a surface-mounted finite-height square prism', *International Journal of Heat and Fluid Flow*

Parts of this chapter were presented at the following conference:

1. R. Chakravarty, N. Rostamy, D. J. Bergstrom and D. Sumner, 'Three-Dimensional Time-Averaged Flow Fields in the Turbulent Wake of a Surface-Mounted Finite-Height Square Prism ', 3rd Symposium on Fluid-Structure-Sound Interactions and Control (FSSIC), August 21-24, 2017, pp. 149-154, Tokyo, Japan.

Abstract

The flow around a surface-mounted finite-height square prism of aspect ratio AR = 3 was studied using large eddy simulation at a Reynolds number of $\mathrm{Re}_D = 500$. The prism was immersed in a thin, laminar boundary layer of $\delta/D = 0.2$ on the ground plane and the flow was simulated over ten vortex shedding periods. The mean flow field revealed a pair of horseshoe vortices and junction vortices (N_w vortex) at the wall-junction. The horseshoe vortex was shown to move away from the symmetry mid-plane in the wake. A pair of counterrotating tip vortices were also seen emerging from the corners of the free end of the prism descending towards the ground plane away from the centerline. This was attributed to downwash effects from the separating shear layer from the free end leading edge. A mean recirculation zone was seen in the vertical symmetry plane behind the trailing edge. Symmetric vortex structures in the spanwise planes were also observed. Surface streamlines provided additional insight into locations of separating layers of flow and various critical points in the flow field.

Key Words: surface-mounted finite-height square prism, mean flow, wake, Q-criterion, tip vortices, horseshoe vortices.

4.1 Introduction

Flows over surface-mounted bluff bodies have various industrial applications such as buildings, chimneys, and aircraft landing gear among others. Such flows are also important for turbulence research because these non-streamlined bodies produce a large complex wake. This wake exhibits several unsteady turbulent features at different scales interacting with each other and thus offers ample scope to pursue both time-averaged and instantaneous flow studies. One such flow field is the flow around a surface-mounted finite-height square prism.

Unlike the flow over a two-dimensional (2D) square prism, the wake and vortex shedding structures of the three-dimensional (3D) surface-mounted finite-height square prism are strongly influenced by the effects of the ground plane and the free end [8, 18, 72, 73, 77, 86, 95, 101]. Flow over a surface-mounted finite-height square prism presents sharp corners that fix the separation points at the leading edges and the stagnation point on the front surface of the prism, the flow structure has thus been shown to be relatively insensitive over a wide range of Reynolds numbers above $\mathrm{Re}_D = 250$ (defined as $\mathrm{Re}_D = DU_\infty/\nu$, where ν is the fluid

kinematic viscosity, U_∞ is the freestream velocity, and D is the prism width) [101]. The flow field has been shown to mainly vary with the aspect ratio of the prism (defined as AR = H/D where H and D represent the height and width of the prism, respectively), the relative boundary layer thickness (defined as δ/D, where δ represents the boundary layer thickness), and the incidence angle α of the approaching flow with respect to the prism.

The flow field past a surface-mounted finite-height square prism is characterized by several structures. A schematic of the most important structures is shown in Figure 4.1. A horseshoe vortex system at the wall-junction of the square prism is formed due to the adverse pressure gradient felt by the approaching flow. Two pairs of streamwise, counter-rotating trailing vortices are seen in the wake of the square prism. The first pair (the tip vortices) originates near the free end of the prism and moves in an inclined direction towards the ground plane in the wake. The second counter-rotating pair of vortices (the base vortices) appears closer to the ground plane in the lower half of the prism wake. A mean recirculation zone is observed immediately behind the rear surface of the prism with a downwash flow in the upper part of the wake. The instantaneous flow is characterized by large-scale periodic Kármán vortex shedding similar to that on a two-dimensional (2D) square prism. In the lower part of the wake, there exists an upwash flow. Both the upwash and downwash flow are induced by the trailing vortex pairs.

There exists a critical aspect ratio $\mathrm{AR}_{\mathrm{critical}}$ for surface-mounted finite-height bluff body flows (both cylinders and square prisms) above/below which there is a significant change in the flow configuration in the wake [1,41,45,59,69,74,84]. For bluff bodies below $AR_{critical}$, the wake exhibits symmetric large-scale vortex shedding in the spanwise planes with arch vortex shedding in the wake [41, 59, 74, 84]. Conversely, above $AR_{critical}$, the wake exhibits anti-symmetric large-scale vortex shedding (more popularly known as Kármán vortex shedding). The values of $AR_{critical}$ reported in the literature have varied considerably depending on the boundary layer thickness and turbulence intensity of the incoming flow field [41,74], but most recent studies for both surface-mounted square prisms and cylinders report values between $AR_{critical} = 3$ to 5 [86].

The boundary layer thickness on the ground plane also has a substantial effect on the wake of a surface-mounted bluff body [96]. Some studies have reported that base vortices are absent in the wake for thin boundary layers [19, 62]. A thicker boundary layer promotes

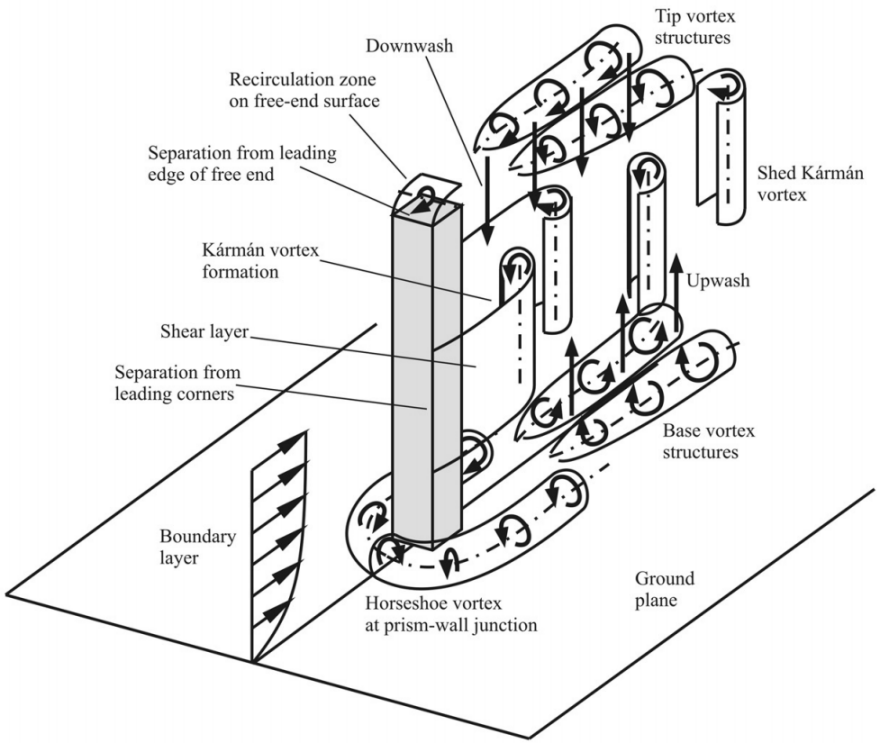

Figure 4.1: Features of the flow past a surface-mounted finite-height square prism.

more upwash from the ground plane and weakens the influence of downwash from the free end. This simultaneously suppresses and enhances the spanwise large-scale vortex shedding near the ground plane and the free end, respectively [96]. Phase-averaged studies [33] show a half-loop structure and a dipole wake for thin boundary layers (also observed by Zhang *et al.* [101]), and a full loop structure with a quadrupole wake for thick boundary layers (the quadrupole wake was also observed by Wang *et al.* [95]).

Furthermore, there also exists a critical incidence angle $\alpha_{critical}$ of the approaching flow where a prism of sufficiently high AR attains the maximum value of the mean lift coefficient and the Strouhal number St (defined as $\mathrm{St} = fD/U_\infty$, where f is the vortex shedding frequency) [87], and a minimum value of the mean drag coefficient [4, 35, 38, 56, 98]. For finite-height square prisms, $\alpha_{critical}$ is also sensitive to the aspect ratio of the prism [54]. In the present study, the focus is on the case $\alpha = 0^\circ$

While heuristic approaches have been used to identify different regions of the prism wake, some recent studies have attempted to propose a unifying flow theory based on the dynamics of the instantaneous vortical structures shed from the prism and the mean flow field struc-

tures. One study [95] for a Reynolds number of $\mathrm{Re}_D = 9300$ and boundary layer thickness $\delta/\mathrm{D} = 1.35$ for square prisms varying in aspect ratios AR = 3 to 7, suggests that the instantaneous flow tends to form arch-type vortices regardless of aspect ratio and is characterized by two spanwise vertical legs perpendicular to the ground plane and a connecting horizontal bridge at the free end. Based on probabilistic analysis and two-dimensional Particle Image Velocimetry (PIV) measurements, they developed a model of an outward-bulging arch vortex, which explains some of the mean flow characteristics in the wake downstream of the finite prism. Another study [8] at a Reynolds number of $\mathrm{Re}_D = 12{,}000$ for a square prism of aspect ratio AR = 4 with a turbulent boundary layer of thickness $\delta/D = 0.18$, proposed a different instantaneous flow paradigm, namely the alternating half-loop vortex structure shed by the finite square prism into the wake. They indicated that the mean flow structure of the wake could be explained by averaging the quasi-periodic half-loop structure over the shedding period. A single half-loop structure is made up of a principal core which is aligned approximately perpendicular to the ground plane and a streamwise connector strand. The strand connects the top of the principal core to the base of the principal core of the next half-loop located upstream. Since the principal cores occur on alternate sides of the wake, each connector strand stretches diagonally across the wake, with an orientation that also alternates. Both of the studies above considered finite square prisms of larger aspect ratio for relatively higher Reynolds numbers.

Saha [73] studied the flow past a finite-height surface-mounted square prism using direct numerical simulation (DNS) at a lower Reynolds number of $\mathrm{Re}_D = 250$ with no incoming boundary layer for four different aspect ratios: AR = 2, 3, 4 and 5. Without trying to propose a unifying theory, the study observed tip vortices, base vortices and horseshoe vortices regardless of aspect ratio. For AR > 2, the near wake showed a symmetric shear layer separation while the far wake showed greater anti-symmetric vortex shedding characteristics.

More recently, Zhang *et al.* [101] in their DNS studies over a surface-mounted finite-height square prism of AR = 4 for 6 different Reynolds numbers ranging from $\mathrm{Re}_D = 50$ to 1000 observed the streamwise vortices in the mean flow field vary from a quadrupole configuration to a six-vortices configuration to a dipole configuration with increasing Reynolds number, and drew similarities between their hairpin vortex model and the results of Wang and Zhou [95].

All the above studies consider different Reynolds numbers and inflow boundary conditions,

which can have a dramatic effect on the characteristics of the respective wakes. Most studies in the literature on finite-height bluff bodies have mainly focused on the 2D mean flow field [86,95], or the 2D conditionally averaged flow field [8,77]. Fewer studies have focused on the 3D mean flow field [73,101]. Thus a detailed description of the 3D mean flow field offers a novel contribution to the literature on surface-mounted bluff body wakes. In the present investigation, a relatively short prism is considered, i.e. AR = 3, and a low Reynolds number, i.e. $\mathrm{Re}_D = 500$. The literature suggests that this aspect ratio is around the region of the critical aspect ratio with a Reynolds number that ensures the onset of turbulent flow. The prism is immersed in a thin laminar boundary layer of $\delta/D = 0.5$ at the prism leading edge. The resolved-scale velocity and pressure fields are obtained from a large eddy simulation (LES) of the flow. To cover approximately 10 shedding cycles of data, the time-averaged 3D flow field used 50,000 instantaneous snapshots. Of interest is to provide additional insight into the 3D flow features in the wake of a surface-mounted square prism immersed in a thin boundary layer with minimal inflow turbulence intensity.

4.2 Numerical Scheme and Post-processing Methodologies

A finite-volume discretization of the filtered Navier-Stokes equations was used as the computational model for this flow. The momentum equations were discretized in time using the Crank-Nicholson method, and the subsequent set of linear equations was solved using the two-step fractional step method. An algebraic multigrid method was used to accelerate the solution of the pressure-correction equation. The subgrid-scale (SGS) stress terms were modeled using a localised Dynamic Smagorinsky model [27,93]. In this approach, the model parameter used to compute the SGS viscosity is calculated as a function of time using a test filter and a grid filter of different characteristic scales. Thus, the subgrid-scale stress term τ_{ij} arising from a filtered Navier-Stokes equations is given by

$$\tau_{ij} = \overline{u_i u_j} - \overline{u}_i \overline{u}_j. \tag{4.1}$$

Using an eddy viscosity formulation, the SGS term is modelled using SGS viscosity ν_t, and the rate of strain tensor $\overline{S}_{ij}$ as

$$\tau_{ij} - \frac{1}{3}\delta_{ij}\tau_{kk} = -2\nu_t \overline{S}_{ij}. \tag{4.2}$$

Using dimensional analysis, the SGS viscosity ν_t can be written in terms of the model parameter C_s, and characteristic filter width Δ as

$$\nu_t = (C_s\Delta)^2\sqrt{2\overline{S}_{ij}\overline{S}_{ij}}. \tag{4.3}$$

A structured, Cartesian grid with 128×96×144 control volumes in the x (streamwise), y (transverse) and z (spanwise) direction, respectively, was used to discretize the flow domain. A Cartesian mesh was used with local refinement around the surfaces of the prism and the ground plane. By convention the velocity and vorticity components in the (x, y, z) directions are defined as (u, v, w) and (ω_x, ω_y, ω_z), respectively. Using air as the fluid, a freestream velocity of $U_\infty = 0.375$ m/s and a prism width $D = 0.02$ m, gave a Reynolds number for the flow of $\mathrm{Re}_D = 500$. The height of the prism mounted on the ground plane was $H = 0.06$ m, which yields the aspect ratio of the prism to be AR = 3. The prism was located approximately $3D$ from the inlet plane and the overall dimensions of the domain were 0.32 m ($16D$), 0.14 m ($7D$) and 0.12 m ($6D$) in the streamwise, transverse and spanwise directions, respectively. As the Dynamic Smagorinsky model was used, the time step changed with every iteration. Through a CFL condition, the time step was arranged to be around 10^{-4} seconds. The approaching boundary layer on the ground plane was laminar and relatively thin ($\delta/D = 0.2$). A no-slip condition was used for the ground plane. The origin of the frame of reference used was set at the centre of the square cross-section at the wall-junction of the prism. A schematic of the frame of reference and the mesh used for the present study is shown in Figure 4.2. Based on a Strouhal number St = 0.11 for this flow field (using Zhang *et al.* [101], for a similar Reynolds number, and Sumner *et al.* [86], albeit for a higher Reynolds number), 50000 realizations almost equally spaced in time (i.e. around 10^{-4} seconds between each snapshot) were used to span approximately 10 shedding cycles of the flow to compute the mean flow field.

Chong *et al.* [14] defined vortices as regions where the local velocity gradient tensor has complex-conjugate eigenvalues. This criterion is also called the Q-criterion. In this study, 3D velocity field data were used to obtain the local velocity gradients. Regions where complex-conjugate eigenvalues were found, were concluded to contain localized vortex structures.

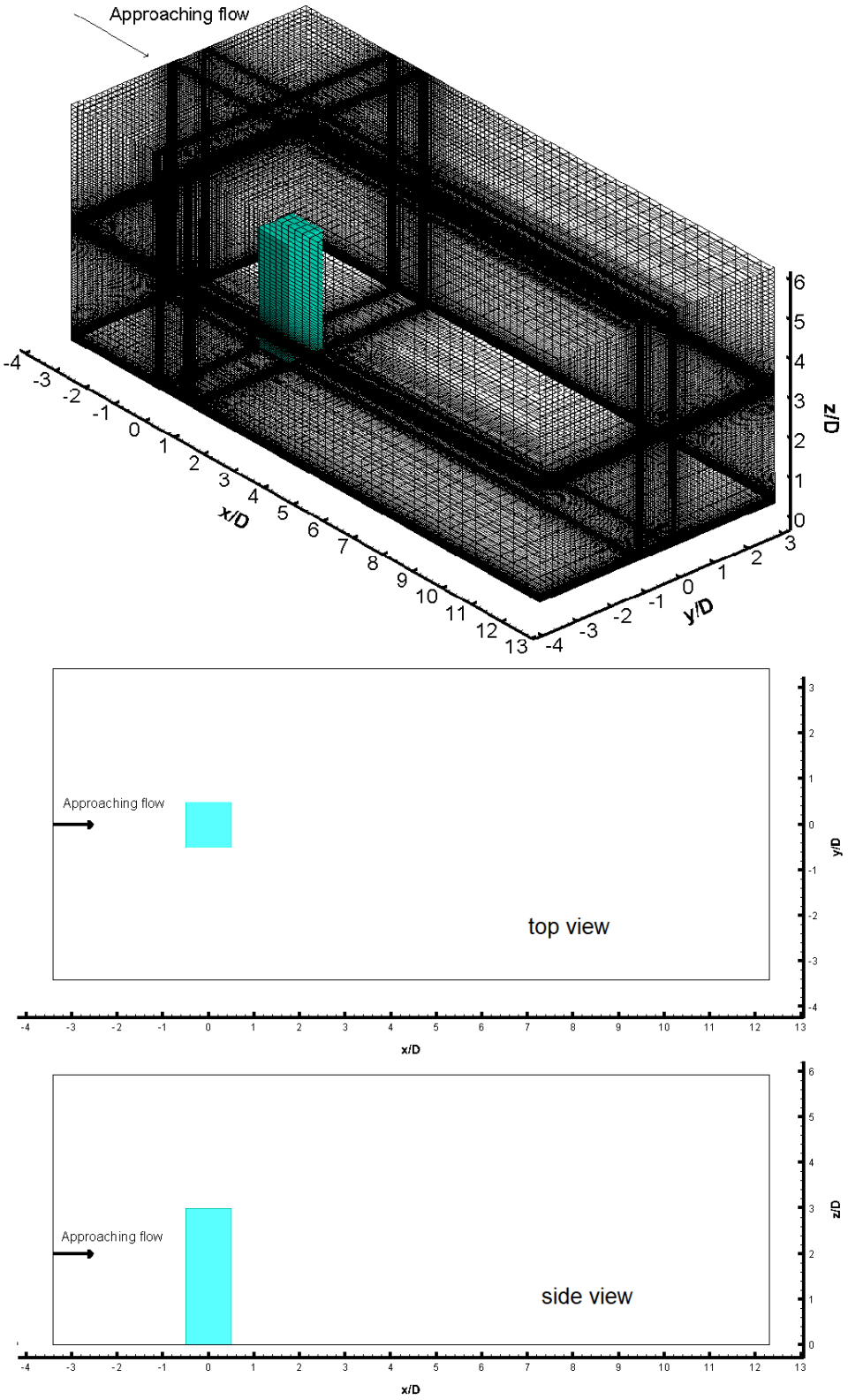

Figure 4.2: Flow domain and mesh used for the LES analysis

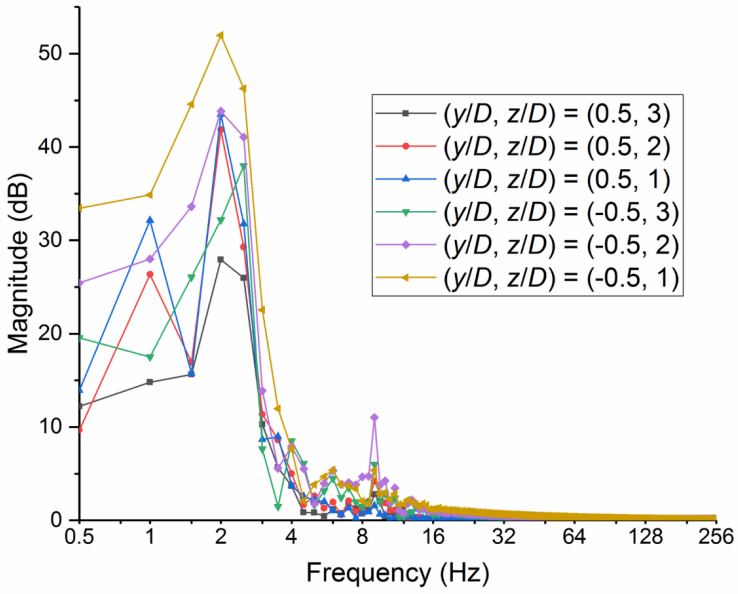

Figure 4.3: The power spectrum for a pressure signal taken at every time step across 10 shedding cycles of the flow at 6 locations along the side walls of the square prism.

4.3 Results and Discussion

4.3.1 Pressure Power Spectrum

Figure 4.3 shows the power spectrum for six locations along the side-walls of the prism located symmetrically at six locations at different heights on the prism surface (x/D, y/D, z/D) = (0, ±0.5, 1), (0, ±0.5, 2) and (0, ±0.5, 3). At these locations, pressure data were taken at every snapshot across the ten periods of data and used to construct the power spectrum. A single-sided magnitude spectrum was obtained using a standard Fast Fourier Transform (FFT) subroutine on MATLAB. This yields a periodogram with the frequency (in Hz) and power (in dB). Except for one case (i.e. (x/D, y/D, z/D) = (0, -0.5, 3)), all other planes show a frequency of 2 Hz. Using this frequency with the prism diameter and freestream velocity gives a Strouhal number of St = 0.106, which is in reasonable agreement with other flows over prism at this aspect ratio and Reynolds number (e.g. Saha [73] reports St = 0.114 for AR = 3 at Re_D = 250, Zhang *et al.* [101] reports St = 0.113 for AR = 4 at Re_D = 500).

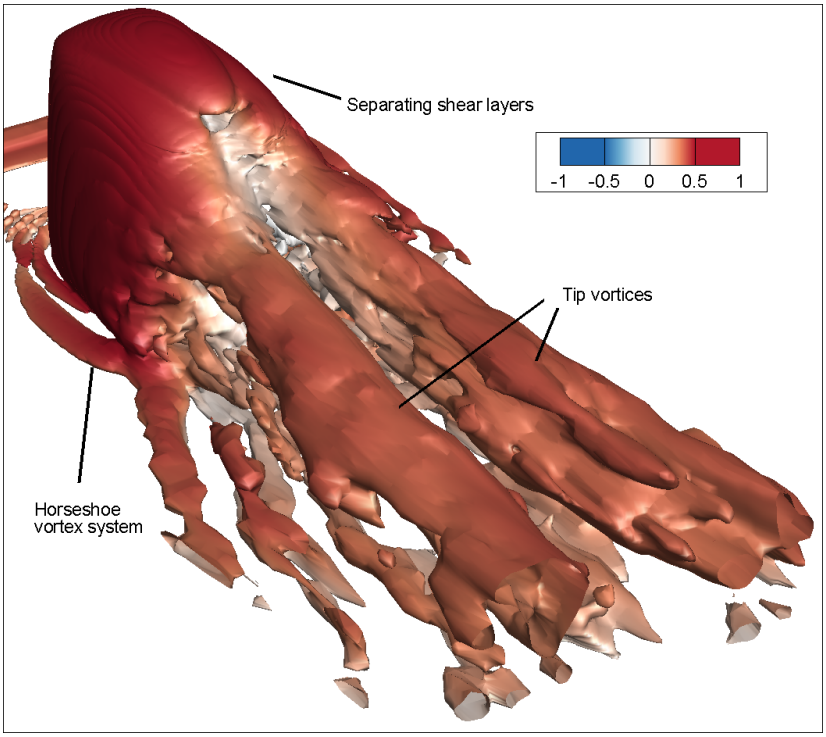

Figure 4.4: 3D time-averaged flow field using an iso-surface of the Q-criterion ($Q = 1$) contoured with the normalized streamwise velocity u/U_∞.

4.3.2 The Three-dimensional (3D) Flow Field

Figure 4.4 shows the 3D time-averaged flow field using an iso-surface of the Q-criterion contoured with the normalized streamwise velocity u/U_∞. The flow is characterized by the inflow separating at the leading edges of the square prism producing shear layers above the side walls and above the free end. The separating shear layers from the side walls closer to the free end of the prism form a pair of symmetric tip vortices moving in an inclined fashion towards the ground plane and away from the vertical symmetry (x-z) mid-plane of the square prism. The flow configuration represents the dipole wake configuration (seen previously by Sattari *et al.* [77] and Zhang *et al.* [101] for similar aspect ratio prisms) suggesting that this prism is below the critical aspect ratio $\mathrm{AR}_{\mathrm{critical}}$ or in a transition across $\mathrm{AR}_{\mathrm{critical}}$. This would thus suggest that based on the present inflow conditions of a relatively low Reynolds number flow and a thin laminar boundary layer, $\mathrm{AR} = 3 < \mathrm{AR}_{\mathrm{critical}}$.

There also appears to be two distinct separating shear layers near the free end of the prism - one coming from the sides of the prism close to the free end corners, and the other

emanating from the free end leading edge of the prism. In addition, a symmetric distribution of horseshoe vortices (system of necklace vortices) on the ground plane about the prism-wall junction is also seen. These are seen to loop around the upstream face and the sides of the prism, and begin moving away from the vertical symmetry plane of the prism as they diffuse downstream. Several small scale structures are also seen above the ground plane in the prism wake, but it remains inconclusive from this figure on whether they represent base vortices. To further explore the formation and interaction of these structures with each other, a closer look at the flow structures around the prism is needed.

Figure 4.5 shows a close up of the free end of the 3D time-averaged flow field using an iso-surface of the Q-criterion (this time at a different value of $Q = 150$) contoured with the normalized streamwise velocity u/U_∞ (as seen in the upstream direction). A higher value of Q was used to remove the weaker structures in order to isolate the more dominant rotational structures. The figure shows the evolution of the tip vortices from the sides of the prism closer to the free end. A separate shear layer coming from the free end leading edge of the prism moves away from above the free end surface of the prism as it moves downstream. This separating shear layer (shown later through vectors) does not reattach to the free end of the prism, but moves downstream towards the ground plane in the prism wake. The outer layer of the Q-criterion iso-surface shows a predominance of velocity in the streamwise direction while the inner layers of the iso-surface conversely show a dominance of reverse flow. The region of blue contours above the free end and below the separating shear layer represents the reverse flow towards the leading edge from the mean recirculation zone (also identified as the B_t vortex) [45] seen in the vertical symmetry plane. There is also reverse flow on the side walls of the prism likely coming from the flow towards the leading edge from the symmetric mean vortex structures seen in the horizontal planes. The presence of a few iso-surfaces behind the downstream face of the square prism enclosed within the separating shear layers from the sides of the prism demonstrate the rotational structure of the mean recirculation zone in the vertical symmetry plane as well.

4.3.3 Streamwise Planes (x/D = 0 to 6)

Figure 4.6 shows the time-averaged normalized in-plane velocity vector field (u/U_∞, v/U_∞) and the normalized streamwise (x-vorticity) contours ω_x^* (i.e. $\omega_x^* = \omega_x D/U_\infty$) for six vertical

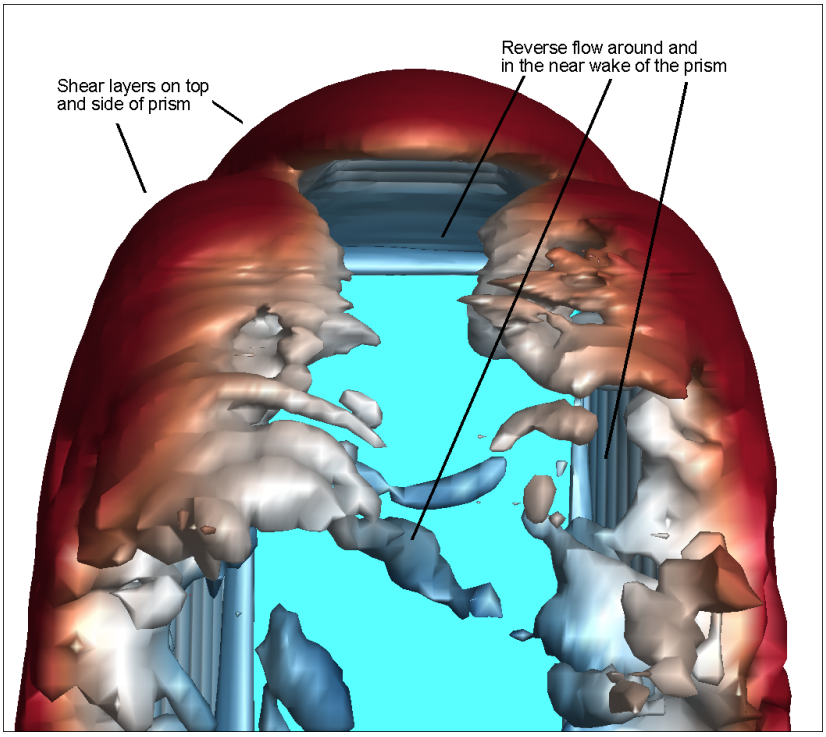

Figure 4.5: 3D time-averaged flow field near the free end of the square prism viewed from downstream, using an iso-surface of the Q-criterion ($Q = 150$) contoured with the normalized freestream velocity u/U_∞.

cross-stream planes (y-z planes) at $x/D = 0$ (Figure 4.6(a)), 0.5 (Figure 4.6(b)), 1 (Figure 4.6(c)), 2 (Figure 4.6(d)), 4 (Figure 4.6(e)), and 6 (Figure 4.6(f)). In the planes around and just after the trailing edge of the prism (i.e. $x/D = 0$ to 2) (also referred to as 'near-wake' in the literature), the flow field is characterized by the horseshoe vortex system on either side of the junction of the prism with the ground plane, a region of separated flow from the free end side edges of the prism forming the anti-symmetric edge vortices (seen in Sumner *et al.* [86]), and an anti-symmetric pair of streamwise vorticity above these edge vortices on either side of the symmetry plane (also seen in Sumner *et al.* [86] closer to the leading edge, though these disappear in their study towards the prism trailing edge). The pairs of edge vortices and the streamwise vortices that are observed above the free end of the prism appear to be below the region of upward moving velocity vectors, likely indicating that these structures are within the separating shear layer emanating from the free end leading edge of the square prism. This vorticity may be explained by a coupling influence of the edge vortex flow system moving towards the vertical symmetry plane and the upward moving streamwise separating shear layer coming from the free end prism leading edge. On the sides of the prism, outside of the shear layer close to the prism side walls, the flow moves away from the prism in a downward direction close to the ground plane. Moving towards the free end, this flow pattern briefly becomes horizontal and then begins moving in the upward direction, indicating the presence of a stagnation point on the upstream surface closer to the ground plane of the prism (seen later in the streamline plots).

In the planes farther downstream (i.e. $x/D = 0.5$ (Figure 4.6(b), and 1 (Figure 4.6(c)), the streamwise vortices above the free end appear to move farther above the free end making more room for the edge vortices as these get thicker while above the free end but gradually disappear in the near wake by $x/D = 2$ as they diffuse into the wake. The horseshoe vortex system is also seen to simultaneously move away from the ground plane and the prism in the downstream x-planes.

At around $x/D = 2$ (Figure 4.6(d)), the flow field shows the onset of counter-rotating tip vortices on either side of the prism symmetry plane. These are likely due to the coupling interactions of the upward moving flow vectors on the sides of the prism (seen previously stemming from the separating shear layers on the side-walls of the prism) and the onset of downwash along the vertical centreline of the wake likely coming from the separating

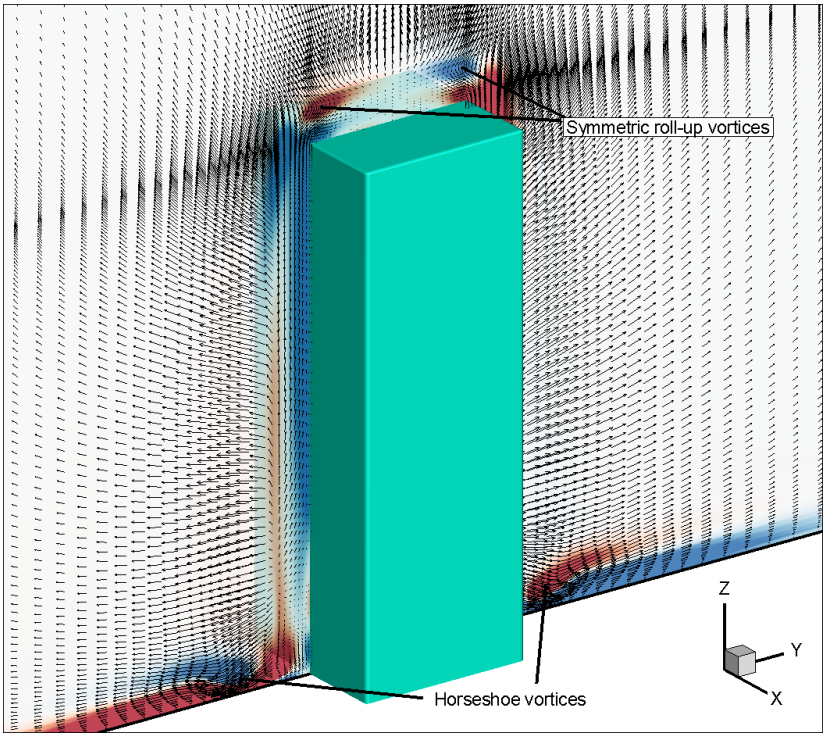
Symmetric roll-up vortices
Horseshoe vortices
Z
Y
X

(a) $x/D = 0$

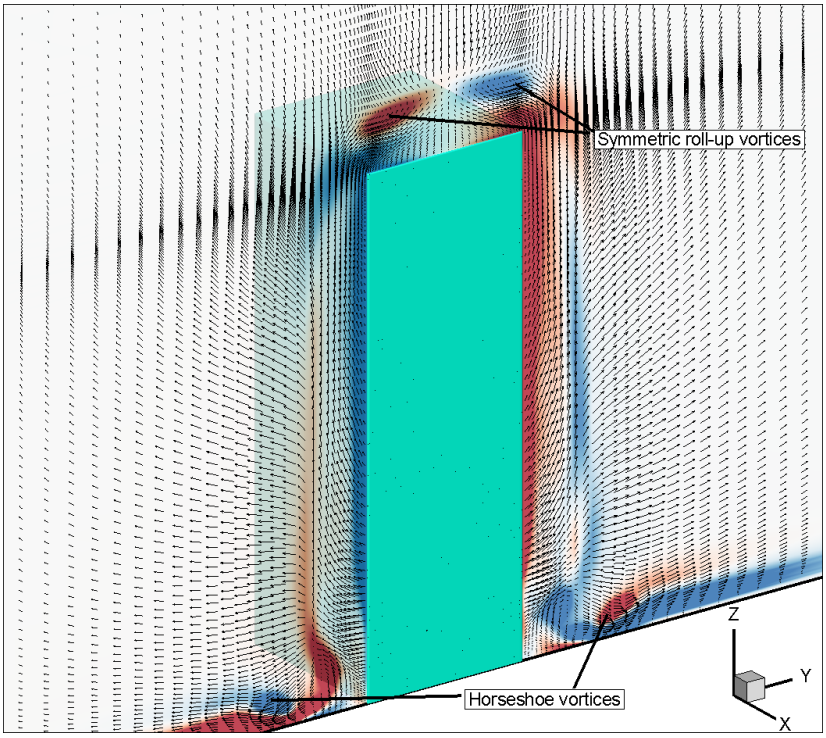
Symmetric roll-up vortices
Horseshoe vortices
Z
Y
X

(b) $x/D = 0.5$

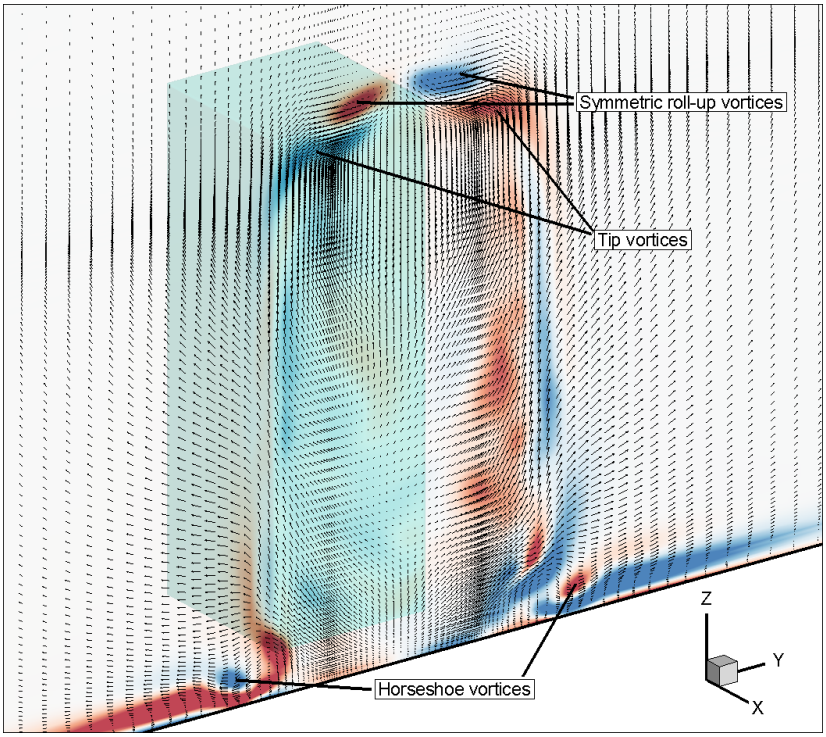
Symmetric roll-up vortices
Tip vortices
Horseshoe vortices
Z
Y
X

(c) $x/D = 1$

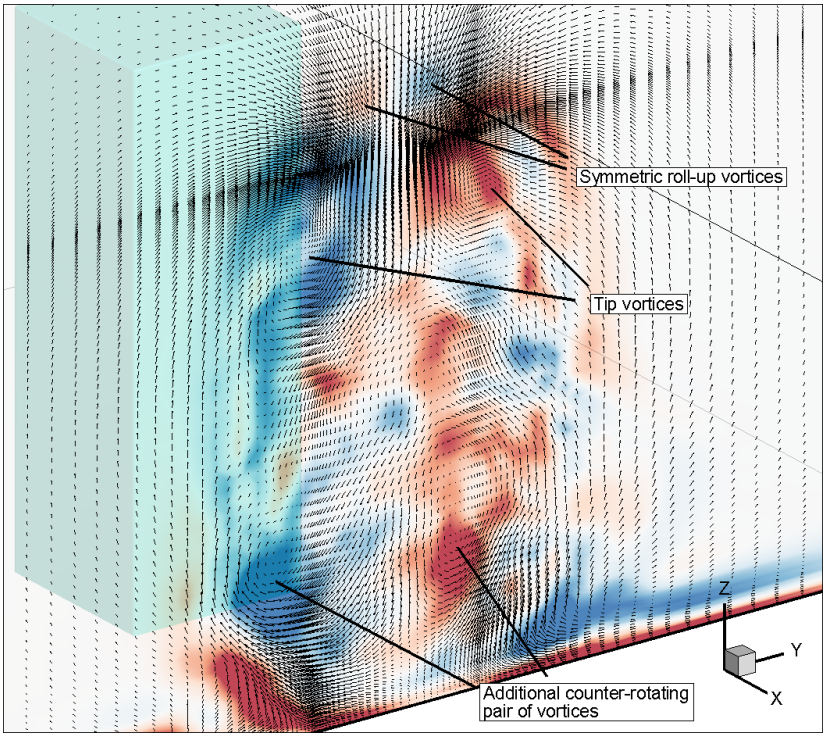
Symmetric roll-up vortices
Tip vortices
Additional counter-rotating pair of vortices
Z
Y
X

(d) $x/D = 2$

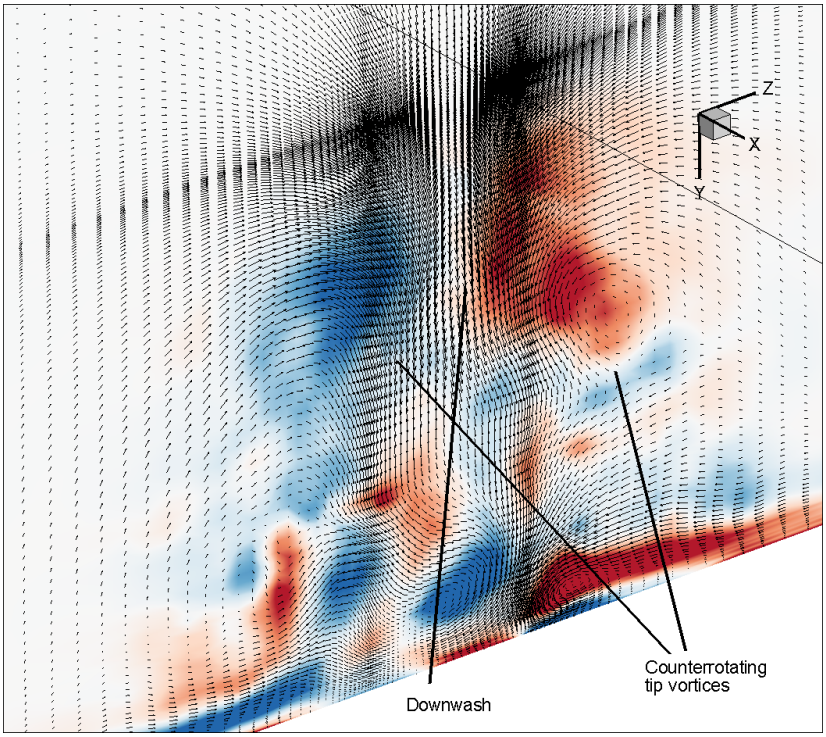

(e) $x/D = 4$

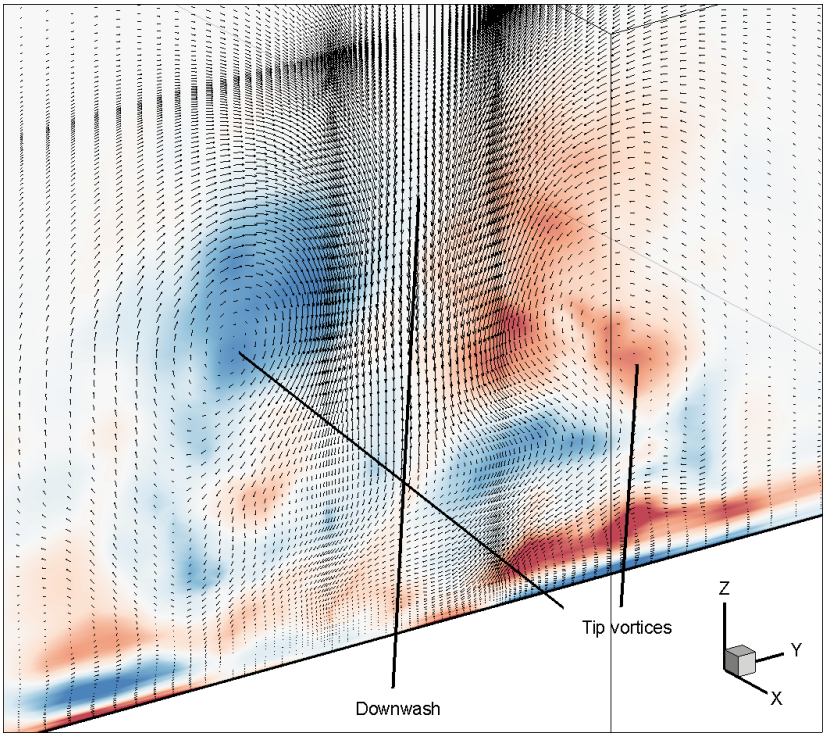

(f) $x/D = 6$

Figure 4.6: The time-averaged normalized tangent vector field (v/U_∞, w/U_∞) superimposed on the normalized x-vorticity contours ω_u^* (i.e. $\omega_u^* = \omega_x D/U_\infty$) for the streamwise planes: (a) $x/D = 0$, (b) $x/D = 0.5$, (c) $x/D = 1$, (d) $x/D = 2$, (e) $x/D = 4$, and (f) $x/D = 6$. Red and blue contours represent positive (CCW) vorticity and negative (CW) vorticity, respectively.

shear layer originating from the free end leading edge as it moves towards the ground plane downstream of the prism trailing edge. Closer to the ground plane for $x/D = 2$ (Figure 4.6(d)), a complex interaction between the downwash flow in the symmetry plane and the upward moving flow coming from the sides of the square prism creates an anti-symmetric system of vorticity about the symmetry plane. However, on further investigation in planes downstream and using streamline plots (not shown), these do not turn out to be base vortices. This is consistent with the streamwise dipole wake configuration results of Zhang *et al.* [101] (for AR = 4, Re = 500 and a boundary layer thickness of $\delta/D = 0.43$). This wake would also indicate that for the given inflow conditions and boundary layer thickness, the prism of AR = 3 lies below the critical aspect ratio $\mathrm{AR}_{\mathrm{critical}}$ [84, 95].

Farther downstream (i.e. $x/D = 4$, 6), the flow is dominated by strong downwash flow around the symmetry plane and the anti-symmetric streamwise dipole wake configuration on either side. The streamwise tip vortices assume a more longitudinally stretched configuration closer to the prism and get progressively shorter in the downstream planes. These tip vortices gradually move towards the ground plane and weaken due to their diffusion with the surrounding freestream flow (similar to Zhang *et al.* [101]). The horseshoe vortex system weakens and gets smeared in the transverse direction by $x/D = 6$. Some evidence of small-scale structures are seen near the ground plane behind the prism trailing edge.

4.3.4 Cross-stream Planes (y/D = 0 to 0.5)

Figure 4.7 shows time-averaged in-plane vector field superimposed on the normalized y-vorticity contours ω_y^* (i.e. $\omega_y^* = \omega_y D/U_\infty$) for three vertical streamwise planes (x-z) at y/D = 0 (Figure 4.7(a)), 0.25 and 0.5. For the $y/D = 0$ plane, the flow is characterized by a clockwise (CW) junction vortex upstream of the leading face of the prism, a counter-clockwise (CCW) junction vortex above the ground plane just downstream of the trailing edge of the prism (called the N_w vortex by Krajnović [45] for a finite cylinder); a separating shear layer from the free end leading edge of the prism that moves downstream without any reattachment on the top surface of the prism; and a CW mean recirculation zone behind the trailing edge of the prism close to the free end (called the B_t vortex by Krajnović [45] for a finite cylinder). The recirculation zone extends about 3D downstream of the trailing face of the prism. In the literature, this has been shown to vary in size depending on the Reynolds number of the

flow [101], and aspect ratio of the prism [69].

A stagnation point is noticed at the leading face of the prism (demonstrated later in Figure 4.9(a)), below which the flow moves towards the ground plane and forms the horseshoe vortex in front of the leading face of the prism. The location of the horseshoe vortex has been shown to be invariant of the aspect ratio of the prism [3]. In this study, it is found at approximately (x/D, z/D) = (-0.9, 0.2), consistent with the results of Ballio *et al.* [3] and Sumner *et al.* [86]. The N_w vortex has not been seen in Sumner *et al.* [86] for the AR = 3 wake, but this may be attributed to a higher Reynolds number (Re = 4.2×10^4) and thicker boundary layer (δ/D = 2.6) employed in their PIV analysis in comparison to this present study. The separating shear layer in the wake moves towards the ground plane and reattaches to the ground plane at $x/D = 4.5$. This separating line disconnects the region of reverse flow upstream of itself that contributes to the mean recirculation zone, and the outer freestream flow downstream of itself. This separating line moving towards the ground plane is responsible for the downwash flow already seen in the downstream x/D planes away from the near-wake in Figure 4.6.

A saddle point is seen at the end of this separating flow line (at the location of the shear layer reattachment seen in Figure 4.7(a)) close to the ground plane. This is understandable given the thin laminar boundary layer for this flow diminishes the upwash effect from the ground plane and pushes this saddle point closer to the ground plane [84]. Downstream of the saddle point, flow is seen to move in an upward direction, likely representative of upwash flow (seen by Wang and Zhou [95]). The reverse flow from this saddle point moves towards the trailing face of the prism and creates another stagnation point on the trailing face of the prism. Above the trailing face stagnation point, the flow vectors move towards the free end along the trailing face of the prism and form the mean recirculation zone. Below the trailing face stagnation point, the vectors move towards the ground plane and form the trailing face junction vortex (seen previously by Rostamy *et al.* [69], and Krajnović [45] albeit for surface-mounted cylinder flows). Reverse flow is also seen above the free end of the prism below the separating shear layer. However, there is no recirculation zone above the free end in the vertical planes (seen in Rostamy *et al.* [69] for a higher $Re_D = 4.2\times10^4$).

In vertical planes away from the symmetry plane (i.e. $y/D = 0.25$, 0.5) (Figure 4.7(b) and 4.7(c), respectively), the horseshoe vortex core expectedly moves closer to the prism leading face as it begins wrapping around the base junction of the prism. The mean recirculation

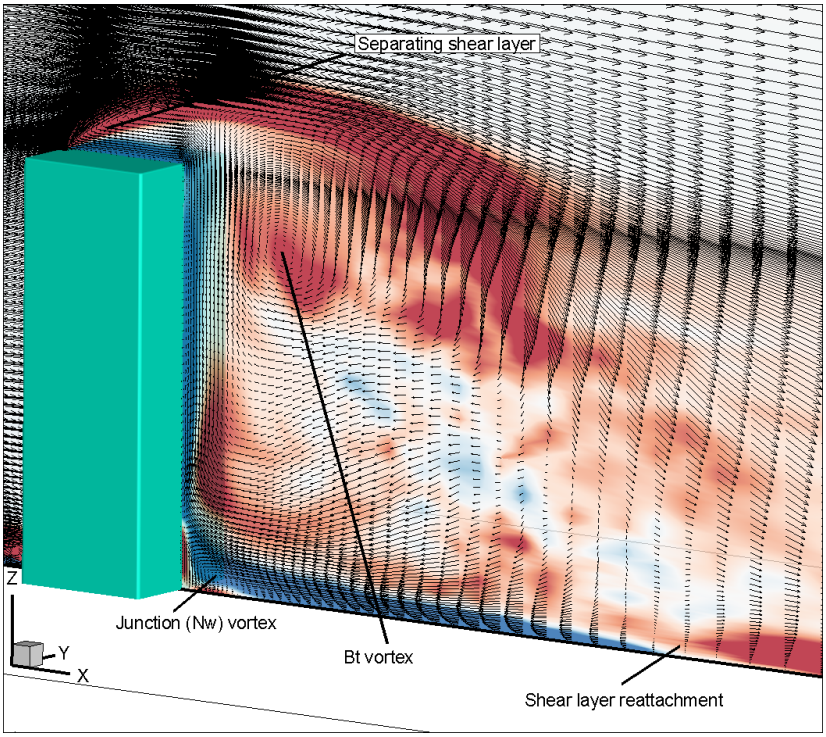
Separating shear layer
Z
Y
X
Junction (Nw) vortex
Bt vortex
Shear layer reattachment

(a) $y/D = 0$

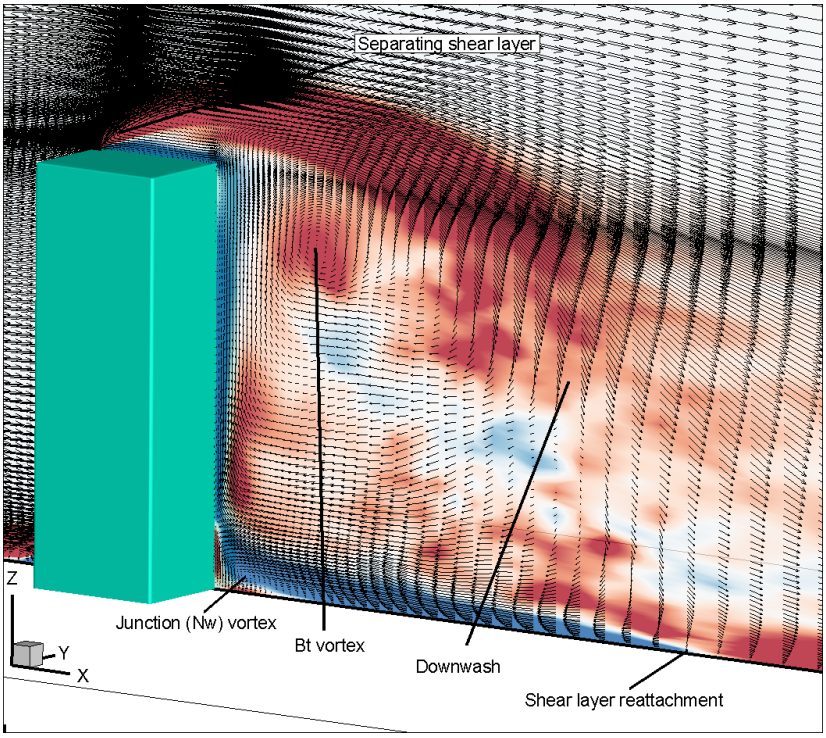
Separating shear layer
Z
Y
X
Junction (Nw) vortex
Bt vortex
Downwash
Shear layer reattachment

(b) $y/D = 0.25$

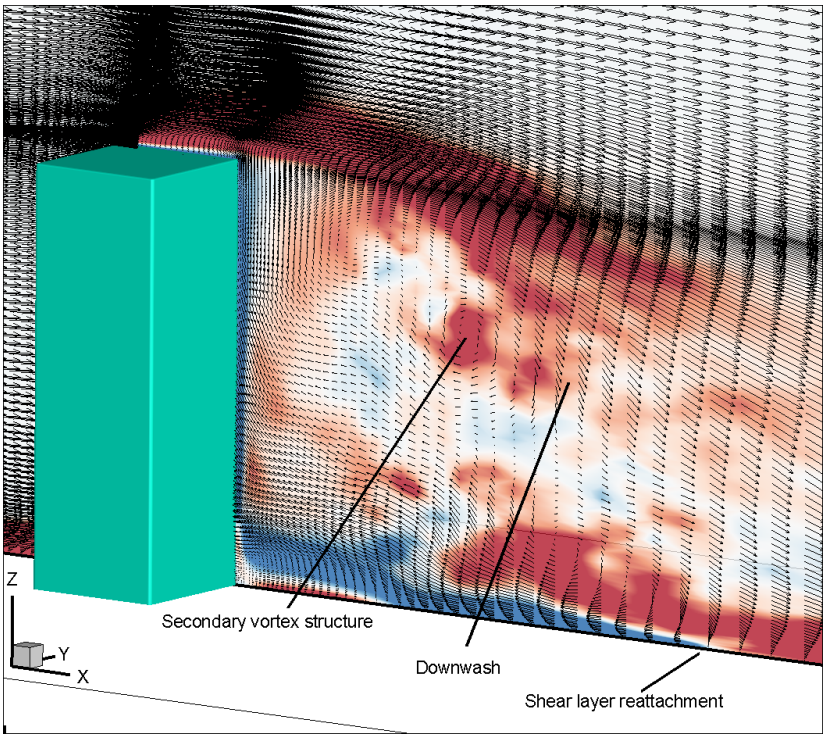

(c) $y/D = 0.5$

Figure 4.7: The time-averaged normalized tangent vector field (u/u_∞, w/u_∞) superimposed on the normalized y-vorticity contours ω_v^* (i.e. $\omega_v^* = \omega_y D/u_\infty$) for the streamwise planes: (a) $y/D = 0$, (b) $y/D = 0.25$, and (c) $y/D = 0.5$. Red and blue contours represent positive (CCW) vorticity and negative (CW) vorticity, respectively.

zone behind the free end trailing edge of the prism (B_t vortex) and the junction (N_w) vortex become smaller in size due to the weakening influence of the freestream flow coming from the sides of the prism. The effect of upwash becomes more prominent close to the ground plane at $x/D = 3$ further substantiating that the weakening of the B_t vortex and downwash go hand in hand in vertical planes away from the symmetry plane.

4.3.5 Horizontal Planes (z/D = 0.5 to 3)

Figure 4.8 shows the time-averaged in-plane vector field superimposed on the normalized z-vorticity contours ω_z^* (i.e. $\omega_z^* = \omega_z D/U_\infty$) for six horizontal spanwise planes (x-y planes) at z/D = 0.5, 1, 1.5, 2, 2.5 and 3. Across all planes, the flow is characterized by separating shear layers from the leading edges of the side walls of the prism and a pair of longitudinal symmetric vortices being shed in the wake, enclosing a region of reverse flow within it towards the downstream face of the square prism. The reverse flow impinges on the downstream face of the prism and separates from the trailing edges of the prism on the side walls. No recirculation is seen around the side walls of the prism. The location of the foci of the symmetric counter-rotating vortices in the wake varies with height across the various horizontal z-planes and is prominently seen in planes below $z/D = 2$ (Figures 4.8(a) to 4.8(c)) towards the ground plane. These are not prominent in the $z/D = 2.5$ (Figure 4.8(d)) and $z/D = 3$ plane (see Figures 4.8(e) and 4.8(f)), owing to lower vector resolution as well z-vorticity contours of the shear layers possibly probably masking any rotational structures in this region.

The region of reverse flow is widest in the horizontal planes closest to the ground plane but becomes thinner in planes closer to the free end. It was also not possible to deduce any vortex shedding using planar contours of the Q–criterion (not shown) on these planes due to the presence of the vertical recirculation zone (the B_t vortex) contributing strongly to the Q-criterion plots in this region. Thus, in the model of Wang & Zhou [95], and in previous studies on a surface-mounted cylinder by Tanaka & Murata [88], where it was suggested that the connection of the spanwise vortices near the free end form an arch vortex, was not verified in this study. However, similar to the results of Etzold & Fiedler [19], Kawamura *et al.* [41] and in the suggested vortical legs model of Wang & Zhou [95], the foci of the symmetric shedding moves farther upstream in the horizontal planes approaching the ground plane in this study. The separating shear layers from the sides of the prism extend the farthest downstream in the

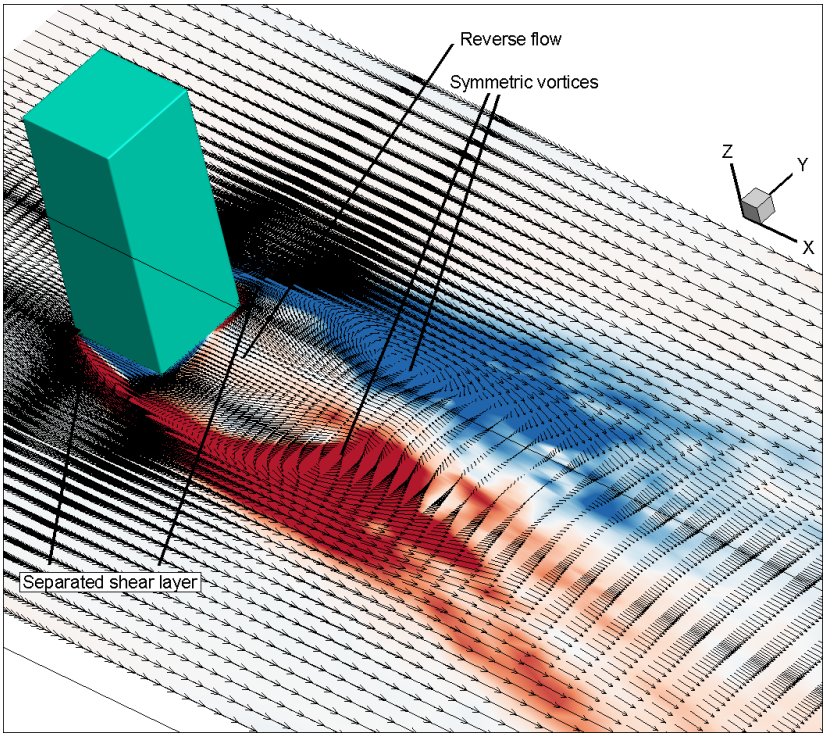
Reverse flow
Symmetric vortices
Z
Y
X
Separated shear layer

(a) $z/D = 0.5$

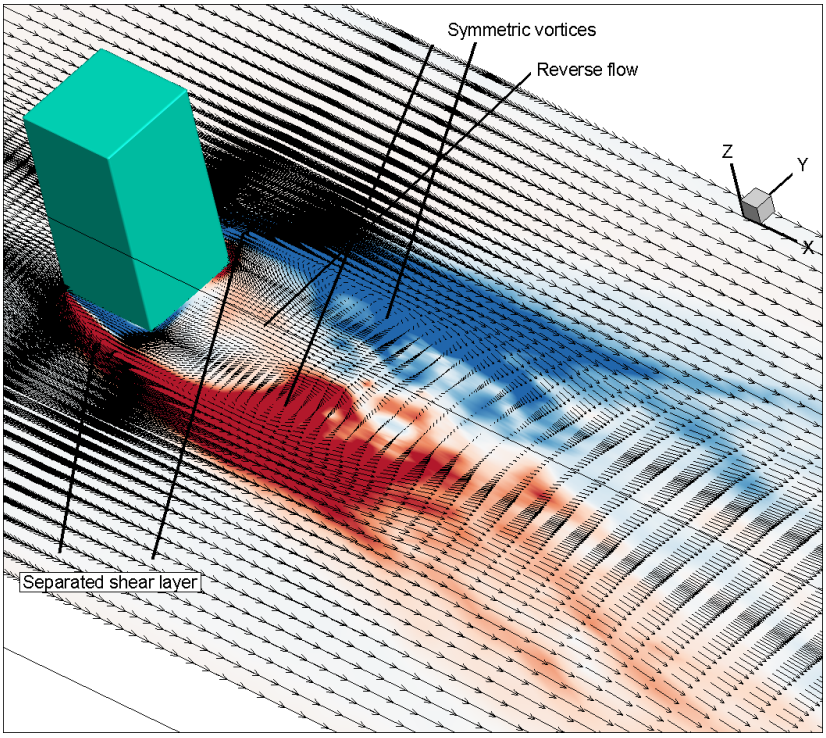
Symmetric vortices
Reverse flow
Z
Y
X
Separated shear layer

(b) $z/D = 1$

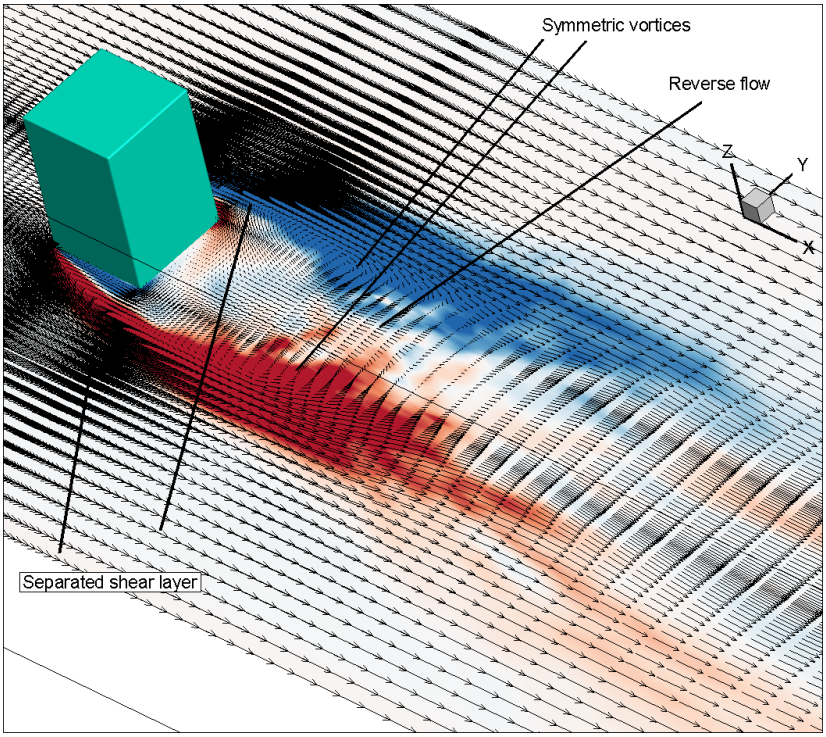
Symmetric vortices
Reverse flow
Z
Y
X
Separated shear layer

(c) $z/D = 1.5$

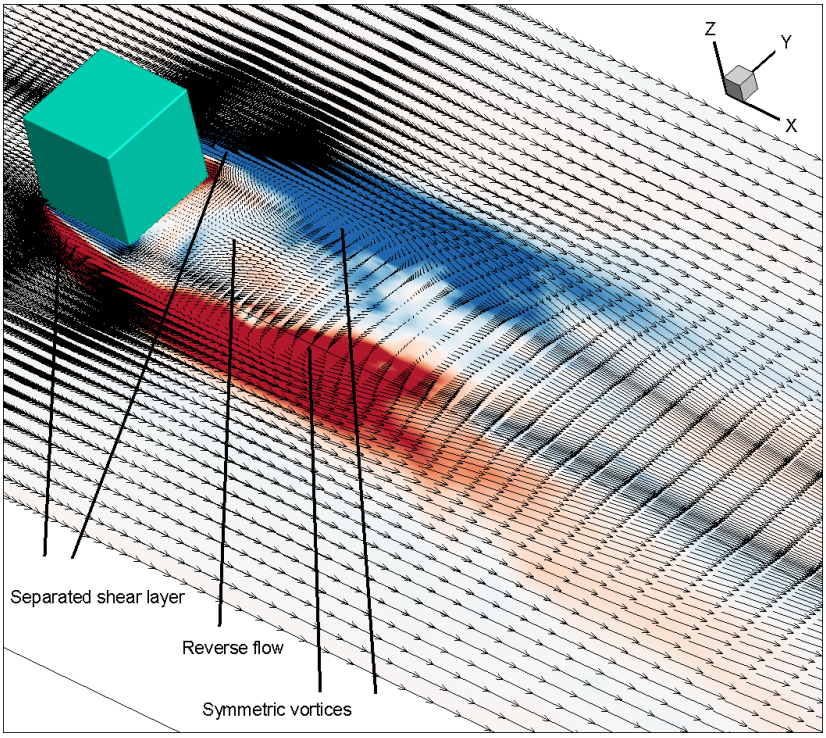
Z
Y
X
Separated shear layer
Reverse flow
Symmetric vortices

(d) $z/D = 2$

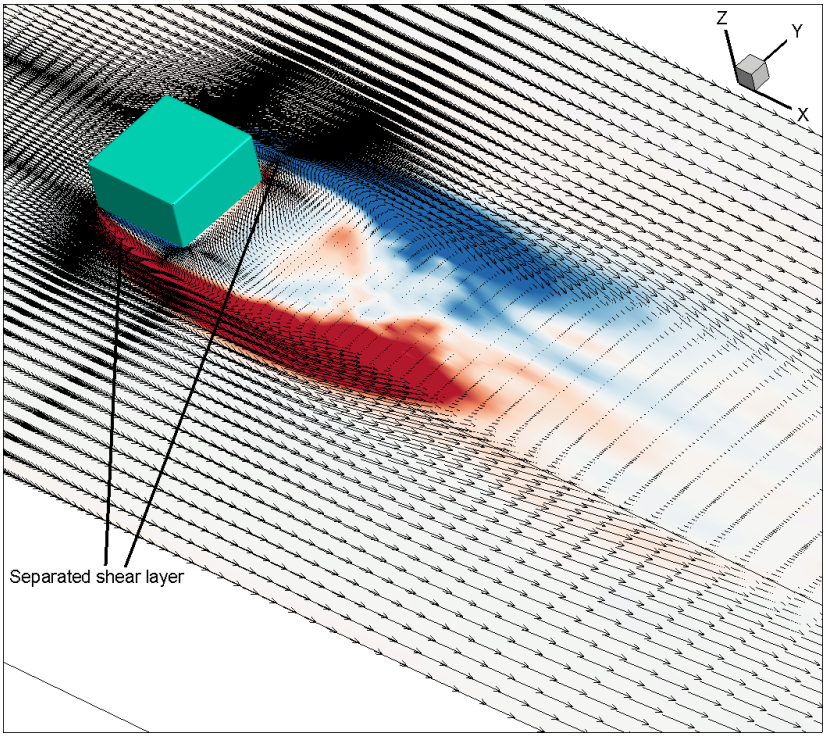

(e) $z/D = 2.5$

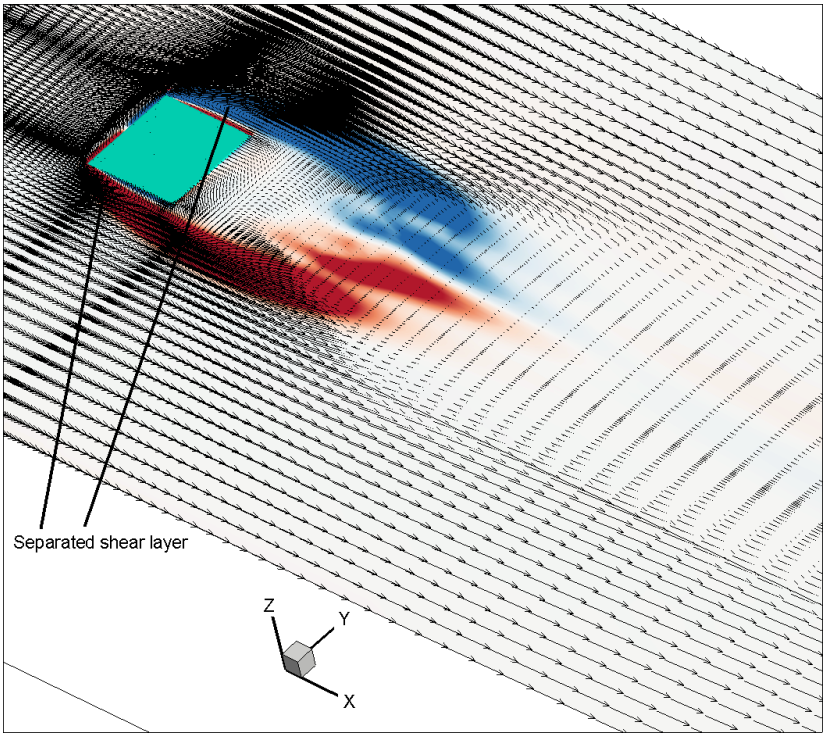

(f) $z/D = 3$

Figure 4.8: The time-averaged normalized tangent vector field (u/U_∞, v/U_∞) superimposed on the normalized z-vorticity contours ω_z^* (i.e. $\omega_z^* = \omega_z D/U_\infty$) for the streamwise planes: (a) $z/D = 0.5$, (b) $z/D = 1$, (c) $z/D = 1.5$, (d) $z/D = 2$, (e) $x/D = 2.5$, and (f) $x/D = 3$. Red and blue contours represent positive (CCW) vorticity and negative (CW) vorticity, respectively.

planes closest to the mid-height of the prism but get progressively shorter towards the free end as well the ground plane. Closer to the free end, the flow interacts with the freestream flow above the prism that promotes rapid diffusion of the shear layer into the wake. Closer to the ground plane, the increased shear stresses from the ground hinder the development of the shear layers as they move downstream.

4.3.6 Surface Streamlines

For further insight into the vortex structures around the square prism, streamline plots around the square prism are useful in explore the directions of flow that produce these vortex structures. Figure 4.9 shows the planar streamline plots very close to the front surface (Figure 4.9(a)), side surface (Figure 4.9(b)), rear surface (Figure 4.9(c)) and free end surface (Figure 4.9(d)). Unlike the two-dimensional (2D) square prism, the streamlines are strongly influenced by the presence of the ground plane and the free end of the prism.

The front face is characterized by a stagnation point close to the ground plane along the symmetry midline (around $z/D = 0.5$). The downward moving streamlines towards the ground plane below this stagnation point leads to the formation of the front surface junction vortex (horseshoe vortex). Similarly, the outward moving streamlines just beyond the leading edge corners below the stagnation point height bend slightly to accommodate for the horseshoe vortex that wraps around the base junction of the prism. The streamlines otherwise move outward from a vertical separation line along the symmetry midline in the spanwise direction slightly inclined towards the free end surface until a height of around $z/D = 2$. Above this height, the separating line vanishes and the streamlines follow a diverging pattern, some of which also begin moving towards the free end of the prism. Incidentally, this is also the height above the ground plane, where the foci of the symmetric vortex structures in the horizontal planes (Figure 4.6) become less pronounced. Thus, the horizontal component of velocity in the planes between $z/D = 0.5$ and $z/D = 2$ is primarily responsible for the formation of these symmetric vortex structures in the horizontal planes. Above $z/D = 2$, the streamlines develop stronger vertical velocity components that then contribute to the separating shear layer from the free end leading edge of the prism.

On the side prism surface (Figure 4.9(b)), the flow is dominated by a strong reverse flow due to the combined contribution of the mean recirculation zone (B_t vortex) close to the free

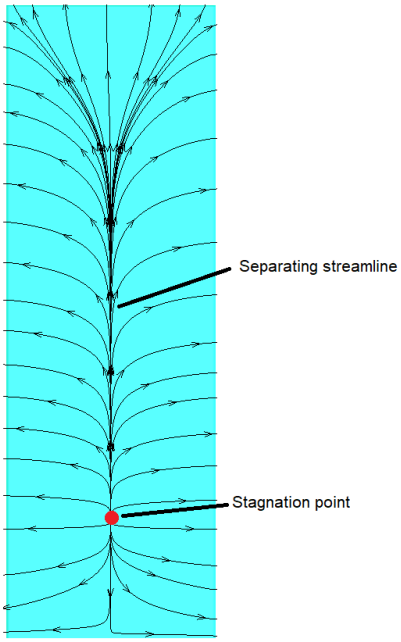

(a) - Front surface - x/D = -0.51

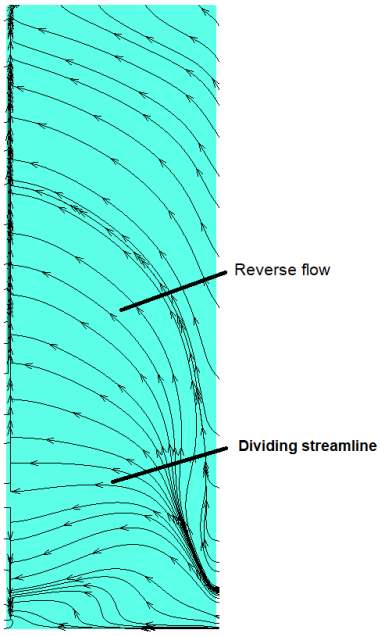

(b) - Side surface - y/D = -0.51

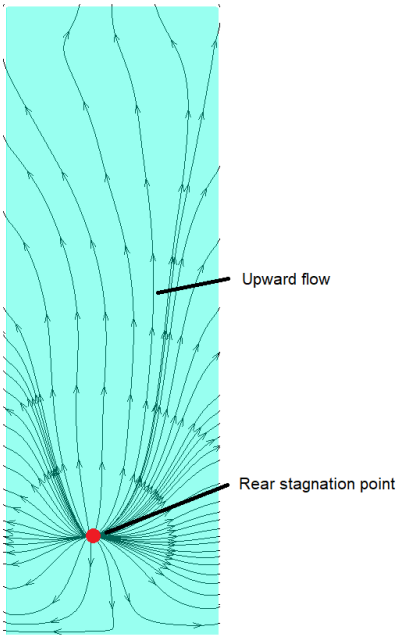

(c) - Rear surface - $x/D = 0.51$

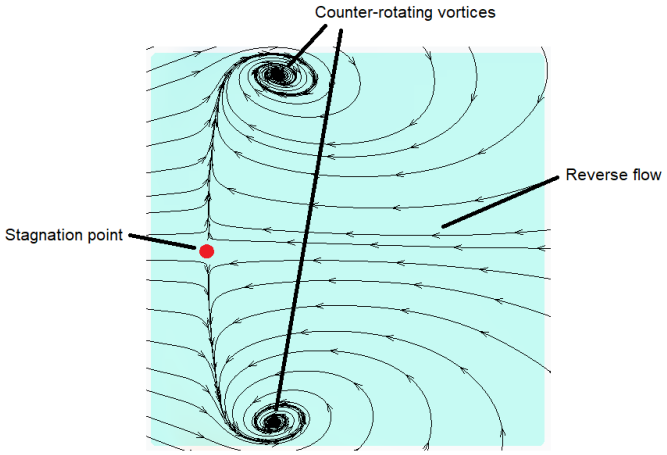

(d) - Top surface - $z/D = 3.01$

Figure 4.9: Surface streamlines based on the planar velocity components near the respective faces of the prism: (a) front face as viewed from upstream (x/D = -0.51, (b) side face (y/D = -0.51), (c) rear face as viewed from downstream ($x/D = 0.51$, and (d) top face ($z/D = 3.01$) as viewed from the top of the prism

end, and the junction vortex (N_w vortex) close to the ground plane. A dividing streamline closer to the ground plane at a height similar to where the stagnation point on the front face is seen (i.e. $z/D = 0.5$) separates the region of predominantly upward moving reverse flow above it, and downward moving reverse flow below it. The reverse flow, as seen earlier in Figure 4.7 and Figure 4.8 is seen due to reverse flow separation from the trailing edge corners of the prism. The reverse flow then meets another dividing streamline near the leading edge corner of the prism, which divides the region of freestream flow separating from the leading edge and the reverse flow. This dividing streamline runs almost parallel with the leading edge corner until it bends towards the freestream direction close to the free end leading edge corner. Close to the ground plane, a weak development of a vortex structure is seen, likely indicating a component of the horseshoe vortex that forms around the base junction.

On the rear surface of the prism (Figure 4.9(c)), a stagnation point is once again found close to the ground plane at a height of $z/D = 0.5$. The centre has been shown to be slightly off the vertical symmetry line, but that may be because the mean flow was computed over a slightly incomplete period of flow. The flow above the stagnation point moves predominantly in the upward direction, as part of the vertical recirculation zone seen in Figure 4.5. The height of this stagnation point also matches the height $z/H = 0.5$ below which the junction vortex (N_w vortex) is seen in the vertical symmetry plane (Figure 4.5).

The free end face (Figure 4.9(d)) is also dominated by reverse flow coming from the sides of the prism free end towards the centreline and the leading edge. A separation line is seen on either side of the free end centreline along the free end leading edge. This line separates the freestream flow upstream and the reverse flow above the free end of the square prism. A pair of counterrotating vortices are formed close to the leading edge corners of the prism. A stagnation point is also found at the centre of the free end leading edge.

The streamline plots show remarkable consistency with the recent numerical studies with similar flow configurations (e.g. Saha [73] for AR = 3 at Re = 250, and Zhang *et al.* [101] for AR = 4 at Re = 500). There are also similarities of the reverse flow characteristics with experimental studies of Sumner *et al.* [86] (for AR = 3 at Re = 4.2×10^4).

4.4 Conclusions

The wake of a surface-mounted square prism of aspect ratio AR = 3 at the Reynolds number $\mathrm{Re}_D = 500$ was analyzed using LES. Of interest was to explore the 3D mean flow features, the reasons for their formation and interaction with each other. 50,000 instantaneous snapshots spanning approximately ten shedding cycles was used to compute the time-averaged flow field using a finite-volume formulation. The Q-criterion was used to extract vortex structures in 3D and to determine regions of interest in the flow field. 2D planes of vectors and vorticity contours was used to develop additional insight on the smaller-scale structures. Flow topologies and additional features like foci of rotational structures, saddle points and stagnation points were analyzed using streamline plots. A summary of the conclusions are as follows:

1. The mean flow field is highly three-dimensional, and characterized by a pair of symmetric tip vortices emanating from the free end and the upper sides close to the free end of the prism. These appear to propagate downstream into the wake away from the symmetry mid-plane, towards the ground plane. Another symmetric system of horseshoe vortices (necklace vortices) is also seen around the base junction of the prism. These are seen to move away from the symmetry plane and away from the ground plane as it moves downstream. However, unlike the tip vortices, these diffuse quickly in the near-wake and are not visible in the far-wake. There is also a separating shear layer above the free end of the square prism which does not reattach to the free end and encloses a mean recirculation zone in the spanwise direction just downstream of the free end trailing face of the prism. This separating shear layer then moves downstream and attaches to the ground plane in the form of a separating streamline. Additional separating shear layers from the sides of the prism go on to form a symmetric pair of longitudinal vortices indicating the presence of Kármán vortex shedding in the wake.

2. On further analysis of the mean flow field on the various planes, additional structures are seen above the free end of the square prism, including a symmetric pair of edge vortices due to the reattachment of the upward flow from the side-walls of the prism on the free end. These structures interact with the separating shear layer in the freestream direction and form another pair of vortices that quickly diffuse downstream in the near wake above the free end. There is evidence that the flows from the side walls close to the

free end move downstream, and form the mean tip vortices. Between these vortices is a strong region of downwash flow, likely coming from the vertical recirculation zone (B_t vortex). In the vertical planes, the horseshoe vortex near the upstream wall junction and another junction vortex (the N_w vortex) was seen near the downstream wall junction. The N_w vortex is formed due to the reverse flow from the bottom of the recirculation zone above it interacts with the adverse pressure gradient of the wall junction and the Reynolds shear stresses from the ground plane. In the horizontal planes, the location of the foci of the symmetric Kármán vortex shedding is seen to vary along the prism height. The foci seem to be furthest downstream in planes away from the free end and the ground plane. The width of the separating shear layers from the sides have also been shown to vary with prism height.

3. Streamlines on the surface of the square prism reveal a stagnation point at the leading edge of the prism close to the ground plane. Flow below this stagnation point contribute to the formation of the horseshoe vortex system near the wall junction, while the upward moving flow separate from the sides and the free end of the prism creating separating shear layers. A pattern of reverse flow is seen on the side walls of the prism enclosed by the separating shear layer. A separating line of flow is also seen along the leading edge corner of the prism and close to the base junction. The reverse flow predominantly moves towards the free end, completing the vertical recirculation zone in the near wake of the prism, with its foci close to the free end of the prism. A stagnation point is also seen on the rear face of the square prism near the base junction, and marks the separation between the mean recirculation zone (the Bt vortex) above it, and the junction vortex (the Nw vortex) below it. On the free end surface, a pair of counterrotating vortices are seen above the leading edge corners of the prism. A separation line along the symmetry line is also seen with a stagnation point and saddle point located along the symmetry line at the leading edge and trailing edge respectively.

Similar studies on the instantaneous and phase-averaged flow features may also be of interest to develop a better understanding of the smaller-scale turbulent flow features that contribute to the overall dynamics of this complex flow field.

Chapter 5

Three-dimensional proper orthogonal decomposition in the wake of a surface-mounted finite-height square prism

Preamble

This study aims to fulfill the fourth objective of the thesis mentioned in Chapter 1.2 and pursue the fourth research contribution outlined in Chapter 1.3. The contribution of this chapter to the overall study is to examine whether improved flow visualization tools like three-dimensional proper orthogonal decomposition (3D POD) and localized vortex identification methods like the Q-criterion are successful in capturing instantaneous turbulent structures and tracking their motion in the wake of a surface-mounted finite-height square prism.

The wake of a surface-mounted finite-height square prism of AR = 3 at a Reynolds number of $\mathrm{Re}_D = 500$ was analyzed using three-dimensional (3D) proper orthogonal decomposition (POD). Data was obtained using large eddy simulation on a sub-domain of interest in the wake using 1000 instantaneous 3D velocity snapshots spanning ten vortex shedding periods. Of interest would be to investigate the energy distribution of the POD modes and compare them with available literature on 2D POD. Structures in the higher energy modes will be compared to similar structures seen in the phase-averaged representations (i.e. the alternating half-loop structure) of this flow field. An investigation of the POD temporal coefficients will reveal the periodic characteristics and phase representations of this flow field.

The development of the large eddy simulation code was done by Nader Moazamigoodarzi. The development and implementation of the 3D POD code, the subsequent analysis and discussion of the results were done by Rajat Chakravarty. This was subsequently edited by Prof. Bergstrom and Prof. Sumner.

A similar version of this chapter is in preparation for submission as:

1. R. Chakravarty, D. J. Bergstrom and D. Sumner, 'Three-dimensional proper orthogonal decomposition in the wake of a surface-mounted finite-height square prism', *Physics of Fluids*

Parts of this chapter were presented at the following conferences:

1. R. Chakravarty, N. Moazamigoodarzi, D. J. Bergstrom and D. Sumner, 'Use of Proper Orthogonal Decomposition to investigate the turbulent wake of a surface-mounted finite square prism', *9th International Symposium on Turbulence and Shear Flow Phenomena (TSFP9)*, pp. 1-6, June 30 - July 3, 2015, Melbourne, Australia.

2. R. Chakravarty, N. Moazamigoodarzi, D. J. Bergstrom and D. Sumner, 'Visualization of the Flow in the Wake of a Finite-height Square Prism', *Fluid-Structure-Sound Interactions and Control*, pp. 181-186, July 5-9, 2015, Perth, Australia.

3. R. Chakravarty, N. Moazamigoodarzi, D. J. Bergstrom and D. Sumner, 'Use of three-dimensional Proper Orthogonal Decomposition to study the wake of a surface-mounted finite-height square prism', *Fluid-Structure-Sound Interactions and Control*, August 21-24, 2017, Tokyo, Japan.

Abstract

The wake of a surface-mounted finite-height square prism of AR = 3 at a Reynolds number of $\mathrm{Re}_D = 500$ was analyzed using three-dimensional (3D) proper orthogonal decomposition (POD). Of interest was to investigate the dominant instantaneous flow structures downstream of the near wake behind the square prism. In the subdomain of interest, 1000 velocity snapshots spanning approximately 10 cycles of flow based on a Strouhal number St = 0.12 were obtained using Large Eddy Simulation (LES). The time-averaged flow field revealed a pair of tip vortices originating from the prism free end, and layers of horseshoe (necklace) vortices around the prism-plane junction above the ground plane. Both these features have been shown to diffuse into the wake away from the vertical symmetry plane. The POD energy modes revealed a very gradual decrement in energy across the modes. Evidence of periodicity in the flow field was confirmed by the sinusoidal variation (although with varying amplitudes) of the first two POD temporal coefficients. The first three POD energy modes revealed a dominance of streamwise structures, some of which bifurcate into two symmetric streamwise structures on either side of the vertical symmetry plane. These structures resemble the traversing streamwise connector strands that bend into the principal cores of the alternating half-loop structures. This was further verified by the instantaneous and reconstructed flow fields observed in two regions opposite in phase having high turbulent kinetic energy (TKE). Consequently, this study substantiates instantaneous flow structures previously speculated heuristically in 2D planes and strengthens the case for using 3D POD in studying instantaneous flows.

Keywords: wake, square prism, proper orthogonal decomposition, half loop

5.1 Introduction

The flow over surface-mounted finite-height bluff bodies is of considerable interest to industry for its applications in aircraft landing gear, buildings, and heat exchangers, among others. An enhanced understanding of these flows is useful for motivating improved designs for these structures. The flow specifically over a finite-height square prism mounted on a ground plane also has significant research appeal due to the nature of its complex flow field. There are various complex turbulent features in space and time seen around the prism and in the wake

interacting with each other.

The flows over two-dimensional (2D or infinite) square prisms have been extensively studied [2, 4, 38, 46, 51]. Depending on the Reynolds number of the flow, several flow regimes exist [2]. At Re ¡ 50, the flow is steady with no Kármán vortex shedding. For Re ¿ 50, fhe flow becomes unsteady, and is characterized by separation at the leading edge corners of the square prism leading to the formation of alternate Kármán vortex shedding. For Re ¿ 160, the flow transitions into a three-dimensional field with the onset of streamwise vortices [2]. The frequency of vortex shedding (or Strouhal number) has been shown to vary with the angle of attack of the square geometry and the Reynolds number of the flow (based on the side length) [55, 58, 79]. Lesser attention has been paid to investigate the flow over a three-dimensional (3D or finite-height) square prism [74, 75, 76]. Unlike, the 2D square prism, the flow field generated by a surface-mounted square prism is strongly three-dimensional owing to the additional presence of the ground plane and the free end [8, 18, 72, 73, 77, 86, 95, 101].

For a surface-mounted finite-height square prism of height H and width D submersed in a freestream flow velocity U_∞, the flow features have been shown to be a function of the aspect ratio of the square prism (defined as AR $= H/D$) [86], the Reynolds number of the flow based on the prism width D (defined as $\mathrm{Re}_D = U_\infty D/v$, where U_∞ represents the freestream velocity) [101], the boundary layer thickness (defined as δ/D or δ/H, where δ represents the boundary layer thickness), and the angle of incidence of the square prism relative to the freestream flow [35, 56, 90, 98]. A schematic summary of the flow features seen in the time-averaged flow field through various studies in the literature on this flow field is shown in Figure 5.1.

Above a critical Reynolds number (i.e. Re_D = 150-200), the flow remains largely invariant, and is characterized by the formation of tip vortices at the free end, and a series of necklace vortices (or horseshoe vortices) around the prism near the wall-junction of the prism [101]. At higher aspect ratios, the flow separates at the side leading edge of the prism and forms an alternate vortex shedding pattern in the wake, called the Kármán vortex street [47]. However, there exists a critical aspect ratio $\mathrm{AR}_{\mathrm{critical}}$, below which the shedding shifts from the Kármánrman type shedding to an arch-vortex type shedding [95]. The value of $\mathrm{AR}_{\mathrm{critical}}$ have varied across studies as it is a function of the inflow conditions and boundary layer thickness [18,34,60,96], but most recent studies report values between $\mathrm{AR}_{\mathrm{critical}} = 3$ to 5 [86].

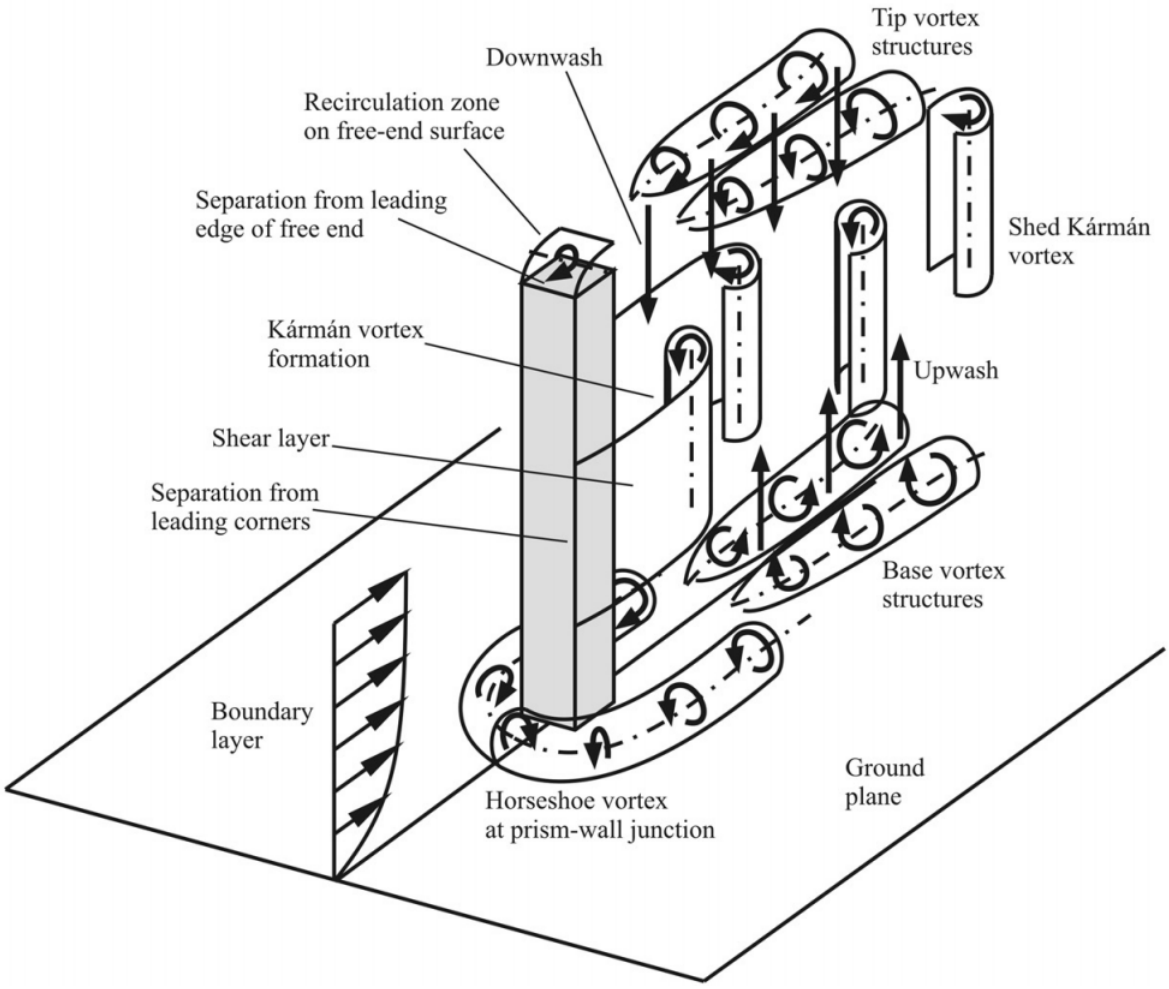

Figure 5.1: Flow around a surface-mounted finite-height square prism for $AR > AR_{critical}$.

Above the critical aspect ratio, an additional pair of base vortices is also seen in the wake, moving from a dipole wake configuration (due to the pair of tip vortices) to a quadrupole wake configuration (due to both pairs of tip and base vortices).

However, the mean flow field is not sufficient to capture the instantaneous turbulent flow features and the periodic characteristics of the flow field that contribute to these mean flow features. Recent experimental studies therefore have also looked at the instantaneous and phase-averaged representations of the flow field [8, 18, 71, 72, 73, 77, 101]. While heuristic approaches have identified the different regions of the prism wake, some recent studies have attempted to propose a unifying flow theory based on the dynamics of the vortical structures shed from the prism.

Wang and Zhou [95] (for Re = 9300, AR = 3 to 7, $\delta/D = 1.35$) suggested that the instantaneous flow tends to form arch-type vortices regardless of aspect ratio and is characterized by two spanwise vertical legs perpendicular to the ground plane and a connecting horizontal bridge at the free end. Based on probabilistic analysis and two-dimensional (2D) Particle Image Velocimetry (PIV) measurements, they developed a model of an outward-bulging arch vortex, which explains some of the mean flow characteristics in the wake downstream of the finite prism.

More recently, Bourgeois *et al.* [8] (for Re = 12000, AR = 4, $\delta/D = 0.18$) proposed a different flow paradigm, namely the alternating half-loop vortex structure shed by the finite square prism into the wake. They indicated that the mean flow structure of the wake could be explained by averaging the quasi-periodic half-loop structure over the shedding period. A schematic of the alternating half-loop vortex structure is given in Figure 5.2. A single half-loop structure is made up of a principal core which is aligned approximately perpendicular to the ground plane and a streamwise connector strand. The strand connects the top of the principal core to the base of the principal core of the next half-loop located upstream. Since the principal cores occur on alternate sides of the wake, each connector strand stretches diagonally across the wake, with an orientation which also alternates. A detailed description of the half-loop and educed phase-averaged structure can be found in Bourgeois *et al.* [8].

Both of the studies above considered finite square prisms of larger aspect ratio for relatively higher Reynolds numbers. Saha [73] studied the flow past a finite-height surface-mounted square prism using direct numerical simulation (DNS) at a lower Reynolds number of Re_D = 250 for four different aspect ratios: AR = 2, 3, 4 and 5. Without trying to propose a unifying theory, Saha [73] observed tip vortices, base vortices and horseshoe vortices in the prism wake regardless of aspect ratio. For AR > 2, the near-wake showed a symmetric shear layer separation while the far-wake showed greater anti-symmetric vortex shedding characteristics. Zhang *et al.* [101] also studied the flow past a finite-height square prism of AR = 4 for six different Reynolds numbers, Re_D = 50, 100, 150, 250, 500 and 1000. They proposed three kinds of spanwise vortex shedding characteristics called the C, Reverse-C and Hairpin Vortex Model, which suggested some features in agreement with the model suggested by Wang and Zhou [95].

Instantaneous flow fields however are difficult to analyze as they yield several flow struc-

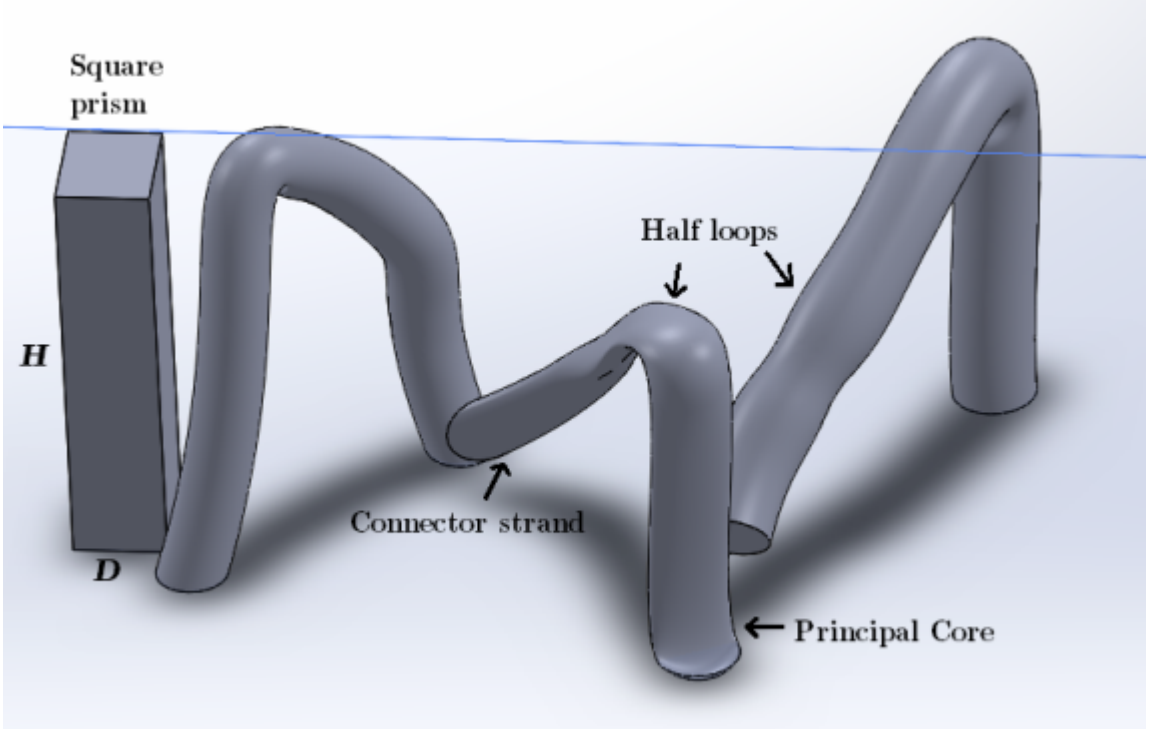

Figure 5.2: Schematic for the alternating half loop structures in the wake of a surface-mounted square prism (based on the model by Bourgeois *et al.* [8]).

tures at different spatio-temporal scales. To isolate the dominant instantaneous flow structures involves studying a large number of instantaneous flow fields over many cycles of flow which can be quite laborious and computationally intensive. A statistical technique called Proper Orthogonal Decomposition (POD) [5,48] has been increasingly used in the literature to extract the most energetic structures in turbulent flows and reconstruct a lower-dimensional representation of the instantaneous flow using an orthogonal transformation of the flow properties. Instantaneous flow fields obtained from both experiments and numerical simulations have often been post-processed using the snapshot POD technique [78].

The snapshot POD has been used to study a variety of flow fields such as jets [28, 29, 64], backward-facing step flows [43] and around 3D square prisms [10, 40, 92, 94] among others. These studies have successfully been able to extract the periodic characteristics of the flow using scatter plots of the temporal coefficient obtained from the POD analysis [92,94]. In the case of 3D square prisms, Bruno *et al.* [10] (AR = 0.25, Re = 4×10^4) showed the presence of a recirculation zone (called the secondary vortex) just behind the front corner of the prism, a primary vortex above the free end, and reverse flow behind the rear corner of

the free end. Kawai *et al.* [40] (AR = 2.7, Re = 1.56×10^4, $\delta/D = 0.3$) has demonstrated the presence of arch in the instantaneous reconstructions of the near-wake flow using a few energy modes. However, a lot of studies have focused on the 2D snapshot POD results [40, 92, 94] while the 3D flow structures using POD have not been sufficiently researched nor well understood. Furthermore, studies employing 3D POD on square prisms have primarily focused on structures around the square prism, and a study on the wake of square prisms provides for a novel research contribution.

In the present investigation, a relatively short prism is considered, i.e. AR = 3, and a low Reynolds number, i.e. $\mathrm{Re}_D = 500$. This is in view of capturing the transitional characteristics of the flow field around $\mathrm{AR}_{\mathrm{critical}}$. The prism is immersed in a thin laminar boundary layer. The resolved-scale velocity and pressure fields are obtained from a large eddy simulation (LES) of the flow. To cover approximately 10 shedding cycles of data, the time-averaged 3D flow field using 50000 instantaneous snapshots, and a subset of 1000 instantaneous flow fields through the 3D snapshot POD analysis in a selected sub-domain of interest in the wake of the square prism will be analysed in this study. Of interest is to provide additional insight into the 3D flow features in the wake of a surface-mounted square prism immersed in a thin boundary layer with minimal inflow turbulence intensity. Both the POD and iso-surface visualisation based on the Q-criterion will be used to draw insight into the vortical structures shed by the prism into the wake and explore its periodic behaviour. It is also hoped that the 3D POD analysis in the wake may provide a better understanding of the flow features at various scales that contribute to the mean and conditionally averaged flow configuration.

5.2 Numerical Scheme and Post-processing Methodologies

A finite-volume discretization of the filtered Navier-Stokes equations and continuity equation was used as the computational model for this flow. The momentum equations were discretized in time using the Crank-Nicholson method, and the subsequent set of linear equations was solved using the two-step fractional step method. An algebraic multigrid method was used to accelerate the solution of the pressure-correction equation. The subgrid-scale (SGS) stress terms were modeled using a localised Dynamic Smagorinsky model. A structured, Cartesian grid with $128\times96\times144$ control volumes in the x (freestream), y (transverse) and z (spanwise) direction, respectively, was used to discretize the flow domain. By convention the flow

velocities and vorticities in the (x, y, z) directions are defined as (u, v, w) and (ω_x, ω_y, ω_z), respectively.

Based on the freestream flow velocity of air of $U_\infty = 0.375$ m/s and prism width $D = 0.02$ m, the Reynolds number for the flow was set as $\mathrm{Re}_D = 500$. The height of the prism mounted on the ground plane was $H = 0.06$ m, which yields the aspect ratio of the prism to be AR = 3. The prism was located approximately $3D$ from the inlet plane. The overall dimensions of the flow domain was 0.32 m ($16D$), 0.14 m ($7D$) and 0.12 m ($6D$) in the streamwise, transverse and spanwise directions, respectively. As the Dynamic Smagorinsky model was used, the time step changed with every iteration. Through a CFL condition, the time step was estimated to be around 10^{-4} seconds. The approaching boundary layer on the ground plane was laminar and relatively thin ($\delta/D = 0.5$). The origin of the frame of reference used was set at the centre of the square cross-section at the wall-junction of the prism. Based on a Strouhal number St = 0.11 for this flow field [86], 50,000 realizations almost equally spaced in time (i.e. around 10^{-4} seconds between each snapshot) were used to span approximately 10 shedding cycles of the flow to compute the mean flow field.

The snapshot POD analysis of the instantaneous velocity fields was taken in a reduced 3D domain in the wake to decrease computational rigour of the POD analysis. However, the region of interest for POD analysis was specifically selected to observe the region of flow where interaction of the major flow features like the tip vortices, downwash and longitudinal vortex shedding are seen in the mean flow field. Based on the literature of the mean flow field where these interactions have been observed to occur [8, 73, 77, 95, 101], the flow domain selected was a structured Cartesian domain with 20×50×50 control volumes in the x (freestream), y (transverse) and z (spanwise) directions, respectively. This domain spread approximately $1.5D$ to $4.5D$ along the freestream direction (x-direction), -0.6D to 0.6D symmetrically along the transverse direction (y-direction) and in the upper half of the prism wake from $1.5D$ to $3D$ along the spanwise direction (z-direction). A schematic of the numerical set-up and the POD domain has been shown in Figure 5.3.

The POD methodology (further elaborated in Berkooz *et al.* [5]) can be used to extract motions of different scales within the evolving dynamics of a flow. The snapshot POD method of Sirovich [78] is applied in the present study to decompose the time-dependent fluctuating part of the flow field into an orthonormal system of spatial velocity modes ($\varphi_m(x)$) and

associated temporal coefficients $a_n(t)$.

The autocovariance matrix C of the fluctuating velocity field is decomposed into an orthonormal system by implementing an eigenvalue problem with eigenvalues and eigenvectors λ^i and A^i, respectively as $CA^i = \lambda^i A^i$. The eigenvectors are then normalized, as shown in Equation 2.1.

$$\varphi^i = \frac{\sum_1^N A_n^i u^n}{\left\| \sum_1^N A_n^i u^n \right\|}, \quad i = 1, 2, \ldots N \tag{5.1}$$

The relative magnitude of the eigenvalues (λ_m) determines the respective energy contribution in each mode. The temporal coefficients are computed using a matrix multiplication $a^n = [\varphi^1, \varphi^2 \ldots \varphi^N] \times u^N$. Finally, the POD modes taking a subset of M snapshots are computed as

$$u^n = \sum_{i=1}^{N} a_i^n \varphi^i \tag{5.2}$$

A set of 1000 snapshots of the time-resolved fluctuating velocity field equally distributed in time across approximately ten shedding cycles of the flow was used to provide the data base for POD analysis. The temporal coefficients obtained from the POD analysis were also analysed to investigate the periodic features of this flow.

Chong *et al.* [14] defined vortices as regions where the local velocity gradient tensor has complex eigenvalues. This criterion is also called the Q-criterion. In this study, 3D velocity field data were used to obtain localized velocity gradients. Regions where complex-conjugate eigenvalues were found, were concluded to contain localized vortex structures.

5.3 Results and Discussion

As the simulation for the present study covered approximately ten cycles of data, this section will briefly touch on the results of the 3D mean flow field. These results are not only useful to benchmark the mean flow characteristics seen in this study with other studies in the literature, but also provide a basis to enhance the understanding of the POD results. This will be followed by the POD results in the reduced domain of interest.

5.3.1 Mean Flow Results

Figure 5.4 shows the 3D time-averaged flow field using an iso-surface of the Q-criterion contoured with the normalized freestream velocity u/U_∞. The flow is characterized by the inflow separating at the leading edges of the square prism producing shear layers on the side walls and above the free end. The separating shear layers from the side walls closer to the free end of the prism form a pair of symmetric tip vortices moving in an inclined fashion towards the ground plane and away from the vertical symmetry plane of the square prism. It does appear from the iso-surfaces, however, that the formation of the tip vortices is largely driven by the separating shear layer from the sides of the prism near the free end and the downwash from the separating shear layer coming from the free end leading edge. The flow configuration represents the dipole wake configuration (seen previously by Sattari *et al.* [77] and Zhang *et al.* [101] for similar aspect ratio prisms) suggesting that this prism is below the critical aspect ratio $\mathrm{AR}_{\mathrm{critical}}$. In addition, a symmetric distribution of horseshoe vortices around the wall-junction at the base of the prism is also seen. These are seen to loop around the leading face and the sides of the prism, and begin moving away from the symmetry mid-plane of the prism as they diffuse downstream. Several small scale structures are also seen above the ground plane in the prism wake, but it remains inconclusive from this figure on whether they represent base vortices.

5.3.2 POD Results

The snapshot POD methodology was used to analyze 1000 instantaneous snapshots obtained from the 3D sub-region of the flow highlighted in Figure 5.3 in the wake of the square prism at a frequency of 200 Hz. Based on the frequency obtained from the power spectrum of the pressure data from the six probes placed on the side walls of the prism (not shown), which was in agreement with available Strouhal number data in the existing literature for wall-mounted square prisms of similar aspect ratios and Reynolds numbers, 1000 snapshots were expected to cover approximately ten shedding cycles. POD analysis was also performed on a reduced basis of 300 snapshots (i.e. across 3 shedding periods) and no appreciable differences were seen in the large-scale structures at the higher energy modes. Thus, the results of ten periods of data have been shown in the present study without loss of accuracy. Figure 5.5 shows the energy distribution as a percentage of the overall turbulent kinetic energy (TKE)

captured by every POD mode (defined as $\lambda_i/\sum\lambda$).

The first three energy modes capture around 12.5%, 10.4% and 5% of the overall energy respectively, and are of interest for studying the dominant energetic structures. The first 11 energy modes capture about 50% of the overall energy, with about 180 modes cumulatively capturing 99% of the overall energy. The energy capture percentages for each mode are substantially lesser than similar studies made by van Oudheusden *et al.* [92] (AR = 11.7, Re = 1×10^4) and Wang *et al.* [94] (AR = 7, Re = 9300, $\delta/D = 1.35$) on 2D planes for square prism flow fields. This may be attributed to the fact that the introduction of an additional dimension of velocity data may provide for a more even distribution of turbulent kinetic energy across the energy modes. Furthermore, the 3D domain selected for POD analysis in this study is located in a region with high turbulence activity, and it thus expected that the POD modes will capture a variety of structures across various length scales. This is different from the 2D snapshot domains taken in van Oudheusden et al. [92] and Wang et al. [94], which include a substantial region closer to the edges of their experimental flow domains which consist of largely unperturbed freestream velocity. The gradual distribution of energy across the POD modes is evidence of the fact that the flow in the selected domain is made up of several small-scale turbulent structures that have been adequately distributed across the energy modes.

Figure 5.6 shows the first POD energy mode using an iso-surface of Q-criterion contoured with normalized fluctuating velocity u^* (i.e. $u^* = (u\text{-}u_{mean})/U_\infty$). The first mode is characterized by several structures, most significantly a single large-scale vortex filament stretching from about $x/D = 2$ to 3.5, before breaking up into two symmetric vortex cores moving downstream. In addition, there is also evidence of some symmetric structures at the sides of the domain, and some vortex structures at the bottom of the POD domain moving downstream. Based on the location of the onset of the symmetric vortex cores in both the streamwise and transverse directions, this pair of structures shows remarkable resemblance with the tip vortices seen in the mean flow field (Figure 5.4). This is an interesting result as the first POD energy mode using bases of fluctuating velocity vectors (i.e. with the mean flow removed) was still able to capture a flow feature similar to what has been seen in the mean flow field. Several other studies also show the dominance of the time-averaged flow field structures in the first energy mode [92, 94].

There are additional symmetric vortex structures on the upper sides of the domain entering from the lower wake of the prism moving upwards unconnected to the streamwise vortex core. These structures likely indicate additional structures coming from the sides of the prism. As these approach the height of the prism, they begin to arch downwards towards the freestream direction, likely due to the influence of the freestream flow coming from above the prism. An additional structure at the base of the POD domain is seen originating from the junction of the streamwise vortex core and the pair of tip-vortex-like structures moves towards simultaneously towards the ground plane and the streamwise direction. The streamwise velocity contours indicate an antisymmetric tendency of velocity with positive and negative u-velocity distributed across the vertical symmetry plane (i.e. $y/D = 0$).

Figure 5.7 shows the second POD energy mode using an iso-surface of Q-criterion contoured with normalized fluctuating velocity u^* (i.e. $u^* = (u\text{-}u_{mean})/u_\infty$). The second energy mode shows some similar and some contrasting flow features from the first energy mode. The flow is mainly characterized by a single streamwise vortex core at the centre of the POD domain moving downstream in the wake. This streamwise vortex largely maintains its vertical height downstream in the POD domain.

Additional structures on the sides of the POD domain, similar to the first POD energy mode, are also seen in the second energy mode. Similar to the first energy mode, these structures on the side also move upwards in the wake and then arch in the freestream direction due to the influence of the freestream flow above. Similar to the first energy mode, the streamwise velocity contours once again indicate an antisymmetric velocity tendency across the vertical symmetry plane. The u-velocity distribution on the symmetric structures coming from the sides of the prism is opposite to that seen in the first energy mode. Given the first two energy modes have little difference in TKE content between them, the opposite alignment of velocity on the same iso-surfaces across the two highest energy modes indicate a periodic shedding tendency similar to longitudinal Kármán vortex shedding from the sides of the square prism.

Figure 5.8 shows the third POD energy mode using an iso-surface of Q-criterion contoured with normalized fluctuating velocity u^* (i.e. $u^* = (u\text{-}u_{mean})/U_\infty$). As expected, the third energy mode having lesser energy reveals more smaller scale structures compared to the first two energy modes and is more complex. The flow field is characterized by smaller streamwise

structures at the base of the POD domain coming from the lower wake of the square prism as well as some structures on the side of the domain (i.e. around the y/D = -0.5 plane). The structures in the lower wake do not cross the verical symmetry plane, unlike the first energy mode. From the velocity contours, once again we notice an antisymmetric distribution of velocity is noticed in both the streamwise direction and the opposite direction across the symmetry plane.

Figure 5.9 shows the variation of the first and second temporal coefficient across snapshots (Figure 5.9(a)) and with each other (Figure 5.9(b)). A periodic tendency in the temporal coefficients is indicative of periodic flow behaviour in the wake of the surface-mounted square prism [44]. The period of oscillation yielded a time period of approximately 0.5 seconds (i.e. 2 Hz), which yields a Strouhal number based on prism width and freestream velocity as St = 0.106. This value is similar to values seen in the literature for this flow field, as discussed earlier, and further validates the estimated selection of POD bases used for analysis to cover at least 10 shedding periods. This also corroborates that the POD temporal coefficients can be used to verify the periodic behavior of the flow field and provide its phase characteristics.

The second temporal coefficient also shows similar periodicity, though out of phase with the first temporal coefficient by about a quarter of the time period. It is thus expected that these POD modes should show structures that match this phase difference. However, as there isn't a consistent sinusoidal nature to the temporal coefficients across the periods, this indicates that periodic phenomena at other frequencies may also be present in the flow field, also seen a similar study [94].

Figure 5.9(b) shows the variation of a_2^* with a_1^* (i.e. $a_i^* = a_i/\sqrt{2\lambda_i}$ where a_i and λ_i represent the i-th temporal coefficient and POD eigenvalue, respectively) (based on an empirical method by van Oudheusden *et al.* [92]). This creates a scatterplot of points, each of which corresponds to a particular snapshot. In previous studies [52, 92, 94], they found these points to lie around a unit circle in a smaller annular region with little scattering. However, these studies were only done with strongly 2D flow fields. It is expected that for more complicated and strongly 3D flows at higher Reynolds numbers, this scatter plot will be more dispersed [94]. This can also be seen from the energy modes, where, unlike other studies, the first few energy modes do not capture a majority of the TKE in the flow field and the characteristics of several energy modes are required to define the dominant energetic structures

in the flow field.

The present study suggests that three-dimensional flow fields at non-laminar Reynolds numbers provide more complexity in yielding reduced-order models. The radius of specific points (i.e. $\sqrt{a_1^{*2} + a_2^{*2}}$) on this scatter plot is directly proportional to the TKE from the higher energy modes, and can thus be used as a metric to categorize the instantaneous snapshots that represent these points accordingly [94]. Furthermore, the angle made by these points with respect to the coordinate axes conveys the phase position of these flow features. It is thus of interest to take two instantaneous snapshots with large radii diametrically opposite in this scatter plot to contrast phase characteristics in the wake.

Figures 5.10 looks at the instantaneous (Figure 5.10(a) and 5.10(c)) and reconstructed (Figure 5.10(b) and 5.10(d)) 3D iso-surfaces of the Q-criterion contoured with normalized u-velocity (u/U_∞) for two arbitrary points that are exactly opposite in phase as per the scatter plot of Figure 5.9(b). The reconstructed fields have been obtained using the first 20 energy modes on an interpolated uniform 20×20×20 mesh to enhance the focus on the large-scale structures. Care has been taken to select points outside the unit circle to extract structures that have a high overall contribution to the TKE.

Figure 5.10(a) and 5.10(b) show one comparatively large-scale structure combined with several small-scale structures in the lower section of the domain. A priori, the reconstructed fields show good agreement with the instantaneous flow fields with respect to the large-scale structures. The large-scale structure in the reconstruction however lacks accurate definition at its ends, as expected with a reconstruction of using only 20 modes. Furthermore, the interpolation has smoothed these iso-surfaces. The large-scale structure resembles the alternating half-loop structure seen in Bourgeois *et al.* [8] albeit for a higher Reynolds number and aspect ratio in the experiments on the wake of a square prism mounted on the ground plane. This half loop consists of the connector strand seen moving across the vertical symmetry plane of the square prism in an inclined direction away from the ground plane. This connector strand on the top then begins arching towards the ground plane and forms the principal core. The principal core is formed outside this domain and thus cannot be accurately substantiated in this study. However, other features like the alignment and direction of propagation of this vortex core has sufficient similarities to conclude that this represents the half-loop structure.

In instantaneous snapshots following this specific snapshot (not shown), this loop is seen

to move further downstream, followed by the formation of another similar half loop on the opposite side of the symmetry plane (shown in Figure 5.10(c) and Figure 5.10(d)). In addition to the half loop, some evidence of a vortex core is seen further upstream on the other side of the vertical symmetry plane. This represents the onset of the growth of the symmetric half loop on the other side of the symmetry plane (shown in Figure 5.10(c) and 5.10(d)). For the specific location of the POD domain, the centres of these vortex cores are approximately at a distance of 2D in the streamwise direction, which is in good agreement with the phase-averaged vortex shedding results of Sattari *et al.* [77] on this flow field.

From the velocity contours, it appears that the flow accelerates in the freestream direction from the connecting strand towards the principal core region upstream. From an energy standpoint, this result corroborates the findings of the scatter plot of the POD temporal coefficients (Figure 5.9(b)) and the first energy mode (Figure 5.6). The scatter plot indicates that the snapshots with the half loop structures have the maximum TKE. Simultaneously, the first POD energy mode also captures the streamwise vortex structure breaking up into two symmetrical structures across the symmetry mid-plane. The structure of the first POD energy mode can thus be explained as a composite flow structure of a central vortex core breaking up into these streamwise connector strands that lead to the principal cores on either side of the vertical symmetry plane. As these half loop structures move downstream into the wake regardless of whichever side of the vertical symmetry plane, they leave a trace of the streamwise connecting strand moving downstream in the region close to the centre of the given domain. This trace is thus present for a majority of the instantaneous flow snapshots, and thus become the most dominant energetic structure for this specific POD domain.

As the half loop structures move downstream, the streamwise velocity components of this vortex core increase. A region of reverse flow and small-scale vortex cores just upstream and below the connecting strand of the half loop always seems to follow and swerve with the connecting strand across the vertical symmetry plane. From the z/D profiles of mean velocity (Figure 5.5), there is a strong region of reverse flow towards the trailing face of the square prism between the two axisymmetric vortex structures due to the symmetric nature of shedding, as is expected in the mean flow. However, this periodic flutter of reverse velocity across the vertical symmetry plane indicates that this reverse flow is making room for a dominant longitudinal vortex structure covering the spanwise width of the prism. This is

comparable to alternate Kármán vortex shedding seen in the wake of the square prism in planes away from the ground plane and the free end of the prism. The reverse flow is only seen at the base of this domain in the upstream region as it makes room above for the vertical recirculation zone closer to the free end trailing edge, seen in the mean flow field of the vertical symmetry plane (Figure 5.4).

5.4 Conclusions

The wake of a surface-mounted square prism of aspect ratio AR = 3 at the Reynolds number $\mathrm{Re}_D = 500$ was analyzed using LES. Of interest was to explore the 3D mean flow features and the instantaneous flow characteristics using POD. 50000 instantaneous snapshots spanning approximately ten shedding cycles was used to compute the time-averaged flow field, while a subset of 1000 snapshots in a reduced sub-domain in the wake was subsequently used for POD analysis. The following inferences were drawn from the study:

1. 3D POD was able to transform the 1000 instantaneous snapshots into an orthonormal system of energy modes with decreasing energy content. The energy distribution was observed to be far more gradual compared to 2D flow fields seen in the literature, with the first three modes capturing a combined 28% of the total energy. The first energy mode demonstrated two dominant symmetric streamwise structures placed symmetrically about the vertical symmetry plane of the square prism. These pair of vortex tubes was consequently identified as the connecting strands of the streamwise connector strand seen in the instantaneous flow field. It is thus inferred that a complex flow mechanism closer to the base of the prism initiates the onset of these half loop structures. The second energy mode demonstrated a single streamwise vortex core moving downstream. This is indicative of the trace of the streamwise connector strand seen in the instantaneous flow fields that overlap in this region as the half loop structures on either side of the vertical symmetry plane move downstream. Both energy modes also show additional small-scale structures close to the base of the domain, indicative of more turbulent activity coming from the ground plane.

2. The temporal coefficients of the first two POD modes were periodic, and its radial distribution and length of radius on a scatter plot gives a phase representation as well

as the amount of TKE in every instantaneous snapshot. Two such snapshots with higher radii diametrically opposite the unit circle revealed a prominent inclined half loop structure. The connector strand was seen to move across the vertical symmetry plane forming a principal core outside the selected domain. In subsequent snapshots (not shown), these are shown to move downstream in an anti-symmetric fashion, as seen in the literature on the phase-averaged representation of these flows. The reconstruction of this flow field using 20 energy modes largely matched well with the instantaneous snapshots, and successfully isolated the half-loop structure seen in the instantaneous flow field. 3D analysis of a larger wake domain would be helpful in further understanding the origin of these instantaneous structures.

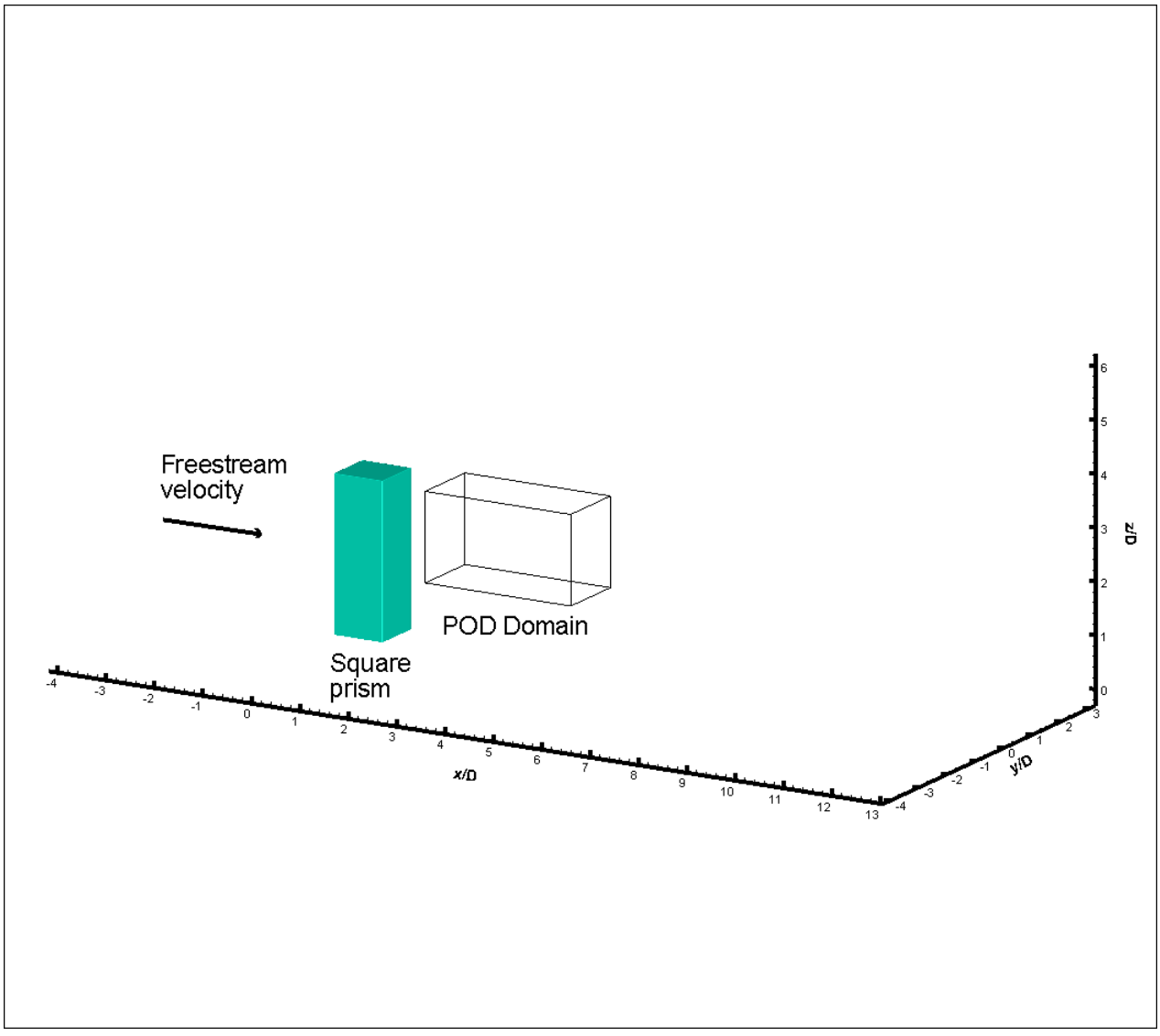

Figure 5.3: Flow domain for the LES analysis of the outer mean flow and the sub-domain for POD analysis.

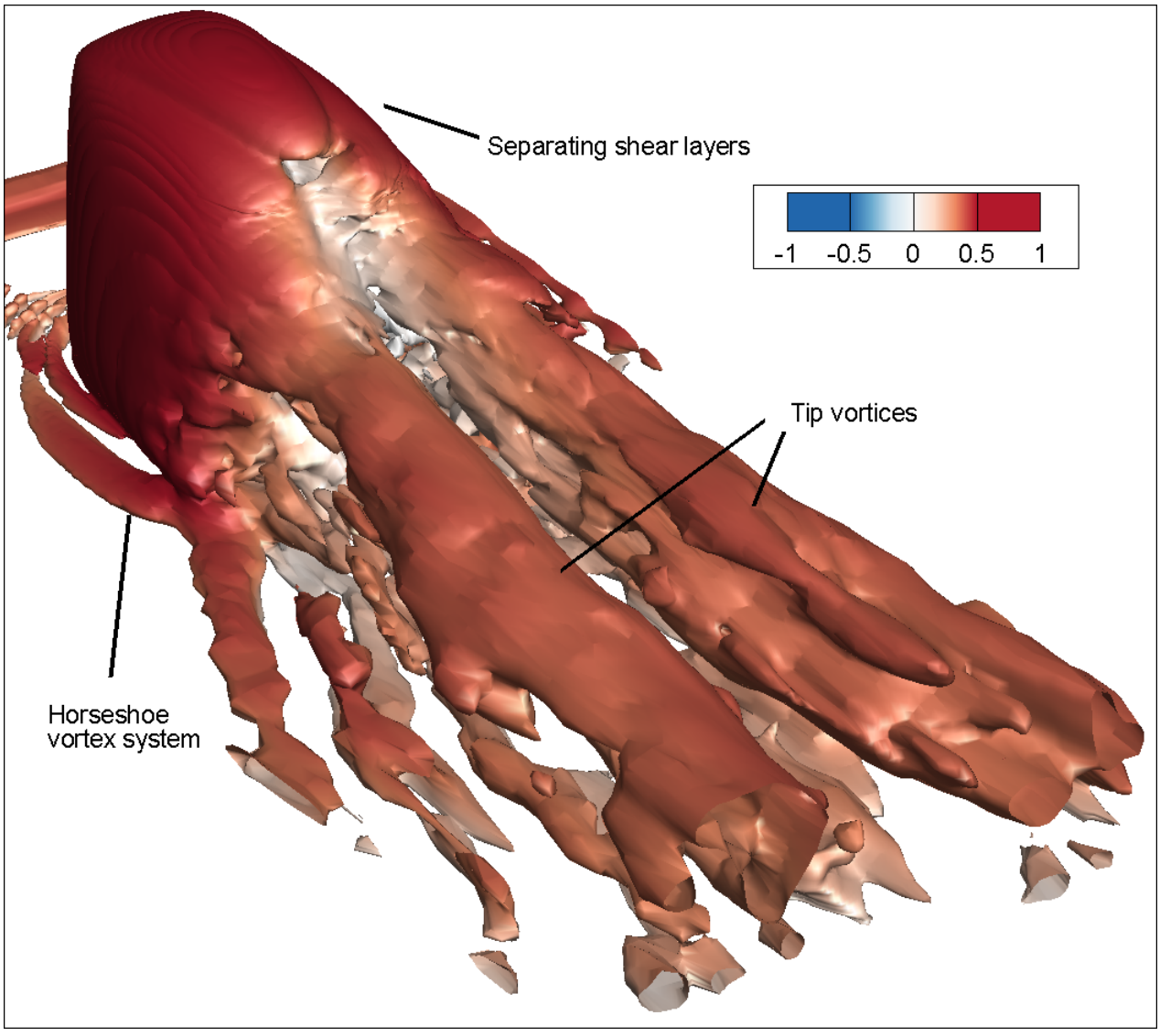

Figure 5.4: 3D time-averaged flow field using an iso-surface of the Q–criterion ($Q = 1$) contoured with the normalized freestream velocity u/U_∞.

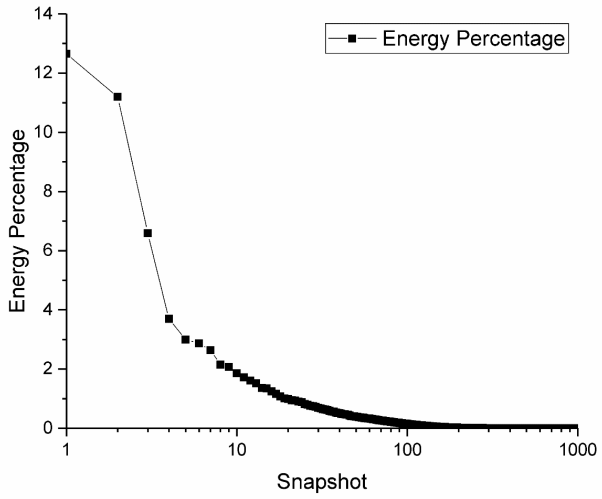

Figure 5.5: The POD energy distribution as a percentage of the overall turbulent kinetic energy (TKE) captured by every eigenmode (defined as $\lambda_i / \sum \lambda$).

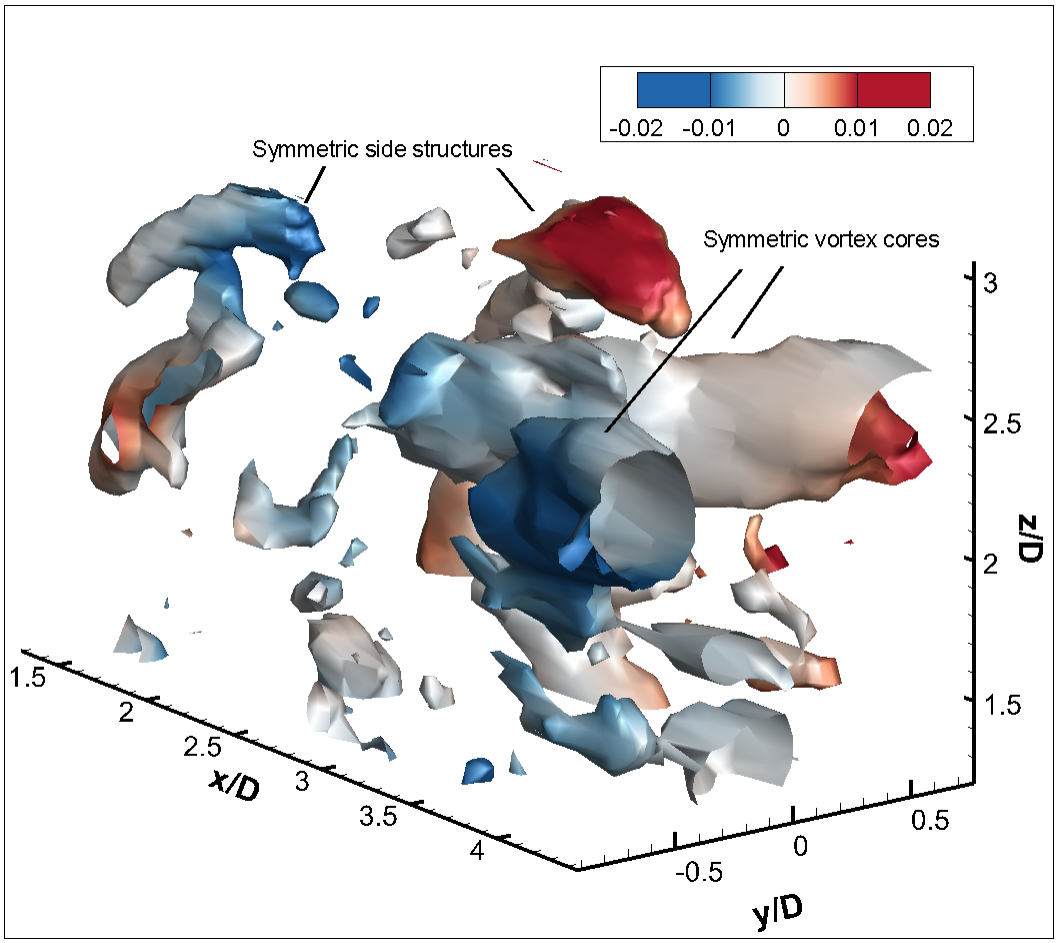

Iso-surface

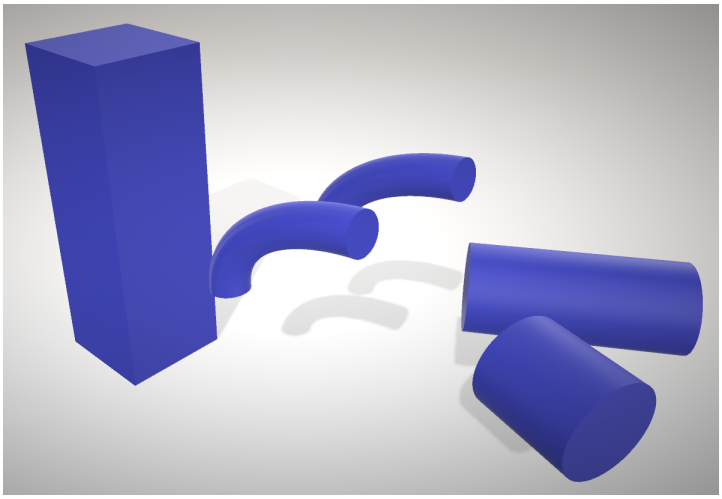

Simplified schematic

Figure 5.6: The first POD energy mode using an iso-surface of Q-criterion ($Q = 0.001$) contoured with normalized fluctuating velocity u^* (i.e. u^* = (u-u_{mean})/U_∞).

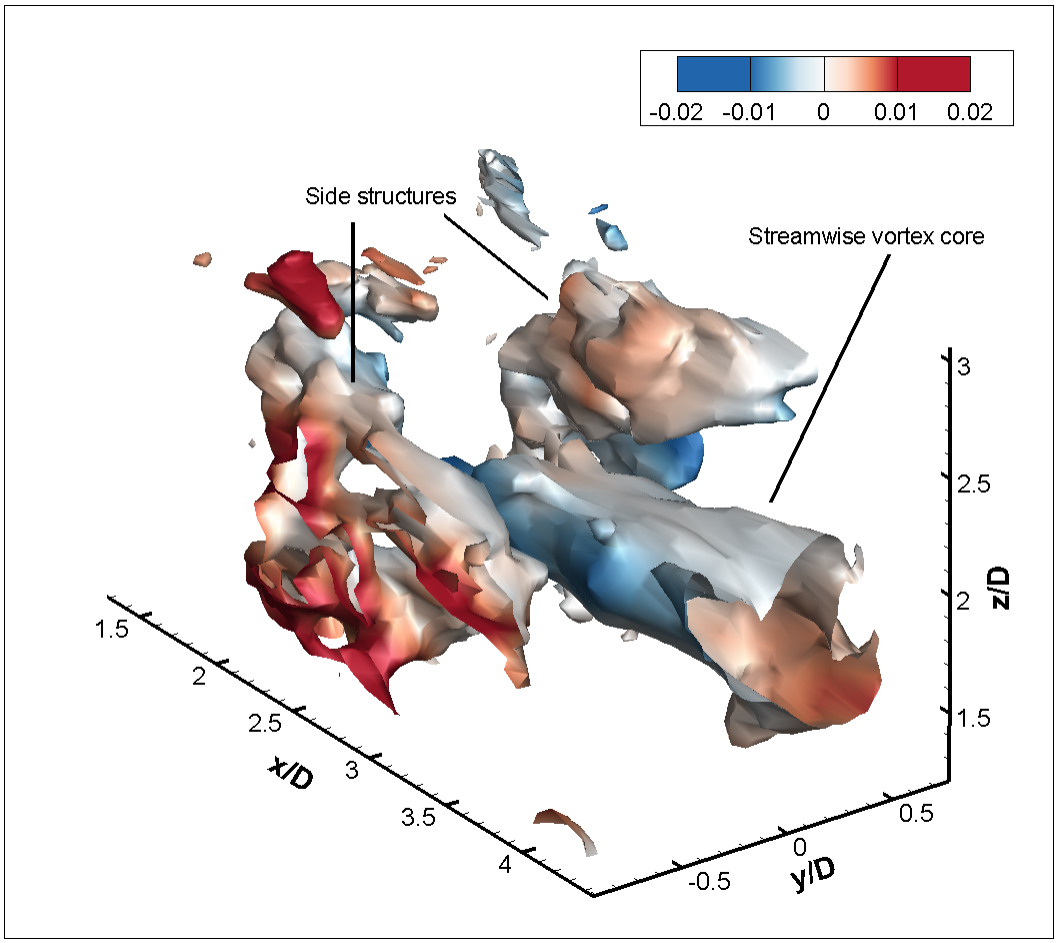

Iso-surface

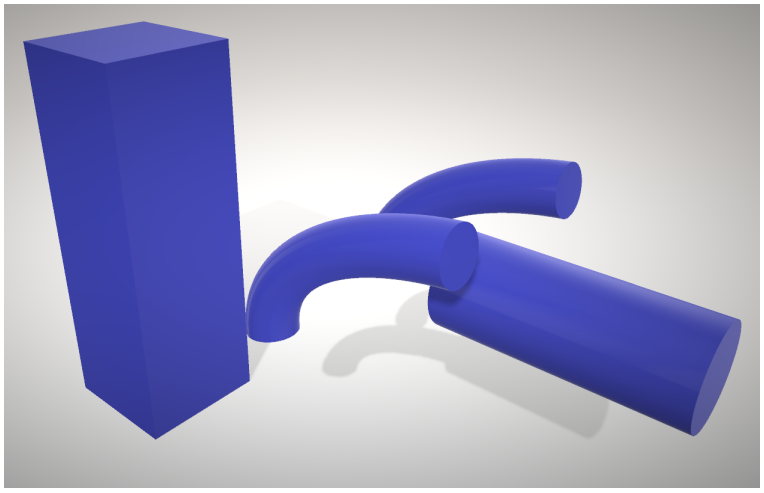

Simplified schematic

Figure 5.7: The second POD energy mode using an iso-surface of Q-criterion ($Q = 0.001$) contoured with normalized fluctuating velocity u^* (i.e. $u^* = (u\text{-}u_{mean})/u_\infty$).

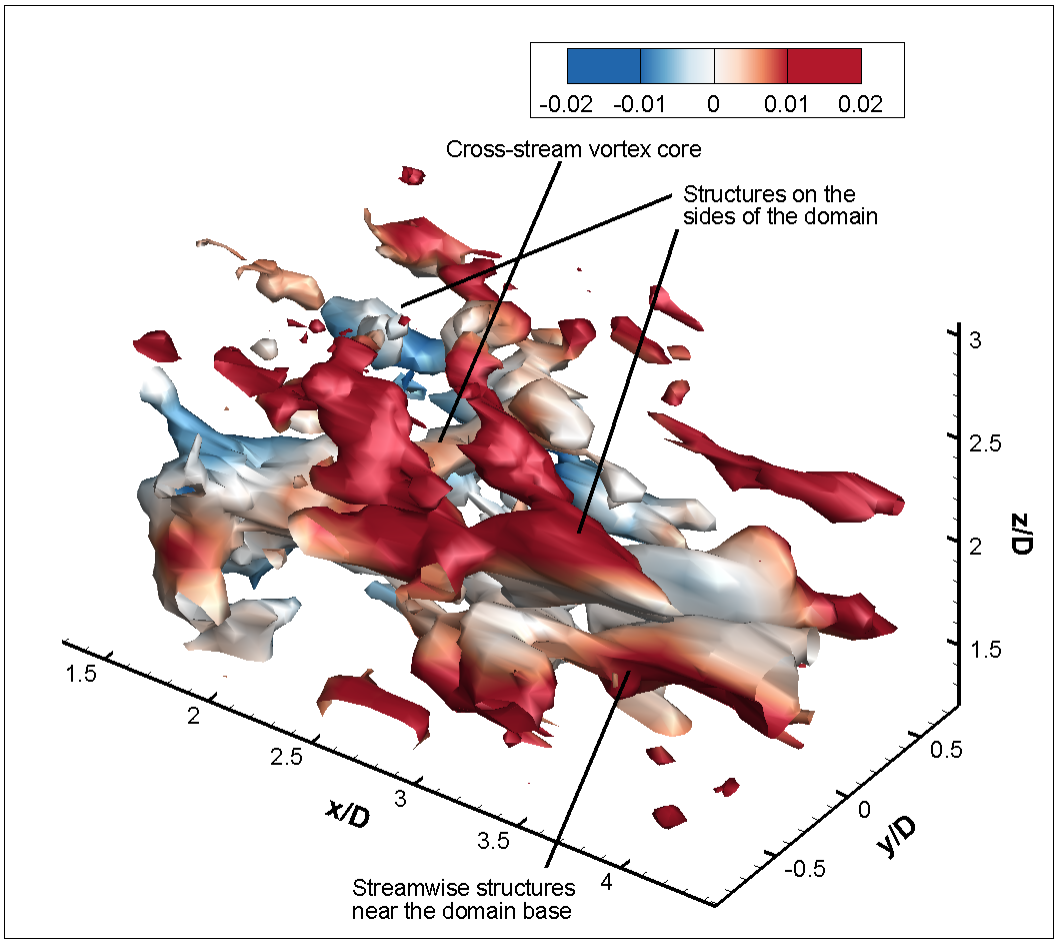

Iso-surface

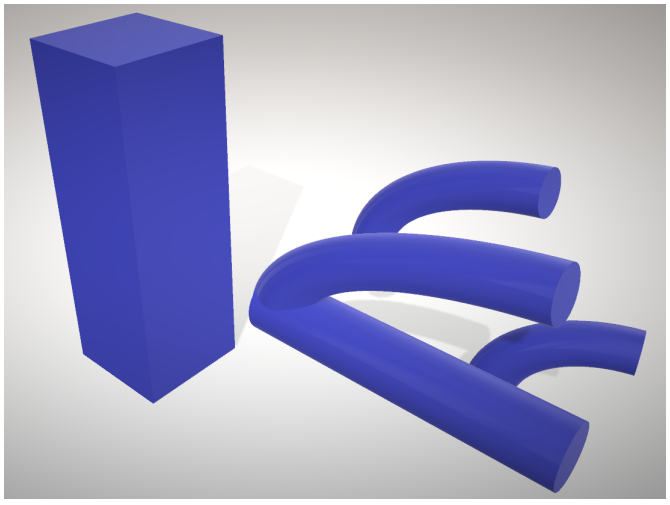

Simplified schematic

Figure 5.8: The third POD energy mode using an iso-surface of Q-criterion ($Q = 0.001$) contoured with normalized fluctuating velocity u^* (i.e. $u^* = (u\text{-}u_{mean})/u_\infty$).

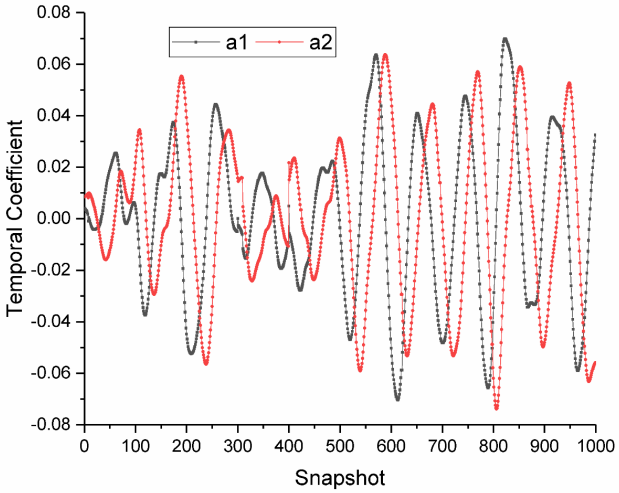

(a)

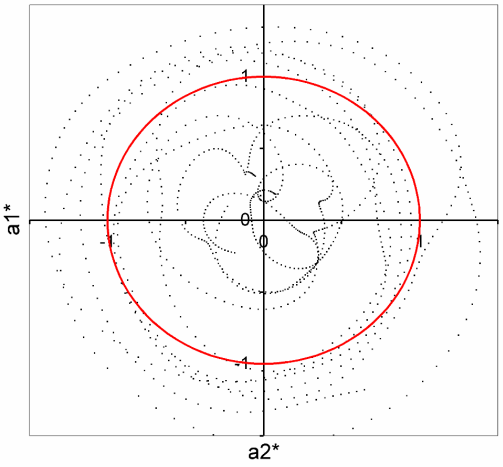

(b)

Figure 5.9: POD temporal coefficient variation with (a) each snapshot (a_1 and a_2 with successive snapshots), and (b) each other (normalized temporal coefficients a_1^* and a_2^*).

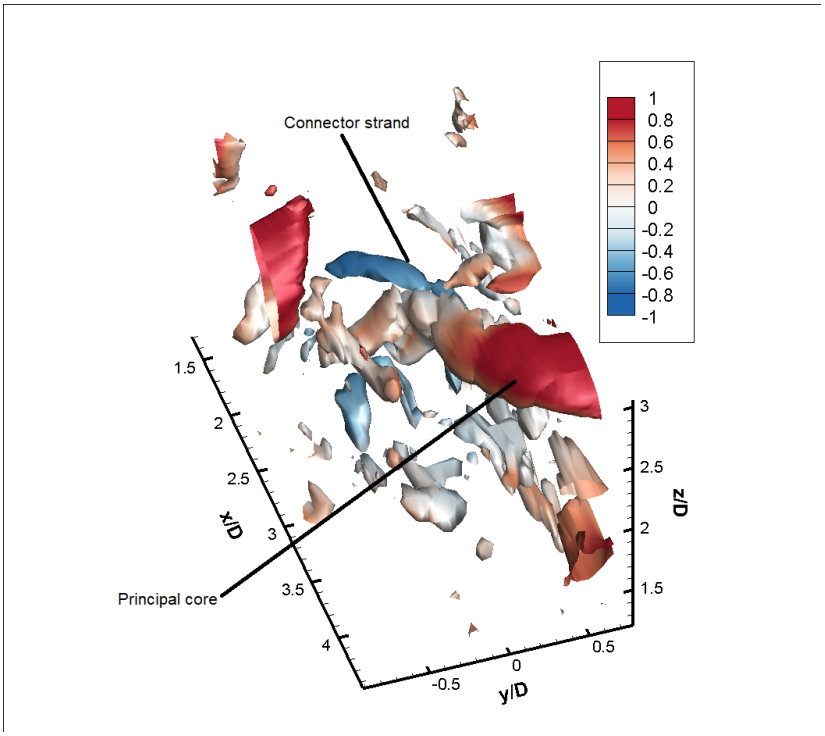

(a) The instantaneous 3D iso-surface of the Q-criterion ($Q = 1500$) contoured with normalized u-velocity (u/U_∞)

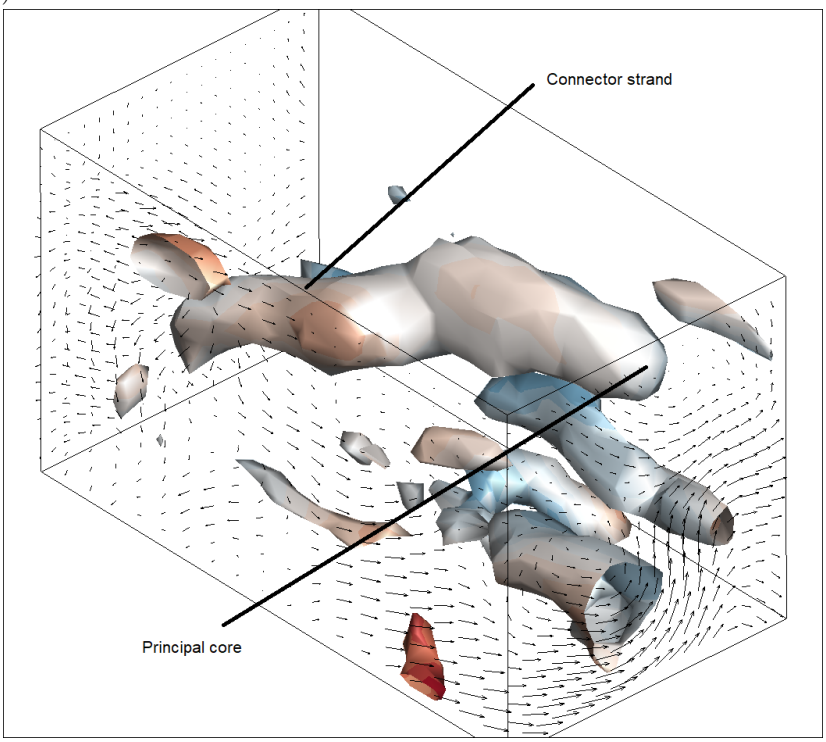

(b) POD reconstruction of the Q-criterion ($Q = 1500$) contoured with normalized u-velocity (u/U_∞) along with velocity vectors at select edges of the domain at the instant shown in Figure 5.10(a).

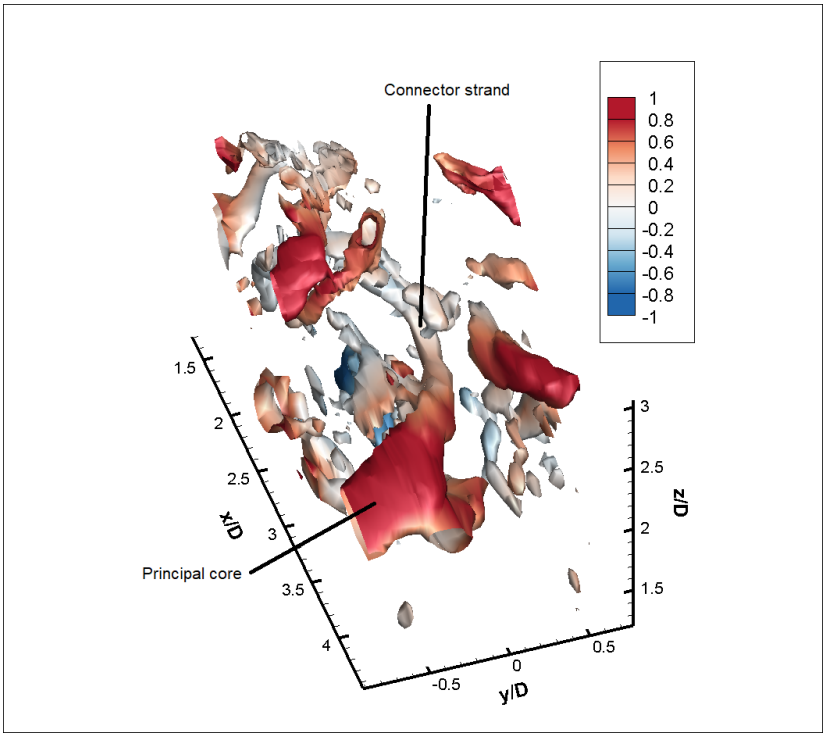

(c) The instantaneous 3D iso-surface of the Q-criterion ($Q = 1500$) contoured with normalized u-velocity (u/U_∞) at an instant opposite in phase to Figure 5.10(a)

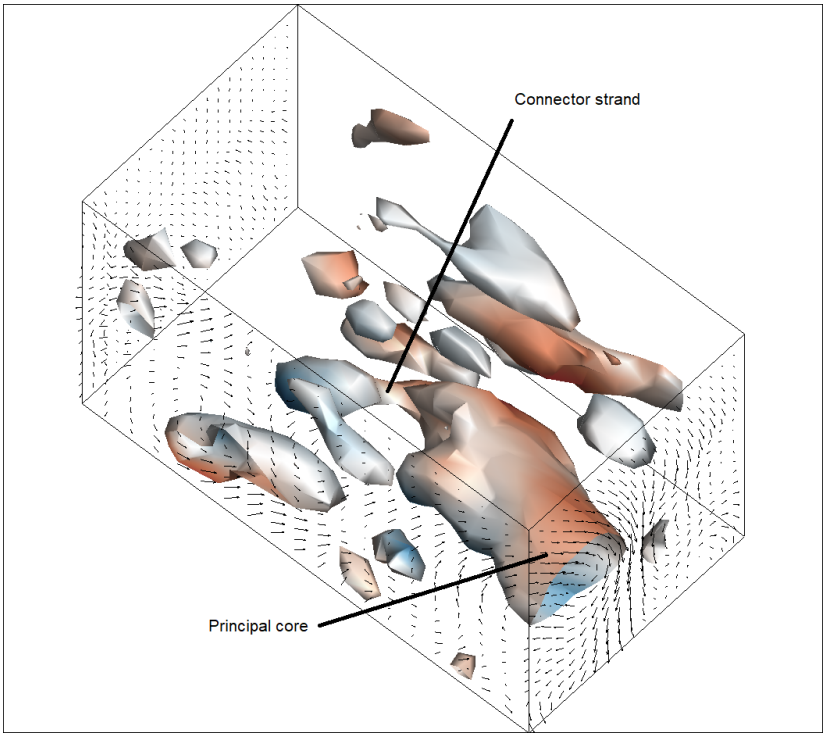

(d) POD reconstruction of the Q-criterion ($Q = 1500$) contoured with normalized u-velocity (u/U_∞) along with velocity vectors at select edges of the domain at the instant shown in Figure 5.10(c)

Figure 5.10: Comparison of the instantaneous flow field and POD reconstructions using 20 energy modes of the isosurfaces of the Q-criterion ($Q = 1500$)

Chapter 6

Conclusions

6.1 Thesis Summary

The central objective of this thesis is to explore the flow over surface-mounted bluff bodies and to use sophisticated post-processing methodologies to gain additional insight into the complex flow structures generated by them. Two bluff-body geometries, namely the circular cylinder and the square prism, have been chosen for analysis. An investigation into the literature revealed that flows over surface-mounted finite-height circular cylinders and square prisms have been extensively studied with varied boundary conditions and flow configurations. However, the flows around these geometries, specifically above the free end, have not been well understood. Furthermore, fewer studies have focused on the three-dimensional flow structures in the wake of square prism and circular cylinder flows. Thus, over four separate studies, this thesis attempts to bridge these gaps in the literature on surface-mounted bluff body flows and provide an enhanced understanding of relatively unexplored flow fields.

The first two studies involved investigating the flows above the free end of a square prism and circular cylinder, respectively. Experimental data were obtained from a low-speed wind tunnel using 2D PIV. Velocity data was then post-processed using proper orthogonal decomposition and the swirling strength criterion. The third study investigated the three-dimensional mean flow structure in the wake of a surface-mounted finite height square prism. Velocity data for this analysis were simulated by a pre-existing in-house LES code. 2D planes at various locations in the wake, as well as the 3D iso-surfaces of the Q-criterion, were used to analyze the mean flow structures. The fourth study looked at features of the instantaneous fluctuating flow field in the wake of a surface-mounted square prism using 3D POD and iso-surfaces of the Q-criterion.

6.2 Research Contributions

The first study sought to investigate the fluctuating flow field above the free end of surface-mounted finite-height square prisms of AR = 9, 7, 5 and 3, at a Reynolds number of $Re_D = 4.2 \times 10^4$ using POD and the swirling strength criterion. The flow fields in the vertical symmetry planes across aspect ratios were of interest. Data for the flow visualization methodologies were obtained from PIV measurements made in a low-speed wind tunnel, which were reported in Rostamy *et al.* (2013) and Sumner *et al.* (2017). Of interest was to look at the flow structures in the vertical symmetry planes across the varying aspect ratios. POD was used to extract the dominant instantaneous flow features. The major research contributions are as follows:

- The POD analysis demonstrated that, for a reasonably large set of uncorrelated snapshots, the energy distribution and the flow features seen in the higher energy modes demonstrate little change with the number of snapshots as well as the time interval between successive snapshots.
- For all four prisms, the first POD energy mode characterized the shear layer separating from the leading edge of the prism as consisting of two distinct shear sub-layers of clockwise and counter clockwise vorticity.
- The higher POD modes further characterized these sub-layers as containing distinct small-scale vortices becoming progressively weaker and smaller as it diffused into the wake. These are identified as Kelvin-Helmholtz shear layer instabilities seen in similar flows at these Reynolds numbers.
- At higher aspect ratios, the tendency for the formation of these instabilities in the regions of the separated shear layer reduced, possibly due to the weaker influence of the ground plane. The height of this separated shear layer from the free end also reduces with increasing aspect ratio.
- For various modes, the swirling strength criterion characterized this shear layer as the formation of vortices detaching from the leading edge of the prism along the shear layer, confirmed previously by the second and third POD energy modes. Swirling strength

was thus able to capture added information on rotational structures over and above the POD vorticity contours.

The second study investigated the fluctuating flow field above the free end of a surface-mounted finite-height cylinder of AR = 9, 7, 5 and 3, at a Reynolds number of $\mathrm{Re}_D = 4.2 \times 10^4$ using POD and the swirling strength criterion. Unlike the previous study, the flow field in planes parallel to the free end and close to the free end were of interest. Data for the flow visualization methodologies were obtained from PIV measurements made in a low-speed wind tunnel. The major research contributions are as follows:

- The first two energy modes across all planes and aspect ratios showed substantial symmetry in the flow features directly above the free end, with the dominant energetic structures being two vorticity sub-layers emerging from the side-tip, a pair of counter-rotating vortices on either side of the midline, and a strong reverse flow coming from the wake of the free end towards the trailing edge of the cylinder.
- The location of these flow features varied with the distance from the free end indicating a possible three-dimensional structure arching downwards with the free end and a rotating three-dimensional structure immediately after and above the trailing edge of the cylinder free end.
- There was also an interaction noted with the side-tip flow structures and the incoming flow from the circumferential leading edge that has been inferred to be the cause of the vorticity sub-layers and a local flow rotation just downstream of the side-tips of the cylinder free end.
- With increasing aspect ratio, the location of the vorticity sub-layers on the side-tips moves further downstream owing a decreased influence of the ground plane on the flow features and a stronger influence of the freestream flow above the free end. The outer vorticity sub-layer is enhanced compared to the inner sub-layer showing an increased effect of flow entrainment from the sides of the cylinder and the weakening influence of the incoming flow from the circumferential leading edge.

The third study investigated the mean 3D flow field in the wake of a finite-height square prism. A surface-mounted square prism of aspect ratio AR = 3 at the Reynolds number

$Re_D = 500$ was analyzed using LES. Of interest was to explore the 3D mean flow features, across various 2D planes in the flow field and a visualization of the 3D iso-surfaces. 50,000 instantaneous snapshots spanning approximately ten shedding cycles was used to compute the time-averaged flow field using a finite-volume formulation. The major research contributions are as follows:

- The flow is characterized by a pair of symmetric tip vortices emanating from the free end and the upper sides close to the free end of the prism. These appear to propagate downstream into the wake away from the symmetry mid-plane, towards the ground plane. Another symmetric system of horseshoe vortices are also seen around the base junction of the prism, moving away from the symmetry plane as it moves downstream.

- A symmetric pair of edge vortices due to the reattachment of the upward flow from the side-walls of the prism is seen above the free end. These structures interact with the separating shear layer in the freestream direction and form another pair of vortices that quickly diffuse downstream in the near wake above the free end. The flows coming from the side walls close to the free end move downstream, and interact with the downwash flow in the wake and form the mean tip vortices.

- In the vertical planes, the Nw vortex is formed due to the reverse flow from the bottom of the recirculation zone above it interacts with the adverse pressure gradient of the wall junction and the Reynolds shear stresses from the ground plane. In the horizontal planes, the location of the foci of the symmetric Karman vortex shedding vary along the prism height. The foci seem to be furthest downstream in planes away from the free end and the ground plane. The width of the separating shear layers from the sides have also been shown to vary with prism height.

- Surface streamlines show stagnation points at the leading edge and trailing edge faces of the prism. Flow below this stagnation point contributes to the formation of the horseshoe vortex system near the wall junction, while the upward moving flow separates from the sides and the free end of the prism creating separating shear layers. On the free end surface, a pair of counterrotating vortices is seen above the leading edge corners of the prism.

The fourth study looked at the 3D fluctuating flow field in the wake of a finite-height square prism. A surface-mounted square prism of aspect ratio AR = 3 at the Reynolds number Re_D = 500 was analyzed using LES. Of interest was to explore the 3D mean flow features and the instantaneous flow characteristics using POD. 50000 instantaneous snapshots spanning approximately ten shedding cycles was used to compute the time-averaged flow field, while a subset of 1000 snapshots in a reduced sub-domain in the wake was subsequently used for POD analysis. The major research contributions are as follows:

- The energy distribution was observed to be far more gradual compared to 2D flow fields seen in the literature. The first energy mode demonstrated two dominant symmetric streamwise structures placed symmetrically about the vertical symmetry plane of the square prism. These pair of vortex tubes was consequently identified as the connecting strands of the streamwise connector strand seen in the instantaneous flow field. It is thus inferred that a complex flow mechanism closer to the prism-wall junction initiates the onset of these half loop structures.
- The second energy mode demonstrated a single streamwise vortex core moving downstream. This is indicative of the trace of the streamwise connector strand seen in the instantaneous flow fields that overlap in this region as the half loop structures on either side of the vertical symmetry plane move downstream.
- The temporal coefficients of the first two POD modes were periodic. With the help of a scatter plot of the first two temporal coefficients, two such snapshots with high radii diametrically opposite the unit circle revealed a prominent inclined half loop structure. The connector strand was seen to move across the vertical symmetry plane forming a principal core outside the selected domain.

In summary, the main contribution of this thesis was to develop additional insight on a complex flow field around and in the wake of surface-mounted finite-height bluff bodies. Regions of the flow field that have not been well understood in the literature were identified for analysis, namely the free end above a surface-mounted finite-height square prism and cylinder, and the three-dimensional wake of a surface-mounted finite-height square prism. This thesis effectively demonstrates the use of advanced post-processing techniques like POD

(both 2D and 3D) and velocity gradient methods like the swirling strength criterion and the Q-criterion in extracting coherent turbulent flow structures, as well as explain its origins and interactions with each other.

6.3 Implications for Current Literature

The first two studies above the free end of surface-mounted finite-height bluff bodies have identified and analyzed a flow field that has not been extensively investigated in the literature. Consequently, all research contributions from these studies provide new information on the instantaneous flow characteristics of this flow field.

The third and fourth studies on the flow structures around and in the wake of a surface-mounted finite-height square prism provide new insight into the three-dimensional mean and instantaneous flow structures, respectively. As there have been very limited studies that have investigated the three-dimensional flow features around a surface-mounted square prism with a low aspect ratio, low Reynolds number and a thin boundary layer, the research contributions of these studies do advance the existing understanding of this flow field. This study does not attempt to propose a model that unifies component structures as some of these components have been shown to be disjointed from each other. Some benchmarks on how structures seen in the present study compare with the existing literature is mentioned below:

For the mean flow field:

- In the wake, the structures seen are predominantly a pair of tip vortices and horseshoe vortices. This implies that for a Re = 500 and a thin incoming boundary layer of δ/D = 0.2, AR = 3 < $\mathrm{AR}_{\mathrm{critical}}$.
- Consequently, the mean flow represents a dipole wake configuration.
- There is a distinction between the shear layers originating from the free end leading edge, and the sides of the prism. This study shows no evidence of a connecting horizontal bridge between these two shear layers to form arch vortices, as postulated by Wang and Zhou [95].
- The tip vortices originate due to a coupling effect created by the upward moving flow on the sides of the prism towards the free end, and the downward moving flow (downwash) of the freestream flow above the prism free end moving towards the ground plane.

For the instantaneous flow field:

- A structure partially resembling the half-loop structure seen by Bourgeois et al. [8] in their phase-averaged results are seen in this study. This study clearly shows the inclined nature of the connector strands that seemingly lead to the formation of the principal core. However, a complete visualization of the principal core would require a larger POD domain.
- The half-loop structure is seen alternating and moving downstream across the vertical symmetry plane.
- Additional structures similar to the half-loop structure are also seen that move in the streamwise direction without crossing the vertical symmetry plane.

6.4 Recommendations for Future Research

The wake flow of surface-mounted bluff bodies have been extensively studied both experimentally and numerically. As the flow structure is sufficiently complex owing to the interaction of various three-dimensional structures with each other, there is still ample scope to further enhance the understanding of this flow field. A few recommendations are as follows:

- The flow above the free end for both the cylinder and square prism flows in this thesis have only investigated select planes of interest. A more comprehensive study on other planes above the free end or a higher resolution 3D simulation of the flow field above the free ends of these geometries will give provide a more rigorous representation of the small-scale structures above the free ends. On the numerical side, this may be achieved by enhancing the computational capabilities of the present in-house LES code by parallelizing the numerical algorithms, or use multiblock methods for more strategic grid refinement at select locations of interest.
- To simulate a more practical flow field, an inflow turbulence boundary condition may be employed. This may be obtained by introducing a numerical perturbation in the inflow velocity. Other parameters like the cross-section geometry or the angle of incidence of the freestream velocity could also be varied for a broader understanding of the wakes produced by these flow fields. Numerically, these can be achieved using immersed

boundary methods. In this method, by way of a body force term, the presence of an obstacle of an arbitrary shape is simulated within the computational domain without restructuring the grid.

- 3D POD has shown great potential in being a definitive tool for visualizing complex fluctuating flow fields. Owing to computational limitations, this thesis has only looked at a small sub-region in the wake of the square prism. Further studies could explore a larger flow field, or other regions of interest, preferably around the bluff-body geometry (like the free end, base junction or the near wake).

- Other statistical tools like POD have shown increasing promise in the literature of post-processing of flow fields. While POD is a spatial decomposition of the flow field into a system of orthonormal modes, another popular technique called dynamic mode decomposition (DMD) may also be used to investigate this flow field to obtain a temporal decomposition of the flow field into its various periodic flow features.

References

[1] M. S. Adaramola, O. G. Akinlade, D. Sumner, D. J. Bergstrom, and A. J. Schenstead. Turbulent wake of a finite circular cylinder of small aspect ratio. *Journal of Fluids and Structures*, 22(6):919–928, 2006.

[2] H. Bai and M. M. Alam. Dependence of square cylinder wake on reynolds number. *Physics of Fluids*, 30(1):015102, 2018.

[3] F. Ballio, C. Bettoni, and S. Franzetti. A survey of time-averaged characteristics of laminar and turbulent horseshoe vortices. *Transactions of the ASME: Journal of Fluids Engineering*, 120(2):233–242, 1998.

[4] P. W. Bearman and D. M. Trueman. An investigation of the flow around rectangular cylinders. *The Aeronautical Quarterly*, 23(3):229–237, 1972.

[5] G. Berkooz, P. Holmes, and J. L. Lumley. The proper orthogonal decomposition in the analysis of turbulent flows. *Annual Review of Fluid Mechanics*, 25(1):539–575, 1993.

[6] D. K. Bisset, R. A. Antonia, and L. W. B. Browne. Spatial organization of large structures in the turbulent far wake of a cylinder. *Journal of Fluid Mechanics*, 218:439–461, 1990.

[7] J. A. Bourgeois, P. Sattari, and R. J. Martinuzzi. Quasi-periodic structure of vortical flows produced in the wake of finite bluff bodies partially immersed in a boundary layer. In *ASME 2010 3rd Joint US-European Fluids Engineering Summer Meeting collocated with 8th International Conference on Nanochannels, Microchannels, and Minichannels*, pages 2827–2836. American Society of Mechanical Engineers, 2010.

[8] J. A. Bourgeois, P. Sattari, and R. J. Martinuzzi. Alternating half-loop shedding in the turbulent wake of a finite surface-mounted square cylinder with a thin boundary layer. *Physics of Fluids*, 23(9):095101, 2011.

[9] J. A. Bourgeois, P. Sattari, and R. J. Martinuzzi. Coherent vortical and straining structures in the finite wall-mounted square cylinder wake. *International Journal of Heat and Fluid Flow*, 35:130–140, 2012.

[10] L. Bruno, D. Fransos, N. Coste, and A. Bosco. 3d flow around a rectangular cylinder: a computational study. *Journal of Wind Engineering and Industrial Aerodynamics*, 98(6):263–276, 2010.

[11] B. Cantwell and D. Coles. An experimental study of entrainment and transport in the turbulent near wake of a circular cylinder. *Journal of Fluid Mechanics*, 136:321–374, 1983.

[12] A. Cesur, C. Carlsson, A. Feymark, L. Fuchs, and J. Revstedt. Analysis of the wake dynamics of stiff and flexible cantilever beams using pod and dmd. *Computers & Fluids*, 101:27–41, 2014.

[13] P. Chakraborty, S. Balachandar, and R. J. Adrian. On the relationships between local vortex identification schemes. *Journal of Fluid Mechanics*, 535:189–214, 2005.

[14] M. S. Chong, A. E. Perry, and B. J. Cantwell. A general classification of three-dimensional flow fields. *Physics of Fluids A: Fluid Dynamics*, 2(5):765–777, 1990.

[15] M. Coutanceau and J. Defaye. Circular cylinder wake configurations: A flow visualization survey. *Applied Mechanics Reviews*, 44(6):255–305, 1991.

[16] G. D. Donnert, M. Kappler, and W. Rodi. Measurement of tracer concentration in the flow around finite-height cylinders. *Journal of Turbulence*, (8):N33, 2007.

[17] D. F. G. Durao, M. V. Heitor, and J. C. F. Pereira. Measurements of turbulent and periodic flows around a square cross-section cylinder. *Experiments in Fluids*, 6(5):298–304, 1988.

[18] M. El Hassan, J. A. Bourgeois, and R. Martinuzzi. Boundary layer effect on the vortex shedding of wall-mounted rectangular cylinder. *Experiments in Fluids*, 56(2):33, 2015.

[19] F. Etzold and H. Fiedler. The near-wake structure of a cantilevered cylinder in a cross-flow. *Zeitschrift fur Flugwissenschaften*, 24:77–82, 1976.

[20] D. J. Farivar. Turbulent uniform flow around cylinders of finite length. *AIAA Journal*, 19(3):275–281, 1981.

[21] T. A. Fox and C. J. Apelt. Fluid-induced loading of cantilevered circular cylinders in a low-turbulence uniform flow. part 3: fluctuating loads with aspect ratios 4 to 25. *Journal of Fluids and Structures*, 7(4):375–386, 1993.

[22] T. A. Fox and G. S. West. Fluid-induced loading of cantilevered circular cylinders in a low-turbulence uniform flow. part 1: mean loading with aspect ratios in the range 4 to 30. *Journal of Fluids and Structures*, 7(1):1–14, 1993.

[23] O. Frederich, J. Scouten, D. M Luchtenburg, and F. Thiele. Numerical simulation and analysis of the flow around a wall-mounted finite cylinder. In *Imaging Measurement Methods for Flow Analysis*, pages 207–216. Springer, 2009.

[24] O. Frederich, J. Scouten, D. M Luchtenburg, and F. Thiele. Large-scale dynamics in the flow around a finite cylinder with a ground plate. *Fluid Dynamics Research*, 43(1):015504, 2010.

[25] O. Frederich, E. Wassen, and F. Thiele. Prediction of the flow around a short wall-mounted finite cylinder using les and des1. *Journal of Numerical Analysis, Industrial and Applied Mathematics*, 3(3-4):231–247, 2008.

[26] J. Fröhlich and W. Rodi. Les of the flow around a circular cylinder of finite height. *International Journal of Heat and Fluid Flow*, 25(3):537–548, 2004.

[27] Massimo Germano, Ugo Piomelli, Parviz Moin, and William H Cabot. A dynamic subgrid-scale eddy viscosity model. *Physics of Fluids A: Fluid Dynamics*, 3(7):1760–1765, 1991.

[28] S. V. Gordeyev and F. O. Thomas. Coherent structure in the turbulent planar jet. part 1. extraction of proper orthogonal decomposition eigenmodes and their self-similarity. *Journal of Fluid Mechanics*, 414:145–194, 2000.

[29] S. V. Gordeyev and F. O. Thomas. Coherent structure in the turbulent planar jet. part 2. structural topology via pod eigenmode projection. *Journal of Fluid Mechanics*, 460:349–380, 2002.

[30] Melissa A Green, Clarence W Rowley, and George Haller. Detection of lagrangian coherent structures in three-dimensional turbulence. *Journal of Fluid Mechanics*, 572:111–120, 2007.

[31] R. Hain, C. J. Kähler, and D. Michaelis. Tomographic and time resolved piv measurements on a finite cylinder mounted on a flat plate. *Experiments in Fluids*, 45(4):715–724, 2008.

[32] N. Hölscher and H. Niemann. Turbulence and separation induced pressure fluctuations on a finite circular cylinderapplication of a linear unsteady strip theory. *Journal of Wind Engineering and Industrial Aerodynamics*, 65(1-3):335–346, 1996.

[33] Z. Hosseini, J. A. Bourgeois, and R. J. Martinuzzi. Wall-mounted finite cylinder wake structure modification due to boundary layer-wake interaction: Half-loop and full-loop coherent structure topologies. In *7th International Colloquium on Bluff Body Aerodynamics and Applications (BBAA7), Shanghai, China*, pages 2–6, 2012.

[34] Z. Hosseini, J. A. Bourgeois, and R. J. Martinuzzi. Large-scale structures in dipole and quadrupole wakes of a wall-mounted finite rectangular cylinder. *Experiments in Fluids*, 54(9):1595, 2013.

[35] R. F. Huang, B. H. Lin, and S. C. Yen. Time-averaged topological flow patterns and their influence on vortex shedding of a square cylinder in crossflow at incidence. *Journal of Fluids and Structures*, 26(3):406–429, 2010.

[36] J. C. R. Hunt, A. A. Wray, and P. Moin. Eddies, streams, and convergence zones in turbulent flows. *Center for Turbulence Research Report CTR-S88*, 1988.

[37] G Iaccarino, A Ooi, PA Durbin, and M Behnia. Reynolds averaged simulation of unsteady separated flow. *International Journal of Heat and Fluid Flow*, 24(2):147–156, 2003.

[38] T. Igarashi. Characteristics of the flow around a square prism. *Bulletin of JSME*, 27(231):1858–1865, 1984.

[39] G. V. Iungo and G. Buresti. Experimental investigation on the aerodynamic loads and wake flow features of low aspect-ratio triangular prisms at different wind directions. *Journal of Fluids and Structures*, 25(7):1119–1135, 2009.

[40] H. Kawai, Y. Okuda, and M. Ohashi. Near wake structure behind a 3d square prism with the aspect ratio of 2.7 in a shallow boundary layer flow. *Journal of Wind Engineering and Industrial Aerodynamics*, 104:196–202, 2012.

[41] T. Kawamura, M. Hiwada, T. Hibino, I. Mabuchi, and M. Kumada. Flow around a finite circular cylinder on a flat plate: Cylinder height greater than turbulent boundary layer thickness. *Bulletin of JSME*, 27(232):2142–2151, 1984.

[42] V. Kolář. Vortex identification: New requirements and limitations. *International Journal of Heat and Fluid Flow*, 28(4):638–652, 2007.

[43] J. Kostas, J. Soria, and M. S. Chong. A comparison between snapshot pod analysis of piv velocity and vorticity data. *Experiments in Fluids*, 38(2):146–160, 2005.

[44] L. Kourentis and E. Konstantinidis. Uncovering large-scale coherent structures in natural and forced turbulent wakes by combining piv, pod, and ftle. *Experiments in Fluids*, 52(3):749–763, 2012.

[45] S. Krajnović. Flow around a tall finite cylinder explored by large eddy simulation. *Journal of Fluid Mechanics*, 676:294–317, 2011.

[46] B. E. Lee. The effect of turbulence on the surface pressure field of a square prism. *Journal of Fluid Mechanics*, 69(2):263–282, 1975.

[47] H. H. Lee and J. J. Miau. An investigation on karman-type vortex shedding from a finite square cylinder. *Journal of Mechanics*, 28(2):299–308, 2012.

[48] J. L. Lumley. Toward a turbulent constitutive relation. *Journal of Fluid Mechanics*, 41(2):413–434, 1970.

[49] John L Lumley. Coherent structures in turbulence. In *Transition and turbulence*, pages 215–242. Elsevier, 1981.

[50] D. A. Lyn, S. Einav, W. Rodi, and J. H. Park. A laser-doppler velocimetry study of ensemble-averaged characteristics of the turbulent near wake of a square cylinder. *Journal of Fluid Mechanics*, 304:285–319, 1995.

[51] D. A. Lyn and W. Rodi. The flapping shear layer formed by flow separation from the forward corner of a square cylinder. *Journal of Fluid Mechanics*, 267:353–376, 1994.

[52] X. Ma and G. E. Karniadakis. A low-dimensional model for simulating three-dimensional cylinder flow. *Journal of Fluid Mechanics*, 458:181–190, 2002.

[53] A. Marshak and A. Davis. *3D radiative transfer in cloudy atmospheres*. Springer-Verlag Berlin Heidelberg, 2005.

[54] J. F. McClean and D. Sumner. An experimental investigation of aspect ratio and incidence angle effects for the flow around surface-mounted finite-height square prisms. *Transactions of the ASME Journal of Fluids Engineering*, 136(8):081206, 2014.

[55] C. Norberg. Flow around rectangular cylinders: pressure forces and wake frequencies. *Journal of Wind Engineering and Industrial Aerodynamics*, 49(1-3):187–196, 1993.

[56] E. D. Obasaju. An investigation of the effects of incidence on the flow around a square section cylinder. *The Aeronautical Quarterly*, 34(4):243–259, 1983.

[57] A. Ogunremi and D. Sumner. On the effects of incidence angle on the mean wake of a surface-mounted finite-height square prism. In *ASME/JSME/KSME 2015 Joint Fluids Engineering Conference*, number Paper. No. AJK2015-15011. American Society of Mechanical Engineers, 2015.

[58] A Okajima. Strouhal numbers of rectangular cylinders. *Journal of Fluid Mechanics*, 123:379–398, 1982.

[59] S. Okamoto and Y. Sunabashiri. Vortex shedding from a circular cylinder of finite length placed on a ground plane. *Transactions of the ASME: Journal of Fluids Engineering*, 114:512–512, 1992.

[60] Y. Okuda and Y. Taniike. Conical vortices over side face of a three-dimensional square prism. *Journal of Wind Engineering and Industrial Aerodynamics*, 50:163–172, 1993.

[61] G. Palau-Salvador, T. Stoesser, J. Fröhlich, M. Kappler, and W. Rodi. Large eddy simulations and experiments of flow around finite-height cylinders. *Flow, Turbulence and Combustion*, 84(2):239–275, 2010.

[62] C. W. Park and S. J. Lee. Free end effects on the near wake flow structure behind a finite circular cylinder. *Journal of Wind Engineering and Industrial Aerodynamics*, 88(2):231–246, 2000.

[63] C. W. Park and S. J. Lee. Flow structure around a finite circular cylinder embedded in various atmospheric boundary layers. *Fluid Dynamics Research*, 30(4):197–215, 2002.

[64] B. Patte-Rouland, G. Lalizel, J. Moreau, and E. Rouland. Flow analysis of an annular jet by particle image velocimetry and proper orthogonal decomposition. *Measurement Science and Technology*, 12(9):1404, 2001.

[65] R. J. Pattenden, S. R. Turnock, and X. Zhang. Measurements of the flow over a low-aspect-ratio cylinder mounted on a ground plane. *Experiments in Fluids*, 39(1):10–21, 2005.

[66] L. Perret. Piv investigation of the shear layer vortices in the near wake of a circular cylinder. *Experiments in Fluids*, 47(4-5):789, 2009.

[67] S. B. Pope. Turbulent flows. Cambridge, UK: Cambridge Univ., 2000.

[68] S. Roh and S. Park. Vortical flow over the free end surface of a finite circular cylinder mounted on a flat plate. *Experiments in Fluids*, 34(1):63–67, 2003.

[69] N. Rostamy, J. F. McClean, D. Sumner, D. J. Bergstrom, and J. D. Bugg. Local flow field of a surface–mounted finite square prism. In *7th International Colloquium on Bluff Body Aerodynamics and Applications (BBAA7), Shanghai, China, Sept*, pages 2–6, 2012.

[70] N. Rostamy, D. Sumner, D. J. Bergstrom, and J. D. Bugg. Instantaneous flow field above the free end of finite-height cylinders and prisms. *International Journal of Heat and Fluid Flow*, 43:120–128, 2013.

[71] M. Saeedi, P. P. LePoudre, and B. C. Wang. Direct numerical simulation of turbulent wake behind a surface-mounted square cylinder. *Journal of Fluids and Structures*, 51:20–39, 2014.

[72] M. Saeedi and B. C. Wang. Large-eddy simulation of turbulent flow around a finite-height wall-mounted square cylinder within a thin boundary layer. *Flow, Turbulence and Combustion*, 97(2):513–538, 2016.

[73] A. K. Saha. Unsteady flow past a finite square cylinder mounted on a wall at low reynolds number. *Computers & Fluids*, 88:599–615, 2013.

[74] H. Sakamoto and M. Arie. Vortex shedding from a rectangular prism and a circular cylinder placed vertically in a turbulent boundary layer. *Journal of Fluid Mechanics*, 126:147–165, 1983.

[75] H. Sakamoto and S. Oiwake. Fluctuating forces on a rectangular prism and a circular cylinder placed vertically in a turbulent boundary layer. *Journal of Fluids Engineering*, 106(2):160–166, 1984.

[76] R. S. Sarode, S. L. Gai, and CK Ramesh. Flow around circular-and square-section models of finite height in a turbulent shear flow. *Journal of Wind Engineering and Industrial Aerodynamics*, 8(3):223–230, 1981.

[77] P. Sattari, J. A. Bourgeois, and R. J. Martinuzzi. On the vortex dynamics in the wake of a finite surface-mounted square cylinder. *Experiments in Fluids*, 52(5):1149–1167, 2012.

[78] L. Sirovich. Turbulence and the dynamics of coherent structures. i. coherent structures. *Quarterly of Applied Mathematics*, 45(3):561–571, 1987.

[79] A. Sohankar, C. Norberg, and L. Davidson. Low-reynolds-number flow around a square cylinder at incidence: study of blockage, onset of vortex shedding and outlet boundary condition. *International Journal for Numerical Methods in Fluids*, 26(1):39–56, 1998.

[80] A. Sohankar, C Norberg, and L Davidson. Simulation of three-dimensional flow around a square cylinder at moderate reynolds numbers. *Physics of Fluids*, 11(2):288–306, 1999.

[81] E. M. Sparrow and F. Samie. Measured heat transfer coefficients at and adjacent to the tip of a wall-attached cylinder in crossflowapplication to fins. *Transaction of the ASME: Journal of Heat Transfer*, 103:778–784, 1981.

[82] B. M. Sumer, N. Christiansen, and J. Fredsøe. The horseshoe vortex and vortex shedding around a vertical wall-mounted cylinder exposed to waves. *Journal of Fluid Mechanics*, 332:41–70, 1997.

[83] D. Sumner. Flow above the free end of a surface-mounted finite-height circular cylinder: a review. *Journal of Fluids and Structures*, 43:41–63, 2013.

[84] D. Sumner, J. L. Heseltine, and O. J. P. Dansereau. Wake structure of a finite circular cylinder of small aspect ratio. *Experiments in Fluids*, 37(5):720–730, 2004.

[85] D. Sumner, N. Rostamy, D. J. Bergstrom, and J. D. Bugg. Influence of aspect ratio on the flow above the free end of a surface-mounted finite cylinder. *International Journal of Heat and Fluid Flow*, 56:290–304, 2015.

[86] D. Sumner, N. Rostamy, D. J. Bergstrom, and J. D. Bugg. Influence of aspect ratio on the mean flow field of a surface-mounted finite-height square prism. *International Journal of Heat and Fluid Flow*, 65:1–20, 2017.

[87] D. Sumner, S. Unnikrishnan, M. Teng, A. Beitel, A. Das, and M. Fulton. The mean wake of low-aspect-ratio surface-mounted finite-height square prisms and the effects of incidence angle. In *8th International Colloquium on Bluff Body Aerodynamics and Applications (BBAA8), Boston, USA, June*, pages 1–10, 2016.

[88] S. Tanaka and S. Murata. An investigation of the wake structure and aerodynamic characteristics of a finite circular cylinder: Time-averaged wake structures behind circular cylinders with various aspect ratios. *JSME International Journal Series B: Fluids and Thermal Engineering*, 42(2):178–187, 1999.

[89] T. Tsutsui and T. Igarashi. Drag reduction of a circular cylinder in an air-stream. *Journal of Wind Engineering and Industrial Aerodynamics*, 90(4):527–541, 2002.

[90] S. Unnikrishnan, A. Ogunremi, and D. Sumner. The effect of incidence angle on the mean wake of surface-mounted finite-height square prisms. *International Journal of Heat and Fluid Flow*, 66:137–156, 2017.

[91] Václav Uruba. Decomposition methods in turbulence research. In *EPJ Web of Conferences*, volume 25, page 01095. EDP Sciences, 2012.

[92] B. W. Van Oudheusden, F. Scarano, N. P. Van Hinsberg, and D. W. Watt. Phase-resolved characterization of vortex shedding in the near wake of a square-section cylinder at incidence. *Experiments in Fluids*, 39(1):86–98, 2005.

[93] B. C. Wang and D. J. Bergstrom. A general optimal formulation for the dynamic smagorinsky subgrid-scale stress model. *International Journal for Numerical Methods in Fluids*, 49(12):1359–1389, 2005.

[94] H. F. Wang, H. L. Cao, and Y. Zhou. Pod analysis of a finite-length cylinder near wake. *Experiments in Fluids*, 55(8):1790, 2014.

[95] H. F. Wang and Y. Zhou. The finite-length square cylinder near wake. *Journal of Fluid Mechanics*, 638:453–490, 2009.

[96] H. F. Wang, Y. Zhou, C. K. Chan, and K. S. Lam. Effect of initial conditions on interaction between a boundary layer and a wall-mounted finite-length-cylinder wake. *Physics of Fluids*, 18(6):065106, 2006.

[97] C. H. K. Williamson. Vortex dynamics in the cylinder wake. *Annual Review of Fluid Mechanics*, 28(1):477–539, 1996.

[98] S. C. Yen and C. W. Yang. Flow patterns and vortex shedding behavior behind a square cylinder. *Journal of Wind Engineering and Industrial Aerodynamics*, 99(8):868–878, 2011.

[99] D. Yu and A. Kareem. Parametric study of flow around rectangular prisms using les. *Journal of Wind Engineering and Industrial Aerodynamics*, 77:653–662, 1998.

[100] M. M. Zdravkovich. *Flow around Circular Cylinders; Vol. 1 Fundamentals*. Cambridge University Press, Cambridge, England, 1997.

[101] D. Zhang, L. Cheng, H. An, and M. Zhao. Direct numerical simulation of flow around a surface-mounted finite square cylinder at low reynolds numbers. *Physics of Fluids*, 29(4):045101, 2017.

[102] J. Zhou, R. J. Adrian, S. Balachandar, and T. M. Kendall. Mechanisms for generating coherent packets of hairpin vortices in channel flow. *Journal of Fluid Mechanics*, 387:353–396, 1999.

Appendix A

Permissions

AIP PUBLISHING LICENSE TERMS AND CONDITIONS

Jun 28, 2018

This Agreement between Mr. Rajat Chakravarty ("You") and AIP Publishing ("AIP Publishing") consists of your license details and the terms and conditions provided by AIP Publishing and Copyright Clearance Center.

License Number	4377531004732
License date	Jun 28, 2018
Licensed Content Publisher	AIP Publishing
Licensed Content Publication	Physics of Fluids
Licensed Content Title	Alternating half-loop shedding in the turbulent wake of a finite surface-mounted square cylinder with a thin boundary layer
Licensed Content Author	J. A. Bourgeois, P. Sattari, R. J. Martinuzzi
Licensed Content Date	Sep 1, 2011
Licensed Content Volume	23
Licensed Content Issue	9
Type of Use	Thesis/Dissertation
Requestor type	Student
Format	Print and electronic
Portion	Photograph/Image
Title of your thesis / dissertation	Turbulent Flow Visualization over Surface-mounted Finite-height Cylinders and Square Prisms
Expected completion date	Jun 2018
Estimated size (number of pages)	153
Requestor Location	Mr. Rajat Chakravarty 57 Campus Drive Department of Mechanical Engineering Saskatoon, SK S7N 5A9 Canada Attn: Mr. Rajat Chakravarty
Billing Type	Invoice
Billing Address	Mr. Rajat Chakravarty 57 Campus Drive Department of Mechanical Engineering Saskatoon, SK S7N 5A9 Canada Attn: Mr. Rajat Chakravarty
Total	0.00 CAD

Terms and Conditions

AIP Publishing -- Terms and Conditions: Permissions Uses

AIP Publishing hereby grants to you the non-exclusive right and license to use and/or distribute the Material according to the use specified in your order, on a one-time basis, for the specified

ELSEVIER LICENSE
TERMS AND CONDITIONS

Jun 28, 2018

This Agreement between Mr. Rajat Chakravarty ("You") and Elsevier ("Elsevier") consists of your license details and the terms and conditions provided by Elsevier and Copyright Clearance Center.

License Number	4377511429839
License date	Jun 28, 2018
Licensed Content Publisher	Elsevier
Licensed Content Publication	International Journal of Heat and Fluid Flow
Licensed Content Title	Instantaneous flow field above the free end of finite-height cylinders and prisms
Licensed Content Author	N. Rostamy,D. Sumner,D.J. Bergstrom,J.D. Bugg
Licensed Content Date	Oct 1, 2013
Licensed Content Volume	43
Licensed Content Issue	n/a
Licensed Content Pages	9
Start Page	120
End Page	128
Type of Use	reuse in a thesis/dissertation
Intended publisher of new work	other
Portion	figures/tables/illustrations
Number of figures/tables/illustrations	1
Format	both print and electronic
Are you the author of this Elsevier article?	No
Will you be translating?	No
Original figure numbers	Figure 3
Title of your thesis/dissertation	Turbulent Flow Visualization over Surface-mounted Finite-height Cylinders and Square Prisms
Publisher of new work	University of Saskatchewan
Expected completion date	Jun 2018
Estimated size (number of pages)	153
Requestor Location	Mr. Rajat Chakravarty 57 Campus Drive Department of Mechanical Engineering Saskatoon, SK S7N 5A9 Canada Attn: Mr. Rajat Chakravarty
Publisher Tax ID	GB 494 6272 12

AIP PUBLISHING LICENSE TERMS AND CONDITIONS

Jun 28, 2018

This Agreement between Mr. Rajat Chakravarty ("You") and AIP Publishing ("AIP Publishing") consists of your license details and the terms and conditions provided by AIP Publishing and Copyright Clearance Center.

License Number	4377531004732
License date	Jun 28, 2018
Licensed Content Publisher	AIP Publishing
Licensed Content Publication	Physics of Fluids
Licensed Content Title	Alternating half-loop shedding in the turbulent wake of a finite surface-mounted square cylinder with a thin boundary layer
Licensed Content Author	J. A. Bourgeois, P. Sattari, R. J. Martinuzzi
Licensed Content Date	Sep 1, 2011
Licensed Content Volume	23
Licensed Content Issue	9
Type of Use	Thesis/Dissertation
Requestor type	Student
Format	Print and electronic
Portion	Photograph/Image
Title of your thesis / dissertation	Turbulent Flow Visualization over Surface-mounted Finite-height Cylinders and Square Prisms
Expected completion date	Jun 2018
Estimated size (number of pages)	153
Requestor Location	Mr. Rajat Chakravarty 57 Campus Drive Department of Mechanical Engineering Saskatoon, SK S7N 5A9 Canada Attn: Mr. Rajat Chakravarty
Billing Type	Invoice
Billing Address	Mr. Rajat Chakravarty 57 Campus Drive Department of Mechanical Engineering Saskatoon, SK S7N 5A9 Canada Attn: Mr. Rajat Chakravarty
Total	0.00 CAD

Terms and Conditions

AIP Publishing -- Terms and Conditions: Permissions Uses

AIP Publishing hereby grants to you the non-exclusive right and license to use and/or distribute the Material according to the use specified in your order, on a one-time basis, for the specified

SPRINGER NATURE LICENSE TERMS AND CONDITIONS

Jun 28, 2018

This Agreement between Mr. Rajat Chakravarty ("You") and Springer Nature ("Springer Nature") consists of your license details and the terms and conditions provided by Springer Nature and Copyright Clearance Center.

License Number	4377511221742
License date	Jun 28, 2018
Licensed Content Publisher	Springer Nature
Licensed Content Publication	Experiments in Fluids
Licensed Content Title	Wake structure of a finite circular cylinder of small aspect ratio
Licensed Content Author	D. Sumner, J. L. Heseltine, O. J. P. Dansereau
Licensed Content Date	Jan 1, 2004
Licensed Content Volume	37
Licensed Content Issue	5
Type of Use	Thesis/Dissertation
Requestor type	academic/university or research institute
Format	print and electronic
Portion	figures/tables/illustrations
Number of figures/tables/illustrations	1
Will you be translating?	no
Circulation/distribution	>50,000
Author of this Springer Nature content	no
Title	Turbulent Flow Visualization over Surface-mounted Finite-height Cylinders and Square Prisms
Instructor name	n/a
Institution name	University of Saskatchewan
Expected presentation date	Jun 2018
Portions	Figure 11
Requestor Location	Mr. Rajat Chakravarty 57 Campus Drive Department of Mechanical Engineering Saskatoon, SK S7N 5A9 Canada Attn: Mr. Rajat Chakravarty
Billing Type	Invoice
Billing Address	Mr. Rajat Chakravarty 57 Campus Drive Department of Mechanical Engineering Saskatoon, SK S7N 5A9

ELSEVIER LICENSE
TERMS AND CONDITIONS

Jun 28, 2018

This Agreement between Mr. Rajat Chakravarty ("You") and Elsevier ("Elsevier") consists of your license details and the terms and conditions provided by Elsevier and Copyright Clearance Center.

License Number	4377510887962
License date	Jun 28, 2018
Licensed Content Publisher	Elsevier
Licensed Content Publication	Journal of Fluids and Structures
Licensed Content Title	Flow above the free end of a surface-mounted finite-height circular cylinder: A review
Licensed Content Author	D. Sumner
Licensed Content Date	Nov 1, 2013
Licensed Content Volume	43
Licensed Content Issue	n/a
Licensed Content Pages	23
Start Page	41
End Page	63
Type of Use	reuse in a thesis/dissertation
Intended publisher of new work	other
Portion	figures/tables/illustrations
Number of figures/tables/illustrations	1
Format	both print and electronic
Are you the author of this Elsevier article?	No
Will you be translating?	No
Original figure numbers	Figure 30
Title of your thesis/dissertation	Turbulent Flow Visualization over Surface-mounted Finite-height Cylinders and Square Prisms
Expected completion date	Jun 2018
Estimated size (number of pages)	153
Requestor Location	Mr. Rajat Chakravarty 57 Campus Drive Department of Mechanical Engineering Saskatoon, SK S7N 5A9 Canada Attn: Mr. Rajat Chakravarty
Publisher Tax ID	GB 494 6272 12
Total	0.00 CAD

CAMBRIDGE UNIVERSITY PRESS LICENSE TERMS AND CONDITIONS

Jun 28, 2018

This Agreement between Mr. Rajat Chakravarty ("You") and Cambridge University Press ("Cambridge University Press") consists of your license details and the terms and conditions provided by Cambridge University Press and Copyright Clearance Center.

License Number	4377510456132
License date	Jun 28, 2018
Licensed Content Publisher	Cambridge University Press
Licensed Content Publication	The Journal of Fluid Mechanics
Licensed Content Title	The finite-length square cylinder near wake
Licensed Content Author	H. F. WANG, Y. ZHOU
Licensed Content Date	Oct 5, 2009
Licensed Content Volume	638
Licensed Content Issue	undefined
Start page	453
End page	490
Type of Use	Dissertation/Thesis
Requestor type	Not-for-profit
Portion	Text extract
Number of pages requested	1
Order reference number	
Territory for reuse	World
Title of your thesis / dissertation	Turbulent Flow Visualization over Surface-mounted Finite-height Cylinders and Square Prisms
Expected completion date	Jun 2018
Estimated size(pages)	153
Requestor Location	Mr. Rajat Chakravarty 57 Campus Drive Department of Mechanical Engineering Saskatoon, SK S7N 5A9 Canada Attn: Mr. Rajat Chakravarty
Publisher Tax ID	123258667RT0001
Billing Type	Invoice
Billing Address	Mr. Rajat Chakravarty 57 Campus Drive Department of Mechanical Engineering Saskatoon, SK S7N 5A9 Canada Attn: Mr. Rajat Chakravarty
Total	0.00 CAD

Appendix B

3D POD Code

```
% Enter POD parameters
nx = 20; % points in the x-direction
ny = 20; % points in the y-direction
nz = 20; % points in the z-direction
N = 1000; % Total number of snapshots
M = 20; % Number of energy modes for the POD reconstruction
T = 50; % Instantaneous snapshot for the POD reconstruction

% Input snapshot coordinates from a data file
load E:\Square_Prism_POD_Files\3D_POD_Data\out_001.dat
X = out_001(:,1); % column vector of x-coordinates
Y = out_001(:,2); % column vector of y-coordinates
Z = out_001(:,3); % column vector of z-coordinates

% Input the velocity arrays
% This is implemented repeatedly for a sequential set of N filenames
load E:\Square_Prism_POD_Files\3D_POD_Data\out_001.dat
U1 = out_001(:,4); % column vector of u-velocities
V1 = out_001(:,5); % column vector of v-velocities
W1 = out_001(:,6); % column vector of w-velocities

% Concatenate velocities into N column vectors
% This is implemented repeatedly for a sequential set of N filenames
for i=1:nx*ny*nz
    V1(3*i-2) = U1(i);
    V1(3*i-1) = V1(i);
    V1(3*i) = W1(i);
end

V = [V1 V2 V3 .. VN];

% Calculate the fluctuating velocity
for i=1:N
    V(:,i) = V(:,i) - (sum(X1,2)/N);
end

% calculate the empirical correlation matrix C
C = V'*V/N;

% Calculate the POD basis
[evectorC,evalueC] = svd(C);
phi = V*evectorC;
lam = diag(evalueC);

% Normalize the POD basis
for i=1:N
    phi(:,i) = phi(:,i)/norm(phi(:,i),2);
end

% Calculate lower order POD reconstruction of an instantaneous field
phi2 = phi(:,M)*evectorC{T,:);
```

```
% Total energy calculations
tenergy = sum(lam);
energy = 0.;
nbasis = 0;
i = 1;
while (((energy/tenergy)*100) < cenergy)
    energy = energy + lam(i);
    i = i+1;
end
nbasis = i;

% Plot energy distribution
plot(lam(1:nbasis)/tenergy/100,'*')
xlabel('Number of POD eigenvalues')
ylabel('Energy captured')

% Output the k-th energy mode
for i=1:nx*ny*nz
    Uk(i)=phi(3*i-2,k);
    Vk(i)=phi(3*i-1,k);
    Wk(i)=phi(3*i,k);
end
outputk = [X Y Z Uk Vk Wk];

% Output the POD reconstruction
for i=1:nx*ny*nz
    Ur(i)=phi2(3*i-2);
    Vr(i)=phi2(3*i-1);
    Wr(i)=phi2(3*i);
end
outputr = [X Y Z Ur Vr Wr];
```